DEVELOPMENT OF FULL-BODY MODELS FOR HUMAN JUMP LANDING DYNAMICS AND CONTROL

by

D. Keoki Jackson

S.B., Massachusetts Institute of Technology, 1989
S.M., Massachusetts Institute of Technology, 1992

Submitted to the Department of Aeronautics and Astronautics
in Partial Fulfillment of the Requirements for the Degree of
Doctor of Science in Aeronautics and Astronautics

at the

Massachusetts Institute of Technology

June 1997

Signature of Author
Department of Aeronautics and Astronautics
May 23, 1997

Certified by
Dava J. Newman, Thesis Committee Chair
Assistant Professor of Aeronautics and Astronautics

Laurence R. Young
Apollo Professor of Astronautics
Department of Aeronautics and Astronautics

Neville Hogan
Professor of Mechanical Engineering

James D. Paduano
Associate Professor of Aeronautics and Astronautics

Accepted by
Jaime Peraire
Professor of Aeronautics and Astronautics
Chair, Departmental Graduate Office

DEVELOPMENT OF FULL-BODY MODELS FOR HUMAN JUMP LANDING DYNAMICS AND CONTROL

by

D. Keoki Jackson

Submitted to the Department of Aeronautics and Astronautics
on May 28, 1997 in Partial Fulfillment of the Requirements for the Degree of
Doctor of Science in Aeronautics and Astronautics

ABSTRACT

Human mechanisms for control of posture and motion are normally optimized to perform in Earth's 1-G environment. The mechanisms by which the central nervous system controls and integrates posture and movement are the subject of considerable controversy and ongoing study. The control of jump landings is particularly interesting: (1) the control algorithm involves elements of preplanned trajectory formulation and sensory feedback; (2) dynamic interaction with the environment must be addressed; and (3) the controller exhibits rapid adaptation when exposed to changes in environmental or perturbation conditions. When modeling the human motor control mechanisms, these issues must all be accounted for at various levels of detail.

Exposure to microgravity in astronaut subjects provide a novel opportunity to test models of human motion control. Microgravity alters the body dynamics, placing considerably different demands on the controller. When astronauts adapt to space flight, they exhibit quantitatively different control strategies, often measured as postflight degradation in performance for balance, locomotion, and jumping. The research described here centers on the development of dynamic models of motor control for human jumping to provide a framework for testing three hypotheses:

1. *Postflight changes in astronaut jump landings result from alterations in commanded impedance.*
2. *The experimentally observed characteristics of downward jumps in humans can be captured by a control model based on an equilibrium point formulation.*
3. *An optimization procedure based on a set of physically and biomechanically plausible variables is sufficient to reconstruct key features of the experimentally observed trajectories for jump landings.*

Three experiments are designed to test these hypotheses, and are performed at Johnson Space Center, MIT, and the Massachusetts General Hospital. Several astronaut subjects are tested before and after space flight to determine the effects of microgravity adaptation on jump landing performance. A "moonwalker" experiment simulates short term partial gravity exposure to supplement the astronaut tests. A novel "false platform" protocol assesses virtual trajectory generation and impedance modulation during jump landings by measuring free limb trajectories when subjects unexpectedly fall through the landing surface.

Three models for the control of jump landings are developed: (1) A linear second order model of center of mass (CM) vertical motion; (2) A second order model of CM vertical motion using a knee joint; and (3) A planar three link inverted pendulum model. The false platform data are used in concert with these models to estimate body stiffness and damping properties immediately following the time of impact. Optimization techniques are used to interpret modeled jump landing trajectories.

Astronaut results indicate that reduced inflight postural control demands result in one of two responses postflight. Postflight-Compliant (5/9) subjects retain somewhat reduced leg stiffnesses after space flight, while Postflight-Stiff (2/9) subjects exhibit an overcompensatory increase in leg stiffness. Moonwalker subjects follow the Postflight-Compliant group, indicating that partial weight unloading provides a useful analogue for certain aspects of microgravity adaptation. Impedance estimates using the false platform data indicate negative stiffnesses during the period immediately following impact. This implied instability suggests that such simple equilibrium point models cannot adequately describe jump landings. Optimization results capture the general features of the jump landing trajectories and indicate that controller requirements include impact force reduction as well as joint coordination to ensure appropriate mass center motion.

Thesis Supervisor:	Dava J. Newman
Title:	Assistant Professor of Aeronautics and Astronautics

This work is dedicated to my grandparents

Henry and Juanita Brodersen
"Papa" Robert and "Tutu" Janet Jackson

And in the twelfth year, on the seventh day of Ielool,
the month of reaping, he climbed the hill without the city walls
and looked seaward; and he beheld his ship coming with the mist.

Then the gates of his heart were flung open, and his joy flew far out to sea.
And he closed his eyes and prayed in the silences of his soul.

But as he descended the hill, a sadness came upon him,
and he thought in his heart: How shall I go in peace and without sorrow?
Nay, not without a wound in the sprit shall I leave this city.
Long were the days of pain I have spent within its walls, and aloneness;
and who can depart from his pain and his aloneness without regret?
Too many fragments of the spirit have I scattered in these streets,
and too many are the children of my longing that walk naked among these hills,
and I cannot withdraw from them without a burden and an ache.
It is not a garment I cast off this day,
but a skin that I tear with my own hands.
Nor is it a thought I leave behind me,
but a heart made sweet with hunger and with thirst.

Yet I cannot tarry longer.
The sea that calls all things unto her calls me, and I must embark.
For to stay, though the hours burn in the night,
is to freeze and crystallize and be bound in a mould.
Fain would I take with me all that is here. But how shall I?
A voice cannot carry the tongue and the lips that gave it wings.
Alone it must seek the ether.
And alone and without his nest shall the eagle fly across the sun.

Kahlil Gibran
The Prophet

ACKNOWLEDGMENTS

I am grateful to the members of my committee for their "advice and consent" on this thesis. Prof. Jim Paduano--thank you for your thorough reading of my draft and the skeptical "outsider's perspective." Prof. Neville Hogan, I appreciate your rigorous questions about the experiments and analysis, as well as the time you took to discuss the results--your enthusiasm makes me sorry to switch fields of work. Prof. Larry Young, your encyclopedic knowledge of the biomedical field and spaceflight literature was invaluable and inspiring. I have thoroughly enjoyed working with you over the past several years, and I am grateful for the tremendous opportunities you granted me to work with the human space program. Above all, I am indebted to Prof. Dava Newman--advisor, teacher, ex-officemate, mentor, and friend. Your unflagging support made the doctoral program endurable and often enjoyable. Now let's go sailing . . . .

Dr. Jacob Bloomberg and his colleagues at the Neuroscience Laboratory at JSC made the astronaut work in this thesis possible, and provided me with several enjoyable and educational visits to Houston. Dr. Bloomberg designed the astronaut jumping experiment, and also sponsored my NASA GSRP fellowship. Thanks also to Brian Peters and Shannon Smith, who performed the astronaut tests, and to Dr. Vernon McDonald for useful discussions and commentary on the analysis. Similarly, I am grateful to Dr. David Krebs of MGH for making available his laboratory and providing me with the opportunity to become intimate with UNIX. Mahalo to all of the great people in the BML who made my time there enjoyable as well as productive: Dan, Ronny, Jose, Lisa, and above all Simone Bortolami, who has been a great friend, advisor, commiserator and fellow caffeine addict. Thanks to all of my experimental subjects: astronauts, fellow students and friends. I'm afraid I have a knack for designing uncomfortable experiments, from scleral coils to "just go ahead and jump--you'll be fine. Trust me!" And then there's the moonwalker harness. Thanks for volunteering--and then coming back to do the exciting balance tests.

I am deeply appreciative of the support of Prof. Win Markey, who hired me to TA undergraduate controls and inspired me to attempt to meet his high standards of teaching. Prof. Markey--I've learned much from you in recent years that goes beyond what you taught me in your course my junior year. Likewise, thanks to Prof. Lenny Gould for the chance to teach "over in Course 6"--I enjoyed your enthusiasm and fine sense of humor. I am also grateful to all of the staff members who helped me to navigate the ways of the Institute: Anne Maynard, Ping Lee, Liz Zotos, Marie Stuppard, Jennie Leith, Barbara Glas, Beverly Linton, Don Wiener and Dick Perdichizzi. And of course, Sherry Modestino and Jim Costello--I was truly sorry to see you leave the MVL.

And cheers to all the fellow MVL students and associates over the years, from Jock and Glaw to the latest crop. A toast to all of the people who made SLS-2 such a blast: Karla Polutchko, Dan Merfeld, Juan-Carlos Mendoza, Ted Liefeld, Scott Stevenson, Corrie Lathan, Stuart Johnston (and George). Clear skies to Karl Schultz, who provided unending hilarity and bottomless beers in his memorable to years at MIT. Hugs and kisses to my outrageous officemate Jen Rochlis (not that I've been in the office much)--you'll get your dessert someday. Grant Schaffner--you've lost your only competitor for "old man of the lab"--keep up the great work and take care of my kids at Next House. Don't forget to invite me to the wedding. Amir--thanks for all of your help and support in the past months--your graciousness and poise provide an example to all of us. Steve Robinson, it was great having you with us at MIT--I look forward to the day when we all rejoin you at JSC. Meanwhile, thanks for the floor space.

One aspect of MIT I will miss the most is my time as a floor tutor at Next House. Good luck to all my "kids", past and present--I hope you enjoyed the food, because certainly I enjoyed your good company, high spirits and wall-shaking music. Bora and Liba Mikic, I am sorry to be leaving you, and not just because of all the incredible food. Thanks to all of the other floor tutors and to the RCA staff for a great sense of community--now let's get in a circle and hold hands. Others I will miss are the noontime "fast" lane at the MIT pool--Phil and Phil, Christian, and Pete and Pete. Keep up the yardage. Best wishes to Joelle, Paula, Charrissa, Peter (Noymer), Harald, Mike T., Piero, Marcos, and all of the others whom my sleep-deprived condition is preventing me from remembering, but who made MIT a place to remember fondly. Finally, thanks to Scott Adams for creating Dilbert, and to McKinsey & Co. for offering me tons of money so that I can feel noble about turning down the job and "staying true to the engineer in me."

To my family--Nicole, Jodi, Keaka, mom and dad--thank you for believing in me, and yes, I really am graduating *this* spring! To the friends who have shared my triumphs and failures, hopes and fears, joys and sorrows--especially Bill Coleman, Alan Nash, Mike Feeney, Peter Neirinckx, Richard Seet, John Carey and Karla Polutchko, I look forward to many years of good times to come (now that this PhD thing is out of the way). And most of all, I thank Nikol Heacock, without whom I could never have accomplished what I did. Experimental subject, data analyst, graphic artist and typesetter--those are only your *direct* contributions to my thesis. More importantly, you have been a constant source of support, encouragement, nourishment both physical and spiritual, and love, and I am forever indebted to you. To all of you--I couldn't have done it without you, and I wouldn't have wanted to.

This work was supported by NASA Grant NGT-51228 and NASA Contract NAS1-18690.

TABLE OF CONTENTS

LIST OF FIGURES

CHAPTER 2

CHAPTER 3

CHAPTER 4

CHAPTER 5

LIST OF TABLES

CHAPTER 3

CHAPTER 4

CHAPTER 5

APPENDIX B

1 INTRODUCTION

Investigation of human postural and full-body motion behavior has largely focused on the descriptive aspects: data on body kinematics, electromyogram (EMG) measures of muscle activation, and ground reaction forces have been collected for a variety of human movements including voluntary actions and reflex motions. In the midst of this profusion of data, however, there is still little agreement on questions as fundamental as whether posture and movement should be considered as independent or integrated control problems. Patterns of movement and muscle synergies have been identified, and the issue of which different sensory modalities contribute to postural corrections has been addressed, yet the answers to very basic questions remain elusive: *how* are postural and movement commands formulated from motor programs and sensory input? Perhaps more important, *why* does the central nervous system (CNS) command certain motions and corrections but not others?

The study of jump landings is no exception. Patterns of muscle activation have been studied for both voluntary jumps and unexpected falls. The body kinematic behavior has been recorded and joint torques have been computed. Experimental conditions such as the height of the jump, the visual surround motion and the composition of the landing surface have been varied, and the effects on muscle and motion patterns have been described. However, the underlying processes by which the CNS generates commands to actuate the joints and control the landing have not been adequately modeled.

Given the ongoing debate about the mechanisms of motor control in tasks ranging from simple single joint arm motions to full-body, multiple joint activities such as locomotion, it is not surprising that many aspects of motor control adaptation in microgravity and readaptation upon return to earth are not well understood. The effects of gravity in the normal terrestrial environment are pervasive, and control of posture and movement has evolved in tandem with the structure of the body to take advantage of life in the gravitational potential field. Even so, the structure of the nervous system permits a marvelous level of adaptability, and astronauts quickly learn to enhance their performance in microgravity during space flight, potentially at the expense of modifying or eliminating patterns of motor control optimized for the 1-g environment. Exposure to microgravity has a substantial effect on human postural control during jump landings, locomotion and even quiet standing upon return to earth-normal gravity.

The central goal of this thesis is to advance the understanding of human motor control by investigating the way humans land from downward jumps. This thesis makes contributions in three particular areas. First, the problem of explaining changes in downward jumping in astronauts following microgravity exposure is addressed, and a simple model based on adaptive control of limb stiffness is formulated to clarify key features of astronaut postflight jumping performance.

Second, the possibility that stiffness may contribute more fundamentally to the motor control of jump landings is considered. The equilibrium point hypothesis for motor control states that posture and movement may be controlled by a common process [Bizzi *et al.*, 1992a] that relies on springlike properties of the muscles and their stretch reflexes. Appropriate choices of muscle length-tension curves may define equilibrium limb positions and simultaneously set impedance properties, allowing the CNS to generate limb trajectories via a control signal that defines a series of equilibrium points in time.

Under the equilibrium point hypothesis, the springlike properties of the neuromuscular system cause torques based on the difference between the actual limb position and the equilibrium point, resulting in limb trajectories that follow the equilibrium trajectory. The actual trajectory depends on the commanded impedance, limb dynamics and environmental perturbations as well as the virtual trajectory. It has been suggested that equilibrium point control could equally well subserve free motions and tasks requiring interaction with the environment. By definition, jump landings require interaction between the body and the environment and are used here to test the applicability of the equilibrium point hypothesis to this class of problems.

Third, an optimization approach is used to evaluate the trajectories observed experimentally in jump landings. Optimal control approaches have been applied successfully to the problem of understanding the takeoff phase in maximum height jumping, but have not yet been applied to the impact absorption phase of jump landings. This thesis considers the possible optimality of jump landings to gain insight into the factors that shape jump landing trajectories.

Initially, the landing control problem might seem relatively simple, requiring only that the kinetic energy developed during the flight phase of the jump be dissipated while moving the body center of mass (CM) to lie over the base of support (the feet). However, the problem is both interesting and complicated for several reasons. The role of sensory feedback from muscle spindles, tendon organs and vestibular and visual modalities must be considered, but the system response is not simply that of a regulator reacting to a disturbance input. Instead, the body trajectory and limb impedance are actively controlled in flight and at impact, indicating some level of motor pre-programming and feedforward trajectory generation. Furthermore, the controller must maintain stability both in free flight and in the face of coupling with the physical environment (the ground). Finally, the CNS controller exhibits adaptive behavior upon exposure to changes in environmental or perturbation conditions.

Currently, better dynamic models are needed to explore the control of downward jumping in humans and provide a theoretical base to address the changes in jump performance following microgravity exposure. Models of the motor control laws that enable successful stable landing from jumps in humans must incorporate the human body dynamics at varying degrees of complexity. The control models described here attempt to replicate the key features found in experimental observations of jump landings, and are used to explicate the effects of microgravity adaptation and evaluate the equilibrium point hypothesis. This thesis describes three experiments and associated dynamic models designed to validate or disprove three hypotheses concerning the way humans control landings from downward jumps. These three hypotheses are detailed in the next section, and followed by an overview of the remainder of the thesis, including the experiments, analysis, modeling and discussion.

1.1. HYPOTHESES

Hypothesis 1: *Postflight changes in astronaut jump landings result from alterations in commanded impedance characteristics which derive from motor adaptation appropriate to the demands of microgravity.*

Upon returning to earth and its gravity field following space flight, astronauts often show remarkable decrements in the performance of everyday tasks. Examples include exaggerated postural sway during standing (especially in the dark, or in the presence of moving visual displays), wide foot placement and difficulty in negotiating turns during walking, and instability during the landing phase of "drop" experiments [Nicogossian *et al.*, 1994]. Recently, research on NASA astronauts has targeted postflight decrements in coordination between eye and head movements, evaluated pre- and postflight muscle activation patterns during gait, and investigated adaptive changes in single-joint kinematics through phase-plane and intersegmental energy transfer analysis [Bloomberg *et al.*, 1997; Layne *et al.*, 1996; McDonald *et al.*, 1996].

However, little quantitative analysis has been performed to explain the underlying adaptive physiological mechanisms, especially in terms of dynamic whole-body motor control. It is believed that motor programs evolved for the control of body motion and limb-environment interactions under Earth-normal 1-g conditions are often inappropriate in microgravity, and astronauts adapt accordingly during space flight. These adaptations appropriate to 0-g prove maladaptive upon return to 1-g, and the astronauts exhibit musculoskeletal responses that result in quantifiable differences from preflight in body posture, locomotion and jumping performance. The hypothesized dependence of postflight jumping changes on leg impedance characteristics is tested using body kinematic data and a simple model of the CM motion.

While the CNS adaptation to the reduced demands on the postural control system in microgravity likely plays an important role in postflight changes, many other effects related to space flight may also take part. For this reason, a ground-based partial weight unloading experiment is designed to supplement the astronaut data. Its aim is to show that simply reducing the support requirements on the legs for a short time can induce changes analogous to those seen in astronauts following space flight, while avoiding potentially confounding issues such as muscular atrophy and vestibular reinterpretation.

Hypothesis 2: *The experimentally observed characteristics of downward jumps in humans can be captured by a control model which defines a "virtual trajectory" for the limbs during the flight and impact absorption phases of the jump landing. The impedance of the limbs with respect to the commanded trajectory is also specified by this model, determining the perturbation response and the actual trajectory of the limbs upon landing.*

Various studies of single and multijoint movement have provided evidence for the equilibrium point hypothesis of motor control [Bizzi *et al.*, 1992]. The majority of studies to date have considered single joint arm motions or planar reaching arm motions involving two joints. Use of a comparable paradigm in the control of robot manipulators has demonstrated stable performance during free motion, motion during contact with a rigid surface, and transitions between the two conditions [Hogan, 1987]. To date, equilibrium point approaches have not been seriously attempted for lower extremity or full-body motion. Furthermore, few attempts have been made to apply the virtual trajectory hypothesis to intact motor control in tasks dealing with substantial environmental interaction.

Extension of this theory to the control of jump landings requires experimentally derived knowledge of the commanded virtual trajectory as well as models of the human body dynamics, the CNS control of limb impedance and the interaction with the environment. Using an experimental protocol previously not applied in human subjects, a false platform landing test is designed to reveal whether or not the CNS commands an attractive virtual trajectory. The equilibrium point hypothesis is interpreted using three models of increasing complexity, from a single degree of freedom linear model of vertical CM motion to a nonlinear three link inverted pendulum model of the human body.

Hypothesis 3: *A trajectory optimization procedure based on a set of physically and biomechanically plausible variables is sufficient to reproduce key features of the experimentally observed trajectories for jump landings. Specific optimization criteria include CM excursions, joint motion, joint torques and impact forces.*

An important goal of this thesis is understanding why certain trajectories are selected by the CNS. Prior work has focused on the optimality of takeoffs in maximum height jumping [Pandy *et al.*, 1990; Pandy and Zajac, 1991; Selbie and Caldwell, 1996]. In this thesis, objective functions are formulated for two models of jump landing dynamics to generate optimal trajectories that closely match the actual trajectories seen in the impact absorption phase of the jump landing. Weights in the cost functions are varied to gain insight into the tradeoffs made by the CNS in selecting appropriate landing trajectories.

1.2. THESIS OVERVIEW

The remainder of this thesis is divided into five chapters. Chapter 2 provides additional background and a literature review of topics relevant to this thesis. Chapters 3 and 4 are devoted to descriptions of the thesis experiments and their results. Chapter 5 develops dynamic models of jump landings, and applies these models to the equilibrium point hypothesis. Optimality properties for the models are also considered in Chapter 5. Finally, Chapter 6 summarizes the conclusions from the thesis work and provides recommendations for future study. The chapter contents are summarized below.

Chapter 2: This chapter presents relevant prior work described in the literature. Specific areas of focus include (1) studies of downward jumping in humans and animals; (2) microgravity adaptation effects on human motor performance; (3) theories of motor control, with emphasis on equilibrium point hypotheses; and (4) optimality in motor performance.

Chapter 3: The experiments dealing with adaptation effects on downward jumping are detailed here. The astronaut pre- and postflight tests are presented first, followed by the "moonwalker" partial weight unloading experiments. A second order model of vertical CM motion is developed and applied to both data sets. The results from the two experiments are compared.

Chapter 4: In this chapter, the false platform jumping experiments are described. Processing and analysis of the kinematic data is covered. The results of the platform (P) and no-platform (NO-P) jumps are compared, and the significance of the NO-P results is discussed.

Chapter 5: Three models are developed for the impact absorption phase of jump landings. The first two models consider only the vertical motion of the full body CM. In one model, the CM is supported by a linear spring and damper. In the second, a knee joint is incorporated about which a torsional spring and damper act, providing a vertical stiffness which depends on the knee joint angle. The third model consists of a planar, three link inverted pendulum pinned to the ground at the ankle. Using the data from the false platform experiment, the equilibrium point hypothesis is assessed for each model. Best fit stiffness and damping values are calculated, and virtual trajectories are computed for suitable stiffness and damping fits. The viability of the equilibrium point hypothesis for the jump landing task is discussed. Also, objective functions are developed for the first and third models to derive optimal trajectories which match the experimental data. The weights in the objective functions are varied, and the results are discussed.

Chapter 6: The conclusions from the experimental and modeling sections are summarized. Based on these conclusions, possible topics for future work are proposed.

1.3. ACRONYMS AND ABBREVIATIONS

The following acronyms and abbreviations are used in this thesis:

'	foot
"	inch
0-g	zero gravity or microgravity
1-g	Earth normal gravity
ANOVA	analysis of variance
BML	Biomotion Laboratory
BW	body weight
cm	centimeter
CM	center of mass

CNS	central nervous system
EC	eyes closed (astronaut jumping experiment)
EMG	electromyogram
EO	eyes open (astronaut jumping experiment)
FAS	feasible acceleration set
FIR	finite impulse response
GRF	ground reaction force
HAT	head, arms and trunk
JSC	Johnson Space Center
kg	kilogram
LED	light emitting diode
LQR	linear quadratic regulator
MANOVA	multivariate analysis of variance
MGH	Massachusetts General Hospital
m	meter
mm	millimeter
ms	millisecond
NASA	National Aeronautics and Space Administration
N-C	no change (subjects in the astronaut jumping experiment)
NO-P	no platform (jumps where the subject falls through the paper target)
P	platform (jumps where the landing platform is present under the paper)
P-C	postflight-compliant (subjects in the astronaut jumping experiment)
POST	postflight test session (astronaut jumping experiment)
PRE1	first preflight test session (astronaut jumping experiment)
PRE2	last preflight test session (astronaut jumping experiment)
P-S	postflight-stiff (subjects in the astronaut jumping experiment)
RMS	root mean square
ROT	postural support dorsiflexion rotations
RTS	Rauch-Tung-Striebel (filter)
SS	sum of squares
TA	tibialis anterior
TRACK	Telemetered Real-time Acquisition of Kinematics
TRANS	postural support backward translations
VT	virtual trajectory

2 BACKGROUND AND LITERATURE REVIEW

This section reviews some of the major relevant work in the fields of biomechanics, posture and movement control, robot control and human space flight adaptation. Literature on jumping and landing from unexpected falls is covered first. Results dealing with the effects of microgravity exposure during space flight on the control of posture and movement are considered next. Posture control and applicable models are discussed in the third section, and further issues relevant to motor control are presented last.

2.1. JUMPING

2.1.1. Voluntary Downward Jumps

Study of jump landings has largely been limited to descriptions of the joint kinematics, EMG activation patterns and lower extremity joint moments. McNitt-Gray [1993] examines the leg kinematics and kinetics for jump landings from three different heights. She finds that ankle moments are plantarflexor throughout the landing phase, and hip and knee moments are also extensor except during the early landing phase. During the first quarter of the landing phase the knee and hip moments tend to oscillate out of phase with each other. Although joint moments tend to peak earlier with increased landing velocity, overall the kinematic and kinetic events are consistent across velocities. Knee and hip flexion (but not ankle flexion) increase for larger drops, as do all three joint angular velocities and joint moments. The relative increase in moment for higher drops is largest for the knee, followed by the hip and ankle respectively, indicating that relatively greater demands are placed on the knee for energy absorption at higher landing velocities. At higher impact velocities, recreational athletes use more hip flexion, lower peak extensor moments and longer landing phases than gymnasts, who favor less hip flexion and higher peak extensor moments. She suggests that a common landing strategy is used for different height jumps, and is progressively adjusted by selectively changing joint moment gains.

McKinley and Pedotti [1992] study changes in joint kinematics and EMG patterns for jump landings on rigid and compliant surfaces. In general they find that the lower limb reaches its largest extension prior to landing, and that the limbs are already slightly flexed at impact. The early part of ground contact is characterized by simultaneous flexion of the ankle, knee and hip joints, while only the knee and hip continue to flex during the latter part of the impact phase. A consistent muscle pattern is also observed. A burst of the biceps femoris in flight corresponds to the slight flexion of the limb before impact. The rectus femoris and vastus lateralis become active slightly before touchdown and remain active throughout the ground contact phase. The ankle extensors are continuously active from mid-flight, while the tibialis anterior activity begins within 150 ms prior to impact, is more burst-like, and peaks during the ground contact.

Skilled subjects exhibit larger ankle extension at impact when landing on the rigid surface as compared to foam surface landings, combined with greater ankle range of motion during impact absorption. Unskilled subjects choose a single "default" angle for both landing conditions in the middle of the range of angles used by skilled subjects on the two surfaces. Both skilled and unskilled subjects show a global shift of muscle activation to onsets closer to impact for landings on the compliant surface. The onset of leg musculature activation in a distal to proximal sequence prior to landing indicates advance preplanning of the motion. Other investigators demonstrate that EMG onset is closely linked to expected time of impact, by using false paper platforms and changing the height of jumps for blindfolded animals [McKinley and Smith, 1983; Dyhre-Poulsen and Laursen, 1984]. The observation that knowledge of the landing surface compliance overrides visual cues regarding time to impact hints that the muscle synergies may well be preprogrammed before flight.

2.1.2. Sudden Falls

In addition to the variable muscle activation patterns seen for voluntary jumps, reflex reactions occur in subjects exposed to sudden drops. The otolith-spinal reflex elicited by sudden falls has been studied by Melvill Jones and Watt [1971b] and Watt *et al.* [1986]. This involuntary response is triggered by otolith excitation and can be observed in many flexor and extensor muscles throughout the body. In the ankle extensors, the reaction takes the form of two bursts of EMG activity. The early burst, which occurs from 50 to 150 ms after fall onset, is fixed relative to the time of release and is independent of fall height. It is proportional to the acceleration stimulus magnitude and is reduced by rotating the gravity vector 90° relative to the body. Furthermore, it does not habituate with repeated testing. It appears that the earliest phase of this early burst is not susceptible to voluntary control, while the later phase is influenced by mental set.

2.1.3. Jump Takeoff Control

Pandy, Zajac and others have applied optimal control techniques to the problem of maximum height jumping [Zajac, 1993; Pandy and Zajac, 1991; Pandy *et al.*, 1990; Selbie and Caldwell, 1996]. They model the body as a four segment planar linkage with frictionless hinge joints. Eight musculotendon actuators incorporate elastic tendons and

Hill-type muscle models driven by a first order representation of activation dynamics. Because the derivatives of the states are linear in the controls, the formulation of the problem leads to bang-bang optimal controls. The solution to the optimal control problem then depends on finding the switching times for the controls. The authors also address the issue of the discontinuity in the system dynamics in the transition from the flat-footed part of the jump to the heel-off portion. They succeed in replicating the major features of maximum height jumps, including muscle activation sequences, limb kinematics and ground reaction forces. Findings indicate that jump height is relatively insensitive to musculotendon compliance, and that uniarticular muscles (gluteus maximus and vastus lateralis) generate the propulsive energy while biarticular muscles fine-tune the coordination.

2.2. SPACE FLIGHT EFFECTS

A wide variety of tests have been performed on astronauts since the beginning of the space age to assess the effects of microgravity on human performance [Nicogossian *et al.*, 1994]. Experiments by Young, Oman and others have demonstrated significant changes in the interpretation of sensory cues following adaptation to microgravity: utricular otolith signals are apparently reinterpreted to indicate head linear acceleration rather than tilt, and increased weighting is placed on visual and tactile cues for posture control and the perception of orientation [Young *et al.*, 1986]. Following space flight, subjects exhibit difficulty maintaining erect posture with eyes closed except within a narrow "cone of stability."

Gurfinkel [1994] reviews some of the results relevant to motor and posture control from two Franco-Soviet space flights. In space, the astronaut tends to maintain the typical erect postural configuration, although he leans forward to a greater extent than on earth for the first 2-3 days of space flight. The distribution of tonic antigravity muscle activity is also altered: the high soleus activity found in earth conditions is replaced by activity in the antagonist tibialis anterior, and increased EMG responses are found in the quadriceps. Interestingly, counterphase motions of the trunk and lower limbs that maintain the mass center over the base of support during significant body tilts are retained in space even though the functional balance requirement have been removed. Rapid arm raising movements which produce anticipatory suppression of soleus activity in 1-g instead cause suppression of tibialis anterior activity in space. Even some low-level postural responses are changed: the stretch reflex of the tibialis anterior is shown to be considerably weakened following 2-3 days of flight.

Experiments conducted by Watt *et al.* [1986] find alterations in the vestibulo-spinal reflex under microgravity conditions. The earliest subcomponent of the "early" phase of the otolith-spinal reflex response to a sudden fall is shown to diminish immediately upon reaching orbit. It continues to decrease during the flight, and stimuli that elicited strong responses preflight are found to be close to or below the response threshold after the first mission day. This result suggests that otolith information is gradually ignored by the nervous system in weightlessness. However, responses found postflight are not significantly different from preflight, indicating that the readaptation process takes place very quickly. All subjects are unsteady postflight, and one falls over backwards consistently, commenting that his legs are always further forward than he expects them to be. Another subject states postflight that he feels the floor is coming up to meet him, and is there before he is ready for it on the way down. Such comments point to altered perception of both vestibular and proprioceptive cues.

Bloomberg *et al.* [1997] observe a "head-locking" strategy during gait in some astronauts postflight, a strategy often adopted by patients with defective vestibular systems. Similarly, astronauts demonstrate abnormal postural sway oscillations and drift immediately postflight for a sway-referenced support surface; the data are almost identical to tests of a patient with reduced vestibular function [Paloski *et al.*, 1993].

2.3. EQUILIBRIUM POINT HYPOTHESIS FOR MOTOR CONTROL

The spatial features of voluntary body and limb movements in extrinsic coordinates appear to be represented and planned at some high level of the CNS such as the motor cortex. An important area of motor control research involves the transformation of desired trajectories into appropriate muscle activations. Some investigators propose that the CNS solves the inverse kinematics problem to determine joint trajectories from the desired limb endpoint trajectory, then explicitly derives the necessary muscle forces using an inverse dynamics solution [Hollerbach and Atkeson, 1987]. Such computations imply internal estimates of body segment inertial parameters and dimensions and muscle moment arms. Slotine [1985] has shown that small errors in the estimates of inertial properties may result in instability. The apparent computational complexity and sensitivity to model errors in this approach has led to a quest for simpler solutions to the inverse kinematics and inverse dynamics problems.

The equilibrium point hypothesis was first proposed by Feldman [1966] and has been the subject of several reviews [Feldman, 1986; Bizzi *et al.*, 1992a; McIntyre and Bizzi, 1993; Feldman and Levin, 1995]. This hypothesis is based on the idea that the neuromuscular system exhibits position-dependent properties which tend to restore the limbs to a commanded equilibrium posture. A key point of the hypothesis is that muscles exhibit spring-like behavior, and somewhat resemble tunable springs with force generation that depends on both length and neural activation [Rack and Westbury, 1974]. Control of relative activation of the relative agonist and antagonist muscles acting about a joint results in the specification of an equilibrium posture for the joint as well as the stiffness about the equilibrium position. A study of perturbations from static arm posture in humans [Mussa-Ivaldi *et al.*, 1985] shows that the conservative components of the elastic force field are much larger than the non-conservative components, indicating that the neuromuscular properties are largely spring-like in the multiarticular arm.

Central commands may generate a sequence of equilibrium positions for a limb, and the spring-like properties of the system will tend to drive it along a trajectory which follows these intermediate equilibrium postures. Hence, the same mechanism applies to the control of both static posture and voluntary movement. Because the equilibrium position is defined as the position which the limbs would attain in the absence of external forces if central commands were frozen at a particular moment, the actual equilibrium point is generally different from the commanded equilibrium in the presence of static loads. Hence, the commanded equilibrium position is often referred to as a virtual position, and a time sequence of commands gives rise to a set of virtual positions known as a virtual trajectory. It has been noted that the virtual trajectory need not remain within the feasible workspace of the limb, and may pass into solid objects or surfaces [Bizzi *et al.*, 1992a].

The equilibrium point hypothesis has two especially attractive features: simplicity and stability. First, the centrally commanded equilibrium trajectory resembles the desired actual trajectory, avoiding explicit solution of the inverse kinematics and inverse dynamics problems. Second, passive stiffness and damping properties of the neuromuscular system provide stability for free motions and movement during contact with the environment. Two main versions of the equilibrium point hypothesis exist, and are known as the "alpha" and "lambda" models.

2.3.1. Lambda Model of Equilibrium Point Hypothesis

The lambda model of the equilibrium point hypothesis is based on the idea that shifts in the equilibrium state of the motor system can be generated by changing the threshold (λ) of the stretch reflex [Feldman, 1986]. When lambda remains constant, an invariant characteristic relates muscle length and force, so that the muscle in concert with central and reflex commands acts like a nonlinear spring (Figure 2.1).

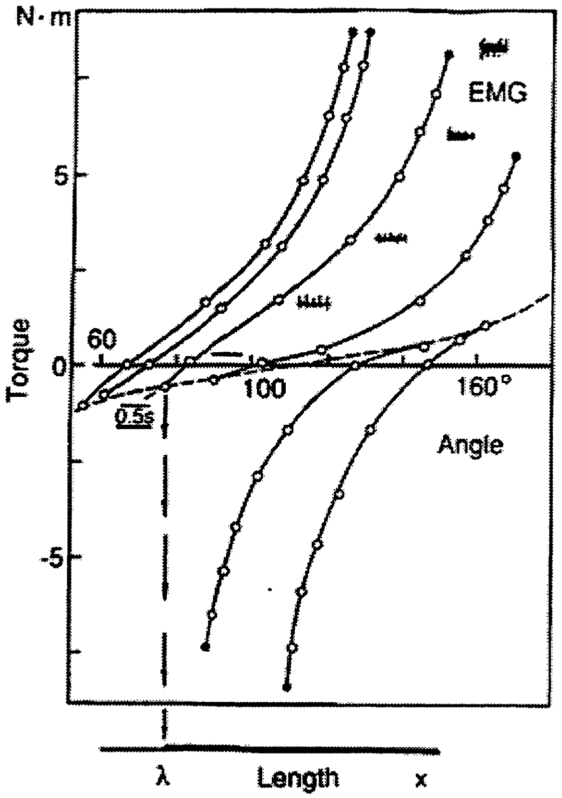

Figure 2.1. Invariant characteristics in lambda equilibrium point model. This family of invariant characteristics (ICs) relates joint angle and joint torque for elbow flexors (upper curves) and extensors (lower curves). The dashed line indicates passive joint characteristics when both muscles are relaxed. The parameter λ for a given IC corresponds to the muscle length where the active IC deviates from the passive curve [from Feldman and Levin, 1995].

Muscle recruitment F is given by

$$F = F(x-\lambda^*) = \begin{cases} 0 \ \ \forall \ \ x-\lambda^* \leq 0 \\ \alpha(x-\lambda^*) \ \cdot\forall \ \ x-\lambda^* \leq 0 \end{cases} \tag{2-1}$$

$$\lambda^* = \lambda - \mu v$$

where x = muscle length
v = rate of change of muscle length
λ = static threshold muscle length for stretch reflex
μ = damping factor
$\alpha(s)$ = monotonically increasing function of s

Muscles are activated reflexively due to perturbations in x or centrally due to changes in λ. Feldman and Levin [1995] suggest that the threshold lengths λ for antagonist muscles acting about a joint are set by descending reciprocal (R) and coactivation (C) commands. Ramp changes in the R and C commands generate shifts in the joint equilibrium position, causing movement of the limb. Movement speed is controlled by varying the duration of the ramp changes.

Three main criticisms have been leveled against the lambda model [reviewed by Bizzi *et al.*, 1992a]. First, its reliance on reflex pathways for the generation of movement is inconsistent with experimental demonstration of the ability of deafferented monkeys to make goal-directed movements in the absence of proprioceptive or visual position feedback. Second, the gain of the stretch reflex during movement appears to be too small to contribute significantly to force generation. Third, time delays in the reflex loops may contribute to instability.

2.3.2. Alpha Model of Equilibrium Point Hypothesis

The alpha model is based on the inherent mechanical properties of muscle. In this model, central commands set rest lengths and stiffnesses for the muscles. For two or more muscles acting in opposition about a joint, combined muscle settings result in an equilibrium position of the joint at which net torques are zero. Displacement of the limb from this position generates restoring torques, and movements can be generated by adjusting muscle activation levels to vary the equilibrium point along the desired path. Appropriate values of muscle stiffness and damping will cause the actual path of the limb to approximate closely the equilibrium point trajectory.

The reliance on intrinsic muscle properties in this model avoids difficulties with time delays in neural feedback, and is consistent with the ability of deafferented monkeys to perform pointing movements in the absence of feedback [Bizzi *et al.*, 1984]. The experiments with deafferented monkeys do show decrements in performance in the absence of feedback, however, and Figure 2.2 shows a formulation of the alpha model which incorporates both intrinsic muscle properties and stretch reflex pathways. Because the inherent stiffness properties of the muscles are essential to the alpha formulation, the validity of the alpha model has been questioned on the basis of negative stiffness measurements in individual muscles and about joints in portions of the normal operating range [Hasan, 1992]. The impact of this criticism is unclear, however, as the force-position relationship need only be positive definite throughout a region which includes the equilibrium point [Bizzi *et al.*, 1992b]. Won and Hogan [1995] demonstrate strong positional stability properties in the arm during perturbed point-to-point arm movements, reinforcing the idea that an attractive virtual trajectory underlies such movements.

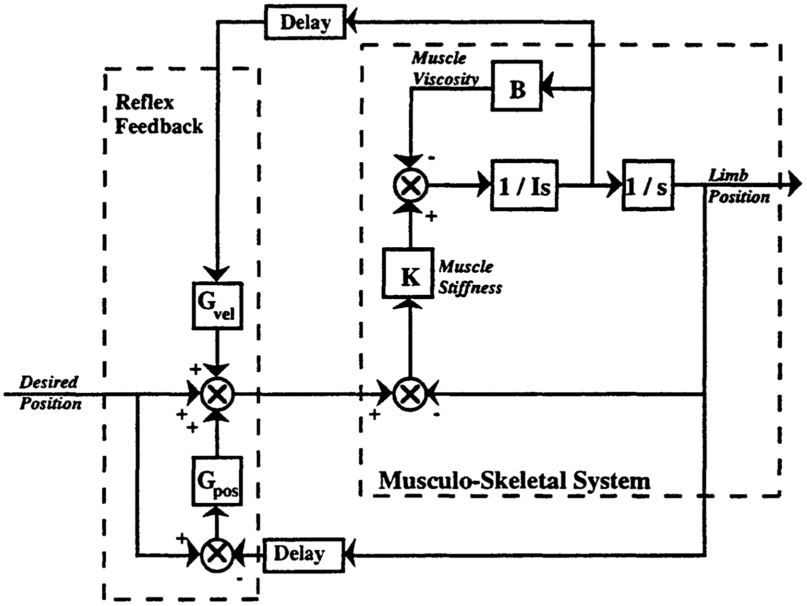

Figure 2.2. Alpha model of equilibrium point control about a single joint. This model includes intrinsic muscle properties (stiffness K and damping B) and reflex function (position gain G_{pos} and velocity gain G_{vel}). I represents the limb inertia, and s is the Laplace transform variable. [From McIntyre and Bizzi, 1993.]

2.3.3. Virtual Trajectories in Voluntary Arm Movements

One of the most attractive properties of the equilibrium point hypothesis is the potential ability to use simple virtual trajectories which can be planned without complex computation. Flash [1987] demonstrates that the equilibrium point hypothesis can be used to model two-joint planar reaching movements in the arm at moderate speeds. She simulates straight-line virtual trajectories with between the two endpoints with unimodal velocity profiles. Using joint stiffness parameters derived from experimentally measured static values, she shows that her model captures both qualitative features and quantitative kinematic details of the experimentally measured trajectories.

However, the simple trajectories found by her and others [McIntyre and Bizzi, 1993] depend on adequate stiffness values. More complex "N-shaped" virtual trajectories have been found necessary by other investigators [Hogan, 1984; Latash and Gottlieb, 1991]. This effect becomes more severe as movement speed is increased. The stiffness required by the simple virtual trajectories would increase with the square of the movement velocity, a possibility that is not supported by experimental results. Gomi and Kawato [1996] perturb reaching arm movements to determine stiffness and damping values during motion, and estimate complex virtual trajectories with multiple velocity peaks.

Such virtual trajectories of greater complexity indicate that servo models of motor control may be inadequate, since the actual trajectories no longer closely resemble the inputs. Furthermore, complex virtual trajectories imply that the CNS must acquire internal models of the limb dynamics. McIntyre and Bizzi [1993] propose augmenting the position trajectory command with a velocity command to allow use of simple virtual trajectories for fast movements in the absence of large stiffness increases. However, Gomi and Kawato [1996] indicate that this modification does not result in appreciably simpler virtual trajectories based on their impedance estimates during movement.

A more fundamental difficulty with the equilibrium point hypothesis is demonstrated in a study by Lackner and DiZio [1994], who use Coriolis forces imposed by a rotating room to perturb reaching arm movements. According to the equilibrium point hypothesis, the movement endpoint should be unaffected as the velocity-dependent Coriolis forces vanish at the static final position. Interestingly, the results show a significant residual deviation in endpoint position during room rotation, a finding that is difficult to explain with a virtual trajectory formulation.

2.4. ADDITIONAL ISSUES IN POSTURE AND MOTION CONTROL

2.4.1. Impedance Control

Impedance control is so named because it monitors the dynamic relationship between force and position, rather than controlling force and position separately [Asada and Slotine, 1986; Hogan *et al.*, 1985]. It permits modulation of the desired apparent "stiffness" and "damping" of a robot manipulator as seen from the environment. In its simplest form, impedance control may be thought of as an extension of a local joint control philosophy, in the sense that manipulator dynamics are not explicitly modeled, but are treated as disturbances. Thus, it shares the advantages of such local schemes, including simplicity and robustness to parameter uncertainty. The limited dynamic performance inherent in local control schemes can be ameliorated with explicit models of the manipulator dynamics.

Impedance control has advantages which make it an attractive option under certain circumstances. It permits a unified treatment of both free motions and motions made during contact with other objects in the environment. Impedance control can serve as a position control scheme with a supplemental disturbance response to deviations through the tracking of a "virtual trajectory" that need not even lie within the manipulator workspace. Interestingly, impedance control allows position control without the explicit solution of the manipulator inverse kinematic equations, which are particularly difficult in the case of redundant manipulators (such as human limbs). In principle, impedance control can even be extended to obtain a desired apparent mass or inertia [Hogan, 1987b], but care must be taken to address stability issues.

Furthermore, robustness to disturbances and parametric uncertainty can be achieved by casting the impedance control law in the form of a sliding surface controller. The controller will then maintain the system as close to the desired impedance as possible within the available control bandwidth. The drawback is that the interaction forces must be explicitly measured.

Impedance control techniques offer important insights into strategies for human motor control. Viewed from an interaction port with the environment, the human neuromuscular system is properly considered an impedance, which takes position inputs and returns force outputs. Likewise, the environment with which the body interacts should be modeled as an admittance, taking force inputs and returning displacements. Synergistic coactivation of antagonist muscles serves to modulate the mechanical impedance about a joint without imposing a net torque; increasing antagonist contractions about a joint yields greater stiffness and viscous damping. In principle, multiarticular muscles (which exert torque about more than one joint) permit control over all the components of the endpoint stiffness and viscous properties of a limb. However, some experimental evidence indicates that the directional properties of the arm stiffness are difficult to modify, and it appears that the stiffness is more nearly invariant in joint rather than endpoint coordinates [Hogan *et al.*, 1987].

The endpoint impedance, as well as the apparent inertia, also depends on the limb configuration. Redundant degrees of freedom in a limb permit multiple limb configurations for a specified endpoint position, permitting modulation of the effective endpoint inertial properties as well as additional control over the endpoint impedance as seen from the environment. As discussed above, musculoskeletal impedance control may be implemented through feedback loops. At least as important, however, is open-loop modulation of impedance, since open-loop behavior dominates at high frequencies (characterizing fast events such as landing or heel strike).

Hogan *et al.* [1987] review results which indicate increased antagonist coactivation levels for unstable loads with greater magnitude of the instability, as well as progressive increases in coactivation as the frequency of perturbations grew higher. Grillner [1972] demonstrates that the earliest response of the lower limb muscles to the disturbances encountered in walking is due to the intrinsic properties of muscle, which can be modulated by appropriate coactivation strategies. In the jumping study cited above [McKinley and Pedotti, 1992], pre-impact changes in lower-limb configuration for different landing surface compliances imply purposeful modulation of endpoint impedance to accommodate surface properties. In a study of space shuttle astronauts, McDonald *et al.* [1996] cite postflight changes in the phase-plane description of knee joint kinematics during gait (most pronounced at heel strike and toe off) as preliminary evidence for changes in leg impedance and intersegmental energy transfer resulting from microgravity exposure.

2.4.2. Posture Control

There has been a considerable amount of research on the postural responses to perturbations during erect quiet standing, largely because of clinical interest in diagnostic posturography. This study of static posture control has yielded considerable information on the motion patterns and muscle synergies seen following various perturbations. To a certain extent a jump landing may be considered a perturbation response, so the posture control findings may well shed insight into the motion coordination and muscular responses involved in jumping.

2.4.2.1. Movement Patterns and Muscle Synergies

Nashner and McCollum [1985] report that muscle synergies in response to postural perturbations tend to move the ankle and hip joints while maintaining the knee in its equilibrium position. They identify two distinct "strategies" (more accurately patterns of motion and muscle activation). The *ankle synergy* moves the body toward an erect posture by contracting ankle, thigh and trunk muscles on the same dorsal or ventral aspect of body in a distal to proximal sequence, effectively controlling the body as a rigid inverted pendulum. The *hip synergy* moves the body toward non-erect balanced positions by contracting a thigh and trunk muscle pair on the aspect opposite to the ankle synergy muscles, and the body behaves as a two-link inverted pendulum. While the ankle synergy is most commonly observed, shortening the support surface to limit the achievable ankle torque forces subjects to employ the hip strategy. Likewise, reducing the friction between foot and support would presumably limit the use of the hip strategy.

Following a change to a shortened support surface, all subjects sequentially mix ankle and hip synergies during the first several trials. Interestingly, the timing of ankle and hip synergies remains distinct within EMG patterns, but adjustments in the relative amplitude of the two components are continuous. They hypothesize that the CNS selects a discrete, preprogrammed control sequence or combination of sequences based upon advance knowledge about body location within distinct regions of the position space, rather than controlling stance by firing all postural muscles in continuously graded amounts. Once selected, sequences can be modulated to vary the magnitude, aim and curvature of the corrective movement within the ankle-hip joint space. They theorize that movement patterns are selected to (1) minimize the number of muscles used, and (2) minimize the necessary calculation accuracy for frequently used controls.

Allum and his coworkers have conducted a series of similar postural studies on both normal subjects and vestibular patients [Allum *et al.*, 1985, 1992, 1993]. By using support dorsiflexion rotations (ROT) or backward translations (TRANS), or combinations of the two, they are able to generate postural disturbances that produce similar initial patterns of ankle dorsiflexion yet result in different upper leg, trunk and head movements requiring different corrective motions (support dorsiflexion tends to cause backward falls, while backward translation results in forward falling). These researchers also report stereotyped timing synergies in response to perturbations, although the synergies are somewhat different from those reported by Nashner *et al.* [1985] They find a *stiffened two-link synergy* (similar to the hip synergy above) in response to ROT stimuli. However, they report a *flexible multilink* synergy in response to TRANS stimuli which includes a significant degree of hip and knee flexion, in contrast to the inverted pendulum sway of the ankle synergy described earlier. They also report evidence for locking of the head with respect to the trunk in response to ROT, but stabilization of the head in space following TRANS.

Unlike Nashner, however, Allum *et al.* postulate that all balance corrections result from the selection of one of the two synergies, and that mixing of the timing synergies does not occur. They present evidence that the CNS uses proprioceptive information acquired over the first 100 ms following the stimulus onset to select the appropriate synergy; muscle stretch from ankle joint rotation appears to select for the ROT synergy, while additional sensory information on ankle and knee rotations triggers the TRANS synergy. Once selected, intersegmental timing appears fixed, although the amplitude of this synergy is modulated in a continuous manner based on joint and link velocities and vestibular inputs. In particular, a study involving vestibular patients indicates that vestibular afferent signals enhance the responses in the tibialis anterior, quadriceps and soleus muscles while inhibiting paraspinal activity [Allum *et al.*, 1994].

Horstmann and Dietz [1990] also utilize translational perturbations to the support surface to explore postural control of the center of gravity location. Partial gravity simulation through water immersion indicates that the amplitudes of muscular responses are approximately linearly related to the effective body weight. A supplementary test out of the water unloads the subjects using a parachute harness and counterweight, then reloads them with weights at either the knees, hips, or shoulders. The responses to the support perturbation increase with increasing height of the reloading weights, leading the investigators to conclude that the center of gravity is the controlled quantity, and to hypothesize that inputs from pressure sensors distributed throughout the joints and vertebral column combine with other proprioceptive information to transduce the center of gravity location.

MacKinnon and Winter [1993] observe postural adjustments in the frontal plane during gait similar to the static postural synergies described by Nashner and McCollum [1985]: small perturbations are controlled almost solely by torques about the ankle joint, while larger disturbances invoke a combination of responses at both the ankle and hip.

2.4.2.2. Anticipatory Postural Reactions and the "Body Scheme"

Gurfinkel [1994] reviews work on the anticipatory and compensatory postural reactions to voluntary movements. Anticipatory components appear to accompany only those movements which lead to displacement of the center of gravity; they precede the muscle activation associated with the voluntary movement and act to decrease the effect of the oncoming disturbance. He notes that anticipatory postural components, while apparently centrally organized and exhibiting a distinct correlation with the oncoming movement, depend on variables including the character of the movement and the subject's initial posture. For example, anticipatory reactions to rapid arm movements are not found when the standing subject is fixed to an immovable support. Further tests on the effect of head turning on postural muscle activity demonstrate that information derived from interaction of the foot with different support surfaces can suppress or enhance postural muscle reflex activity. He concludes that "an internal representation of the body, abstracted from the primary sources of information, can be used . . . for motor control, including movement reactions directed toward maintaining stable body position." He also reasons that the internal representation is not necessarily a direct reflection of various afferent activity, but depends on a *body scheme*--an internal model of the body configuration and its spatial orientation.

2.4.2.3. Simplified Inverted Pendulum Models

Hemami and colleagues [Hemami and Katbab, 1982; Camana et al., 1977] use linearized dynamics from one and two link inverted pendulum models to study the use of constant gain feedback controllers for postural stabilization. They find that reasonable predictions of behavior can be made, and compute minimal gains for stable feedback. Barin [1989] uses a multiple regression to compute state feedback gains from experimentally determined kinematics for a two segment model, and is able to predict center-of-pressure excursions. McCollum and Leen [1989] consider the unstable time constants associated with linearized one and two link inverted pendulum models, and conclude that the longer time constant associated with the simple pendulum (comparable to the ankle strategy) requires a lower bandwidth controller than the faster modes of the two link pendulum.

2.4.2.4. Performance Constraints and Optimization

Kuo and Zajac [1992] provide a more mathematically rigorous examination of the postural synergies exhibited in response to perturbations of erect stance. They utilize a four-segment model (foot, shank, thigh and head-arms-trunk) constrained to move in the sagittal plane. The linkage incorporates frictionless hinge joints and is actuated by 14 muscle groups; each musculotendon actuator is a scaled Hill-type model. Quasistatic conditions are assumed, and velocity terms in the dynamic equations and muscle model are neglected. They map the 14 dimensional cube of feasible muscle activations to a polyhedron in the three-dimensional joint acceleration space (ankle, knee and hip). The volume contained by this polyhedron is termed the *feasible acceleration set* (FAS); the surface of the polyhedron comprises the outer bound on all accelerations for a given body configuration. The ratio of a given desired acceleration to the maximum feasible acceleration in that direction provides a measure of *neural effort* for that acceleration.

Based on Nashner and McCollum's observation that the knees generally remain fixed in postural corrections, they find the intersection of the FAS with the plane defined by zero angular acceleration of the knee. The resulting polygon describes the ankle-hip FAS. A "flat-foot" constraint corresponds to the maximum joint accelerations that do not cause lifting of either the toes or heels. Postures at the boundaries of stable balance configurations (defined as configurations where the CM lies above the feet, between the heels and toes) also define a "stable balance" constraint on possible accelerations. Based on the configuration of the FAS, Kuo determines that the hip strategy requires considerably less neural effort than the ankle strategy for a given amount of horizontal center of mass acceleration. Furthermore, at the stable balance boundaries or under a shortened support surface condition, an ankle strategy is insufficient to maintain balance. They conclude that considerations other than neural effort, such as maintenance of erect stance or minimization of head motion, contribute to selection of an ankle strategy when permitted by toe- and heel-off constraints. When necessary, further accelerations can be achieved by combinations of ankle and hip strategies.

Kuo [1992] then develops a linear quadratic regulator (LQR) control model to test the hypothesis that optimal control and state estimation can explain the responses to perturbations of stable upright balance; he concentrates on the LQR model and does not address the estimation problem. The LQR methodology provides a means for determining feedback gains which produce an optimal return function--that is, a state trajectory which minimizes a set of performance objectives. The controls are weighted in the cost function to reflect the different neural efforts associated with the ankle and hip strategies. The cost functions associated with the states are selected to compare three objectives: (1) minimization of the CM deviation, (2) minimization of deviation from erect posture, and (3) minimization of head (actually trunk) angle. Kuo concludes that regulation of the CM position with the additional objective of maintaining upright stance reproduces the main features of the hip strategy. He also finds that the hip strategy shows more robustness to time delays.

2.4.3. Hierarchical Control Design

Much of the motor control capability of the vertebrate central nervous system is organized functionally and physiologically into a series of levels which govern successively more complex behaviors [McMahon, 1984]. These blocks are sufficiently autonomous that severing the neural pathways to higher levels permits lower levels of control to continue functioning. Transecting the spinal cord at the first cervical vertebra preserves the stretch reflex. If an animal is placed on its feet the limb extensors contract, and the hind limbs will even "walk" on a moving treadmill if the animal is supported. Section higher up at the level of the midbrain adds righting reflexes which depend on the vestibular apparatus. Removal of the cerebral cortex alone leaves an animal which performs many common motor functions almost completely normally, but cannot learn new skills. The cerebellum is a major center for integration of muscle, skin and joint afferents. While decerebellate animals exhibit a nearly normal range of motor behavior, they are awkward and clumsy. Thus, the cerebellum appears to depend on sensory input below the conscious level to integrate and smooth motor behaviors.

Raibert [1990] also uses a hierarchical design in his ambulatory robots which decomposes the gait control system into separate parts for the control of hopping height, forward running velocity and body attitude. Research into neural network control of a mobile robot show that a hierarchical arrangement of networks decreases network size to enable real time control and reduces the number of required training patterns [Nagata *et al.*, 1990]. The robot behaves according to a "reason" network when sensory information is available to determine actions, and relies on an "instinct" network in the absence of such information.

Much of the work on control of static posture cited above implies a hierarchical structure for the control of posture and full body motion. Both Nashner and Allum argue for a central selection of appropriate muscle synergies, which are then modulated at a lower level based on incoming sensory data. In his optimal control model for standing posture, Kuo also incorporates a "control selection center" which selects a synergy by setting parameters which determine the controller bandwidth and the relative proportions of various goals in the cost functional.

Results reported by Nashner and McCollum [1985] indicate that lower levels of control may maintain stability while higher level motor programs are adaptively tuned. For example, when confronted with sudden transitions between perturbations requiring suspensory and sway synergies, subjects immediately select the appropriate synergy. However, the subjects also demonstrate high antagonist muscle coactivation levels initially, which are reduced in subsequent trials. It may be that coactivation is used to increase the system stiffness and damping while the higher level of control is being tuned. Another relevant example of apparent hierarchical control is seen by Bloomberg *et al.* [1992], who document reductions in vertical head motion during gait with near visual targets. Such fixation distance-specific modulation of ankle and knee joint excursions may indicate the activation of higher-level control mechanisms devoted to gaze stability.

3 JUMPING ADAPTATION VIA MICROGRAVITY AND PARTIAL WEIGHT UNLOADING

This chapter describes two experiments that explore the adaptive effects of microgravity and reduced load bearing requirements on jump landing performance. These experiments examine the hypothesis that the reduced load bearing demands experienced during space flight result in adaptive changes to the control of leg impedance properties. The first experiment tests astronaut subjects before and after space flight, while the second investigation attempts to replicate some of the effects of weightlessness by using partial weight unloading to simulate partial gravity exposure.

3.1. ASTRONAUT JUMPING FOLLOWING MICROGRAVITY EXPOSURE

A variety of studies of astronaut performance following space flight indicate that exposure to microgravity can cause profound changes in human balance, posture control and locomotion. Kenyon and Young [1986] find decrements in standing ability with the eyes closed for several days following space flight; subjects are only able to maintain upright posture if they stay within a very narrow cone of static stability near the vertical [Young *et al.,* 1986]. In posture platform tests, astronauts demonstrate abnormal postural sway oscillations and drift immediately postflight when the support is sway-referenced to eliminate ankle proprioception cues [Paloski *et al.*, 1993]. Watt *et al.* [1986] test astronauts subjected to sudden drops and report that all subjects are unsteady postflight, and that one subject falls over backwards consistently.

Anecdotal descriptions of astronaut locomotion postflight reveal abnormalities in walking, including adopting a wide stance during gait and difficulty in rounding corners [Homick and Reschke, 1977]. Chekirda *et al.* [1971] also report a "stamping" gait, shift of the body toward the support leg and deviations from straight paths while walking on the first day following space flight. Bloomberg *et al.* [1997] observe alterations in head-trunk coordination during locomotion that may contribute to postflight postural and locomotion disturbances.

Such performance decrements may result from various changes in the sensorimotor complex due to microgravity exposure. Parker *et al.* [1985] find direct evidence for reinterpretation of graviceptor inputs during space flight. Young *et al.* [1986] also provide evidence for sensory compensation during space flight resulting in interpretation of utricular otolith signals as linear acceleration rather than head tilt, as well as increased dependence on visual cues for perception of orientation. The otolith-spinal reflex, which helps prepare the leg musculature for impact in response to sudden falls, is dramatically reduced during space flight [Watt *et al.*, 1986]. However, postflight results are not significantly different from preflight responses, indicating a rapid course of readaptation upon return to earth. Other work indicates that space flight may affect proprioception of limb position: Watt *et al.* [1985] find a considerable decline in arm pointing accuracy while blindfolded during and immediately following space flight. Furthermore, the subject who falls consistently in the drop test reports that his legs are always further forward than he expects them to be.

Other possible explanations for postflight postural instability include atrophy of the antigravity muscles [Riley and Ellis, 1983; Martin *et al.*, 1988; LeBlanc *et al.*, 1995], inflight changes in tonic leg muscle activation patterns, or microgravity-induced alterations in stretch reflexes [Gurfinkel, 1994; Layne *et al.*, 1995]. Gurfinkel also reports reorganization of higher-level anticipatory postural responses to rapid movements during space flight. Altered patterns of leg muscle coactivation may result in changes in the modulation of limb impedance that controls the dynamic interaction of the limb with the environment. McDonald *et al.* [1996] cite postflight changes in the phase-plane description of knee joint kinematics during gait as preliminary evidence for changes in joint impedance resulting from exposure to weightlessness.

The aim of the present study is to determine the effects of microgravity exposure on the astronauts' performance of two-footed jump landings. This study is intended to elucidate how exposure to an altered gravitational environment affects control of lower limb impedance and preprogrammed motor strategies for impact absorption. The joint kinematics of the lower extremity during the jump landings, as well as the kinematics of the whole-body mass center, are of particular interest. The results suggest that different subjects adopt one of two response modes upon return to 1-g following space flight, and that postflight performance differences may result largely from adaptive changes in open-loop lower limb impedance modulation. The altered jumping kinematics seen postflight may reflect decrements in limb proprioception, altered interpretation of otolith acceleration cues, and reduced requirements for maintenance of posture under microgravity conditions.

3.1.1. Astronaut Jumping Experiment Methods

3.1.1.1. Astronaut Jumping Experiment Design

The subject pool for this study consists of 9 NASA Space Shuttle astronauts. In order to protect the subjects' anonymity, they are designated by letter codes (S-1, S-2,...S-9). Informed consent is obtained for all experiments, human use approval is granted for the study by the NASA Johnson Space Center Institutional Review Board for Human Research, and the tests are therefore performed in accordance with the ethical standards laid down in the 1964 Declaration of Helsinki. Subjects are permitted to withdraw from the study at any time and for any reason. The subjects range in age from 36 to 50 years. The astronauts are in good health and show no signs of vestibular or postural control deficits. Of the 9 subjects, 8 are male and 1 is female. The first preflight testing (PRE1) takes place 2-6 months before launch. Another preflight test (PRE2) occurs 9-15 days prior to launch, while the postflight tests (POST) are performed within 4 hours of Shuttle landing. Mission lengths vary between 7 and 14 days. Preflight tests are performed in the Neuroscience Laboratory at the Johnson Space Center in Houston, Texas. Postflight testing takes place at the landing site (either Edwards Air Force Base, California or the Kennedy Space Center, Florida).

At each data collection session, the jumping protocol consists of 6 voluntary two-footed downward hops from a 30 cm platform. Three jumps are performed while fixating continuously on a ground target 1 meter forward of the subject's initial toe position. The other three jumps are performed with the eyes closed, and subjects are instructed to look at the ground target, then close their eyes and fixate on the imagined ground target position during the jump. Eyes open (EO) and eyes closed (EC) trials are alternated. Because of safety concerns related to subject instability postflight, the first jump is always performed with the eyes open. The subjects are instructed to land on both feet at the same time, although no specific instructions are given regarding the jump takeoff. A safety harness connected to an overhead frame prevents subjects from falling to the floor, but does not interfere with mobility during a normal jump.

Full-body kinematics data are collected with a video-based motion analysis system (Motion Analysis Corporation, Santa Rosa, CA). This system tracks the three-dimensional position of 14 passive reflective markers placed on the body. Markers are placed on the right side of the body at the toe, ankle, malleolus, knee, hip, shoulder, elbow, wrist, and ear. The remaining markers are located at the left heel and along the body centerline at the sacral bone, seventh cervical vertebra, occipital prominence and head vertex. For some of the subjects, foot switches located in the shoes underneath the heel and great toe of both feet are used to record the times when the feet are in contact with the ground.

3.1.1.2. Astronaut Data Analysis

The motion analysis system provides the marker positions in three dimensions at a sampling rate of 60 Hz. The ankle, knee and hip joint angles in the right leg are computed using the positions of the markers at the toe, ankle, knee, hip and shoulder (Figure 3.1).

These calculations assume that the foot, shank, thigh and trunk are rigid segments. For all three joints, larger positive joint angles represent greater joint flexion while negative values denote joint extension. In order to account for the possibility of variation in marker placement from session to session, average resting joint angles during quiet standing are calculated for each data collection session. These average resting angles are subtracted from the joint angle time series data for that session. Hence, the data shown here represent deviations from quiet standing posture, and positive joint angles indicate increased flexion from the rest position. Joint angular velocities are found by numerically differentiating the joint angle data using a four point centered difference. Before differentiating, the angle data are smoothed by filtering forward and backward (to eliminate phase shift) using a 3rd order Butterworth filter with a corner frequency of 15 Hz. Impact results in large and nearly instantaneous increases in the joint angular velocities. In order to avoid excessive smoothing of this feature, the data segments prior to and following impact are filtered and differentiated separately. Care is taken to minimize startup and ending filter transients by matching initial conditions.

The time of foot impact with the ground is extracted from the foot switch data for those subjects who are tested using the switches. For the other subjects, the impact time is calculated by determining when the downward velocity of the toe marker drops to less than 10 mm/s. Comparisons of the two methods for finding impact time in the subjects with foot switch data yields excellent agreement. For each jump, peak flexion angles and flexion rates after impact are computed for the ankle, knee and hip joints as well as joint angles at the time of impact.

The position of the full-body center of mass (CM) in the sagittal plane is estimated from the marker positions, using an 8-segment body model (feet, shanks, thighs, trunk, upper arms, forearms, neck and head). Lateral symmetry is assumed, allowing combination of the left and right segments in the arms and legs. The approximate distribution of the body mass among the body segments is found using a regression model based on the subject's weight and height [McConville *et al.*, 1980; Young *et al.*, 1983]. CM position is computed in an X-Z coordinate system, where the X value represents the fore-aft position and the Z direction corresponds to the gravitational vertical. Positive values for X and Z correspond to forward and upward, respectively. The velocity of the CM is found using the same numerical differentiation procedure described above for the joint angular velocities.

Initial analysis of the joint and CM kinematics indicates a non-uniform pattern of postflight responses across the subject pool. Therefore, preflight and postflight data sets

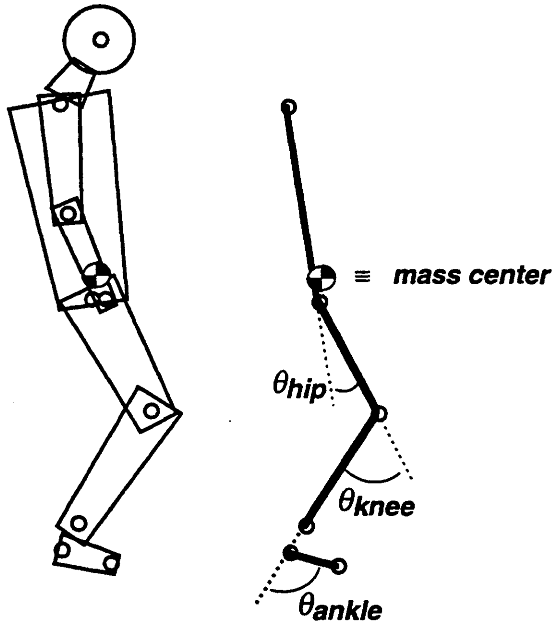

Figure 3.1. Astronaut subject sagittal plane body model.
Reflective marker placement (denoted by "o") and eight segments used for CM calculation (feet, shanks, thighs, trunk, forearms, upper arms, neck and head) are shown at left. The joint angle convention is shown at right.

are compared for each subject individually for peak joint flexion angles, peak joint flexion rates, and 3 CM-related measures: (1) maximum downward deflection, (2) time from impact to maximum downward deflection, and (3) peak upward recovery velocity. A two-way analysis of variance (ANOVA) is used to examine the effects of test session (PRE1, PRE2, POST) and vision (EO, EC). Test session effect is computed two ways: (1) PRE1 vs. PRE2, and (2) PRE1 and PRE2 together vs. POST. Tests yielding $p<0.05$ are considered statistically significant.

Changes preflight to postflight in 9 measures (3 peak joint angles, 3 peak joint rates, and 3 CM quantities) are considered for classification of the subjects into groups based on postflight performance. For each quantity, the number of subjects showing a significant change between the two preflight sessions is compared with the number demonstrating a significant difference between preflight and postflight (Table 3.1).

Table 3.1. Significant test session effects in measures pre- and postflight.

Measure	# Subjects Exhibiting Significant Change		Ratio of # changes (PRE1&PRE2 vs. POST) / (PRE1 vs. PRE2)
	Preflight: PRE1 vs. PRE2	PRE1&PRE2 vs. POST	
Peak Hip Angle	4	3	0.75
Peak Knee Angle	3	8	2.67
Peak Ankle Angle	5	6	1.20
Peak Hip Rate	2	7	3.50
Peak Knee Rate	2	6	3.00
Peak Ankle Rate	1	1	1.00
Peak CM Deflection	2	4	2.00
Time from Impact to Peak CM Deflection	0	4	∞
Peak CM Upward Recovery Velocity	3	3	1.00

Of the 9 measures, 5 are selected for classification purposes because they prove relatively insensitive to day-to-day variations. These measures (peak knee angle; peak hip and knee rates; peak CM deflection and time to peak CM deflection) show differences between pre- and postflight in at least twice as many subjects as they did between the two preflight sessions. The 5 variables are tested together for the effects of test session and vision, using a two-way multivariate analysis of variance (MANOVA). Again, the contrast for test session effect is computed for pre- vs. postflight. Probabilities are based on Wilks' Lambda (likelihood ratio criterion) and Rao's corresponding approximate (sometimes exact) F-statistic. Subjects who do not exhibit significant differences between pre- and postflight for the multivariate measure are classified as "No Change" (N-C).

The other subjects are classified as either "Postflight Compliant" (P-C) or "Postflight Stiff" (P-S) by scoring the 5 individual measures used in the MANOVA. For each measure, the subject receives a [+1] for a significant change toward greater compliance postflight, a [-1] for a significant change toward lower compliance postflight, and a [0] for no significant change. The results for the individual measures are summed to get an overall score ranging from -5 to +5. Subjects with positive scores are designated P-C, while negative scores are labeled P-S. All statistical computations are performed using SYSTAT [Wilkinson, 1989].

3.1.1.3. Model of CM Vertical Motion

A simple mechanical body model is developed to investigate the vertical motion of the CM following impact with the ground. In this single degree-of-freedom model (Figure 3.2), the vertical (Z) motion is assumed to decouple from the horizontal motion, which is neglected. The entire body mass is concentrated at the CM, supported by a massless, constant stiffness Hookean spring representing the legs. Similar models have been used by Alexander and Vernon [1975] and McMahon and Cheng [1990] to examine hopping and running. The upward restoring force exerted by the spring is proportional to the downward displacement of the CM from the uncompressed spring length Z_0 (nominally the height of the CM at the moment of impact). Energy dissipation, or damping, is modeled by a linear dashpot in parallel with the leg spring, which opposes the CM motion with a force proportional to CM velocity.

This model leads to a second order linear differential equation that describes the CM motion:

$$M\ddot{z} + B\dot{z} + K(z - Z_0) = Mg \tag{3-1a}$$

$$\ddot{z} + \frac{B}{M}\dot{z} + \frac{K}{M}(z - Z_0) = g \tag{3-1b}$$

where $z, \dot{z}, \ddot{z}$ = CM vertical position, velocity, acceleration respectively
g= gravitational acceleration
M = body mass
K = spring stiffness
B = damping.

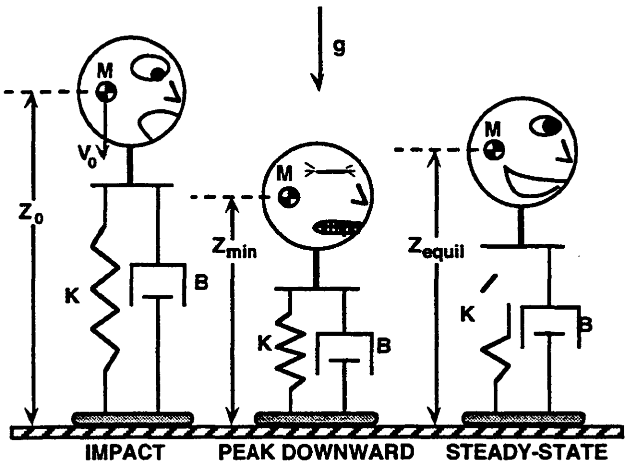

Figure 3.2. Second order model of CM vertical (Z) motion following impact. Body mass (M), located at the CM, is supported by linear spring (K) and dashpot (B). The unloaded length of the spring is Z_0 (nominally the height of the CM at impact), minimum spring length is Z_{min}, and the spring length at the final equilibrium is Z_{equil}.

The initial conditions needed to find the time solution of the equations are given by the vertical position and velocity of the CM at the moment of impact. In order to compare the pre- and postflight limb impedance properties for each subject, best fit values for each jump are determined for the coefficients $\frac{K}{M}$ and $\frac{B}{M}$ (the stiffness and damping, respectively, normalized by subject body mass). The best fit values are found using the MatLab System Identification Toolbox (The MathWorks Inc., Natick, MA). Model fitting is accomplished by minimizing a quadratic prediction error criterion using an iterative Gauss-Newton algorithm [Ljung, 1993]. The best fit for the rest spring length Z_0 is determined concurrently, although this parameter is nominally set by the height of the CM at impact. Unfortunately, the sampling rate is too low to provide an adequate estimate of the Z_0 value: with CM velocities greater than 2 m/s at impact, an uncertainty of one sampling interval in the time of impact can result in errors in Z_0 exceeding 3 cm. Since peak deflection of the CM following impact typically ranges from 8-15 cm, this level of uncertainty requires simultaneous estimation of the spring length using the MatLab identification routines.

Equation 3-1 can be rewritten in canonical second order form:

$$\ddot{z} + 2\zeta\omega_n\ddot{z} + \omega_n{}^2(z - Z_0) \;=\; g \qquad (3\text{-}2)$$

where $\omega_n = \sqrt{\frac{K}{M}}$ = natural frequency

$\zeta = \frac{B}{2\sqrt{KM}}$ = damping ratio

The natural frequency is roughly equivalent to the bandwidth of the system and provides a measure of the speed of response, since higher natural frequencies correspond to faster transient responses. Clearly, increasing the stiffness K leads to a higher natural frequency. The damping ratio measures how oscillatory the transient response is, with lower damping ratios indicating more overshoot and oscillation or "ringing" in the system behavior. Increasing the stiffness K decreases the damping ratio, as does reducing the damping coefficient B.

3.1.2. Astronaut Jumping Results

3.1.2.1. Astronaut Joint Kinematics

Phase plane plots, where joint angular velocities (degrees per second) are plotted against the joint angles (degrees), yield the best format for comparing the joint kinematics of several jumps. Figure 3.3a shows phase portraits for subject S-1 comparing a time

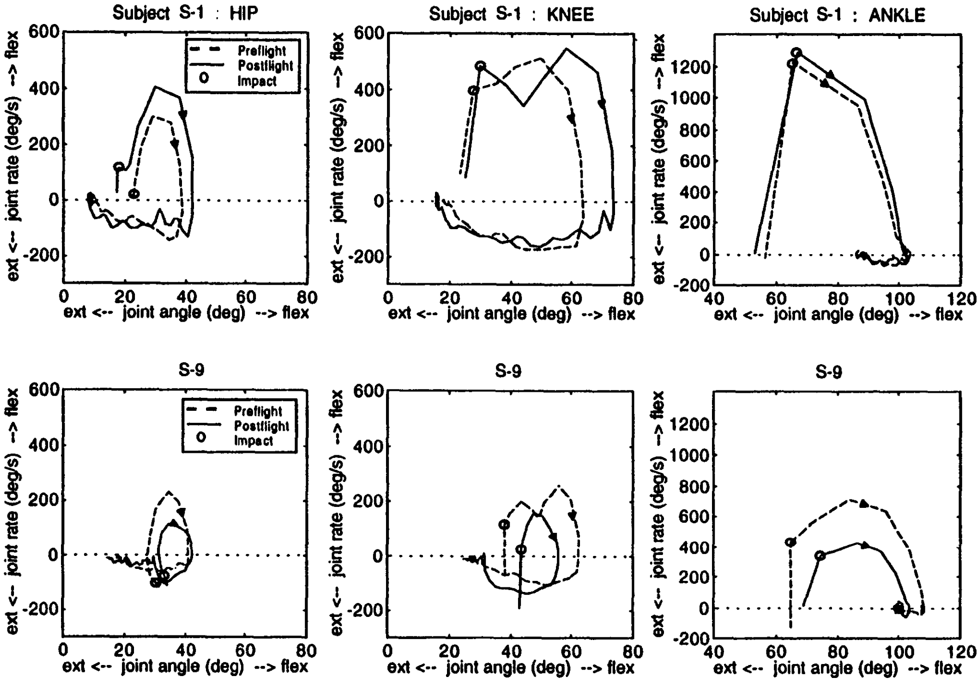

Figure 3.3. Comparison of pre- and postflight joint phase-plane portraits. Preflight (dashed) and postflight (solid) results are shown for the hip, knee and ankle. (a) Upper plots. For subject S-1, the postflight phase diagram is expanded with respect to the preflight diagram. (b) Lower plots. In contrast, subject S-9 demonstrates postflight contraction of the phase portrait in comparison to preflight results.

synchronized average of 12 preflight and 6 postflight jumps for the hip, knee and ankle joints. The time of impact is marked by an open circle (o) on each plot, and the plots are traversed in the clockwise direction through the impact absorption and recovery to an upright posture. In general, after impact the peak flexion rate is reached rapidly; the peak flexion rate is the uppermost point on the phase portrait. Moving further along the phase diagram, the joint angular velocities drop to zero as the muscles act to decelerate the body's downward motion. When the joint flexion rate reaches zero, the joint is at its peak flexion angle, the rightmost point on the plot. After this point, the flexion rate becomes negative, indicating joint extension as the subject recovers to the upright resting posture. These plots depict averages of the jumps for the preflight and postflight sessions, with the time scales for each data series synchronized at the time of foot impact with the ground.

The plots for subject S-1 clearly illustrate expanded postflight phase diagrams for each joint with respect to the preflight measurements. Postflight, this subject exhibits greater peak joint flexion angles than during the preflight jump landings, indicating that the subject reached a more crouched body position postflight while absorbing the impact from the jump. Furthermore, the peak joint angular velocities seen postflight are greater than the joint rates observed preflight. In contrast, the phase-plane diagrams for subject S-9 in Figure 3.3b demonstrate the opposite effect; the postflight portraits are consistently smaller than the plots of the preflight jumps. This postflight contraction of the phase diagrams denotes a decrease in peak joint flexion postflight, indicating that this subject retains a more upright posture while absorbing the impact. In addition, this subject shows smaller peak joint flexion rates in postflight testing than in the preflight jumps.

3.1.2.2. Center of Mass (CM) Kinematics

As with the joint angle data, the kinematics of the CM are plotted in a phase-plane format. Figure 3.4 shows the CM motion for subject S-1. Once again, the plots depict averages of the 12 preflight and 6 postflight trials. Figure 3.4a shows the average motions of the CM in the X-Z (sagittal) plane. Figure 3.4b and Figure 3.4c present the phase-plane trajectories in the X (fore-aft) and Z (vertical) directions traversed in the clockwise direction, respectively. The open circles (o) denote the moment of impact coinciding with peak downward CM velocity. Deceleration of the CM downward motion takes place until the CM is at its lowest point and the Z velocity is zero. Then the Z velocity becomes positive as the CM recovers to the steady-state value for standing posture. The peak upward velocity occurs at the uppermost point on the trajectory. The trajectory may spiral in around the equilibrium point if there is oscillation about the final steady-state position.

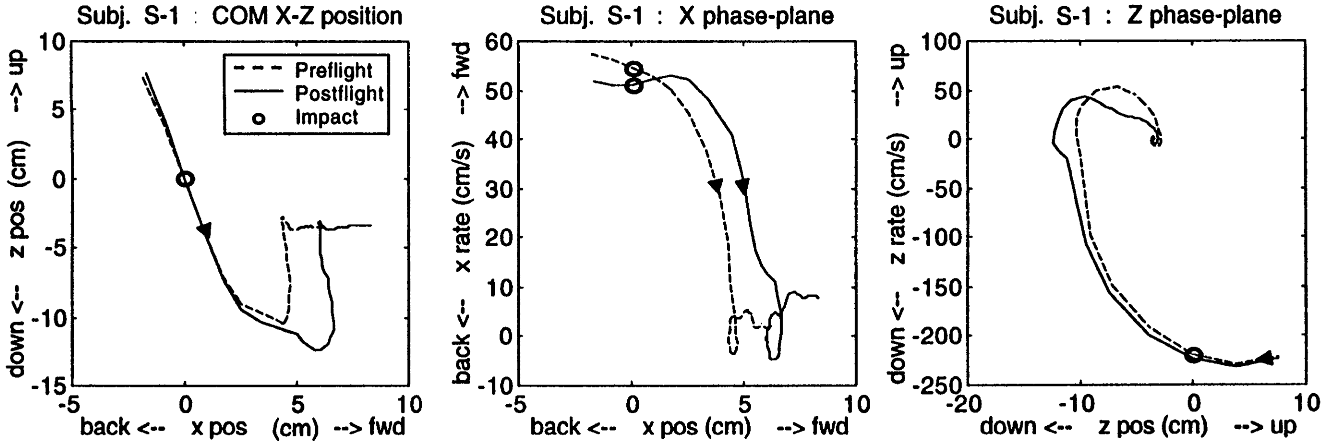

Figure 3.4. Comparison of pre- and postflight CM motion for P-C subject S-1. (a) The CM trajectory in the sagittal (X-Z) plane; peak deflection of the CM is greater postflight. (b) Phase-plane motion of the CM in the horizontal (X) difection. (c) Phase-plane motion of the CM in the vertical (Z) direction indicates greater downward deflection and slower upward recovery postflight.

3.1.2.3. Subject Classification

The joint angle phase diagrams for these two astronauts suggest that the subjects who exhibit postflight changes in joint kinematics compared to preflight values may be divided into two distinct groups. Using the analogy of a spring of variable stiffness, the first group is denoted "postflight compliant", or P-C. Just as a more compliant spring compresses more under a given load, this group generally exhibits greater joint flexion postflight than preflight, accompanied by increased postflight flexion rates. The second group is labeled "postflight-stiff", or P-S, indicating lower peak flexion and flexion rates for the jump landings following space flight.

The CM kinematics provide complementary information for classification of subject performance following space flight. If the legs are considered to be roughly springlike in supporting the mass of the upper body, the maximum downward deflection of the CM following impact gives a measure of the stiffness of the lower limb "spring" (*e.g.*, an *increase* in the downward deflection of the mass center indicates a *decrease* in the spring stiffness). The time from impact to the point of peak downward deflection also provides an indicator of the effective stiffness of the lower limbs. A decrease in the time between impact and maximum deflection implies an increase in the stiffness.

Table 3.2 contains the scoring of the 5 measures used to classify each subject. Positive entries indicate significant changes toward greater compliance postflight, corresponding to increases in peak joint angles or peak joint flexion rates, greater downward CM deflection, or longer times from impact to maximum CM vertical deflection. Negative entries represent significant differences in these quantities that indicate greater stiffness postflight. The statistical significance for the preflight/postflight MANOVA contrast of the 5 measures are shown for each subject. As previously mentioned, subjects with significant MANOVA results are denoted P-C or P-S based on positive or negative overall scores respectively for the 5 classification measures; the remainder are designated "No Change" (N-C).

Four subjects (S-1, S-2 , S-3 , S-4) are classified P-C. All four have significantly increased peak knee flexion combined with significantly greater peak knee and hip flexion rates postflight; for 3 of the 4 (all except S-4) CM downward deflection and the time from impact to peak CM downward deflection also increase postflight. Both of the subjects designated P-S (S-8 and S-9) exhibit significantly decreased peak knee flexion postflight. Subject S-9 also shows significant decreases in peak hip and knee flexion rates after space flight, as well as a decrease in the average time from impact to peak CM downward

Table 3.2. Subject classification based on kinematic measurements.

Subject	S-1	S-2	S-3	S-4	S-5	S-6	S-7	S-8	S-9
Peak Knee Flexion	+1	+1	+1	+1	+1			-1	-1
Peak Knee Flexion Rate	+1	+1	+1	+1	+1				-1
Peak Hip Flexion Rate	+1	+1	+1	+1	+1		+1		-1
Peak CM Deflection	+1	+1	+1					-1	
Time to Peak CM Deflection	+1	+1	+1						-1
Overall Score	+5	+5	+5	+3	+3	0	+1	-2	-4
p-value	0.005	0.003	0.002	0.003	0.277	0.275	0.051	0.002	$4x10^{-6}$
Classification	**P-C**	**P-C**	**P-C**	**P-C**	N-C	N-C	N-C	**P-S**	**P-S**

deflection. Peak CM downward deflection is significantly reduced for subject S-8. The remaining three subjects (S-5, S-6, S-7) do not show a significant change between preflight and postflight based on the multivariate criterion.

Because the measures of peak joint angle, peak joint rate and maximum CM vertical deflection are affected by the magnitude of the impact force as well as lower limb stiffness, the changes observed cannot be attributed to limb impedance changes unless the impact loading is the same pre- and postflight. For this reason, the CM vertical velocity at the moment of impact is compared for each subject's pre- and postflight jumps. Only two subjects (S-9 and S-2) show significant differences between pre- and postflight impact velocities at the $p<0.05$ level. For subject S-9, the average postflight impact velocity is reduced by almost 20% compared to the preflight jumps. This change probably contributes to the decrease in knee flexion, joint rates and CM displacement observed for this subject. Subject S-2 also exhibits a significant postflight decrease of about 5% in impact velocity. In spite of the postflight reduction in impact loading, subject S-2 exhibits consistent *increases* in peak joint flexion, flexion rate and CM downward deflection. Thus, the impact velocity result actually adds support to the P-C classification for S-2. All other P-C and P-S subjects showed small, non-significant differences between pre- and postflight CM impact velocity.

In summary, the P-C subjects exhibit significant increases in postflight joint flexion and flexion rates; the P-S subjects show the opposite effect, although the trend is less apparent in subject S-8. Figure 3.5 compares the average preflight and postflight values for maximum knee flexion, based on two preflight sessions of six jumps each and one postflight session of six jumps. Figure 3.6 and Figure 3.7 contain pre- and postflight peak

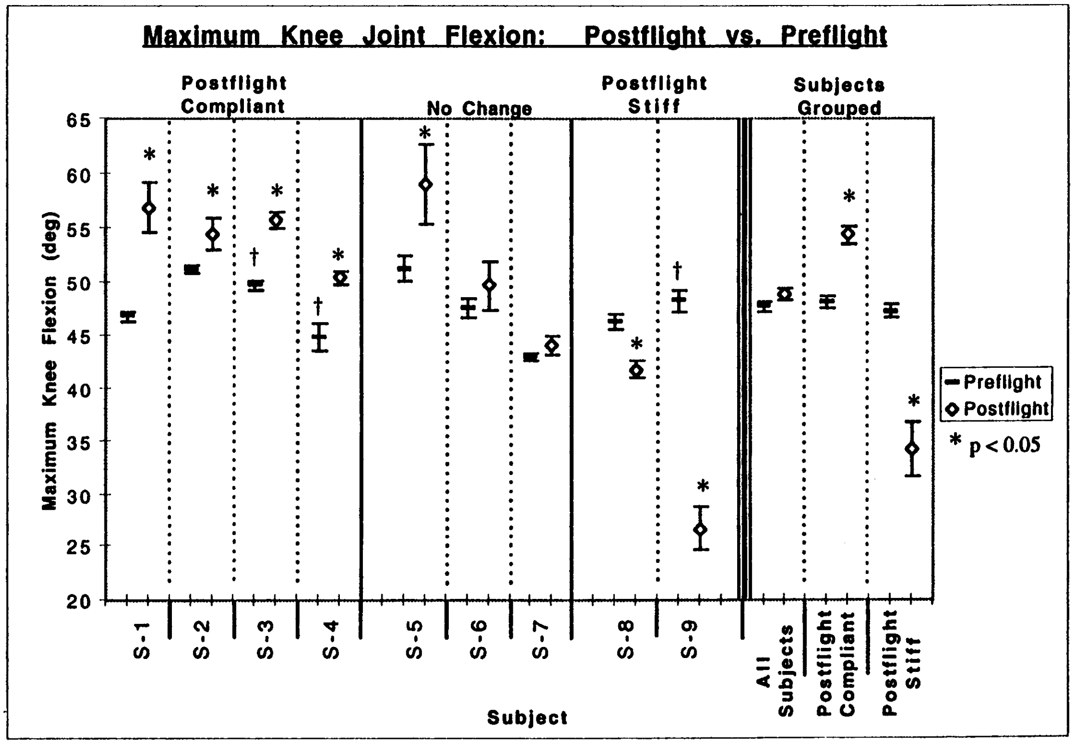

Figure 3.5. Peak knee flexion after impact for all subjects. Average preflight and postflight values shown with error bars indicating standard errors of the mean. Statistical significance for preflight-postflight comparison ($p<0.05$) is indicated by "*", while a "†" denotes significant test day effect for the two preflight sessions.

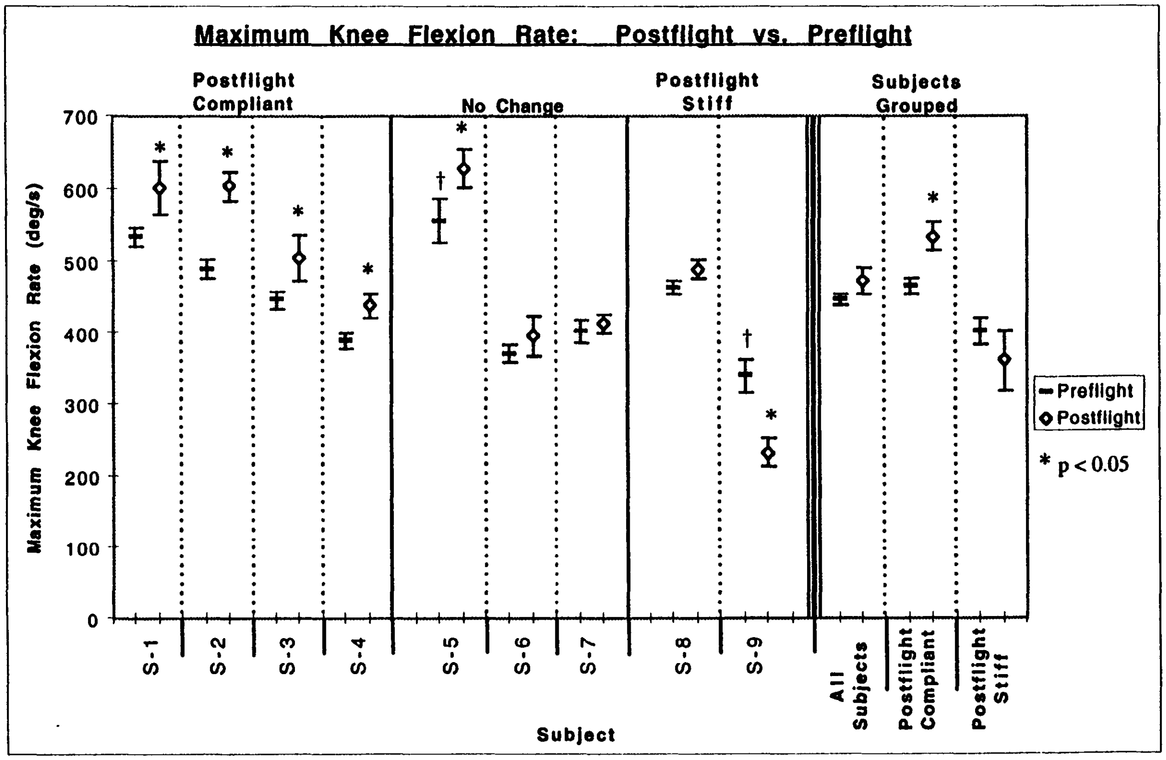

Figure 3.6. Peak knee flexion rate after impact for all subjects. Average preflight and postflight values shown with error bars indicating standard errors of the mean. Statistical significance for preflight-postflight comparison ($p<0.05$) is indicated by "*", while a "†" denotes significant test day effect for the two preflight sessions.

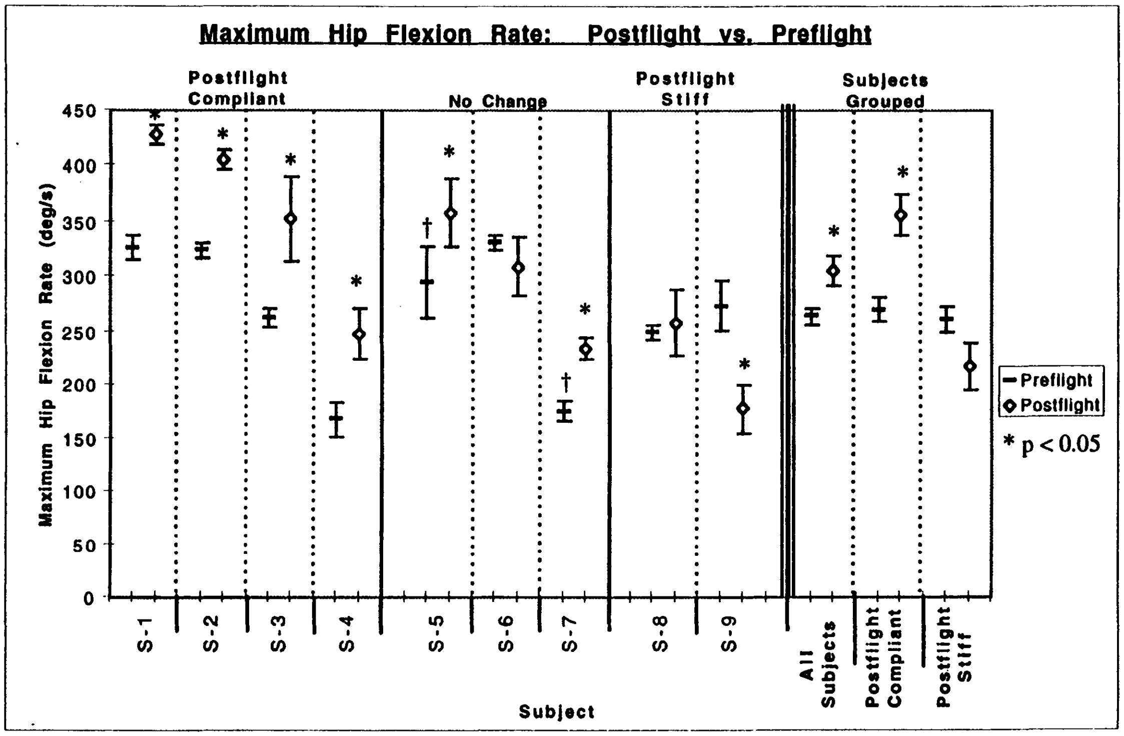

Figure 3.7. Peak hip flexion rate after impact for all subjects.
Average preflight and postflight values shown with error bars indicating standard errors of the mean. Statistical significance for preflight-postflight comparison (p<0.05) is indicated by "*", while a "†" denotes significant test day effect for the two preflight sessions.

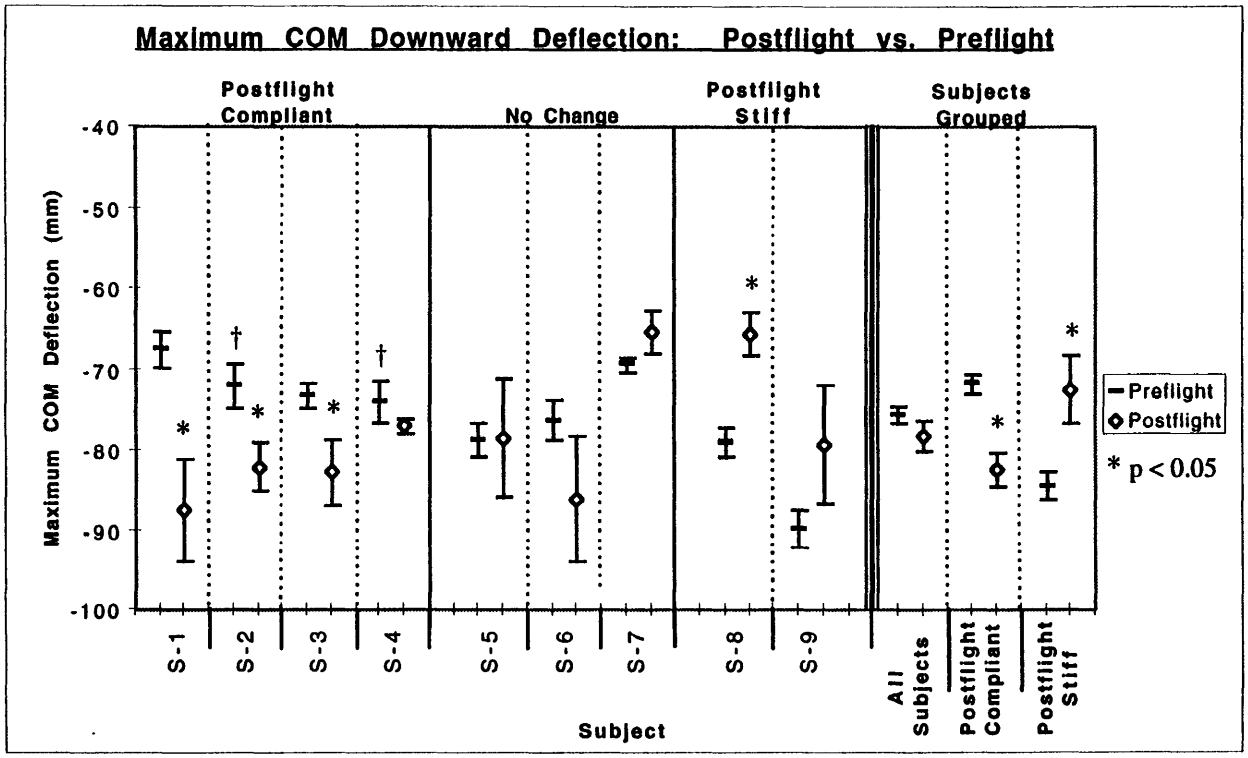

Figure 3.8. Peak CM downward displacement for all subjects. Average preflight and postflight values shown with error bars indicating standard errors of the mean. Statistical significance for preflight-postflight comparison ($p<0.05$) is indicated by "*", while a "†" denotes significant test day effect for the two preflight sessions.

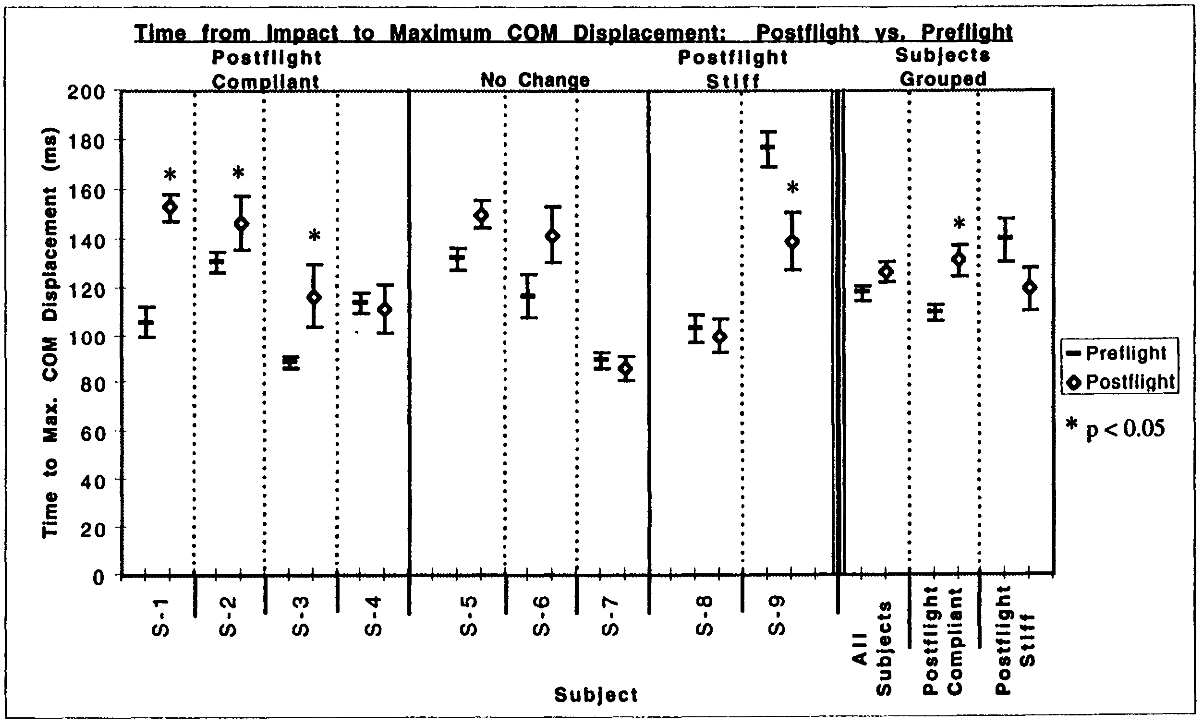

Figure 3.9. Time from impact to peak CM displacement for all subjects. Average preflight and postflight values shown with error bars indicating standard errors of the mean. Statistical significance for preflight-postflight comparison ($p<0.05$) is indicated by "*", while a "†" denotes significant test day effect for the two preflight sessions.

flexion rates for the knee and hip joints, respectively. Figure 3.8 and Figure 3.9 show the preflight and postflight values for the two CM-related measures: peak downward CM deflection and time from impact to peak deflection. With the exception of subject S-4, all of the P-C and P-S subjects demonstrate a significant change in one or both of the CM measures, supporting their classification.

The error bars are standard errors, and significant differences between the pre- and postflight data are denoted with asterisks (*). Cases marked by a "†" indicate a significant test day effect for the contrast between the two preflight sessions. Group averages for pre- and postflight data are also calculated for the P-S subjects, the P-C subjects, and all subjects taken together, and are shown at the right in Figure 3.5 - Figure 3.9. Taken as a group, the P-C subjects show significant increases in all 5 measures. Grouping the two P-S subjects reveals significant decreases in peak knee flexion and maximum CM downward deflection.

3.1.2.4. Modeled CM Vertical Motion

Figure 3.10 shows predicted CM model responses using parameters estimated for representative pre- and postflight jumps for P-C subject S-1. Model fits for the 12 preflight (Figure 10a upper) and 6 postflight (Figure 3.10a lower) trials are staggered along the vertical axis. Figure 3.10b shows preflight (upper) and postflight (lower) average CM vertical trajectories; the shaded region indicates ± 1 standard deviation. Simulated model results using the pre- and postflight stiffness and damping averages are included as well. The CM motion in the preflight jump exhibits a substantial overshoot above the final equilibrium posture, indicating a fairly low damping ratio. The postflight jump shows a much slower response with little overshoot. Thus, the postflight response is consistent with a decreased natural frequency and increased damping ratio in comparison to the preflight jump. P-S subjects, in contrast, demonstrate the opposite trend toward faster responses postflight with greater overshoot.

Table 3.3 summarizes the stiffness and damping coefficients that were estimated for each subject and show an excellent match with the subject classification based on kinematics. Note that these values have been normalized by the subject body mass. The modeled stiffnesses are shown in Figure 11. All four P-C subjects (S-1, S-2 , S-3, and S-4) and S-5 show large (23%-55%), statistically significant decreases in postflight stiffness compared to preflight values. Stiffness increases for P-S subjects S-8 and S-9 were not significant. The surprising lack of a significant postflight stiffness increase for subject S-9 (considering the consistent P-S changes in the joint and CM kinematics) may be due to this subject's postflight decrease in impact velocity. The change in impact loading is explicitly

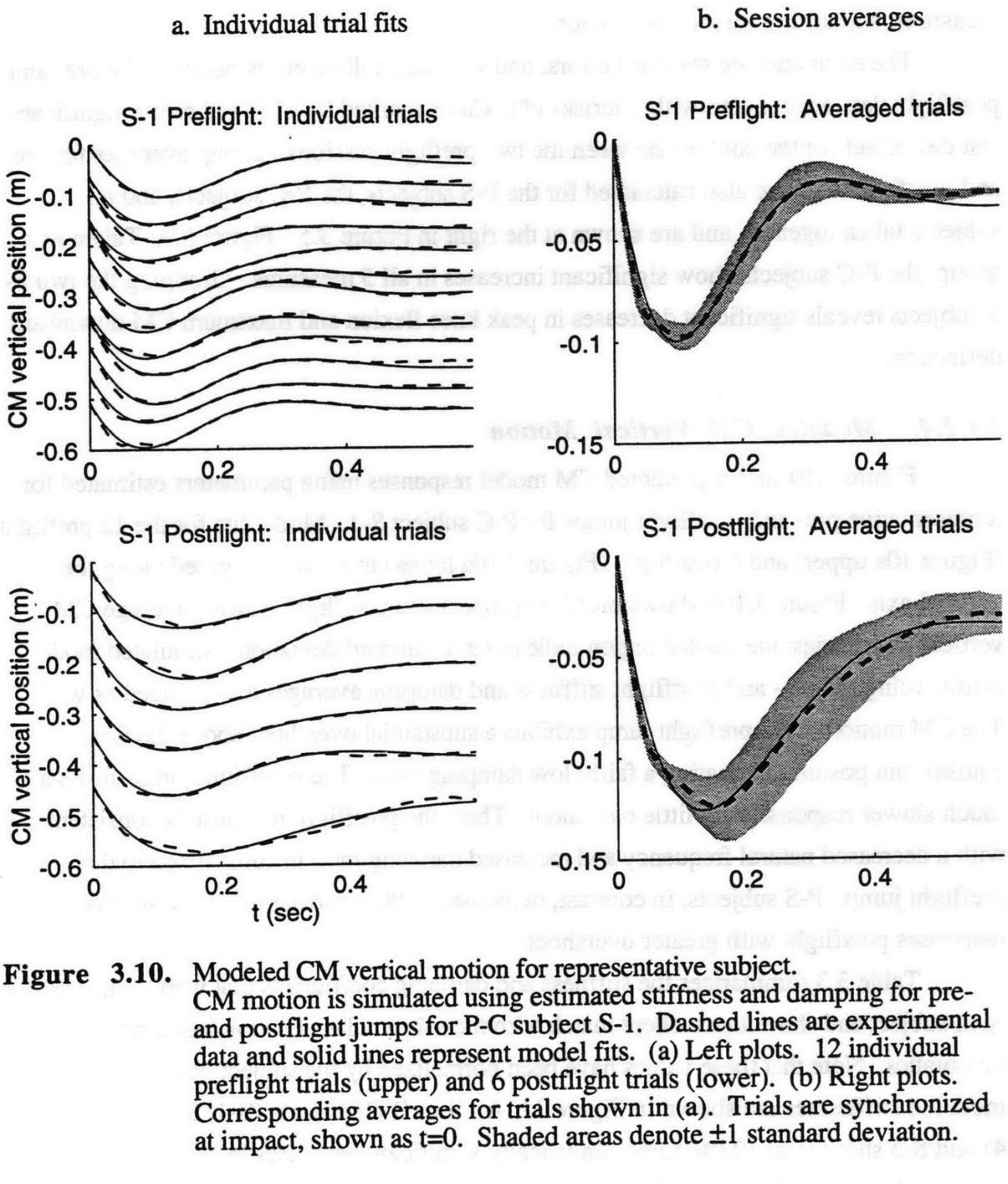

Figure 3.10. Modeled CM vertical motion for representative subject. CM motion is simulated using estimated stiffness and damping for pre- and postflight jumps for P-C subject S-1. Dashed lines are experimental data and solid lines represent model fits. (a) Left plots. 12 individual preflight trials (upper) and 6 postflight trials (lower). (b) Right plots. Corresponding averages for trials shown in (a). Trials are synchronized at impact, shown as t=0. Shaded areas denote ±1 standard deviation.

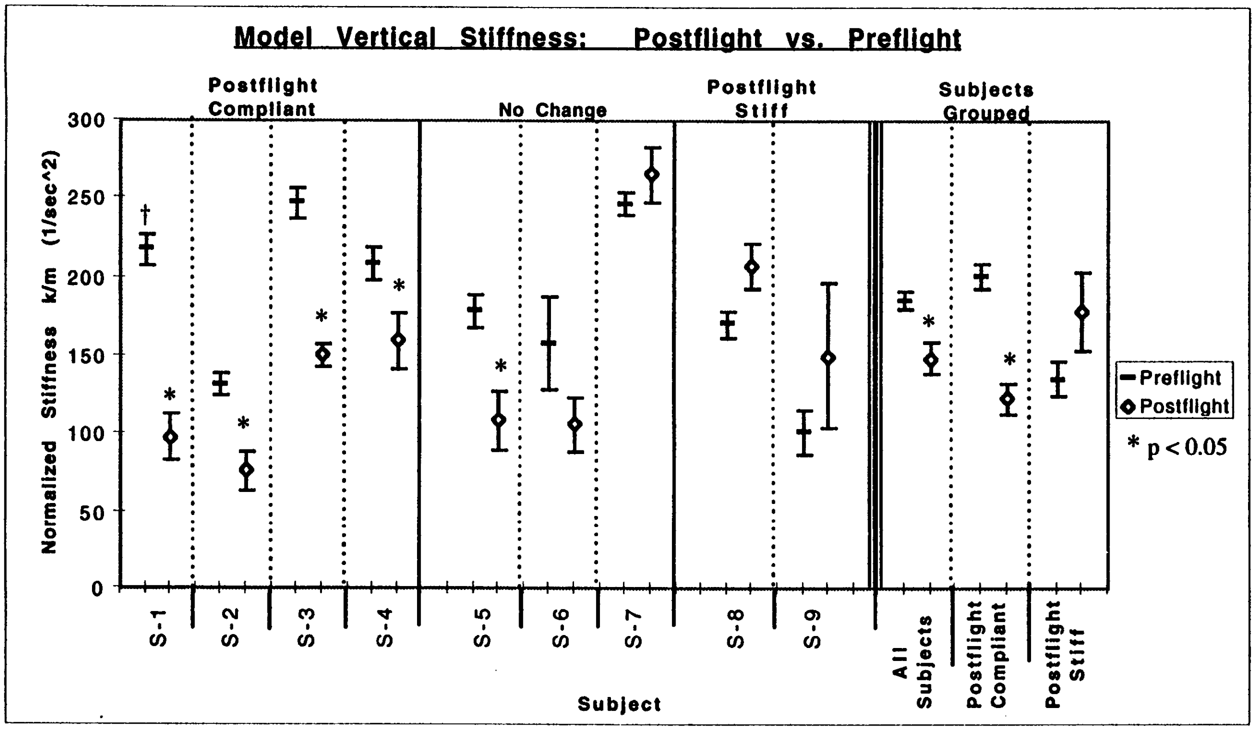

Figure 3.11. Mean pre- and postflight model vertical stiffnesses. Average preflight and postflight values shown with error bars indicating standard errors of the mean. Statistical significance for preflight-postflight comparison ($p<0.05$) is indicated by "*", while a "†" denotes significant test day effect for the two preflight sessions.

Table 3.3. Stiffness and Damping in Second Order Model

	STIFFNESS (K/M) ($1/s^2$)				DAMPING (B/M) (1/s)			
Subject	Pre-flight	Post-flight	Percent change	p-value	Pre-flight	Postflight	Percent change	p-value
S-1	217.2	98.3	-54.7%	0.0001	14.2	12.8	-9.7%	0.1490
S-2	132.0	76.6	-42.0%	0.0007	14.0	14.0	+0.1%	0.7150
S-3	247.2	150.7	-39.1%	0.0001	16.2	12.5	-22.9%	0.0030
S-4	208.2	159.9	-23.2%	0.0240	13.7	12.5	-8.6%	0.0740
S-5	178.6	108.9	-39.0%	0.0100	12.3	13.4	+9.5%	0.2630
S-6	158.3	106.3	-32.8%	0.1990	14.6	14.8	+1.8%	0.6590
S-7	247.1	265.4	+7.4%	0.3230	15.2	16.2	+6.5%	0.3030
S-8	170.5	207.8	+21.9%	0.0510	14.4	13.6	-5.9%	0.2280
S-9	101.4	150.4	+48.3%	0.1720	12.8	13.7	+7.1%	0.4620

accounted for in the CM motion model. In contrast with the changes in stiffness, examination of the damping coefficients reveals few differences between pre- and postflight performance, with only subject S-3 exhibiting a significant change (decrease). Furthermore, there is no apparent pattern of increases or decreases in the level of damping that corresponds to either subject classification or the changes in stiffness.

From the definitions of ω_n and ζ in Equation 3-2, a decrease in stiffness for a constant damping level should result in a lower natural frequency and a higher damping ratio. The calculated values for ω_n and ζ are shown in Table 3.4. As anticipated, the four P-C subjects all exhibit significant decreases of 13%-33% in the natural frequency as well as S-5, and hence reduced bandwidth postflight. Four of these subjects have increased damping ratios postflight as well, although significant changes are seen only for subjects S-1, S-2. and S-5. The P-S subjects demonstrate the opposite trend: increased natural frequency postflight, combined with decreases in the damping ratio (significant only for S-8 damping ratio).

Table 3.4. Second Order Response Parameters

	NATURAL FREQUENCY, ω_n				DAMPING RATIO, ζ			
Subject	**Pre-flight**	**Post-flight**	**% change**	***p*-value**	**Pre-flight**	**Post-flight**	**% change**	***p*-value**
S-1	14.7	9.8	-33.3%	0.0001	0.49	0.66	+36.5%	0.0004
S-2	11.4	8.6	-24.6%	0.0003	0.61	0.83	+35.4%	0.0010
S-3	15.7	12.3	-21.8%	0.0001	0.52	0.51	-2.5%	0.7600
S-4	14.4	12.6	-12.7%	0.0200	0.48	0.50	+5.6%	0.2850
S-5	13.3	10.3	-22.5%	0.0090	0.47	0.67	+43.0%	0.0100
S-6	14.3	10.1	-18.0%	0.1870	0.61	0.74	+20.7%	0.1020
S-7	15.7	16.2	+3.4%	0.3260	0.49	0.50	+3.0%	0.5920
S-8	13.0	14.4	+10.5%	0.0540	0.56	0.48	-14.7%	0.0090
S-9	9.8	11.7	+20.0%	0.1500	0.68	0.61	-10.4%	0.2600

3.2. *PARTIAL WEIGHT UNLOADING EXPERIMENTS*

The results of the pre- and postflight comparison of astronaut jumps suggest that adaptive changes in the controlled leg impedance account for altered performance in jump landings after space flight. In particular, the responses of the P-C group indicate that the reduced demands on the postural control system in microgravity permit reduction of the leg stiffness, altering the kinematics of the postflight jumps. However, a variety of explanations exist for the hypothesized changes in leg impedance, including altered central control of leg stiffness, deconditioning of the postural muscles, and changes in vestibular feedback or spinal stretch reflexes.

Short term unloading of the leg anti-gravity muscles provides an opportunity to test the possibility that adaptive changes in leg impedance control can occur as a consequence of reduced requirements for load bearing by the lower limbs. With adaptation periods limited to approximately 2 minutes, muscle atrophy is not a concern. Moreover, vestibular sensing is not affected during unloading in a terrestrial 1-g environment. For these reasons, a test of jumping following short term exposure to simulated partial gravity was devised to investigate further the results of the astronaut experiments.

The following sections describe the adaptation experiments that are designed to imitate the astronaut jumping tests, using short term exposure to partial body weight unloading as a model of the reduced demands of the postural control system in microgravity. The experimental design is covered first, followed by an explanation of the processing and analysis of the data. Finally, the results of the experiments are detailed.

3.2.1 "Moonwalker" Partial Weight Unloading Experiment Design

3.2.1.1. *Experimental Apparatus*

This section describes the equipment used to perform the partial weight unloading adaptation tests. The partial gravity simulator, known as the "moonwalker," is described first. The data acquisition hardware is then reviewed. Measurements taken in this experiment include ground reaction forces and body segment kinematic data. A single-camera video tracking system was designed and implemented to track body segment motion.

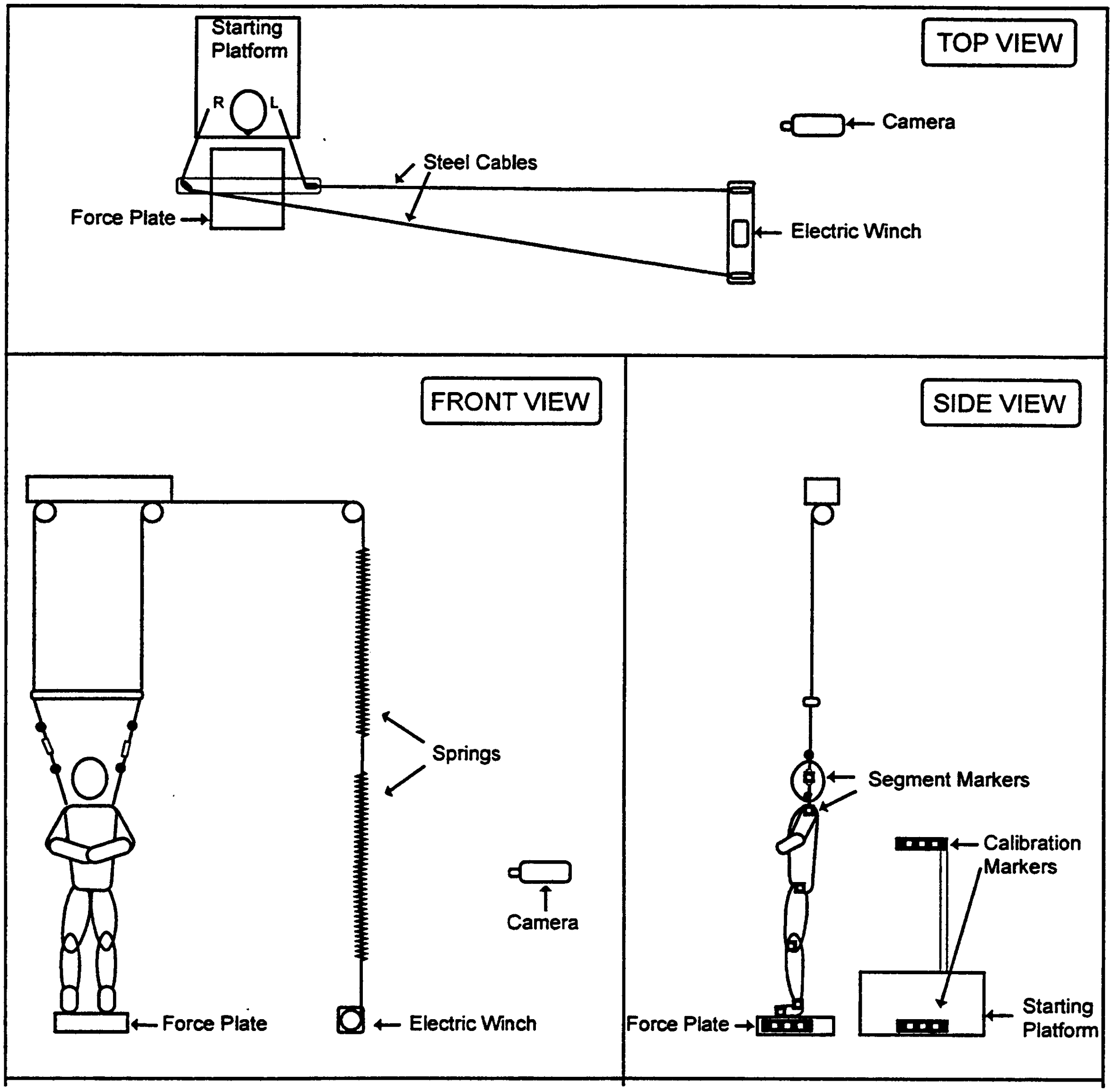

Figure 3.12. Moonwalker suspension system and jump apparatus. The subject is suspended by a harness attached to steel cables. Unloading is controlled by varying the spring tension with the electric winch. The camera views the subject's left side. The marker locations are indicated in the side view.

"Moonwalker" Partial Gravity Simulator

The moonwalker apparatus is derived from a design used at the Harvard Field Station [He *et al.*, 1991]. The moonwalker uses an overhead suspension system to partially or fully unload the legs, and is depicted in Figure 3.12. The subject wears a safety harness (Mori Safety Products, Toronto) of nylon webbing. The harness consists of two loops that buckle snugly about each thigh and connect to straps that pass over the shoulders.

When a subject is suspended in the harness, the main upward force is applied along the region where the leg loops contact the inner thighs and buttocks. A horizontal force is also applied to the back and chest by the shoulder straps, and tends to pull the subject horizontally forward or backward toward the overhead attachment point. This horizontal component acts as a restoring force toward upright posture when the subject is directly beneath the overhead attachment. However, if the subject is not standing beneath the attachment point, the horizontal forces pull the subject away from an upright stance. The horizontal force is equal to the tension in the cables multiplied by the sine of the cable angle with respect to vertical, and is approximately proportional to the cable angle for small deviations.

Each shoulder strap is connected to a steel cable that runs to a pulley overhead. The two pulleys are held by carabiners attached to large eye bolts screwed into a 4"x4"x3' (8.9 cm x 8.9 cm x 91 cm) wooden beam in the center of the ceiling. The steel cables run along the ceiling to another pair of pulleys similarly attached to another wooden beam next to the wall. Each wooden beam is mounted into the concrete ceiling cross beams with four 3/8" (0.95 cm) Hilti inserts. After passing through the second set of pulleys, the two cables are joined together by a carabiner attached to the upper end of two garage door springs mounted in series. The two springs run vertically along the wall, and the bottom of the lower spring is attached to a heavy steel cable wound around an electric winch. The winch is mounted to the concrete floor with Hilti inserts, and draws power from a 12V car battery.

The upward force exerted by the harness on the subject is determined by the distance the two springs are stretched. The electric winch is used to control the stretch of the springs. Because the winch is used to fix the end position of the lower spring, the actual spring length varies with vertical motion of the subject, as does the resulting force exerted on the subject. Figure 3.13 shows the force-length relationship for the two springs in series. The stiffness is linear over most of the range of operation, with a spring constant of approximately 265 N/m. For a downward jumping distance of 30 cm, the upward force

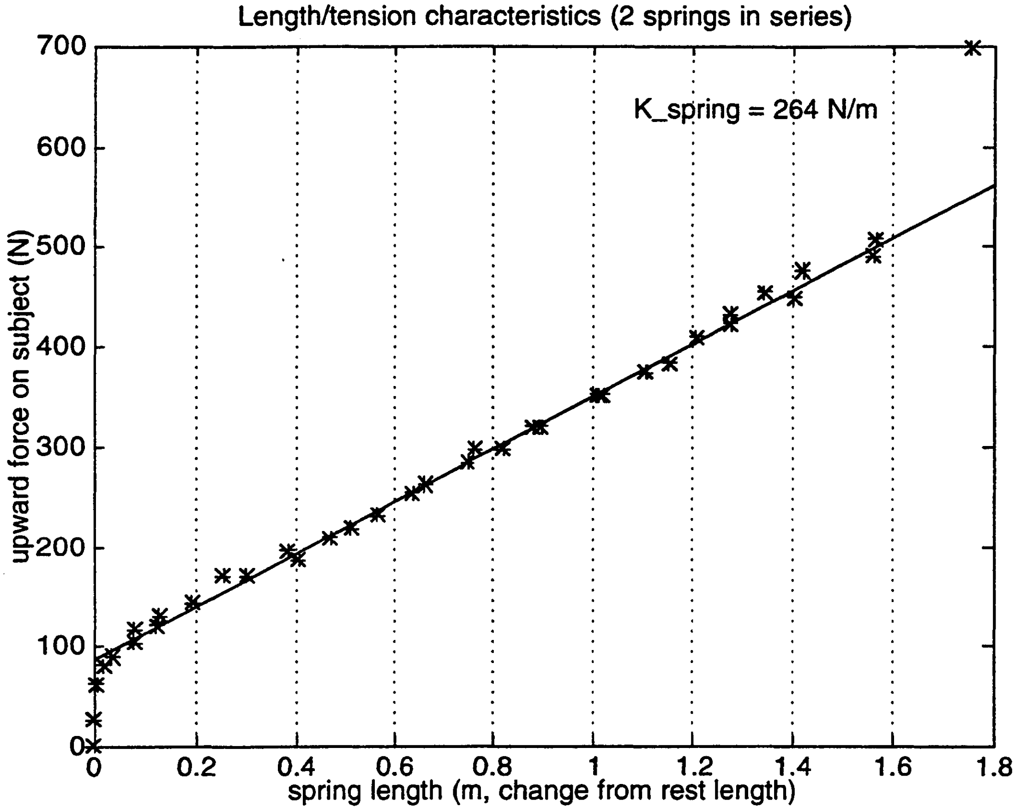

Figure 3.13. Moonwalker spring length-tension data and linear fit. Least-squares linear fit (solid line) does not include the first 3 points (below the line) or the last point (above the line).

from the harness is approximately 80 N greater when the subject is standing on the force plate than when the subject is standing on the starting platform. The subjects for this experiment weigh between 511 N and 645 N, so the change in upward force over the vertical range of the jump ranges from 12% to 16% of body weight.

The main goal of the partial weight unloading procedure is to reduce the load borne by the legs. However, the suspension harness also exerts horizontal forces when the subject is not directly below the overhead attachment. Furthermore, the main area of support is somewhat below the body mass center. Thus, the equilibrium posture of the subject during unloading is of interest. One subject (C) is tested with the harness detached from the cables, and also with the cables supporting 60% of the subjects body weight.

The trunk angle is measured with a straight metal rod taped securely to the torso at the level of the armpits and the iliac crest. At either end of the rod, markers are placed so that the rod orientation may be measured by the video system described below. The results of this test are described in Table 3.5. Upright stance while standing on the force plate with the harness disconnected from the cables is defined as a trunk angle of 0 degrees.

Table 3.5. Trunk rest angle at various harness loading conditions. Subject C is tested standing on the force plate, standing on the starting block, and hanging above the force plate. Positive angles correspond to leaning forward.

Condition	Trunk angle from vertical (degrees)
Standing on force plate, harness detached	0
Standing on block, harness detached	-0.5
Standing on force plate, cables loaded (60% Body Wt).	12.1
Standing on block, cables loaded (60% Body Wt).	23.4
Hanging above force plate on cables (60% Body Wt).	12.2

These results indicate that the unloading technique alters the standing trunk angle, causing the subject to lean forward about 12 degrees when standing beneath the attachment point. Standing on the starting block, which is located somewhat behind the attachment point, requires the subject to lean further forward, to a trunk angle of 23 degrees, in order to maintain balance. With the subject hanging fully supported by the cables, the trunk angle is again 12 degrees, similar to the standing posture under partial unloading. Even though the vertical force is applied below the body mass center, this position is quite stable due to horizontal restoring forces exerted by the shoulder straps.

Jump Platform and Landing Surface

The jump platform is constructed so that the upper surface is 30 cm higher than the upper surface of the force plate. For normal jumps, when the subject is not connected to the harness, the edge of the starting platform is located 5 cm behind the edge of the force plate. However, this position is not acceptable for the jumps performed while unloaded by the harness, because the horizontal force due to the suspension cables prevents upright posture and makes balance difficult. For this reason, the starting platform is designed to slide forward and rest on the floor on either side of the force plate, so that it can be positioned closer to the center of the overhead attachment. In this configuration, the forward extent of the force plate does not provide sufficient space for landing. A platform of the same height as the force plate upper surface is used to extend the area available for landing in the forward direction. The starting block and landing surface extension are constructed of 2"x4" (3.8 cm x 8.9 cm) pine and 1/2" (1.3 cm) thick plywood sheathing.

Force plate Data Acquisition

A single AMTI OR6-5 series force plate (Advanced Medical Technology, Inc., Newton, MA) is used to measure ground reaction forces in 3 axes. The force plate is bolted to the concrete floor using Hilti inserts, and is positioned directly beneath the center of the two pulleys supporting the subject harness. The force plate is 51 cm by 41 cm, with a maximum load capacity of 4500 N and a resonant frequency of 500 Hz. It incorporates full bridge strain gages mounted on four elements at the corners of the plate, providing the three orthogonal force components and the accompanying moments. The force plate has less than 2% crosstalk on all channels. High gain, low noise amplification of the force plate signals was provided by an AMTI MCA amplifier. The amplifier has variable gain settings of 1000, 2000 or 4000, and low-pass filter cutoff frequencies of 10.5 Hz or 1050 Hz. For all of the tests described here, the gain and filter settings were 2000 and 1050 Hz, respectively.

Force plate data digitization and acquisition are performed using a Power Macintosh 8100/80 computer equipped with a National Instruments NB-MIO-16L data acquisition board. The data acquisition board receives input signals from a BNC adapter card, the National Instruments BNC-2080. The amplifier outputs are connected to the BNC-2080 by BNC cables. The 6 channels of force plate data are sampled at 2000 Hz.

Video Marker Tracking System

The positions of the body segments on the left side of the subject are tracked using a single Sony Handycam 8 mm camcorder. The center of the camera lens is placed 2.66 m from the left edge of the force plate at a height of 1.01 m above the floor. The camera is tilted 90° from the normal orientation, so that the long, normally horizontal dimension of the field of view is aligned with the gravitational vertical. The vertical field of view is adequate for capturing the entire jump trajectory. However, a portion of the horizontal field of view is blocked by the left edge of the door frame. Thus, if the subject jumps or leans too far forward, some body segments may be hidden from view. In practice, this is rarely a problem.

The video camera is used to record the position of six markers placed at various anatomical landmarks on the left side of the body (see Figure 3.15). The toe marker is placed at the 5th toe metatarsal-phalangeal joint. The ankle marker is placed over the lateral malleolus. The knee joint is marked at the lateral femoral epicondyle. The hip marker is placed over the greater trochanter of the femur. The shoulder is marked at the acromian process. The head marker is placed directly over the center of the ear.

The markers consist of white labels measuring 1" x 0.75" (2.5 cm x 1.9 cm). The subjects wear opaque, skintight black stockings on the legs. Another black stocking is worn on the left arm, pulled up over the shoulder. A black, form fitting cap is worn on the head, and covers the ears. The white markers provide excellent contrast against the black background. Double-sided tape is placed on the skin over the desired landmarks before the stockings are donned, in order to secure the stockings over the areas of interest. Black electrical tape is used to help secure the edges of the marker labels to the black cloth.

Three calibration markers are fixed at 10 cm intervals along the side of the force plate, below the landing surface. Another three calibration markers are placed 10 cm apart on the lower edge of the side of the starting platform, at the same height as the markers on the force plate. A final set of three markers, also spaced at 10 cm intervals, is mounted on a wooden meter stick attached to the starting platform, such that the markers lie in the same plane as the other two sets. These markers are positioned directly above the markers attached to the base of the starting platform, at a height 1 m above the lower two sets. A black cloth is draped behind the subject to improve the marker contrast in the video image.

The video camera optics cause some distortion of the image, especially in areas far from the center of the field of view where straight lines in the scene are noticeably curved in the video image. An array of calibration markers is constructed in order to provide a mapping of the true spatial coordinates to the camera focal plane coordinates. The calibration array consists of the same white marker labels placed at intervals on a black door that had been removed from its hinges. This door provides a large, flat, rigid surface for the markers.

The markers are aligned in an array of 11 rows and 6 columns, as shown in Figure 3.14. The columns are spaced 14 cm apart, with the rightmost column aligned with the vertical centerline of the camera field of view. All tracked body segment motion occurs in the left half of the field of view. Rows 1-5 and 7-11 (counting upward from the bottom) are evenly spaced 20 cm apart. Row 6 is set between rows 5 and 7 at the level of the horizontal centerline of the camera field of view. Alignment accuracy of the markers in the calibration array is better than 1 mm in each dimension. Only markers in rows 1, 3, 5, 6, 8 and 10 (counting from the bottom) and in columns 1, 4 and 6 (counting from the left) are used to calibrate the camera field of view. The use of the calibration array data in the processing of the video images is described later with the data analysis procedures in Section 3.2.2.3.

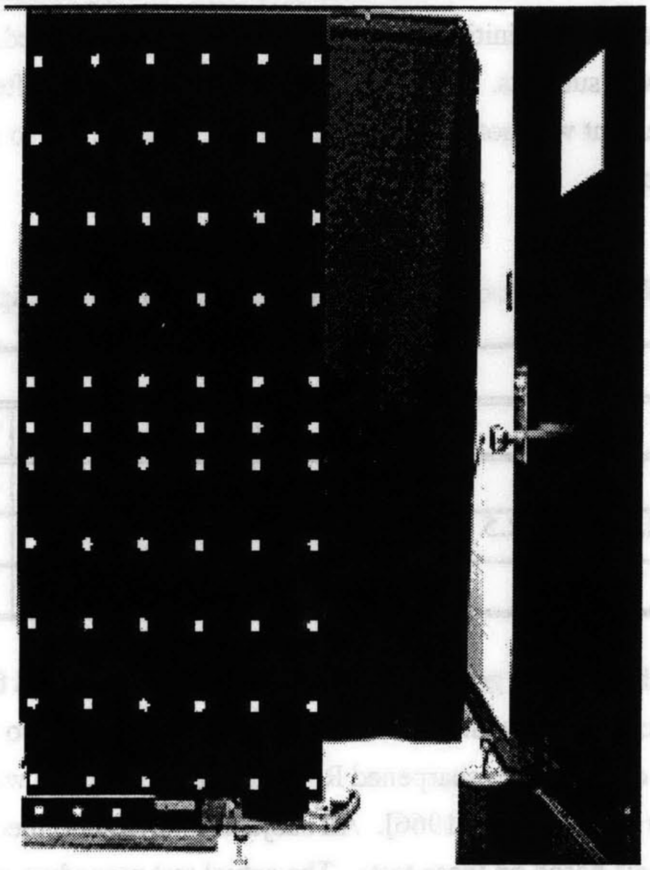

Figure 3.14. Array of video image calibration markers.
The video image is rotated 90° clockwise so that the longer dimension is aligned with the vertical. The calibration markers are placed on a black door, which is resting on the force plate (lower left).

3.2.1.2. Moonwalker Experimental Protocol

The moonwalker suspension protocol is approved for use with human subjects by MIT's Committee On the Use of Humans as Experimental Subjects (COUHES). All subjects gave informed consent. A copy of the informed consent statement is included in Appendix A. The moonwalker experimental protocol consists of 3 stages: (1) subject preparation; (2) baseline jumps; and (3) partial weight unloading adaptation and jumping.

Subject Selection

All seven volunteer female subjects in the moonwalker experiment are female for consistency with the false platform experiments described later. The subjects range from 22 to 27 years of age. Subject age, height and weight are listed in Table 3.6. The subjects are designated by letter codes B-H. The letter A is used to designate an initial trial subject tested during the protocol definition stage, and his data is not analyzed. Force plate data are available for all seven subjects. However, the video camera was shifted during subject D's tests, and the movement was not noticed until after the experiment, so video data is not available for subject D.

Table 3.6. Moonwalker experimental subject descriptions

	Subject Code						
	B	**C**	**D**	**E**	**F**	**G**	**H**
Age (years)	23	23	23	26	22	25	27
Height (cm)	162.5	162.5	160	173	165	170	172.5
Weight (kg)	56	59	71	59	52	57	66

All subjects are athletic and in good health. The subjects are screened for ataxia that might indicate the presence of vestibular defects. Each subject performs two tests: (1) quiet standing with eyes closed in the sharpened Romberg stance, and (2) walking a line with the eyes closed [Fregly and Graybiel, 1966]. All subjects are found to meet the ataxia criteria for vestibular normals based on these tests. The actual test procedure and detailed test scores are described in detail in Appendix B.

Subject Preparation

Before beginning the experiment, the subject reads and signs a statement of informed consent. The subject then dons the black stockings on the legs and arm, as well as the black cap. The six white markers are placed on the anatomical landmarks, as described earlier in the video motion tracking section. No shoes or socks are worn during the tests. The lateral dimension of the subject's body with the feet together is measured at the fifth toe, lateral malleolus, knee, hip, shoulder and ear. These measurements are used in the video data processing to estimate the marker position in the direction parallel to the camera viewing axis. Last, the subject dons the suspension harness. However, the harness is not initially attached to the suspension cables.

Baseline Jumps

The starting platform is placed with its front edge located 4 cm behind the back edge of the force plate. Before the initial baseline jump, the subject stands with the toes at the edge of the starting block, and the feet are aligned on either side of an 8.9 cm (3.5") wide wooden block to be parallel and facing straight. The location of the outside edge of the 5th toe on each foot is marked on the block with black electrical tape, and the subject places her feet in the same position before each jump.

The subject performs 6 baseline jumps. These jumps are performed with the arms folded across the abdomen, so that one hand grips the opposite wrist. The subject is instructed to look down at the landing platform before jumping, and then perform two-footed downward jumps, taking off and landing with both feet simultaneously. Upon landing, the subject is instructed to recover to an upright standing position at a comfortable pace, and to look straight ahead. The command to the subject for each jump is: "Look down. One, two, ready, jump." Force plate data acquisition is triggered at the command "ready," and 4 seconds of force plate data are taken for each jump. The subject jumps at the command, "jump."

After the subject returns to an upright stance, the position of the fifth toe and lateral malleolus of the left foot are measured relative to the left edge of the force plate. The inter-ankle distance (left lateral malleolus to right lateral malleolus) is also measured. These measurements are used in the video processing to estimate marker positions along the direction parallel to the camera axis.

Partial Gravity Adaptation Jumps

After the baseline jumps, the subject repeats the following sequence 6 times: (1) 10 jumps under 60% body weight unloading; then (2) 1 jump with no unloading. For the 10 partially unloaded jumps, the subject's harness is attached to the overhead suspension cables using carabiners. With the springs unstretched, the subject stands on the force plate, and the body weight is recorded. The winch is then used to stretch the springs until the force plate output reads 40% of the subject's body weight. Thus, the upward force on the subject due to the harness varies between approximately 45% body weight when the subject stands on the 30 cm starting platform, to 60% body weight when the subject stands upright on the force plate.

The starting platform is moved forward to minimize the horizontal forces on the subject while standing on the platform. The subject performs 10 jumps with the same instructions used in the baseline jumps. However, no force plate data is acquired during the unloaded jumps, and no measurements of final foot position are taken. After each jump, the subject steps or hops back up onto the starting platform and positions the feet for the next jump.

After the tenth adaptation jump, the subject is quickly prepared to make a single jump while supporting her full body weight. The starting block is moved back to its original position behind the edge of the force plate. The subject steps up onto the starting platform, and the winch is used to reel out the cable and release the tension in the springs. The harness is detached from the suspension cables, and the subject places her feet according to the tape marks on the platform. The subject jumps, following instructions identical to those given for the baseline jumps. After the jump, the final positions of the feet relative to the force plate are measured as described for the baseline jumps.

All preparation steps following the final unloaded adaptation jump are performed as quickly as possible, in order to minimized the time during which the subject might readapt to the normal loading condition. Occasionally, joint markers need readjustment following a set of adaptation jump. This is especially true for the hip marker, because the leg loops on the extension harness tend to cover the hip marker area when the subject is unloaded. If extra time is needed to readjust the markers, the jump is still performed. However, data from this jump is excluded from the analysis, and the adaptation jump sequence is repeated to get the full complement of data for 6 usable adapted jumps.

3.2.2. Moonwalker Video Data Processing

Extracting body segment and CM kinematic data from the jump videotapes takes place in 4 stages: (1) digitization of the video images; (2) extraction of marker locations from the digitized video images; (3) estimation of marker positions in three-dimensional space using the camera calibration data, body measurements, and foot initial and starting positions; and (4) calculation of joint angles and CM location estimates from the marker positions in space. The first three steps are described here, while the fourth step is identical to the processing performed for the astronaut jumping experiment described earlier.

3.2.2.1. Video Digitization

The first stage in extracting marker information is obtaining digitized still frames of the videotaped jump. The digitization actually requires two steps. First, the video segments of interest are dubbed from Hi-8 8 mm format onto Beta format videotapes. In the dubbing process, a visible time code is burned into the video image using an Edit Code Master ECM-4000 (Evertz Microsystems; Burlington, Ontario, Canada). The ECM-4000 generates characters giving the hour, minute, second and frame number. These characters are placed within the image in an area that does not interfere with the body segment markers during the jumps.

The Beta video segments are then digitized using the built-in video card in a Power Macintosh 8500. Thirty frames of video are acquired from each second of videotape. The Adobe Premiere software package is used to perform the digitization and storage of the images. The Sony SL-HF1000 Beta format videocassette recorder permits the user to step easily through each individual frame sequentially. The time code in each image allows the operator to ascertain that no frames are skipped or duplicated. Adobe Premiere is used in snapshot capture mode to create a digital movie from the individually captured frames. Using this stop action technique is necessary because the video card lacks the capacity to capture normal speed video at the full 30 frames/sec with sufficient resolution. The images are captured with a resolution of 280 pixels vertically and 320 pixels horizontally (in the video image, not with respect to gravity), using 8 bits per pixel for 256 levels of gray. Once all frames for a jump have been digitized, the frames are stored as a numbered sequence of PICT images.

3.2.2.2. Marker Position Within Video Images

A LabView program *pict_get_points_save.vi* is written to extract the positions of the individual markers from each stored video frame. This program loads each stored frame in sequence. Figure 3.15 shows a typical jump video frame. The program displays the current frame, and with the mouse the data analyst draws a small box around each marker of interest. The program applies a threshold operation to the pixels within the box, so that the bright marker pixels are set to a value of one and the dark background pixels receive a zero value. The centroid of the pixels within the box is then calculated with respect to the upper left corner of the image. This process is repeated for each marker selected by the analyst. For the jump images, 9 markers are selected in each frame, corresponding to the 6 body markers and 3 fixed calibration markers. After all markers are selected for the current frame, the program loads the next frame in the sequence. The marker positions for a complete jump are stored in an ASCII file that can be loaded into MatLab.

The LabView program permits the analyst to select the image threshold level interactively in order to account for varying image contrast levels. It also allows the analyst to revise selection of individual marker areas or repeat marker selection for an entire frame if necessary. However, this method of tracking body motion is extremely labor intensive, especially when the time needed to dub the video and digitize the frames is considered.

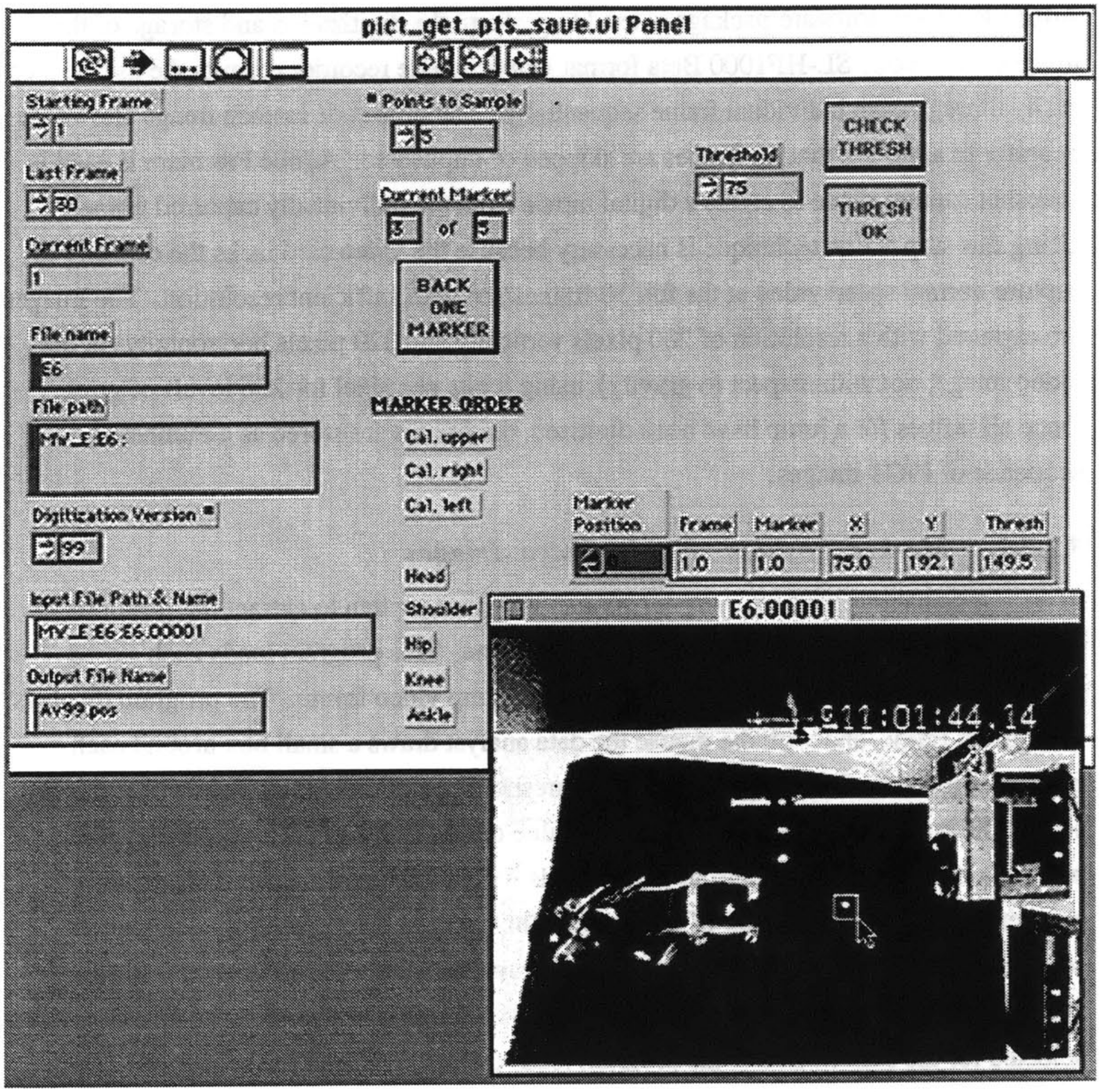

Starting Frame: 1
Last Frame: 30
Current Frame: 1
File name: E6
File path: MV_E:E6:
Digitization Version: 99
Input File Path & Name: MV_E:E6:E6.00001
Output File Name: Av99.pos
Points to Sample: 5
Current Marker: 3 of 5
Threshold: 75
Marker Position: 0

Frame	Marker	X	Y	Thresh
1.0	1.0	75.0	192.1	149.5

Figure 3.15. LabView program to select and record marker positions. The program *pict_get_points_save.vi* displays the video frames sequentially, and prompts the user to select an area around each marker with the mouse.

3.2.2.3. *Estimation of 3-D Marker Coordinates from Image Coordinates*

The first step in estimating the marker positions in 3 dimensions requires mapping of the image coordinates to coordinates in the plane of the calibration array, which corresponds to the vertical plane passing through the edge of the force plate nearest the camera. The procedure for mapping camera coordinates to calibration plane coordinates consists of the following steps:

1. Determination of calibration array marker positions in camera coordinates. Camera coordinates of the array markers are found by digitizing six frames containing the calibration array, then extracting the marker positions using the LabView program described above. The position of each marker is found by averaging the results from the six frames.

2. Rotation of the calibration array coordinate system to align with the camera coordinates. The distortion from the camera optics is assumed to be symmetric about the center of the field of view. The markers in column 6 (counting from the left) and in row 6 (counting from the bottom) are approximately aligned with the camera vertical and horizontal centerlines, respectively, and these markers are used to estimate the rotation between the two coordinate systems. The rotation angle is estimated using a Simplex method in MatLab. The objective function is the sum in the rotated coordinate system of the squared vertical deviations from the mean of the markers in row 6 and the squared horizontal deviations from the mean of the markers in column 6. The angle that minimizes this objective is the best estimate of the rotation between the two coordinate systems.

3. Determination of best linear mapping from camera coordinates to calibration array coordinates. Once the coordinate systems have been aligned rotationally, the best linear estimate of the mapping from camera coordinates to calibration coordinates is determined as follows:

$$\hat{\vec{r}}_{cal} = \begin{bmatrix} \hat{x}_{cal} \\ \hat{y}_{cal} \end{bmatrix} = \begin{bmatrix} K_{xx} & K_{xy} \\ K_{yx} & K_{yy} \end{bmatrix} \begin{bmatrix} x_{image} \\ y_{image} \end{bmatrix} + \begin{bmatrix} x_{0,cal} \\ y_{0,cal} \end{bmatrix} \qquad (3\text{-}3)$$

where

$\hat{\vec{r}}_{cal}$ = estimated marker position in calibration array coordinates

K_{xx}, K_{xy}, K_{yx}, K_{yy} = best fit scaling factors

$x_{0,cal}$, $y_{0,cal}$ = calibration array origin distance from image origin

4. Computation of residual error from linear fit. A table of the residual errors at each calibration marker location is computed and stored:

$$\Delta\hat{\bar{r}}_{cal\,i,j} = \begin{bmatrix}\Delta\hat{x}_{cal}\\ \Delta\hat{y}_{cal}\end{bmatrix}_{i,j} = \begin{bmatrix}\hat{x}_{cal}\\ \hat{y}_{cal}\end{bmatrix}_{i,j} - \begin{bmatrix}x_{cal}\\ y_{cal}\end{bmatrix}_{i,j} \qquad (3\text{-}4)$$

where $\Delta\hat{\bar{r}}_{cal\,i,j}$ = residual error from bet linear fit
$\hat{x}_{cal}$, $\hat{y}_{cal}$ = best linear fit estimates of marker calibration coordinates
x_{cal}, y_{cal} = measured marker calibration coordinates
i, j = row, column of calibration marker

This calibration procedure is performed only once. In order to convert marker image coordinates to calibration array coordinates for the jump video, the best linear fit is computed using the scaling factors described above. Then a correction term is estimated by interpolating the residual error using the nearest 4 points in the residual lookup table.

However, this procedure only returns the estimated marker positions as projected upon the plane of the calibration array. Because the markers are actually further from the camera than the calibration array plane, the distance discrepancy in the direction parallel to the camera axis introduces errors in the computed marker position. The error increases linearly with the distance from the calibration array plane and the in-plane distance from the camera axis, as given by the following relationship:

$$\Delta r = \frac{|\bar{r}|}{z_{cal}} \cdot \Delta z \qquad (3\text{-}5)$$

where Δr = scalar position error offset in the plane parallel to the calibration array
$|\bar{r}|$ = distance of the marker projection from the camera axis in the calibration array plane
z_{cal} = normal distance from camera to calibration array plane
Δz = normal distance of marker to calibration array plane

The distance from the camera to the plane of the calibration array is 266 cm. Thus, for a marker whose projection on the calibration array plane is 100 cm from the camera axis, the error introduced in the actual distance from the camera axis is approximately 0.38 cm for every cm the marker is moved away from the calibration plane.

The single camera system provides no means to estimate distance in depth (along the camera axis). For this reason, measured body dimensions and initial and final foot positions are used to estimate the horizontal distance of the markers from the calibration array plane (which corresponds to the left edge of the force plate). The body centerline is assumed to lie halfway between the left and right feet, so the initial and final foot position measurements provide initial and final depth measurements of the body centerline.

The trajectory of the body center along the camera axis is assumed to be piecewise linear in time, moving from the initial to the final position while the subject is airborne, then remaining at the final position after impact. Likewise, the feet are assumed to follow similar piecewise linear trajectories between the measured initial and final positions. The hip, shoulder and head coordinates in the direction along the camera axis are calculated by subtracting one half of the measured body width at these heights from the body centerline trajectory. The knee marker is assumed to lie halfway between the hip and ankle markers in the camera depth direction. The geometry of the camera arrangement is shown in Figure 3.16 in two dimensions.

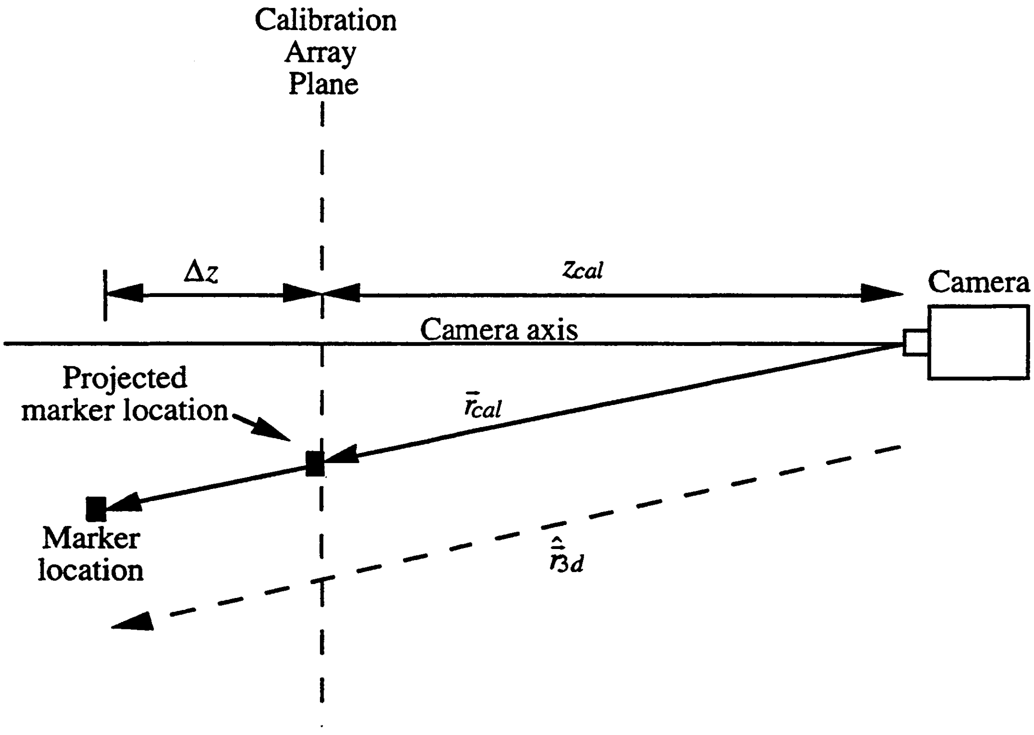

Figure 3.16. Video camera field of view geometry.
Two dimensional projection shows camera, calibration array plane and actual marker position.

The marker position estimates in 3 dimensions are computed from:

$$\hat{\vec{r}}_{3d} = \frac{z_{cal} + \Delta z}{z_{cal}} \cdot \vec{r}_{cal} \qquad (3\text{-}6)$$

where $\hat{\vec{r}}_{3d}$ = 3-d position of marker in space
z_{cal} = distance from camera lens to calibration array plane along camera axis
Δz = distance from calibration array plane to marker along camera axis
$\vec{r}_{cal}$ = projection of marker position from camera onto calibration array plane

Two tests are performed to estimate the resolution of this marker tracking method. Both tests are performed within a plane normal to the camera axis; no measurements of errors introduced by out-of-plane motion are attempted. First, the position of a calibration marker is measured in 180 frames taken from 6 jumps. The standard deviation of the marker position in each direction is:

$$\begin{aligned} \sigma_{horizontal} &= 0.18\,cm \\ \sigma_{vertical} &= 0.16\,cm \end{aligned}$$

These numbers provide an estimate of the variability of the method caused only by variation in the video signal and digitization process.

In the second test, a thin sheet of plywood with 3 markers mounted at 10 cm intervals is pinned to a support through the center of the marker at one end. As the plywood is rotated about the pin, the center of the other two markers describe circles of 10 cm and 20 cm radii respectively. With the pin fixed, the plywood is rotated sequentially to 8 positions spaced 45 degrees apart, and video images are captured in each position. This process is repeated at 3 locations in the camera field of view. In the first, the pin is located 50 cm above the camera axis. In the second, the pin coincides with the camera axis, while the pin is fixed 40 cm below the camera axis in the third position.

The distance from the central marker to each of the radially mounted markers is calculated, and the standard deviation from the mean for the 8 measurements in each pin position is presented in Table 3.7. If the resolution in locating a single marker is considered to be half the standard deviation of the inter-marker distances, the measurement resolution of this system is 3 mm or better in much of the camera field of view. Not surprisingly, the resolution becomes poorer at greater distances from the camera axis.

Table 3.7. Variability in measurement of constant inter-marker distance. The standard deviation in measured inter-marker distance is shown for two markers fixed to a base which is rotated about a fixed point in three different regions of the camera field of view.

	Standard Deviation in Inter-marker Length (cm)	
Height above camera axis	Marker 1 - Marker 2	Marker 1 - Marker 3
50 cm	0.248	0.356
0	0.193	0.168
-40 cm	0.496	0.630

3.2.3. Moonwalker Adaptation Results

The results of the partial weight unloading experiment are presented in two parts. First, the vertical ground reaction force data are described. Next, the leg joint kinematic data are considered. In each case, the baseline jumps are compared to the jumps following adaptation to partial weight unloading using the moonwalker.

3.2.3.1. Force Plate Data

Figure 3.17 shows force plate results for subjects B-H. The vertical ground reaction force traces shown are averages of the 6 post-adaptation jumps superimposed over the average of the 6 baseline force traces. All data are aligned at the impact sample, which is the origin of the time axis. Two trends in the force data are apparent. First, the force traces for the adapted jumps tend to lag behind the forces from the baseline jumps. This effect may be most easily observed by comparing the times when the ground reaction force decreases below the 1 body weight level. At this moment during the recovery toward upright posture after landing, the mass center is no longer being accelerated upward.

These plots also show that the *minimum* ground reaction force generally increases in the adapted jumps, compared to the minimum level seen in the baseline jumps. The minimum force level occurs during the portion of the recovery period when the mass center is moving upward toward the standing posture while being decelerated to a state of zero vertical velocity. The minimum vertical ground reaction force, or force undershoot, is used here to quantify the system's oscillatory behavior.

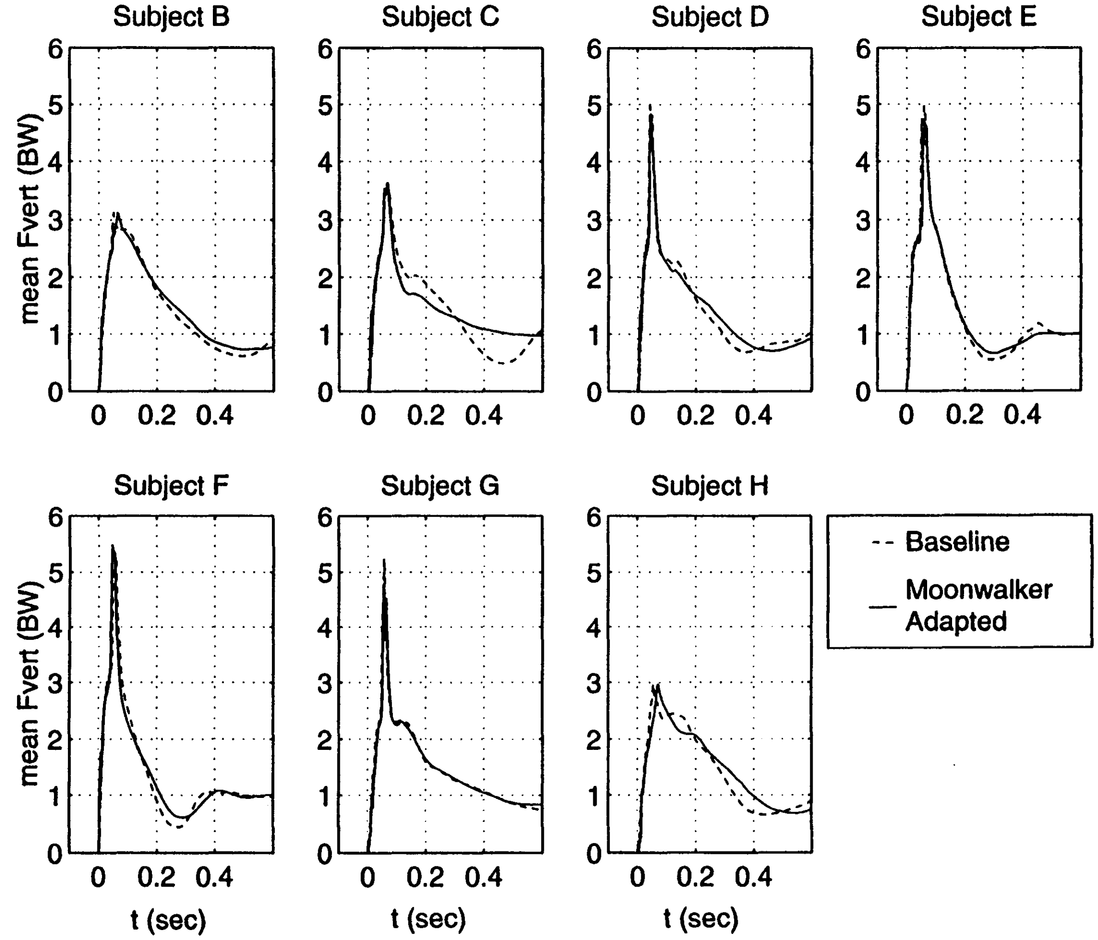

Figure 3.17. Moonwalker experiment vertical ground reaction force traces.
Baseline and moonwalker-adapted averages. Trials aligned at impact, shown at t=0.

In order to quantify the lag in the force traces for the adapted jumps, the time after impact at which the vertical GRF falls below 1 body weight is computed for each jump. Figure 3.18 shows the timing data for each subject. The average time to the body weight crossover point is shown to increase after unloading adaptation for all subjects. Using an unpaired, two tailed Student's t-test, this effect is significant at the $p<0.05$ level for subjects C, D, F and H, as well as for all subjects grouped together. Hence, a general pattern of slower recovery after unloading adaptation is indicated by the force plate data.

A similar comparison of the minimum vertical GRF is presented in Figure 3.19. In this case, the average value of minimum GRF increases for each subject following unloading with the moonwalker. The increases are significant ($p<0.05$, Student's t-test) for subjects C, F and G, and for the data of all subjects grouped together. This reduction in the amount of undershoot below the final 1 body weight value suggests that the system becomes less oscillatory after exposure to simulated partial gravity.

The magnitude of the peak vertical GRF is also examined. This analysis shows no significant changes in the peak GRF for any of the subjects following adaptation to partial weight unloading exposure.

3.2.3.2. Leg Joint Kinematics

Changes in the maximum joint flexion following impact are considered here for comparison with the astronaut jumping data. Table 3.8 shows maximum ankle, knee and hip flexion angles for each subject for the baseline and moonwalker-adapted jumps. Four of the subjects exhibit significant increases ($p<0.05$, Student's t-test) in maximum flexion at one or more joints. No significant decreases in peak joint flexion were observed at any joint in any subject. No significant changes were found with all subjects grouped together.

Subject B has a small but significant increase in maximum ankle flexion following moonwalker adaptation. Subject C exhibits a significant average increase in peak knee flexion of approximately 5 degrees, combined with a significant, very large increase of nearly 30 degrees in peak hip flexion. Subject H demonstrates a significant increase in maximum knee flexion of 10 degrees after unloading exposure, while a significant increase of about 3 degrees in peak hip angle is noted for subject F.

Average knee and hip phase plane portraits are shown in Figure 3.20 for subjects C, F and H. For these plots, the baseline and adapted trials are averaged separately, then superimposed. The individual trials are aligned for averaging at the sample of impact. In each plot, the peak joint flexion is seen at the right edge of the phase plane trajectory. The

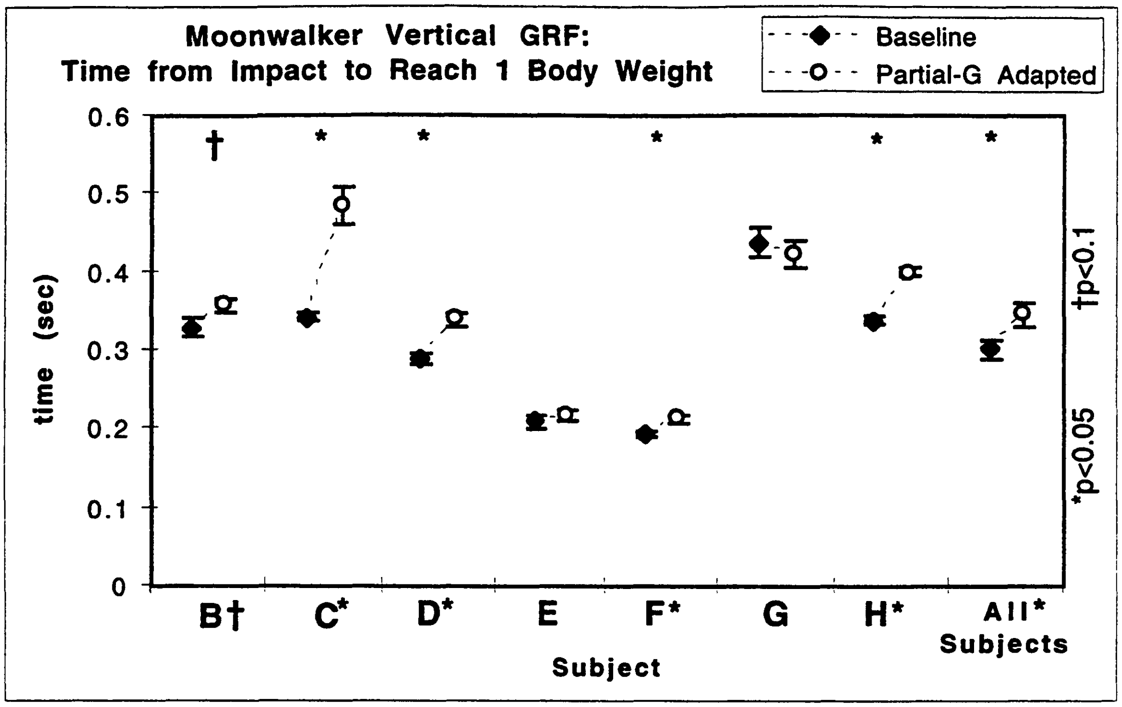

Figure 3.18. Moonwalker GRF time from impact to reach 1 body weight.
Error bars indicate one standard error of the mean.

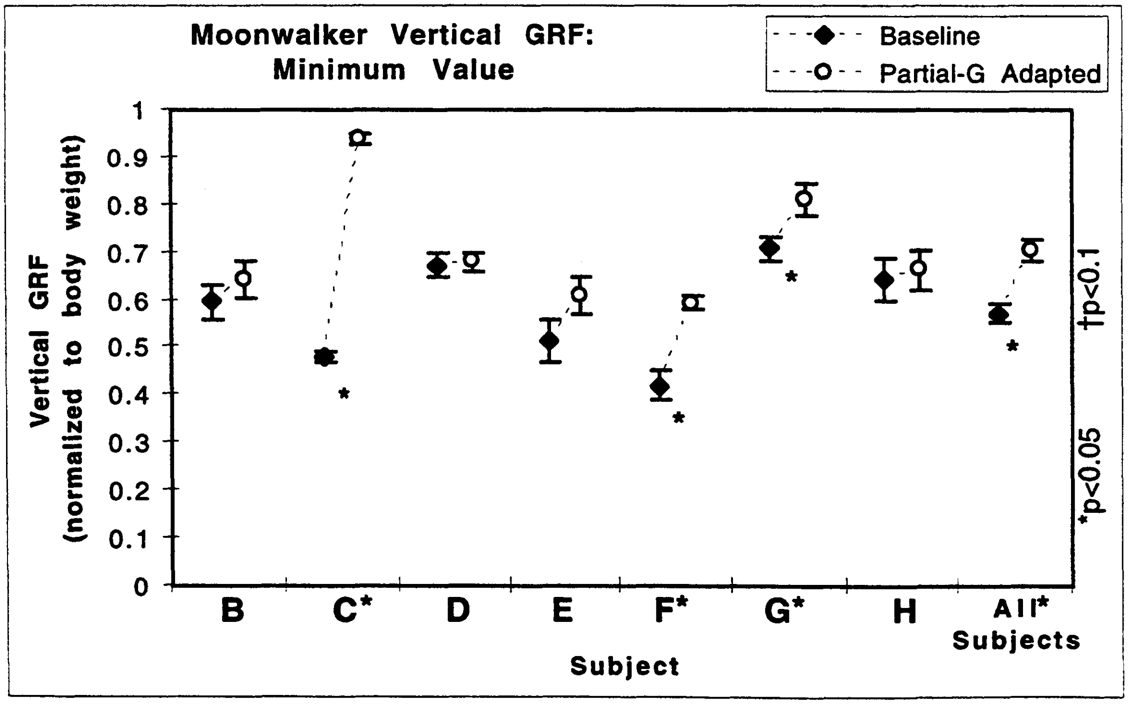

Figure 3.19. Moonwalker vertical GRF minimum value.
Error bars indicate one standard error of the mean.

Table 3.8. Moonwalker experiment maximum joint flexion after impact.

a. Maximum Ankle Angle

	BASELINE		PARTIAL-G ADAPTED		CHANGE	
Subject	Mean	S.E.M.	Mean	S.E.M.	mean diff	p=? (t-test)
B	96.0	0.7	98.8	0.8	2.8	**0.025**
C	102.9	0.6	102.3	1.0	-0.6	0.586
E	86.9	1.0	85.6	0.5	-1.2	0.294
F	87.1	0.8	86.5	1.7	-0.6	0.749
G	90.5	0.7	90.9	0.7	0.4	0.723
H	99.5	0.8	100.5	0.7	1.0	0.385
All Subjects	94.0	1.1	93.9	1.2	-0.1	0.971

b. Maximum Knee Angle

	BASELINE		PARTIAL-G ADAPTED		CHANGE	
Subject	Mean	S.E.M.	Mean	S.E.M.	mean diff	p=? (t-test)
B	78.4	0.8	81.6	1.5	3.2	0.084
C	73.0	1.0	77.3	1.3	4.4	**0.025**
E	54.9	1.0	54.8	1.4	-0.2	0.921
F	46.6	0.6	47.9	1.4	1.3	0.415
G	72.3	1.6	73.1	1.8	0.8	0.743
H	80.2	1.1	90.4	0.6	10.2	**2.1e-5**
All Subjects	67.7	2.2	70.3	2.6	2.6	0.449

c. Maximum Hip Angle

	BASELINE		PARTIAL-G ADAPTED		CHANGE	
Subject	Mean	S.E.M.	Mean	S.E.M.	mean diff	p=? (t-test)
B	62.1	2.2	62.4	2.9	0.3	0.938
C	44.0	1.8	72.0	4.4	28.0	**1.6e-4**
E	24.5	1.9	30.0	2.4	5.5	0.100
F	18.7	1.0	22.1	1.0	3.4	**0.040**
G	64.7	3.0	61.7	3.5	-3.0	0.548
H	64.6	2.6	67.9	1.6	3.2	0.340
All Subjects	46.4	3.3	52.3	3.5	5.9	0.224

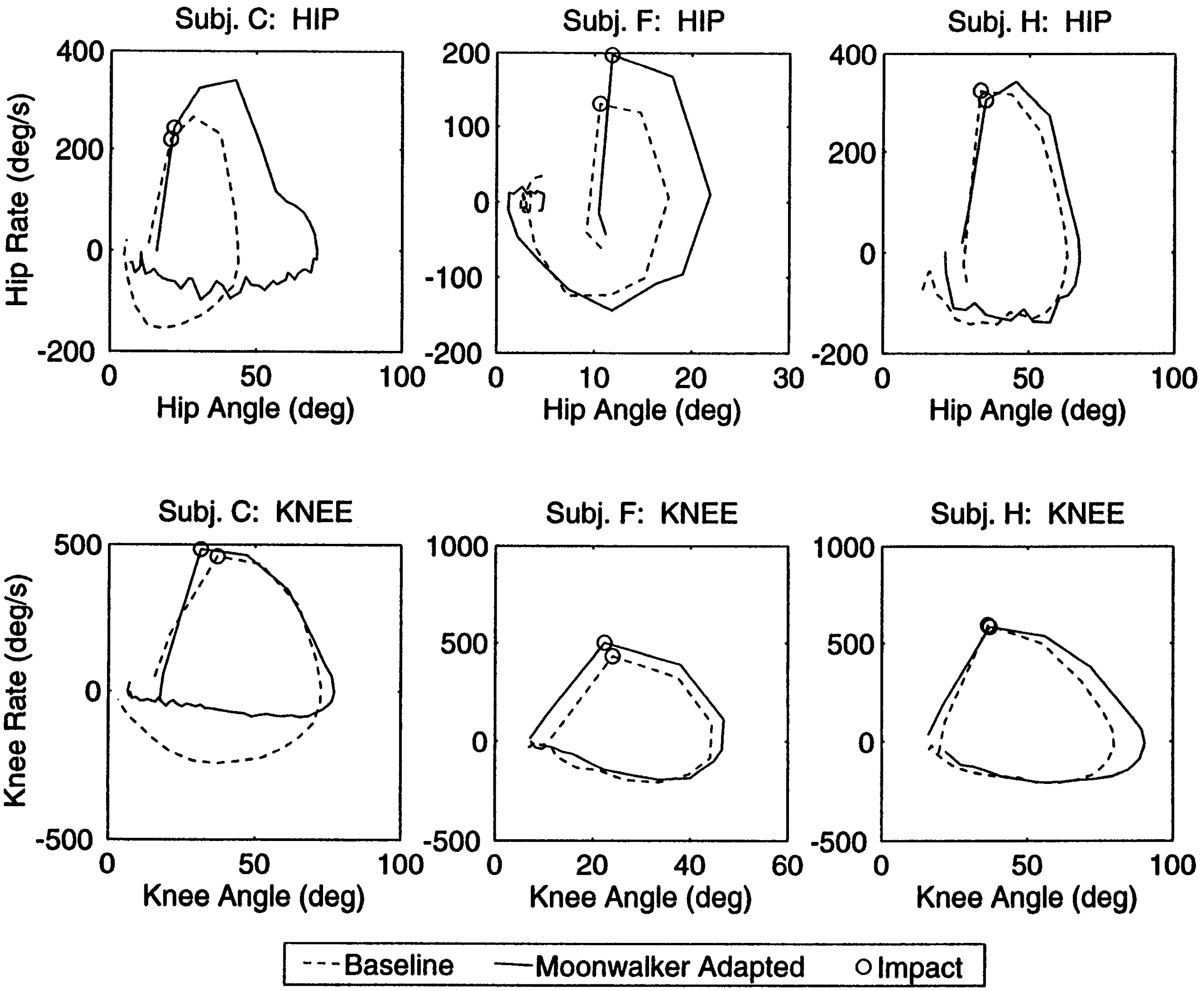

Figure 3.20. Moonwalker baseline and adapted joint phase-plane portraits.
Each trace represents the average of 6 trials. Trials are aligned at impact.
Phase-plane portraits are traversed in the clockwise direction.

average increases in peak flexion after moonwalker adaptation are clear in these plots. Also noteworthy are the substantial decrease in the peak extensional joint rates for subject C, as seen at the bottom of her phase trajectories. The reduced extensional rates correspond to the much slower return to upright equilibrium previously noted in her force plate records for the adapted case.

3.2.3.3. Second Order, Single Degree of Freedom Model of Vertical CM Motion

Using the same second order model of vertical CM motion that is applied to the astronaut jumping data, linear leg stiffness and damping values are fit to the CM data for each jump. Average values for the baseline and adapted jumps are presented in Figure 3.21. Individual subject baseline and adapted parameter means are compared using an unpaired t-test. This plot shows that the average leg stiffness decreases following partial weight unloading exposure in 5 of the 6 subjects for whom kinematic data are available, while one subject (G) exhibits a small, non-significant increase in stiffness after moonwalker adaptation. The decrease in stiffness is significant for all subjects grouped using a two-way ANOVA with subject and condition (baseline or adapted) as the independent variables. Significant effects of subject and interaction between subject and condition are also noted. An interesting feature of the stiffness plot is the wide range of stiffnesses observed, even though the stiffnesses are normalized by subject body mass. The average baseline stiffness is less than 40 for subject G, while F's baseline stiffness averages over 300. Thus, comparison of these two extremes reveals an upper value over 7 times larger than the lowest measured value.

Of the 5 subjects with reduced stiffness, C and F demonstrate significant decreases of 79% and 28% respectively for the adapted jumps. Subject H also shows a 28% decrease in average stiffness following adaptation, although this change is not significant ($p = 0.079$). The lack of statistical significance for this subject's stiffness change is likely due to the small number of data points, as only 4 of her 6 adapted trials provided usable CM trajectories for the model fits. (Because the shoulder marker disappears temporarily from the camera field of view in 2 of the adapted jumps, complete CM trajectories were unavailable and the system identification routines could not perform the model fits.) However, subject H's stiffness decrease appears to complement the significant changes observed for this subject in GRF traces and peak knee flexion after exposure to partial weight unloading.

Table 3.9 gives the average stiffness and damping model fits for each subject, along with percentage changes from baseline and exact *p* values. No significant changes are found for the damping parameter in the model. From the stiffness and damping coefficients, the natural frequency and damping ratio are calculated for each jump, and these results are presented in Table 3.10. The natural frequency results are the same as those seen for the stiffnesses, as the natural frequency is simply the square root of the normalized stiffness. Increases in damping ratio in the range 8% - 132% are seen in all subjects. When the subjects are considered individually, subjects C and F exhibit significant damping ratio increases that reflect their decreases in stiffness after moonwalker adaptation. The decrease in natural frequency and increase in damping ratio are significant for all subjects grouped together based on the two-way ANOVA. Significant effects of subject and the interaction between subject and condition are seen as well.

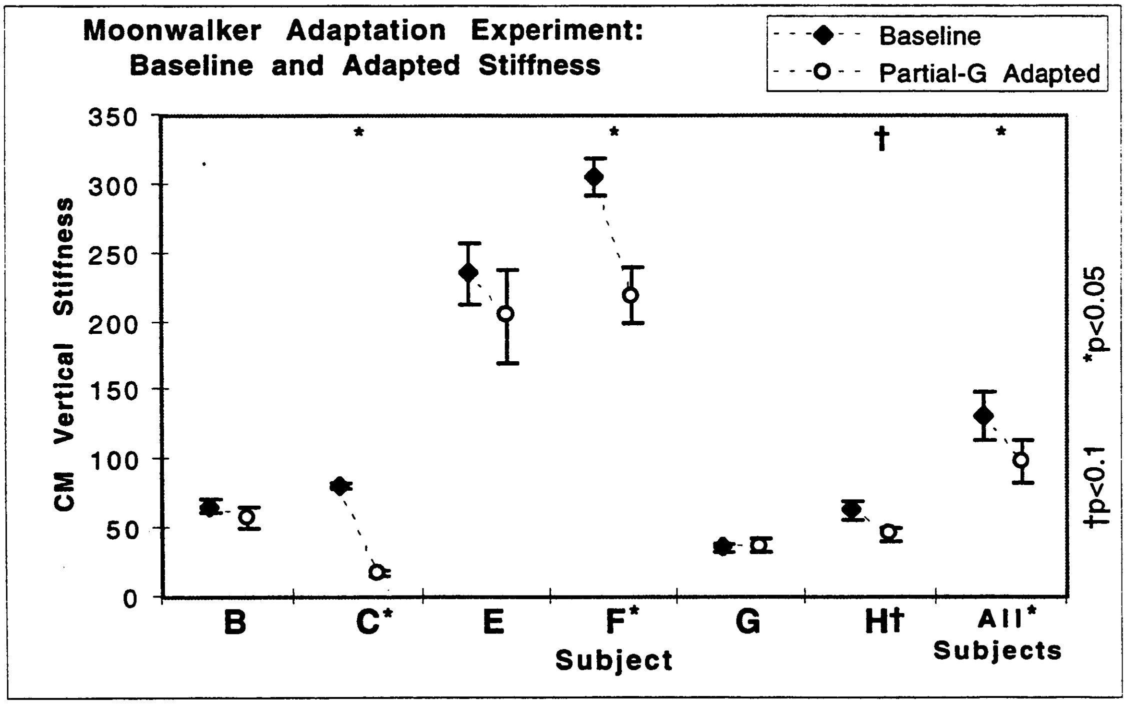

Figure 3.21. Moonwalker model stiffness estimates for all subjects.
Error bars indicate ±1 standard error about the mean. Significance levels from t-test for individual subjects; ANOVA for subjects grouped.

Table 3.9. Moonwalker second order model stiffness and damping estimates. (a) stiffness; (b) damping; (*) indicates p-value from ANOVA for all subjects grouped.

a. Stiffness [(N/m)/kg]

	BASELINE		PARTIAL-G ADAPTED		CHANGE	
Subject	Mean	S.E.M.	Mean	S.E.M.	mean diff	p=? (t-test)
B	66.6	4.2	58.6	7.8	-12%	0.370
C	81.1	2.0	17.4	2.7	-79%	**3.2e-9**
E	235.3	22.8	204.1	33.0	-13%	0.445
F	305.6	12.8	219.3	20.9	-28%	**0.006**
G	36.4	3.1	37.4	4.2	3%	0.846
H	63.2	6.1	45.6	5.3	-28%	0.079
All Subjects	132.2	17.5	98.8	16.2	-25%	**7.7e-5***

b. Damping [N/(m/s)/kg]

	BASELINE		PARTIAL-G ADAPTED		CHANGE	
Subject	Mean	S.E.M.	Mean	S.E.M.	mean diff	p=? (t-test)
B	9.2	0.5	8.9	0.5	-3%	0.69
C	9.3	0.3	9.6	0.7	4%	0.65
E	16.5	0.8	16.6	0.6	1%	0.93
F	18.7	1.6	20.9	1.1	12%	0.28
G	9.4	0.4	10.3	0.7	9%	0.30
H	7.7	0.4	7.4	0.3	-4%	0.61
All Subjects	11.8	0.8	12.5	0.9	6%	0.28*

Table 3.10. Moonwalker model natural frequency and damping ratio. (a) natural frequency; (b) damping ratio; (*) indicates p-value from ANOVA for all subjects grouped.

a. Natural Frequency (radians/sec)

	BASELINE		PARTIAL-G ADAPTED		CHANGE	
Subject	Mean	S.E.M.	Mean	S.E.M.	mean diff	p=? (t-test)
B	8.13	0.26	7.55	0.56	-7%	0.342
C	9.00	0.11	4.11	0.31	-54%	**4.2e-8**
E	15.25	0.76	14.10	1.15	-8%	0.414
F	17.46	0.37	14.72	0.71	-16%	**0.007**
G	6.01	0.26	6.09	0.32	1%	0.863
H	7.89	0.42	6.72	0.38	-15%	0.087
All Subjects	10.68	0.72	8.94	0.78	-16%	**5.7e-7***

b. Damping Ratio

	BASELINE		PARTIAL-G ADAPTED		CHANGE	
Subject	Mean	S.E.M.	Mean	S.E.M.	mean diff	p=? (t-test)
B	0.573	0.043	0.619	0.083	8%	0.623
C	0.514	0.014	1.195	0.099	132%	**4.8e-5**
E	0.553	0.046	0.603	0.044	9%	0.450
F	0.539	0.049	0.713	0.027	32%	**0.012**
G	0.792	0.055	0.854	0.065	8%	0.486
H	0.498	0.047	0.558	0.048	12%	0.416
All Subjects	0.572	0.023	0.771	0.048	35%	**1.4e-6***

3.3. DISCUSSION OF ASTRONAUT AND MOONWALKER RESULTS

The results of the astronaut experiments are examined first. The implications of the two postflight kinematic behavior patterns, postflight-compliant (P-C) and postflight-stiff (P-S), are discussed. Potential causes for the postflight changes are considered, including the possible effects contributing to changes in leg stiffness. Next, the results of the moonwalker experiment are reviewed and related to the space flight experiment. The moonwalker and astronaut experiment protocols are compared, and limitations of the suspension protocol are surveyed. The similarities between the results from the second order model of jump landing for the astronaut and moonwalker data are evaluated.

3.3.1. Adaptive Changes in Astronaut Performance

3.3.1.1. Astronaut Joint Kinematics

Pre- and postflight comparisons of the joint kinematics during jump landings indicate that the astronaut subjects may be separated into two different classes based on examination of the phase-plane descriptions, namely, P-C and P-S. The P-C group exhibits expanded phase-plane portraits postflight in comparison to preflight baseline data and the P-S group shows the contrary. The lower leg musculature may be thought of as contributing a resistance to joint displacements, or stiffness (modeled as a torsional spring-like element), as well as a resistance to joint angular velocity, or damping (represented by a viscous damper or dashpot). These stiffness and damping elements represent the displacement and velocity dependent components of the joint impedance, respectively.

Using this description, the P-C group exhibits postflight increases in the majority of both peak joint flexion angles and rates indicating a *reduction* in stiffness about the joints following microgravity exposure. In these subjects, increases in joint flexion provide quantitative support for the reports of Watt *et al.*'s [1986] astronaut subjects that their legs bend more during drop landings postflight. In the unexpected drop case, the mechanisms which determine leg stiffness at impact may be somewhat different from voluntary jumps. The major leg EMG responses in drops appear to be reflexively triggered by otolith stimulation and the onset is keyed to the beginning of the fall, while in voluntary jumps the EMG responses prior to impact appear to be pre-programmed for the expected impact time.

The P-C changes are also consistent with reductions in joint torques, and a reduction in the bandwidth of the postural control system as a whole. In contrast, two of the subjects demonstrated an opposite, postflight-stiff response after returning from space flight. Their postflight contraction in the phase-plane plots indicates increases in limb stiffness and bandwidth of the postural controller.

A number of possible explanations exist for the observed changes in joint impedance during these jump landings, including loss of strength in the anti-gravity musculature, altered sensory feedback (muscle stretch reflexes, vestibular, or visual), and changes in open-loop modulation of limb stiffness. Since the stiffness and damping that can be exerted about a joint are directly related to the forces in the muscles acting about the joint, significant strength decreases in the anti-gravity muscles of the legs could well account for the expanded phase-plane portraits observed in the P-C group of astronauts. However, the P-S subjects exhibit postflight increases in stiffness indicating *increased* joint torques; thus, the results from these subjects undermine the hypothesis that loss of muscle strength alone can account for the observations in this study.

3.3.1.2. Sensory Feedback

Sensory feedback pathways also contribute to the stiffness and damping of the closed-loop postural control system. Feedback quantities that could play a role in the jump landings include postural muscle stretch (modulated through spinal reflexes), vestibular sensing of head orientation and angular velocity, and visual inputs. The stretch reflexes effectively increase the stiffness about the joints by recruiting additional muscle fibers to counteract perturbations to the muscle lengths; the stretch reflexes in concert with Golgi tendon organ force feedback probably serve to modulate the tension-length behavior (stiffness) of the muscles [Nichols and Houk; 1976; Houk, 1979].

Several studies report changes in lower limb stretch reflexes during and after space flight. Baker *et al.* [1977] observe decreased Achilles tendon reflex activity immediately postflight in Skylab astronauts. Gurfinkel [1994] reports decreases in the strength of the stretch reflex in tibialis anterior following space flight, and Kozlovskaya *et al.* [1981] find amplitude reductions in Achilles tendon stretch reflexes after long-duration flight. Such decreases could have the effect of reducing the stiffness about the leg joints, and hence the stiffness of the leg "spring" supporting the body mass. However, Melvill Jones and Watt [1971a] demonstrate that the monosynaptic stretch response (occurring approximately 40 ms after forcible dorsiflexion of the foot) does not contribute to gastrocnemius muscle tension. Rather, the development of force is found to correspond to a sustained EMG burst with a latency of 120 ms following dorsiflexion stimuli, that they term the "functional stretch reflex." Since the peak joint angle deflections in the jump landing occur only 100-150 ms after impact, stretch reflex activity is unlikely to play a major role in the impact absorption phase.

Studies by Allum and Pfaltz [1985] and Greenwood and Hopkins [1976] find vestibulo-spinal reflex latencies for postural muscles of 80 ms. Visual influences are found to be delayed after a postural disturbance by 80 ms and 100 ms, respectively by Allum and Pfaltz [1985] and Nashner and Berthoz [1978]. These latencies comprise most of the interval from impact to peak joint deflections, indicating that sensory feedback information from these sources following impact cannot be expected to contribute significantly to the impact absorption phase of jump landings. However, vestibular and visual inputs during the takeoff and flight phases of the jump may well contribute to the motor activity during impact absorption, as Wicke and Oman [1982] show that altered downward acceleration and visual surround motion during sudden falls cause variation in the reflex leg muscle EMG. Interestingly, in the current study the eyes were closed in half of the jumps without a measurable effect on performance, indicating that vision's effect during the jump landings was minimal. This qualitative finding is intriguing in light of evidence for increased dependence on visual cues following space flight for posture control and perception of body orientation and self-motion [Young *et al.*, 1986]. However, McKinley and Smith [1983] describe jump-down behavior in normal and labyrinthectomized cats with and without vision and conclude that normal cats that jump from a known height do not rely on visual input to program pre-landing EMG responses, but when jump height is uncertain and visual input is absent they speculate that vestibular input becomes more important. In our study, the astronaut subjects have full knowledge of the jump height after the first jump, which is always conducted with the eyes open. Furthermore, even in the EC jumps, the subjects have visual information about the jump height even though they close their eyes immediately prior to jumping. Therefore, the apparent ability to program pre-landing responses without vision may account for the lack of difference in jumps with and without vision.

3.3.1.3. Limb Stiffness

The limitations on the sensory feedback pathways indicate that the stiffness properties of the lower limbs may be largely predetermined before impact. The stiffness about the joints is determined by the level of muscle activation, and the overall impedance of the leg to CM motion is also affected by the configuration of the limbs at impact (in general, less joint flexion results in greater vertical stiffness due to the reduction of the moment arm about the joint centers). McKinley and Pedotti [1992] find that the knee extensor muscles (rectus femoris and vastus lateralis) are activated slightly before impact, while the ankle plantarflexors (gastrocnemius and soleus) are continuously active from mid-flight during jumps. Furthermore, the legs reach their largest extension before impact, and are already slightly flexed again by the time of impact. Other investigators [Dyhre-Poulsen and Laursen, 1984; Thompson and McKinley, 1988] have determined that the timing of the preparatory muscle activation and limb configuration is keyed to the expected time of impact. For downward stepping and repetitive hopping, Melvill Jones and Watt [1971a] find that muscular activity commences from 80-140 ms prior to ground contact, and conclude that the deceleration associated with landing is due to a pre-programmed neuromuscular activity pattern rather than stretch reflex action.

Melvill Jones and Watt [1971b] demonstrate activation of both gastrocnemius and tibialis anterior approximately 75 ms following an unexpected fall; this reflex activity is most likely due to vestibular system otolith inputs. Such activation of antagonist muscles could contribute to stiffening of the limbs prior to impact. Furthermore, Watt *et al.* [1986] show that the amplitude of this response is markedly decreased during space flight. However, Watt's tests on landing day show that the response has returned to normal almost immediately postflight, so changes in the otolith-spinal reflex may not account for the changes observed in the jumps described here. Reschke *et al.* [1986] use the H-reflex to examine the effect of drops on the sensitivity of the lumbosacral motoneuron pool, which is presumably set by descending postural control signals. A large potentiation of the H-reflex (recorded in the soleus muscle) begins approximately 40 ms following an unexpected drop. The investigators find that on the seventh day of space flight, the potentiation of the H-reflex during drops vanishes. Immediately following space flight, 2 of 4 subjects demonstrate a significant increase in potentiation during the drop compared to preflight testing. While an increase or decrease in the sensitivity of the motoneuron pool might correspond to respective increases or decreases in the leg stiffness via a gain change in the spinal reflex pathway, the link to preprogrammed muscular activity is not clear.

In addition to the muscular commands linked to the flight and impact phases of the jump, the underlying tonic activation in the leg musculature may contribute to the impedance in the lower limbs during jump landing. Clément *et al.* [1984] find an increase in tonic ankle flexor activity combined with a decrease in tonic extensor activity during space flight, that if carried over postflight could lead to a reduction in the stiffness about the ankle joint against gravitational loads. It is well established that suppression of vestibular function results in depression of the gamma-static innervation to the leg extensors, causing reduction in extensor tone [Molina-Negro *et al.*, 1980]. However, because relative enhancement of the knee flexor is not observed, Clément's group views the changes at the ankle as a "subject initiated postural strategy" rather than a functional deafferentation of the otoliths due to microgravity. Regardless of the origin, significant changes in leg muscle tone could well contribute to altered leg stiffness postflight.

3.3.2. Moonwalker Analogue to Astronaut Experiments

The results of the astronaut experiment suggest that gravity plays an important role in determining what levels of stiffness the neuromuscular system selects. Partial gravity simulation through suspension reduces the load-bearing demands on the limbs and increases the time constant associated with the motion of a inverted pendulum. The required authority of the postural control system in reduced gravity therefore lies somewhere between the requirements for 1-g and weightlessness. Changes observed as a result of unloading exposure can provide additional insight into the sometimes dramatic alterations observed in astronaut performance postflight. While the moonwalker experiments are believed to provide an ground-based analogue to microgravity exposure, the differences between the moonwalker experiments and the astronauts' experience must be considered.

3.3.2.1. Limitations of the Moonwalker Experiments

The moonwalker experiments are designed to examine whether acute exposure to partial weight unloading can induce adaptive changes in jump landings. The upward forces exerted by the suspension system reduce the load-bearing requirements placed on the legs in a rough approximation of the effects of lower gravity. However, there are no changes in the gravitational forces on the otoliths, and the suspension system also exerts forces on the body that are not comparable to true partial gravity.

First, the upward force is applied locally by the harness. Although the unloading counteracts the weight normally borne by the legs, the gravitational forces on the distributed mass of the body segments are unchanged. Also, the actual upward force exerted by the springs varies with the amount the springs are stretched. As discussed in the description of the suspension system, the actual upward force increases by approximately 15% of body weight over a drop of 30 cm, although the variation in upward force over the range of motion seen following impact is considerably smaller.

The horizontal forces exerted by the harness should also be considered. The relatively short distance from the shoulder attachment point to the overhead pulleys results in a non-negligible horizontal force on the subject when she is not directly under the pulleys. The horizontal force causes a forward-leaning posture prior to jump initiation, and acts as a restoring force directed toward upright stance when the subject lands under the pulleys. The horizontal force necessitates a shift of the starting block to a position more directly below the pulleys for the partial-gravity jumps, and as an additional consequence the subjects tend not to travel as far in the horizontal direction during these jumps. Finally, a test of the posture of a subject hanging fully supported by the suspension cables shows that the subject remains in at a stable equilibrium with a forward tilt of approximately 12°. This stable posture, to which the subject returns after perturbing pushes, contrasts with the neutrally stable rotational orientation of the subject during the normal free fall portion of a jump.

The effects that these differences may produce in comparison to true partial gravity are difficult to assess. However, the moonwalker does provide an effective means of reducing the vertical load-bearing requirements of the legs, and as such permits testing of the hypothesis that reduced demands on the postural control system can induce adaptive changes in the system stiffness and jumping kinematics.

In addition to the mechanical effects of the suspension apparatus, some methodological differences between the astronaut and moonwalker experiments exist. First, the exposure times are considerably different: the astronauts spend between 1 and 2 weeks in microgravity, while the adaptation time using the moonwalker lasts between 1 and 2 minutes for the 10 partial gravity jumps. The motor experience during the adaptation periods of the two experiments differs as well. For the moonwalker, the adaptation protocol is specifically geared to downward jumps, while the astronauts perform a wide variety of activities during their stay in orbit, most of which do not require impact absorption.

The postflight tests are performed a few hours following the astronauts' return to earth. During the post-landing interval, the subjects have the opportunity to stand and walk, and presumably readapt to the 1-g environment. In contrast, the moonwalker subjects perform their partial-g adapted jumps immediately following removal of the suspension harness, and are not permitted to walk or jump beforehand. Furthermore, the moonwalker subjects are exposed to the suspension protocol before each jump, while the astronauts perform their postflight jumps in sequence, with no intervening tasks.

3.3.2.2. Moonwalker Results Follow P-C Pattern of Astronauts

Of the six moonwalker subjects for whom kinematic data are available, three exhibit significant post-adaptation increases in peak knee angle (F), hip angle (H), or both (C). These results are similar to the peak joint angle increases observed the P-C group of astronaut subjects. None of the moonwalker subjects demonstrate decreases in peak joint flexion comparable to the P-S astronauts.

The joint angle results are supplemented by force plate records in the moonwalker experiment that reinforce the similarities of these 3 subjects with the P-C group. Overall increases in the decay time of the vertical ground reaction force are seen together with smaller undershoots below the one body weight level. The slower time to reach one body weight was significant for subjects C, F and H, as well as for subject D. Subjects C and F also showed significant reductions in the amount of undershoot below one body weight.

The two effects noted in the partial-g adapted force plate data indicate a more heavily damped response following suspension. The slower, less oscillatory responses are consistent with a general reduction of the leg stiffness (see also the similar results obtained in the consideration of optimal behavior in the 2nd order model, Section 5.5.1). Hence, the aggregate data indicate that at least 3 of the 7 moonwalker subjects show results similar to those observed in P-C astronauts, while none exhibit characteristics like those of the P-S crew members.

Like the astronaut postflight effects, the changes following exposure to simulated partial gravity appear to be explained best by alterations in the controlled stiffness of the legs. Neither muscle atrophy nor changes in vestibular sensing can account for the moonwalker results. The arguments listed above against an explanation based on changes in spinal stretch reflexes still hold. Furthermore, Shultz [1995] shows that short term exposure to partial weight unloading using a similar protocol has no effect on patellar tendon reflexes.

The fact that a targeted unloading adaptation stimulus can replicate the effects of space flights lasting longer than a week is very interesting. These results indicate that the postural control system can tune stiffnesses quickly to account for variations in the gravitational environment. The experiments of Schultz [1995] also support the notion that short term unloading exposure can have significant effects on motor behavior. He tests the hypothesis that the "heavy legs" phenomenon reported following acute partial-g adaptation results from decreases in postural control gains.

After moonwalker testing, subjects report a temporary feeling of weakness in the legs, and Schultz suggests that this effect results from a CNS-moderated decrease in muscular gains as a result of adaptation to the partially unloaded condition. He observes that the RMS sway in postural stabilograms increases significantly following moonwalker exposure, and shows that this RMS increase can be explained by a decrease in ankle joint feedback gains using a simple optimal estimator model of postural control about upright stance. This gain change is strikingly similar to the stiffness reductions exhibited by the P-C astronauts and the majority of the moonwalker jumping test subjects.

Interestingly, one of Schultz' 10 subjects exhibits an opposing change following moonwalker adaptation, with decreases in the RMS sway. He proposes that the subject is aware at some level of his reduced gains after adaptation, and compensates by strongly activating the leg musculature to minimize postural sway. This explanation is equivalent to the interpretation presented here for the results observed in the P-S astronaut group. Schultz also determines that the RMS sway effects are quickly eliminated by countermeasures consisting of several broad jumps, and that deep knee bends provide a less effective countermeasure. Thus, the activities performed by the astronauts following landing may have had a significantly re-adaptive effect even in the short period between shuttle landing and jump testing.

In general, the results of Shultz' experiment back the hypothesis that microgravity and simulated hypogravity result in adaptive changes in the stiffness of the leg system. Furthermore, the behavior of his anomalous subject may relate to the differences seen between the P-C and P-S subjects in the astronaut jumping experiment.

3.3.3. Modeled Stiffness in the Astronaut and Moonwalker Experiments

The hypothesis that the joint impedance characteristics transform into lumped leg stiffness and damping parameters governing the vertical CM motion following impact provides the basis for the second order mechanical model postulated here. These parameters are assumed to remain constant through the impact absorption and recovery to upright stance. This assumption is a simplification of the actual behavior of the leg, as Greene and McMahon [1979] show that leg stiffness increases with increasing knee flexion. They estimate the effective lumped stiffness by determining the natural oscillation frequency of a system consisting of the subject standing on a compliant board of known spring stiffness.

The stiffness values estimated for 5 subjects at a 90° knee flexion angle range from 255 - 700 (N/m)/kg, with an average of 473 (N/m)/kg. These values are substantially higher than the stiffnesses reported here, which range from 101 - 247 (N/m)/kg for the astronauts preflight, and from 36 - 305 (N/m)/kg for the moonwalker baseline. The discrepancy may be attributed to differences in the task. In the Greene and McMahon study, subjects were asked to perform small oscillations about a fixed leg angle displaced from upright standing. For this task, a high level of co-contraction in antagonistic muscle pairs can be expected, with a corresponding rise in stiffness.

Also, the high joint velocities and kinetic energy dissipation in jump landings imply that damping properties may contribute heavily to the landing response, decreasing the need for high stiffness. The damping ratios found in the present studies average 0.55 for the astronauts preflight, and 0.57 for the moonwalker baseline. These damping ratios are higher than the value of 0.34 reported by Greene and McMahon [1979], indicating the relative importance of damping in the two tasks. An analysis of the stance phase of human running by McMahon and Greene [1979] gives a damping ratio of 0.55, which compares favorably with the average values found here.

A study by McMahon and Cheng [1990] of running provides support for the constant-stiffness model used here. They summarize evidence indicating that the legs behave much like a linear spring of near-constant stiffness over a wide range of forces and running speeds. The constant leg stiffness value that best describes human running in McMahon and Cheng's model is approximately 150 (N/m)/kg. Although this value represents the stiffness of the single support leg, Greene and McMahon [1979] and Cavagna [1970] reported reductions in stiffness going from two legged support to a single leg of about 19% and 34% respectively. Thus, a two-legged stiffness value might lie in the region of 185-225 (N/m)/kg, which falls well within the range of two-legged stiffnesses computed for the jump landings here.

Based on the arguments of McMahon and Cheng, and the generally close fits to experimental data obtained for the jumps in the present study, the simplifying assumptions of constant stiffness and damping appear reasonable. Comparison of the astronaut pre- and postflight fits for this model indicates that variations in the model parameters can adequately predict the alterations in CM motion seen in astronaut jump landings following space flight. More specifically, changes in the lumped leg stiffness appear to govern the differences in transient response observed upon return to earth. The postflight decreases and increases in the vertical leg stiffness found for these subjects correspond to the classifications of P-C and P-S made previously on the basis of kinematics alone. However, the lack of statistical significance in the P-S postflight increases in stiffness indicates that other factors may contribute to the kinematic changes. For example, the reduction in impact velocity for P-S subject S-9 probably results from a different takeoff strategy postflight.

Likewise, the changes in joint kinematics and force plate data following partial-g exposure in the moonwalker experiment correlate well with the changes in estimated stiffness. Five of the six subjects for whom video data are available show decreases in stiffness after adaptation. Subjects C, F and H exhibit significant changes in joint kinematics and force plate responses that resemble the P-C astronaut results, and these three subjects also show large reductions in stiffness following adaptation (significant for C and F; $p<0.08$ for H).

In the model, decreases in leg stiffness lead to decreases in bandwidth, with slower and less oscillatory time responses. In contrast, increased stiffness results in faster, higher bandwidth performance with greater overshoots. These decreases and increases in leg stiffness postflight match the changes found in the transient performance for the P-C and P-S subjects, respectively. Interestingly, the model fits do not show changes in the leg damping to play a significant role in the postflight differences.

This result is counterintuitive, since an increase in antagonist muscle activation to raise the limb stiffness might be expected to cause a corresponding increase in the mechanical damping properties of the muscles as well. Furthermore, changes in damping in accordance with increases or decreases in stiffness would help to prevent large deviations in the damping ratio (see Equation 3-2), which is often desirable from a control system standpoint. Regardless, the evidence presented here indicates that the damping properties of the limbs can be modulated independently of the stiffness, or simply that the damping characteristics are largely constant in the face of large changes in leg stiffness. The astronaut results are supported by the moonwalker tests, where no significant changes in the damping coefficient are observed in spite of large changes in the stiffness properties.

The final equilibrium positions predicted by the model lie somewhat below the actual final CM rest values (see Figure 3-10), implying that the stiffness for these model fits is less than the values that would have been calculated from the final equilibria alone. In many cases, it is not possible to find parameter values that gave good predictions for both the transient portion of the response and the steady-state equilibrium. Because this study focuses on impedance modulation during the impact absorption phase of the jump, the parameter estimation procedure is designed to find best fits for the transient portion of the response, often resulting in differences between the predicted and actual equilibrium positions. Interestingly, the pattern seen in Figure 3-10 is consistent across the subject pool: on average, predicted equilibria lie below the actual values. This result is attributed to a transition in control mode and limb posture from the impact absorption phase to the maintenance of upright posture near equilibrium. In equilibrium posture control, the flexed joints and greater compliance used in impact absorption give way to the more upright resting stance, where the alignment of the leg joints results in high vertical stiffness.

The changes in the model parameters corresponding to altered joint and mass center kinematics observed in the astronauts postflight are likely due to changes in the preprogrammed muscle activity prior to impact, which sets the limb impedance in an open-loop fashion by controlling the muscle tension-length properties and the limb configuration. The changes observed in this study in the impact absorption phase support the notion that space flight contributes to altered neuromuscular activity during the flight phase of the jump, even though EMG records are not available. The presumed alterations in muscle activation patterns following space flight could reflect changes in the relative recruitment of antagonist muscles, or differences in the timing of activation (*e.g.*, failure to activate anti-gravity muscles early enough during the flight phase to stiffen the limbs for impact).

4 FALSE PLATFORM JUMPING EXPERIMENT

Pre-programmed aspects of the jump landing body kinematics are obscured by the overriding effects of the impact perturbation. Likewise, pre-programmed muscular activity is difficult to distinguish from segmental stretch reflex activity due to the mechanical effects of the impact. The false platform jumping experiments are designed to provide insight into the control of jump landings by eliminating the impact perturbation during an otherwise "normal" jump. Removing the landing platform without the subject's knowledge permits measurement of the free trajectory of the body and limbs for a short time after impact would normally occur because the subject is still in free fall. The free trajectory and EMG activity during this period elucidate the role of pre-programmed motor control activity and permit estimation of limb impedance properties using appropriate models.

The specific goals of the false platform experiment are:

1. Examine the commanded behavior of the body in jump landings during the impact phase by removing the impact perturbation.
2. Estimate the commanded body trajectory from the "free" false platform trajectory, and calculate the body impedance properties about this free trajectory using the measured forces, estimated torques, and the measured difference between normal jump landing trajectories and the free trajectory.
3. Assess the viability of an equilibrium point control strategy for jump landings.
4. Provide simultaneous measurement of body kinematics, ground reaction forces and muscle EMG data not available in the astronaut jumping or moonwalker experiments.

4.1. FALSE PLATFORM EXPERIMENT DESIGN

The requirements for the false platform experiment are:

1. Provide data on a sequence of nominal jumps, as well as a number of jumps designed to eliminate the perturbation due to impact with the ground upon landing by unexpectedly removing the normal landing platform. This protocol permits examination of the pre-programmed aspects of the impact absorption phase which are masked by the overriding effects of the impact.
2. Provide at least 100 ms of "free body trajectory" motion following the nominal impact time. This time is selected as an approximation of the time in which the neuromuscular system can respond to the removal of the expected impact, based on the approximately 75 ms delay between otolith stimulation (from a sudden fall) and

anti-gravity muscle activation in humans [Melvill Jones and Watt, 1971b]. The same authors [1971a] report that significant muscle force generation is delayed by approximately 150 ms following impact for the "functional stretch reflex," even though stretch reflex EMG activity is observed as early as 40 ms after impact.

3. Prevent the subject from expecting the removal of the impact perturbation and changing the landing strategy accordingly. McKinley and Pedotti [1992] demonstrate that the muscle activation pattern is timed for the expected moment of impact when the jump height is known. Thus, the subjects would be expected to alter the coordination of their jump landings if the landing platform is lowered with their conscious or unconscious knowledge. Since the goal is to maintain the same nominal jump landing strategy while removing the impact, the landing platform must be removed without alerting the subject.

4. Permit landing of the subject in a safe, controlled manner without damaging the experimental apparatus. Due to the unexpected nature of the landing surface removal, precautions are taken to minimize the possibility of injury to the subjects or damage to the data collection equipment.

5. Allow enough trials to assess the variability and stationarity of jump landings, without fatiguing the subject.

4.1.1. Experimental Apparatus

All false platform experiments are performed at the Biomotion Laboratory (BML) of the Massachusetts General Hospital (MGH). The BML data acquisition system provides the ability to collect 6-degree of freedom full body kinematics, ground reaction forces and muscle electromyograms (EMG). A brief overview of each the data acquisition system capabilities is provided here. The components are described in detail by Antonsson and Mann [1989], Riley [1988], and Fijan [1985]. After the data acquisition systems are described, the design of the false platform apparatus is presented.

4.1.1.1. Body Segment Kinematic Data Acquisition (TRACK)

Kinematic data are collected using the hardware and software of the TRACK system (for Telemetered Real-time Acquisition of Kinematics). This system is used to monitor the position and orientation of 11 body segments: left and right feet, left and right shanks, left and right thighs, pelvis, trunk, left and right upper arms, and head (Figure 4.1). Each segment is fitted with a rigid array of 3-5 light emitting diodes (LEDs). A minimum of 3 LEDs must be observed per array to estimate the position and orientation of the array.

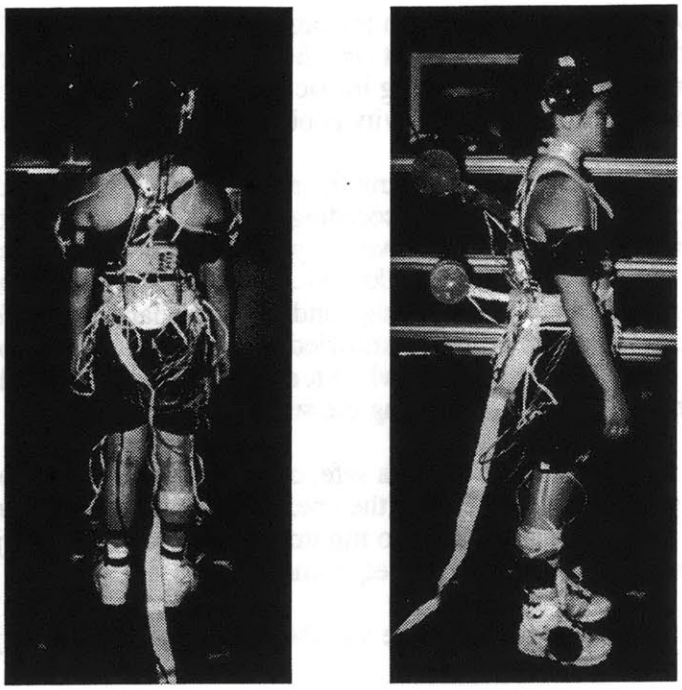

a. Subject Back View   b. Subject Side View

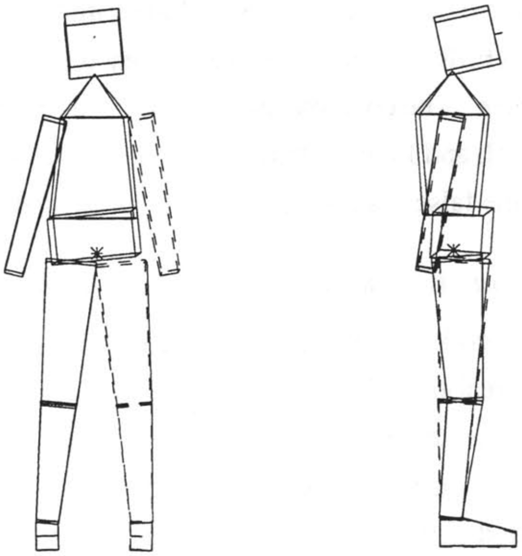

c. Model Front View   d. Model Side View

Figure 4.1. TRACK measures kinematics of LED arrays on 11 body segments. (a), (b) Subject wears LED arrays on feet, shanks, thighs, pelvis, trunk, arms, and head. (c), (d) 11 segment model uses LED array information to determine body segment position and orientation.

Bilateral data acquisition is performed by 2 sets of 2 Selspot II infrared cameras mounted on optical benches to permit simultaneous stereoscopic observation of the left and right sides of the body (Figure 4.2). The Selspot II cameras contain 2-dimensional lateral photo-effect diodes which register the horizontal and vertical location of an infrared light source in the focal plane of the camera. Each camera views a volume corresponding to an angle of ±15° as measured horizontally or vertically from the camera viewing axis. The center of the viewing volume is located at the intersection of the viewing axes from the 4 cameras. At this location, the maximum height at which an LED is still visible to the cameras is 188 cm.

Because the cameras can only determine accurately the position of a single light source at one time, each of the LEDs in the set of body segment arrays is strobed in sequence. The time required to sample 64 LEDs is approximately 1/153 sec, giving the system an effective sampling rate of 153 Hz. The LEDs are powered by a sequencer module connected to the arrays by ribbon cables. An umbilical from the subject connects the sequencer module to the Selspot administrating unit that synchronizes the cameras and LEDs.

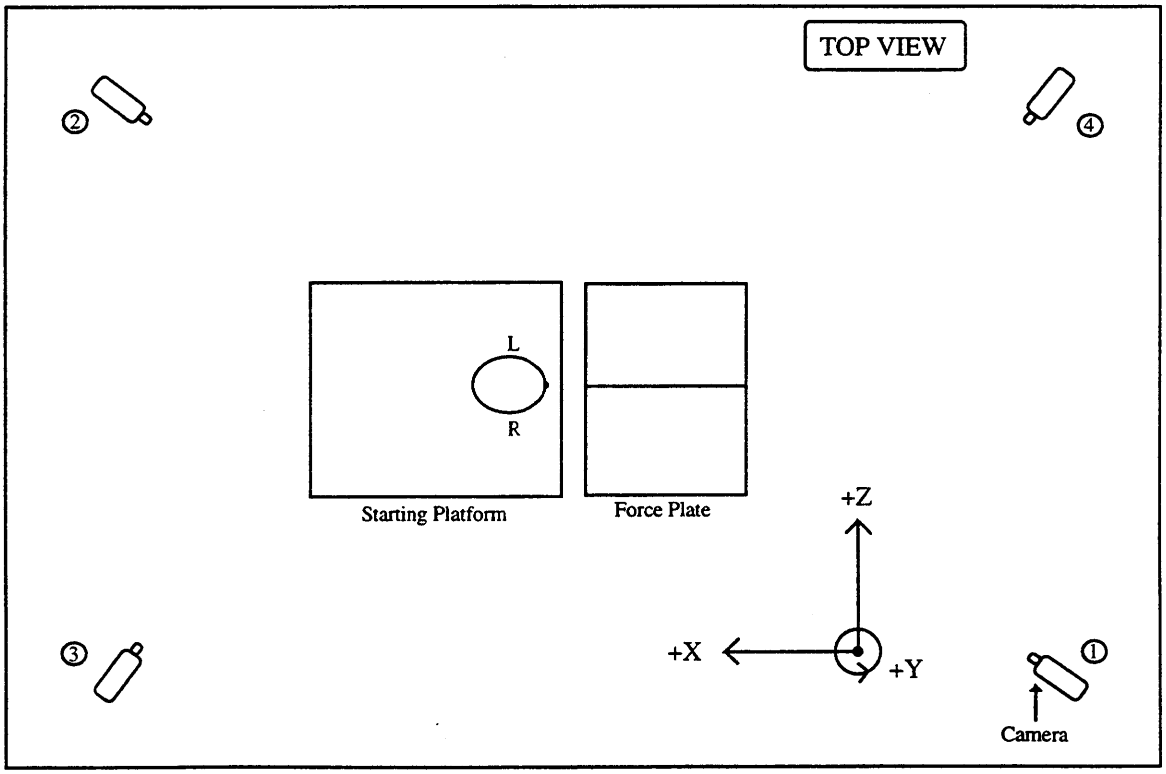

Figure 4.2. Position of Selspot II cameras, jump platform and force plates. Cameras 1 and 3 measure array kinematics of the right side of the body, while cameras 2 and 4 measure the left side array motion.

Each of the leg and arm segments is fitted with a single array of LEDs that is viewed only by the cameras on the corresponding side of the body. The pelvis and trunk arrays are mounted on stiff, lightweight outriggers that extend backward away from the body. The outriggers prevent the arms from obscuring the LEDs. Each outrigger supports two arrays (right and left), which provide redundant kinematic information for the trunk and pelvis from the two sets of cameras. The pelvis outrigger extends directly backward and measures 20.8 cm from the mounting collar to the array centerline. The trunk outrigger extends backward with an upward slant of 45°, and measures 25 cm from the plastic mount to the array centerline. The head has only a single array mounted on a plastic headband, which is viewed by the cameras on the right side of the body. The arrays for the legs and arms are attached to the segments by mounts incorporating Velcro straps that can be tightened enough to permit minimal motion of the array with respect to the underlying tissue. However, some motion of the soft body tissue with respect to the skeletal structure is inevitable.

The foot, shank, arm and head arrays are attached to the Velcro straps and supporting structure by a ball and socket mechanism that permits 3 degree of freedom rotations of the array for optimal viewing by the cameras. However, the ball joint is prone to slipping under the relatively high inertial loads supplied by the array during the sharp deceleration experienced during the impact phase of the jump landings. Therefore, prior to the jumping experiments, each of these arrays is rotated downward to the lower limit of the adjustable range and the set screw is tightened as firmly as possible. Figure 4.3 shows comparison of the results of this procedure with the typical experimental practice. Preliminary test subject *pxs* is tested without rotating and tightening the arrays. The shank arrays slip downward by approximately 25° by the end of the jump session, resulting in erroneous estimates of the segment orientations and joint centers (upper left). In contrast, the outcome for subject *aqk* is typical of the results for the experimental subjects, for whom the arrays are rotated downward and tightened. The subject *aqk* shank slip is on the order of 5°, indicating a substantial reduction in slip compared to *pxs*.

The first and last data points in the lower plots of Figure 4.3 indicate the static standing trials at the beginning and end of the test session. These are the only two trials in which the subjects are positioned with the feet aligned in the same stance, while the data points in between are the uncontrolled stance measured after the jump landing. The static stand results show that the true shank array slip may have been as small as 2° for *aqk*, compared with approximately 20° for *pxs*. The residual slip incurred for the experimental subjects is eliminated using the joint optimization procedure described below.

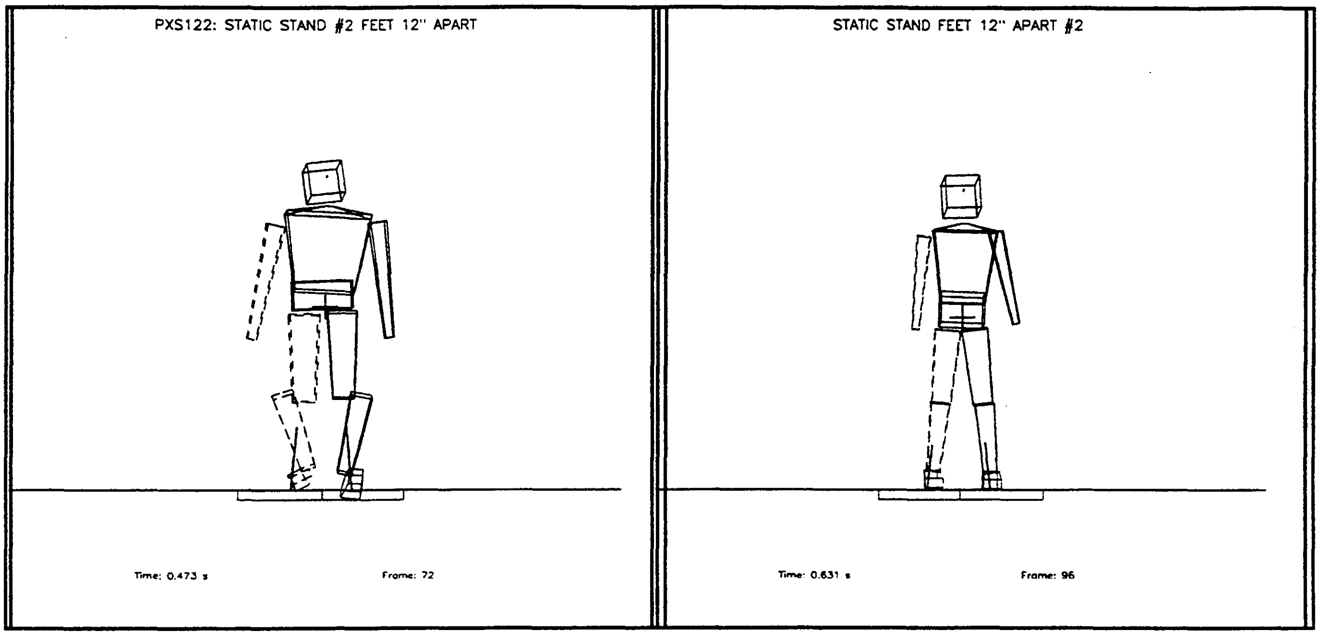

a. Subject *pxs* final configuration

b. Subject *aqk* final configuration

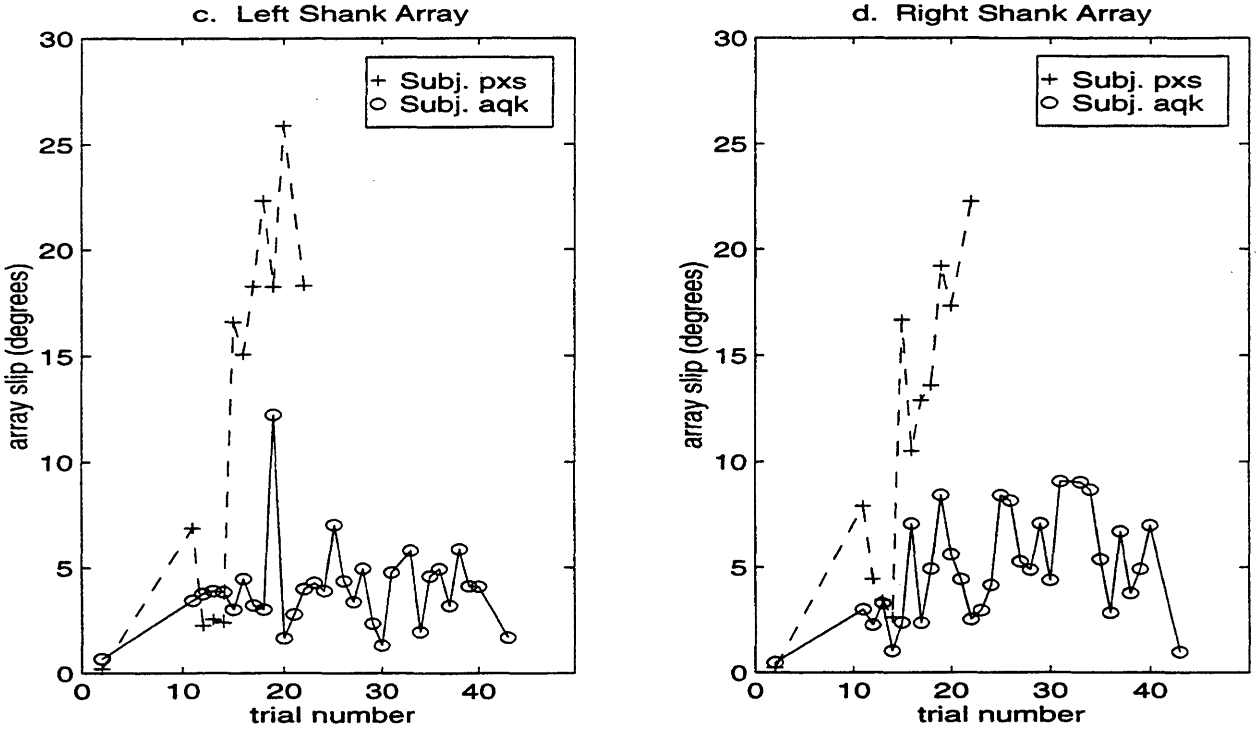

Figure 4.3. Array slip is reduced by tightening, rotating downward.
a. Practice subject *pxs* (arrays not tightened) after completing jump sequence
b. Subject *aqk* (arrays tightened, rotated downward) after jump sequence
c. Left shank array slip, comparison of *pxs* and *aqk*
d. Right shank array slip, comparison of *pxs* and *aqk*

The resonant frequency of vibration of the array/tissue system is tested and found to range between approximately 6 and 20 Hz for different arrays. In these vibration tests, the subject dons the arrays and stands quietly. An array is given several sharp taps, with enough time allowed between taps for all oscillations to subside. The resulting array oscillations are recorded and the power spectral density (PSD) of the motion is computed. This procedure is employed for the shank, pelvis and trunk arrays. The pelvis and trunk arrays are of special concern due to the length of the outriggers used in the mounting (20.8 cm and 25 cm for the pelvis and trunk respectively). The ball joint mounting of the foot, arm and head arrays is the same as that in the shank, so the shank results may be generalized to these arrays. Each array is tested first with the straps well tightened, as in the actual jumping experiments. The array is then tested with the straps loosened somewhat. The array resonant frequencies are estimated from the peaks in the PSDs, and are recorded in Table 4.1.

Table 4.1. Resonant frequencies of array vibration.

	Mean Resonant Frequency (Hz)	
Array	*Straps Tight*	*Straps Looser*
Shank	21.1	12.0
Pelvis	7.5	6.6
Trunk	10.0	6.6

4.1.1.2. Ground Reaction Forces

Two Kistler™ force plates located at the center of the camera viewing volume are used to collect ground reaction force data. Although the two plates permit simultaneous collection of bilateral data, this capability is not used because the landing platform for the jumps rest upon both force plates. The force plates are mounted side by side on granite slabs in the floor of the BML, with the upper surfaces of the plates flush with the floor. The floor and force plates are covered by a thin carpet. In each force plate, a three-axis piezoelectric force transducer is mounted under each of the four corners, giving 4 individual signals for each of the three dimensions. The force plates are sampled at the same frequency (153 Hz) as the individual LEDs.

4.1.1.3. Muscle Electromyograms (EMG)

Eight channels of EMG data are recorded using surface EMG electrodes. Each active electrode (Cyberthetics; Mashpee, MA) includes a built-in preamplifier close to the skin surface, reducing motion artifacts. The preamplifier gain is approximately 3500 (71 dB) within a pass band of 45-550 Hz. Common mode rejection ratio is 95 dB, input impedance is 1 million Mohm, and noise is less than 1 μV. A ground lead is attached on the subject's limb with a pediatric EKG electrode.

The EMG electrode leads are routed to a small connector box that is worn by the subject at the base of the trunk LED array support. This box is connected to the Cyberthetics 8 Channel Isolated EMG signal conditioner by a modular telephone-style cable that is routed from the subject with the LED umbilical. The signal conditioner is set for AC coupling, with signals passed from 50-500 Hz with 2 dB rolloffs. The entire system is electrically isolated from the subject at a level of 1500 V AC.

4.1.1.4. Data Acquisition and Processing Computers

All kinematic, force plate and EMG data are acquired simultaneously on a 486 PC. The data acquisition program permits viewing of the LED positions and raw analog data in "live" mode for real-time verification of LED visibility and the incoming analog signal quality. Before saving the data from each trial, the collected data can also be checked in graphical form to verify that each channel is acquired successfully. The 486 PC is also used for storage of the raw data, until the data can be transferred to the processing computer. All data processing is performed on a DECStation 5000/200 Workstation.

4.1.1.5. False Platform Jumping Equipment

The false platform apparatus is depicted in Figure 4.4. The subjects jump from a wooden "starting" block 60 cm in height. The upper surface of this block measures 81 cm wide by 96 cm long. The front end, including all forward facing edges, is covered with foam padding to minimize the chance of injury to the subject in the case of a fall. The normal landing surface is a second wooden block 30 cm in height, providing a nominal vertical jumping distance of 30 cm. The landing block is sized to fit within the confines of the combined force plate surface, and rests completely within the force plate area during the tests. The landing surface is 56 cm wide by 64 cm long. Both blocks are constructed of 2"x4" (3.8 cm x 8.9 cm) pine and 1/2" (1.3 cm) thick plywood sheathing.

The starting block is placed approximately 10 cm behind the edge of the force plates. The interior of the starting block is hollow, and the lower portion of the front face is open, allowing the landing block to be placed completely underneath the starting block. Wheels are mounted to the back end of the landing block so that they do not contact the ground when the landing block is resting flat. After tilting the landing block slightly, it is easily wheeled under the starting block.

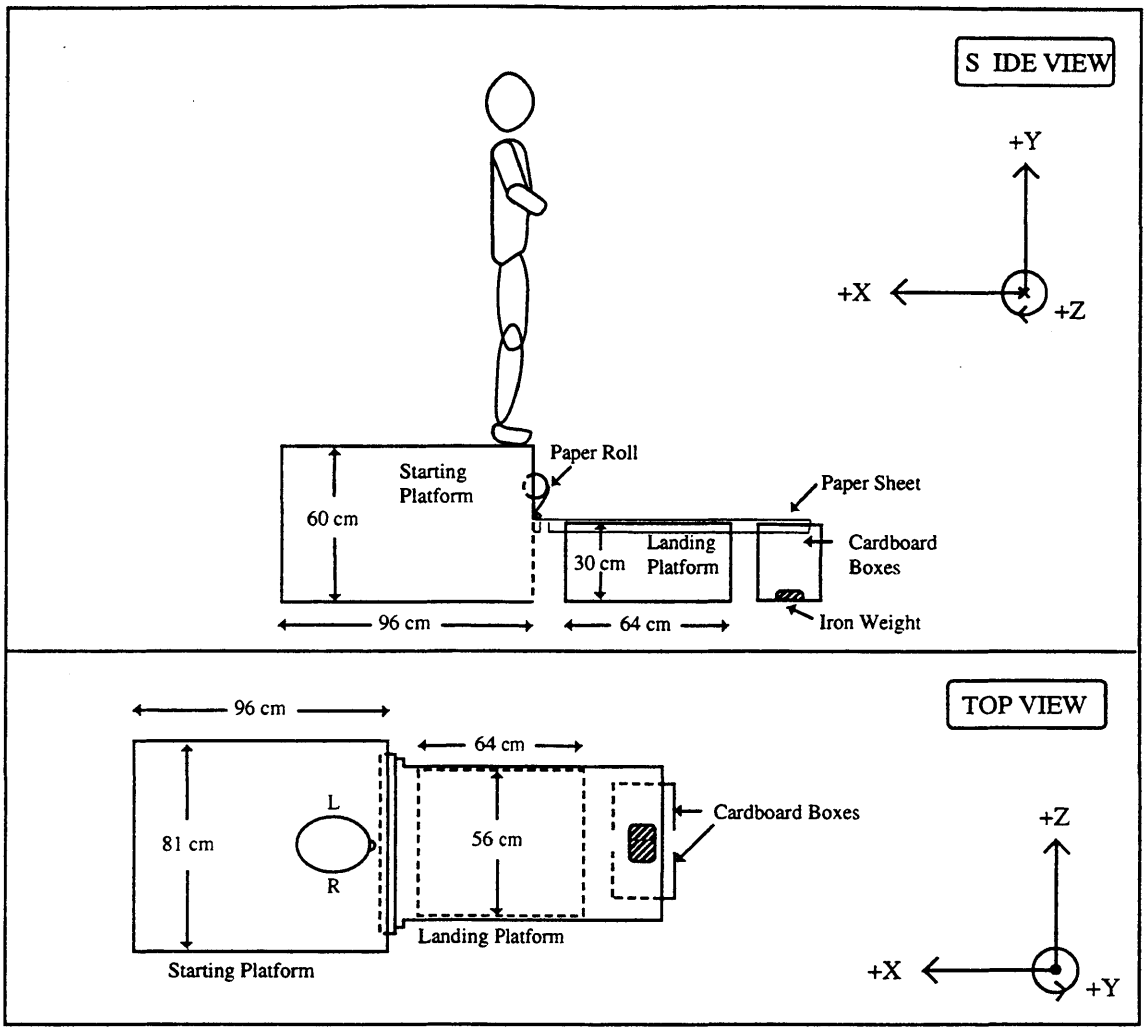

Figure 4.4. Schematic of false platform jumping apparatus. The landing platform area is covered by a sheet of paper running from the starting platform to two cardboard boxes forward of the force plate. The landing platform can be rolled underneath the starting platform. Coordinates X, Y, Z are global laboratory reference frame.

In order to prevent the subject from knowing if the landing block is present, the landing surface is completely hidden from above by a sheet of brown postal wrapping paper. When the landing block is present, the paper is suspended less than 5 mm above the landing surface. The sheet of paper is pulled from a roll mounted to the front of the starting block using a wooden dowel supported at either end by an eyehook. Because the roll can rotate freely, the paper is fixed with pushpins at each side of the starting block to a small horizontal wooden block covered with cork board. The pushpins are tied to the block with thread as a means of restraint, because the pins are often pulled loose when the subject falls through the paper target. At the front side of the landing platform, the paper is attached to the upper surfaces of two cardboard boxes slightly higher than the landing surface. These cardboard boxes are arranged on their sides with their open ends facing inward, and a flat iron weight is placed inside them to immobilize them when the paper is attached. An additional advantage of the cardboard boxes is their inherent compliance, which would help to protect the subject from injury in the case of a forward fall. The paper is pulled taut and fixed to the cardboard with pushpins, which are also tethered with thread. The lateral edges of the paper are then folded down and creased sharply. This provides the paper some rigidity and gives the subjective impression of a solid landing surface. After the paper is fixed in place, a square is drawn upon it to indicate the edges of the underlying landing surface for the subject.

In a normal "platform" jump landing (condition P), the landing platform is placed upon the force plates between the starting block and the cardboard boxes. In the "no-platform" jumps (condition NO-P), the landing block is replaced with a low, stiff 2 cm thick foam exercise mat to provide some padding for the landing. In the NO-P jumps, the landing platform is wheeled underneath the starting block, hiding it from the subject's view. Likewise, the foam pad is placed under the starting block during the P jumps. For the NO-P jumps, the total vertical distance traveled by the subject is approximately 58 cm, accounting for the thickness of the foam pad, resulting in an additional fall of 28 cm for the subject. This height is chosen to provide approximately 100 ms of free fall beyond the nominal time of impact, based on the mass center velocities at impact of approximately 2.5 m/sec found for downward jumps of 30 cm. In both P and NO-P cases, the placement of the paper is identical, and it is not possible to determine visually from above whether or not the landing platform is in place.

In order to prevent the subject from obtaining auditory cues during the preparation of the landing surface, the subject wears earphones and listens to a radio tuned to an inter-station region of the FM dial. The resulting white noise is set to a volume high enough to mask any preparation noises while not being painful to the subject.

4.1.2. Experimental Subject Selection

Six volunteer female subjects affiliated with MIT are tested using the false platform protocol. All subjects are athletic and ranged in age from 19 to 31 years. The most important criterion in subject selection is small stature. The limited height of the viewing volume (188 cm), combined with the heights of the starting and landing platforms (60 and 30 cm, respectively), places a constraint on the maximum height of the subject. Full-body kinematic data are required for the time immediately prior to impact with the paper target and throughout the landing phase. To meet this requirement, the maximum subject height is specified to permit viewing of all arrays from the time the subject's feet cross a threshold 5 cm above the paper target.

Because the highest LED in the head array lies approximately 3 cm below the top of the head, and the subjects land in a somewhat crouched posture, a maximum subject height of 163 cm is designated. Due to the relative difficulty of recruiting male subjects below this height, only female subjects are selected. During the jumping experiments, all arrays are visible for all subjects prior to the time of impact. In addition, all leg arrays are visible when the subject stands on the 60 cm starting block.

All subjects are screened for ataxia that might indicate the presence of vestibular defects. Each subject performs two tests: (1) quiet standing with eyes closed in the sharpened Romberg stance, and (2) walking a line with the eyes closed [Fregly and Graybiel, 1966]. All subjects meet the ataxia criteria for vestibular normals based on these tests. The actual test procedure and detailed test scores are described in detail in Appendix B.

Table 4.2. False platform subject parameters.

	Subject Code					
	djn	***aqk***	***czl***	***mjg***	***yak***	***ssy***
Age (years)	31	23	26	22	26	19
Height (cm)	162.5	157.5	157.5	157.5	162.0	157.5
Weight (kg)	52	43	55	46	52	57
Foot length (cm)	22.9	23.5	23.5	22.9	23.5	22.9
Ankle circ. (cm)	21.0	21.6	21.6	21.6	22.2	21.6
Knee height (cm)	43.8	40.0		43.2	41.9	40.6
Knee circ. (cm)	33.7	30.5	31.2	29.8	33.0	34.3
Thigh circ. (cm)	48.3	41.3	47.0	41.9	47.0	48.8
Waist circ. (cm)	71.1	68.6	69.8	61.0	67.3	76.2
Chest circ. (cm)	81.3	76.2	81.3	80.6	80.0	87.6
Arm length (cm)	48.3	47.0	50.8	48.9	50.8	49.5
Arm circ. (cm)	22.9	21.6	22.9	20.3	24.8	24.8
Neck circ. (cm)	28.6	30.5	30.5	31.1	30.5	31.1
Head circ. (cm)	52.1	55.2	55.2	52.7	53.3	55.2

4.1.3. False Platform Experimental Protocol

4.1.3.1. Human Use Approval

The false platform jumping experiments are approved by MIT's Committee on the Use of Humans as Experimental Subjects (COUHES). All subjects are volunteers, and before participating in the study each subject reads and signs a statement acknowledging informed consent. A sample subject informed consent statement is included in Appendix A.

4.1.3.2. Subject Preparation

The subjects wear athletic shorts, jog bras, T-shirts, and athletic shoes. Initially, a number of body dimensions are measured and recorded for use in processing of the kinematic data: height, weight, foot length, ankle circumference, knee circumference, thigh circumference, waist circumference, chest circumference, upper arm circumference, arm length, neck circumference, and head circumference. The surface EMG electrodes are then placed to record EMG data from 8 muscles on the right side of the body: (1) Tibialis anterior; (2) Gastrocnemius; (3) Quadriceps; (4) Hamstring; (5) Abdominus; (6) Paraspinal; (7) Trapezius; and (8) Sternocleidomastoid. The skin surface is cleaned with rubbing alcohol, and each electrode is taped securely to the skin with athletic tape. The EMG leads are attached to the connector box, which leads to the signal conditioner. Each muscle signal is checked on an oscilloscope to verify acceptable signal quality when the subject contracts the muscle.

Next, the LED arrays are affixed to the body segments. All arrays are strapped as tightly as possible without causing discomfort to the subject. EMG electrode leads are secured with the array straps where possible. The subject is asked to stand, make knee bends, and take several steps to ensure that the arrays, ribbon cables and EMG electrode leads do not interfere with subject mobility. The array cables are connected to the umbilical leading to the LED sequencer module, and the subject stands in the center of the viewing volume, over the force plates. At this point, the cameras and LEDs are powered, and LED visibility is checked for all 4 cameras.

4.1.3.3. Test Procedure

A nominal test procedure consists of the following steps, which are described in further detail in the following sections:

1. Resting EMG
2. Initial establishment of segment to array coordinate transformations
    a. Static Standing
    b. Joint Center Pointing trials
    c. Leg Joint Range of Motion trials
3. Baseline Jumping
4. False Platform Jumping Sequence
5. Final establishment of segment to array coordinate transformations
    a. Leg Joint Range of Motion trials
    b. Static Standing
    c. Joint Center Pointing trials

4.1.3.4. Resting EMG

A single set of EMG data is taken while the subject sits resting quietly for 10 seconds.

4.1.3.5. Establishment of Segment to Array Coordinate Transformations

A standard set of trials is performed both before and after the jumping trials in order to establish the relationship between the LED arrays and the joint centers, as well as the rotational relationship between the arrays and the corresponding body segments. If the subject bumps one of the arrays during the jumping tests, or an array requires adjustment during the jump sequence, another set of these calibration trials is performed. A static standing trial is performed first, in which the subject stands upright and looking straight ahead with the feet aligned to be parallel and 30.5 cm apart. This trial establishes body segment relationships in upright standing posture.

Next, a clinician performs a series of "pointing" trials, with the purpose of providing additional geometric information needed for joint center determination. The "pointers" are two separate, hand-held LED arrays (one for each side of the body). Each pointer is shaped like a paddle, with a sharp point extending from the tip. The geometry of the point is known precisely in relation to the pointer LEDs. During the pointing trials, the subject remains in the position and stance established for the static standing trial. Six pointing trials are performed, with the pointing for the left and right sides of the body done simultaneously:

1. *Ankle Pointing:* The pointer tip points to the medio-lateral center of the ankle joint at the vertical level of the joint. The pointer is aligned rotationally to match the external rotation of the foot, as determined by the pointer tip and the second metatarsal.
2. *Knee Pointing:* The pointer array defines the knee flexion-extension plane passing through the approximate center of the knee joint. The tip points to the tibial tubercle, and the array is aligned to indicate the external rotation angle of the knee.
3. *Hip Pointing:* The pointer array defines the hip joint flexion-extension plane, as well as the angle of pelvic tilt. The tip of the pointer indicates the mid-plane of the hip joint, as approximated using the midpoint of the line connecting the anterior superior iliac spine and the pubis.
4. *Trunk Pointing:* The pointer tip indicates the peak of the iliac crest.
5. *Arm Pointing:* The pointer tip is placed on the acromian process. The orientation of the pointer array defines the orientation of the arm in all three rotational planes.

6. *Head Pointing (right side only):* The pointer tip is placed on the right side mastoid process. The array is aligned in three dimensions with the head orientation.

Following the pointing trials, two "Range of Motion" trials are performed. The data from these trials are used to estimate average rotation axes for the knee and hip. The specific task is a constrained chair rise, in which the subject starts from a seated position on a platform equal in height to the standing knee height. In the starting position, the subject's feet are aligned 10 cm apart in a position resulting in 18° of ankle dorsiflexion, and the trochanters of the hip are less than 4 cm from the forward edge of the seat. The arms are folded across the stomach, with the elbows against the sides.

4.1.3.6. Baseline Jumps

Four 30 cm baseline jumps from the starting block onto the landing platform are performed. If the subject takes a step on any of the baseline jumps, she completes an additional baseline jump. In the baseline configuration, the starting and landing platforms are arranged exactly as in the subsequent false platform sequence, including placement of the paper target over the landing platform. However, in the baseline jumps the subject is allowed to ascertain that the landing platform is actually in place. No instructions are given to the subject about the forward extent of the jump, other than to jump a comfortable distance while landing within the bounds of the landing surface.

The following instructions are read to the subject:

> Fold your arms across your stomach, with your elbows against your sides and one hand grasping the other wrist. Keep your arms in this position throughout the jump. Look down at the landing surface before you jump. Jump so that you take off and land with both feet simultaneously. When you land, stand up normally and stay as still as possible until I say "stop."

Before each jump, the subject stands at the edge of the starting block and the feet are aligned facing forward by having the subject place them on either side of a 10 cm wide block of wood. The instructions to the subject are always the same before each jump: "Are you ready? Look down. One-Two-Ready-Jump." Data acquisition is initiated at the count of "Two," and the subject jumps at the command "Jump." Five seconds of data are collected for each jump. During the baseline and subsequent false platform sequence, two spotters are present, one on each side of the subject. The spotters stand at a sufficient distance that the views of the cameras are not blocked. In this position, the spotters are close enough to catch the subject in the event of a fall.

4.1.3.7. False Platform Jumps

The false platform jumping sequence consists of 24 jumps. Of these, 18 are performed with the landing platform present (P), so that the subject jumps the standard 30 cm vertical distance. In the other 6 jumps the landing platform is removed (NO-P), so that the subject falls through the paper target for a total jump height of 58 cm. The subject is not informed of the order of the NO-P jumps within the sequence. A pseudo-random jump order is assigned, so that the placement of the of the NO-P trials in the sequence cannot be predicted by the subject. The same jump sequence, listed in Table 4.3, is used for all subjects except *djn*.* The order is purposely selected to exclude repeated NO-P jumps, so that the subject has the opportunity to recalibrate to the normal 30 cm jump height (McKinley and Smith [1983] find that cats time muscle activation for the height of the previous jump when the jump height is uncertain.)

Table 4.3. False platform jump order (all subjects except *djn*).

Jump #	Platform/No-Platform	Jump #	Platform/No-Platform
1	P	14	P
2	P	15	P
3	P	16	P
4	NO-P	17	NO-P
5	P	18	P
6	P	19	P
7	P	20	P
8	P	21	P
9	P	22	NO-P
10	NO-P		
		23	P
11	P	24	NO-P
12	P		
13	NO-P		

The following instructions are read to the subject prior to the beginning of the jumps:

> You will be performing several downward jumps from a 2 foot (60 cm) high step. The landing surface will be hidden by a sheet of paper. For most of the jumps the landing surface will lie a fraction of an inch below the paper, so that the jump height is 1 foot (30 cm). On a few of the jumps, the landing surface will be removed, so that you will fall through the paper

---

*Due to time constraints, a different jump order is used for subject *djn*. The NO-P jumps are numbers 4, 12, 17 and 19 out of a total of 19 jumps.

> target onto a foam pad 1 foot below the paper. You will not know in which of the jumps the landing surface is missing. On each trial, you are to perform a two footed jump. You are to assume that the landing surface is at the height of the paper (as it will be for most of the jumps), and you should try to land normally for that height.
>
> It is important that you do not know when the landing surface will be missing. While the landing surface and paper target are being arranged, you will sit behind the jump step, facing away from the landing surface. You will wear headphones playing static (white noise) at a volume which is not painful but is loud enough to hide the setup noises. During this time, you will be permitted to read.

As indicated in the instructions, precautions are taken to prevent the subject from knowing whether or not the landing platform would be present for the jumps. These precautionary measures include preventing the subject from observing the setup of the jump platform, foam pad and paper between jumps, and preventing the subject from listening to the sounds associated with the setup. After each jump, the subject is returned to a seat facing away from the jumping platforms. Preparation of the platforms for the next jump begins only after the subject is seated and the headphones are in place.

In order to standardize the time between trials and present the same general setup noises, a similar procedure is followed after both P and NO-P jumps. First, the paper is lifted from the landing area and folded up over the jumping platform to permit access to the landing area. After each NO-P jump, the paper is cut off and discarded, and a new section of paper is rolled out. The paper is also replaced in the infrequent cases when the paper is damaged during a P jump. Next, the foam pad is placed on top of the starting block. For an upcoming P jump, the landing platform is rolled halfway under the starting block, then rolled back out onto the force plates, and the foam pad is placed under the starting block. If the next jump is to be NO-P, the landing platform is rolled completely under the starting block, and the foam pad is placed over the force plates instead. The paper is then folded back over the landing area, pulled taut and pinned in place. All subjects indicate that they are unable to determine whether or not the landing platform is present prior to jumping.

4.2. FALSE PLATFORM DATA ANALYSIS

The processing and analysis of the 11 segment kinematic data forms the greatest portion of the analysis procedures. The software used at various states in the kinematic data processing is detailed, then the minimal processing associated with the force plate and EMG data is described.

4.2.1. Body Segment Kinematics

Processing of the kinematic data consists of two stages: (1) calculation of array position and orientation; and (2) determination of the coordinate transformations between arrays and their respective body segments, combined with estimation of the joint center locations relative to the arrays. Following processing of the raw array data, joint angles and joint positions are calculated. Next, mass centers and inertial properties of the body segments are estimated. Selection of a consistent subset of the P jumps is addressed. Finally, because the comparison of the P and NO-P jumps is a central goal of the experiment, the method of aligning the P and NO-P jumps is described.

4.2.1.1. Reference Frames

Three types of reference frames are used in processing and analyzing the body segment kinematic data: a global (laboratory) frame, LED array frames, and segment frames. The global right handed coordinate system (G) is defined in the following manner: the positive X-direction is defined by the vector from camera 1 to camera 3, as shown in Figure 4.1. All tests are performed with the subject facing in the negative X-direction, so that cameras 1 and 3 are on the subject's right side while cameras 2 and 4 are on the subject's left. The global Y-direction is along the gravitational vertical, with positive Y pointing upward. Thus, the global positive Z-direction is the same as the vector from camera 1 to camera 2, pointing from the subject's right to the subject's left.

Each LED array has its own coordinate system, defined in relation to the known geometry of the LEDs. The X-Y plane of the array frame is coincident with the plane containing the LEDs. The array Z-direction is perpendicular to this plane.

The body segment reference frames are coincident with the global laboratory frame when the subject is standing upright, facing forward along the global negative X-direction with the feet flat on the floor. Thus, in this posture the segment positive X-direction is from anterior to posterior, the positive Y-direction is from inferior to superior, and the positive Z-direction is from right to left.

4.2.1.2. *Array Position and Orientation*

Using a triangulation procedure, the LED positions in 3-dimensional space are calculated from the raw data in camera coordinates. The position of each LED is determined from the best approximation to the intersection of the vectors from each of the 2 viewing cameras to the LED. The LED position data is then passed through a Kalman filter and a Rauch-Tung-Striebel smoother, which provide smoothed estimates of the LED positions, velocities and accelerations [Gelb, 1974; Bortolami *et al.*, 1997]. Each of the 3 dimensions is filtered independently. For the current experiments, the bandwidth of the filter is set very high, so that smoothing of the LED position data is minimal. The half-power frequency for the filter is greater than 75 Hz; the frequency response is shown in Figure 4.5. The Kalman filtering and smoothing of the LED positions provide the only smoothing of the data.

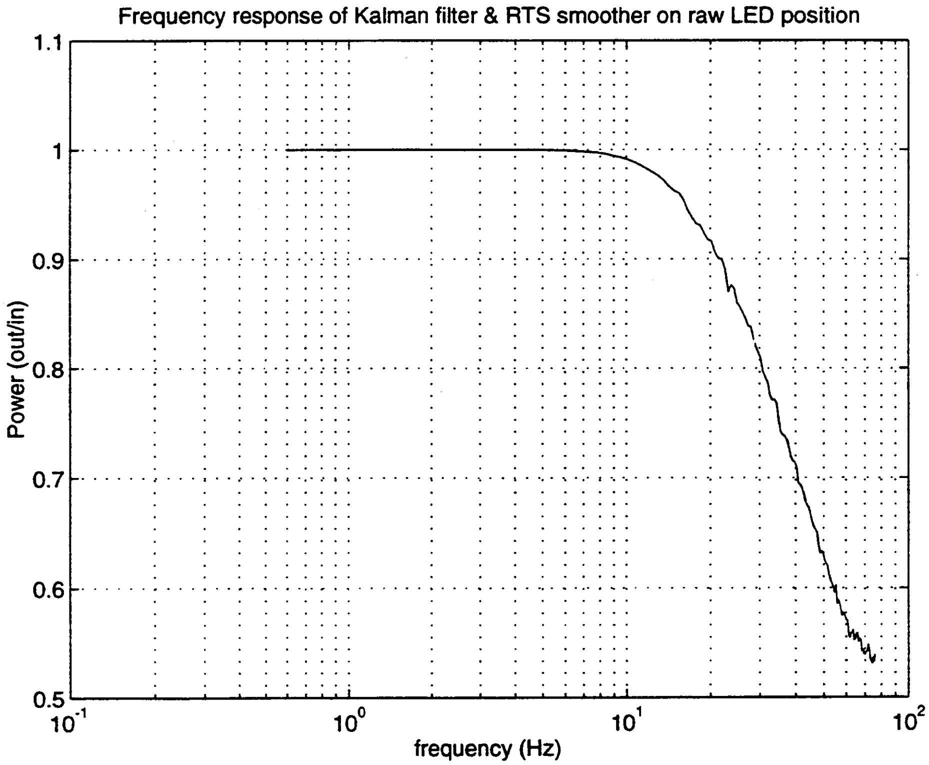

Figure 4.5. Frequency response of the Kalman filter and RTS smoother.

From the computed LED positions in each array and the known LED geometry for that array, the position and orientation of the array in space is calculated to fit the data best in a least-squares sense [Antonsson and Mann, 1989]. The array positions and orientations are determined from the raw camera data by a set of programs known collectively as

TRACKPC. TRACKPC returns the three-dimensional position of the center of each array, as well as a rotation matrix describing the transformation from each local array coordinate system to the global laboratory coordinate system. The programs also combine and reduce the force plate data to provide net forces in each of the three dimensions, as well as the center of pressure in each of the horizontal directions and the net moment about the gravitational vertical.

4.2.1.3. Joint Centers and Segment to Array Transformations

The location and orientation of the LED arrays relative to the corresponding body segments is required to complete the calculation of the position and orientation of the body segments in inertial space. Joint center locations and baseline body segment alignment are determined from a combination of kinematic data from the joint range of motion trials, and anatomic landmark references provided by the pointing trials.

The nominal procedure for joint center determination and segment alignment is described by Riley [1988]. The ankle joint center is located from the ankle pointing trial, one ankle radius posterior to the pointer tip in the plane of the pointer. Knee and hip average screw axes of rotation are determined from the range of motion trial [Fijan, 1985]. The knee and hip joint centers are defined by the intersection of the rotation axes with the pointer planes determined in the knee and hip pointing trials. Vectors from the proximal to distal joints determine the segment flexion and abduction for the shank and thigh, while the external rotation angle is determined from the knee pointer plane.

The lower back joint is located at the midpoint of the line between the left and right iliac crests, at approximately the L4-L5 level. Pelvis flexion is determined from the trunk pointing trial using the angle of the pointer arrays in the sagittal plane. Pelvis and trunk external rotation are also determined from the orientation of the pointer planes in the trunk pointing trial. Trunk flexion and abduction angles in the upright static posture are defined by the line from the lower back joint to the midpoint of the line joining the acromian processes found from the arm pointing trial. The shoulder joints are approximated by the location of the acromian processes. The neck joint is located one neck radius medial to the pointer tip in the head pointing trial. Arm and head orientations in all three planes are determined from the pointer orientations in the arm and head pointing trials, respectively.

Each joint location is first determined in the coordinate systems of the arrays immediately proximal and distal to the joint. The flexion, abduction and external rotation angles for each segment define a set of Euler angles from which the transformation from segment coordinates to global coordinates may be obtained for the upright posture in the pointing and static standing trials. Using the averaged global to array coordinate transformations for the static standing and pointing trials, the segment to array coordinate transformations are obtained.

Because a vector from the array to the joint center location is estimated for both the proximal and distal arrays about each joint, an averaged joint location is determined in global coordinates for each joint in the upright standing posture using the predicted location from the proximal and distal array. The vectors from the proximal and distal arrays to each joint are then recalculated using this average joint location, resulting in approximately zero discrepancy between the joint location estimate from the proximal and distal arrays for the upright standing posture. The above procedures for segment orientation and joint center estimation are implemented in a program *pcjoint.c*.

This joint center location procedure is found to generate discrepancies in the location of the joint as predicted from the proximal and distal arrays. Some discrepancy is expected, as the joints are only approximated by ideal pin joints, and there is some motion of the arrays relative to the underlying skeleton. However, a joint optimization procedure is developed to reduce the discrepancy between the joint center estimates. This procedure also proves useful when arrays are found to have slipped during the experiment. Array slipping is a particular problem for the shank and foot arrays, resulting in a change in the array orientation and array center position relative to the segment. The optimization routine allows recalculation of the array to joint vectors in array coordinates, and new determinations of the segment to array transformations for the shanks and feet.

The goal of the optimization is to minimize the summed squared discrepancy between the predicted joint locations from the proximal and distal arrays, measured as the absolute distance in 3 dimensions between the two predictions:

$$J = \sum_{i=1}^{n} \Delta r_i^T \Delta r_i + \alpha z^2$$

where

Δr = joint discrepancy vector

z = distance from joint center to segment midline (4-1)

α = constant weight

i = sample number

n = number of samples

Because this optimization does not constrain the joint center position along the joint axis, an additional cost term is added to penalize the distance of the joint from the segment mid-line, as previously determined from a pointing trial. In practice, the shank segment mid-line is determined from the thigh segment, because the thigh array does not slip appreciably. The optimization uses a Nelder-Meade simplex search algorithm [Grace, 1993]. Joint centers are optimized for the ankle, knee, hip and neck. The lower back joint estimate is not improved by the optimization routine, and the shoulder joints are irrelevant as the subjects held the arms in a fixed position throughout the tests. Figure 4.6 shows a sample reduction in joint estimate discrepancy for a jumping trial using the optimization procedure.

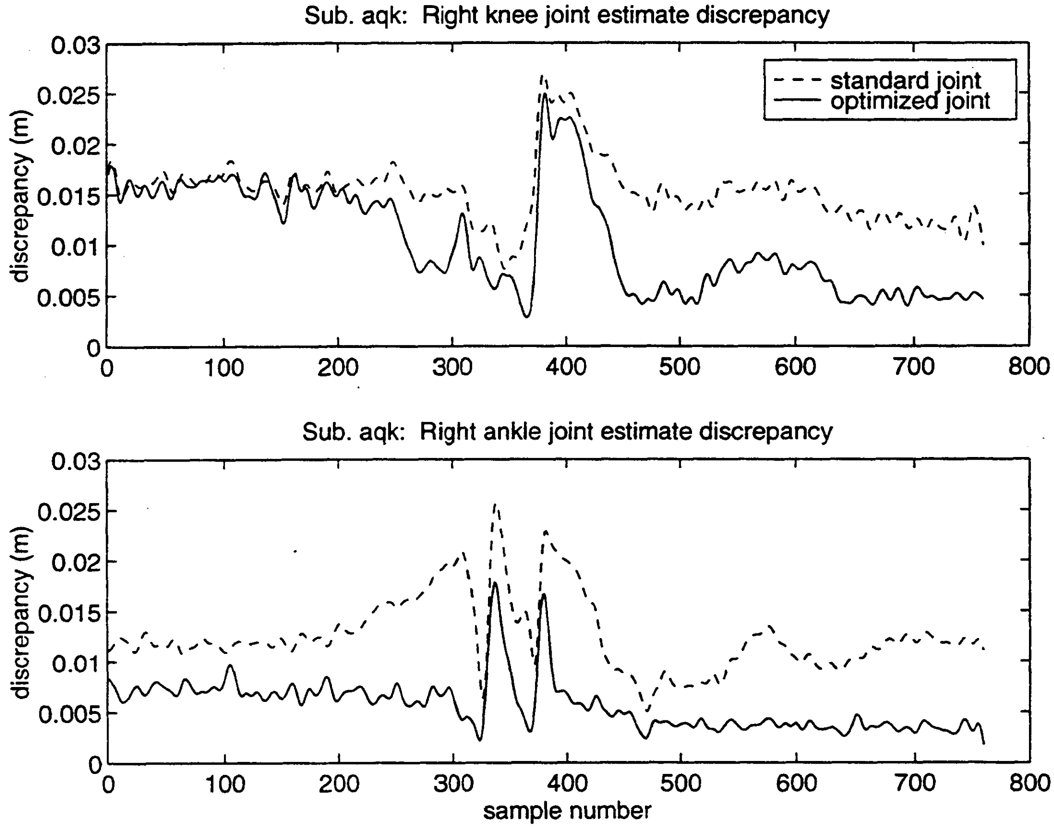

Figure 4.6. Optimization improves discrepancy in estimated joint locations. In a representative jump trial, the discrepancy between joint center estimates from the proximal and distal arrays is shown for the right knee (upper) and ankle (lower).

The data from each jump are assessed to evaluate the effects of array slipping, and the optimization procedure is used to recalculate ankle and knee joint centers as needed. Because the feet are aligned prior to each jump, new foot segment to array transformations are calculated using the samples prior to initiation of the jump takeoff movements. Using the vector joining the recalculated ankle and knee joints, the flexion and abduction of the shank segments are determined, and the shank segment to array rotations are recomputed. Figure 4.7 shows the result of shank array slipping and the subsequent correction using the joint optimization and recalculation of segment to array transformations. Between 4 and 7 sets of joint centers and segment transformations are calculated for each subject as required at various intervals throughout the jump sequence. Each individual jump is analyzed using the appropriate set of joint and segment information.

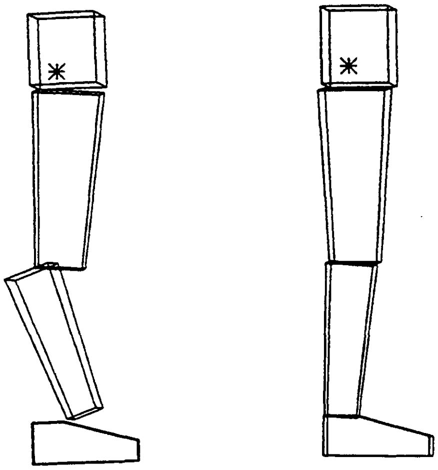

Figure 4.7. Joint optimization to re-estimate array to segment transformations. Right shank array slip for subject *yak*. The estimated segment positions and orientations are shown at left for the initial transformations, which are no longer valid. The joint optimization routine is used to recompute the array to segment transformations for the leg segments (right).

4.2.1.4. *Joint Angle and Joint Center Calculations*

Joint angles are calculated for contiguous segments from the rotation matrix which relates segment coordinates.

$$\begin{aligned} {}^{S2}_{S1}R &= {}^{S2}_{A2}R \cdot {}^{A2}_{G}R \cdot {}^{G}_{A1}R \cdot {}^{A1}_{S1}R \\ {}^{S2}_{S1}R &= R(Y,\theta_e) \cdot R(Y,\theta_a) \cdot R(Y,\theta_f) \end{aligned} \qquad (4\text{-}2)$$

where

${}^{S2}_{S1}R$ = rotation from segment 1 frame to segment 2 frame
${}^{S}_{A}R = {}^{A}_{S}R^{T}$ = rotation from segment to array frame
${}^{A}_{G}R = {}^{G}_{A}R^{T}$ = rotation from global to array frame
$R(j,\theta)$ = positive rotation about axis j by an angle θ
$\theta_f, \theta_a, \theta_e$ = flexion, abduction, external rotation angles respectively

The rotation matrices are equivalent to 3 sequential rotations defining a set of 3-1-2 Euler angles. The first rotation is about the original Z axis, and corresponds to joint flexion/extension. The second rotation is about the new X axis (X'), corresponding to joint abduction/adduction. External/internal rotation is provided by the third rotation, taken about the newest Y axis (Y").

Joint centers can be estimated from the array belonging to the segment either proximal or distal to the joint. When both arrays are visible, the joint center is set to equal the average of the joint positions estimated from the two arrays.

4.2.1.5. Body Segment Inertial Properties

The body segment mass distribution properties are estimated from a set of regression equations determined by Young *et al.* [1983] using stereophotometric volume measurement on a subject group of 46 living adult females. Segment masses and centroidal moments of inertia are estimated from regression equations based on subject height, weight and head circumference. Average principal axes of the segment inertia tensors are given in relation to anatomical landmarks, and segment centroid locations are determined from population averages with appropriate scaling for subject-specific segment dimensions.

Young *et al.* define separate abdomen, thorax and neck segments. These three segments are lumped together using the parallel axis theorem to yield the trunk segment used in the BML 11-segment model [Grierson, 1992]. Likewise, the upper arms, forearms and hands are assumed to remain fixed in the crossed configuration described in the experimental protocol. Hence, lumped mass properties are obtained for each complete arm in the crossed configuration.

4.2.1.6. Full Body Mass Center Calculation

The segment position and orientation data from the segment arrays are used together with the segment centroid locations and mass estimates to compute the location of the full body CM. The CM location $\bar{r}_{CM}$ is given by

$$\bar{r}_{CM} = \frac{\sum_{i=1}^{11} m_i \bar{r}_i}{\sum_{i=1}^{11} m_i} \qquad (4\text{-}3)$$

where m_i = segment mass

$\bar{r}_i$ = segment centroid location

i = segment index (1 ... 11)

In order to assess the accuracy of the CM estimates, the CM data are smoothed and twice differentiated using a quintic spline fit [Woltring, 1986]. The knot spacing for the spline fits is set at 5 samples for the first 30 samples after impact, and is increased to 20 samples after this point (the knots are the values of the independent variable [sample number] used in fitting the piecewise polynomials). The CM vertical acceleration should be related to the vertical ground reaction force data by

$$ma_{CM} = F + mg \tag{4-4a}$$

$$1 - \frac{a_{CM}}{g} = -\frac{F}{mg} \tag{4-4b}$$

where

m = body mass
a_{CM} = CM vertical acceleration
F = vertical ground reaction force
$g = -9.8 \text{ m/s}^2$

The quantity on the left side of Equation 4-4b is the vertical GRF that is predicted from the CM acceleration (normalized by the body weight); it is found from the CM vertical acceleration estimate and the known value of g. The quantity on the right side is determined by normalizing the force plate vertical data by the average vertical GRF determined during quiet standing. These two quantities are plotted together in Figure 1.8. The agreement is excellent and provides a high level of confidence in the CM estimates.

4.2.1.7. Data Stationarity and Selection of Platform (P) Jumps

Within the set of 4 baseline jumps and 18 P jumps, some variability is noted. This variability can be observed in force plate data, CM trajectories, and joint angle range of motion and timing of pre-impact joint trajectories. For each subject, some P jumps are excluded from the analysis based on 4 criteria: (1) stumbling or stepping in the course of the landing; (2) large anomalous oscillations in the joint angles and CM trajectories, associated with near-loss of balance upon landing; (3) anomalous pre-impact joint trajectories; and (4) large differences from the average CM trajectory. The first two criteria are self-explanatory.

The third criterion deals with the normal pattern of joint motion observed prior to impact. It is found that the subjects extend their legs during most of the flight phase of the jumps. Just before the moment of impact, the subjects begin to flex their legs again, so that the point of maximum joint extension occurs a few samples before impact. However, in some cases the maximum joint extension takes place well before impact, giving a delay

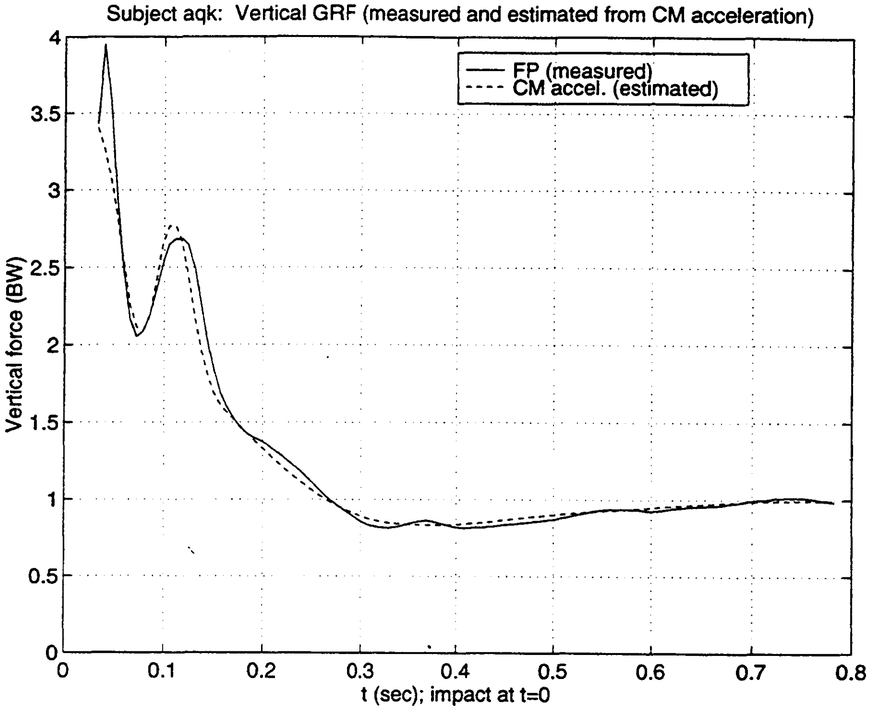

Figure 1.8. Measured vertical GRF and predicted GRF from CM estimates. Vertical GRF values are normalized by the subject body weight (BW).

from peak extension to impact 2-3 times longer than normal. Because such jumps appear to indicate a different pre-programmed movement pattern, they are excluded from the analysis.

The fourth criterion is used to select reasonably consistent jumps from the remaining P trials based on the CM trajectories. For each jump, three parameters are determined from the full-body CM motion: (1) peak downward deflection of the CM after impact; (2) time of peak downward CM deflection after impact; and (3) time to reach 98% of the final average equilibrium CM height, as measured above the ankle. Means and standard deviations for the complete P jump set are computed for each of these parameters. The eight trials that give results closest to the mean for these parameters are selected for further analysis. If additional trials fall within ±1.5 standard deviations of the mean for all 3 parameters, they are included in the analysis. In general, the 3 measures are well correlated: jumps resulting in larger vertical CM deflection give longer times to peak CM deflection and longer times for recovery to the upright position.

4.2.1.8. Alignment of Platform (P) and No-Platform (NO-P) Data

The P trials are aligned at the time of impact as determined by the first force plate data sample above a threshold value. The NO-P trials are aligned in a similar fashion. The P and NO-P trial sets are aligned with each other at the sample when one or both of the foot arrays fall below a computed vertical threshold. This threshold is determined by calculating the mean height of the foot array plus one standard deviation at the time 2 samples prior to impact for the set of P jumps. Because some subjects tend to lead slightly with one foot, separate candidate thresholds are calculated for the left foot array, the right foot array, and for the average of the two array heights. The predicted impact time is then recalculated for each of the three candidate thresholds as the moment two samples after threshold crossing. The threshold crossing (left foot, right foot, or both feet) that accurately predicts the highest number of correct impact times is chosen as the measure for aligning the P and NO-P trials. For 5 of the 6 subjects, the impact sample is predicted precisely in 75% to 90% of the cases. The impact sample predictions are correct in only 56% of the cases for the sixth subject (*yak*). This method always predicts impact samples that are correct to within one sample for all of the subjects, including *yak*.

4.2.2. Force Plate and EMG Data

Because the landing platform rests upon both force plates, the signals from the two force plates are summed to give net reaction forces in 3 dimensions. Force plate data is normalized to the subject's body weight, as determined by averaging the results of the vertical reaction force for the static standing trial.

EMG data for the 8 muscles measured are high-pass filtered, rectified and smoothed. The high pass filtering process uses a 34th order finite impulse response (FIR) digital filter with a -3 dB frequency of 70 Hz. The FIR filter is the windowed inverse Fourier transform of the ideal high pass filter with a break frequency of 70 Hz, based on a Hamming window of 35 samples [Krauss *et al.*, 1994]. The filter magnitude response as a function of frequency is shown in Figure 1.9. After application of the high pass filter, the data are smoothed using a moving window root-mean-square (RMS) procedure. The RMS signal is calculated for windows of 5 samples, decimating the data from 1000 Hz to 200 Hz.

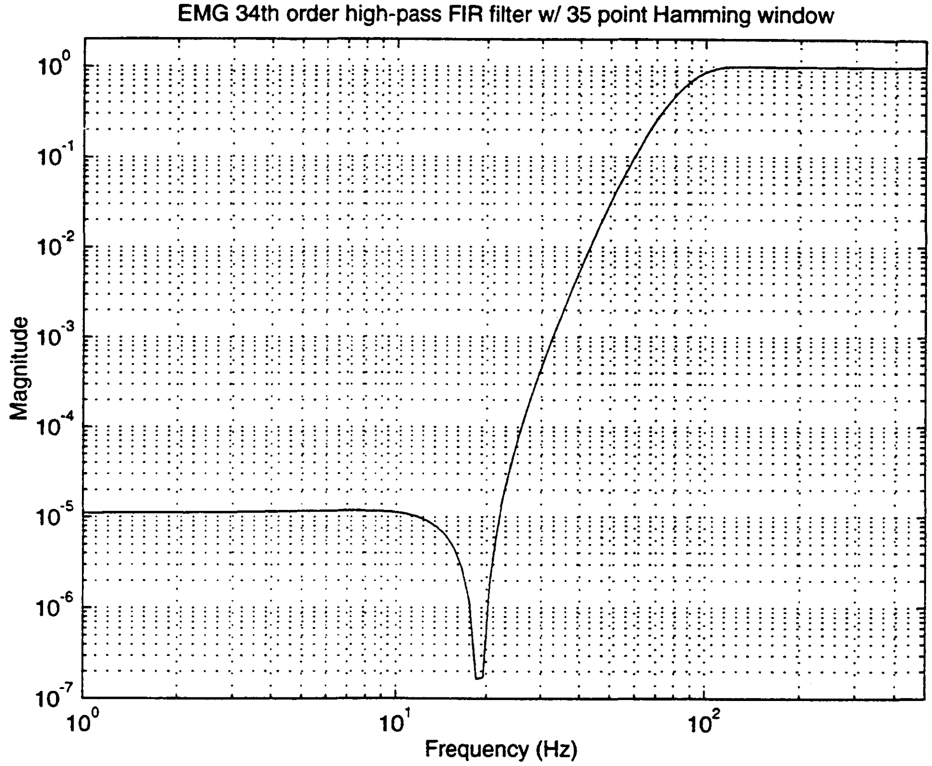

Figure 4.9. Frequency response of high-pass FIR filter for EMG data.
In order to reduce motion artifacts, the EMG data are filtered forward and backward (to eliminate phase shift) using a 34th order high-pass FIR filter with a 35 point Hamming window.

4.3. FALSE PLATFORM RESULTS

This section describes the joint angle and body center of mass (CM) kinematics, vertical ground reaction forces and muscle electromyograms. Patterns observed in the platform (P) jumps are discussed first. The force plate data is related to the CM trajectories. Next, the body configuration is described for the no-platform (NO-P) jumps. Emphasis is placed on the interval immediately prior to the nominal impact time (passing through the paper target), and the 100 ms between nominal impact and the actual impact with the foam pad landing surface. The limb trajectories between the nominal impact time and actual impact correspond to the free or no-force trajectories, due to the absence of the usual impact perturbation. Last, the EMG data for the leg muscles are examined for the P and NO-P jumps.

4.3.1. Platform Jumps

The important features of the CM vertical trajectory after impact and the vertical ground reaction force (GRF) are exemplified by the data for a typical subject (*djn*) in Figure 4.10. Corresponding data for all subjects are included in Table 4.4 - Table 4.6. At impact, the vertical velocity of the CM averages 2 m/sec in the downward direction. Ankle plantarflexion prior to impact results in downward extension of the foot, so that the CM is about 0.5 cm higher at impact (for 5 of 6 subjects) than in the final upright standing position after recovery from the landing. The CM reaches its maximum downward vertical deflection approximately 150 ms after impact, giving a minimum ankle to CM vertical distance of approximately 80% of the ankle-CM length in upright standing. This corresponds to a 16 cm average downward deflection of the CM from its upright equilibrium position. The CM recovers to within 2% of its final upright equilibrium position (as measured by the vertical distance from the ankle to the CM) by a time that varies from 500 to 900 ms after impact (660 ms average) for different subjects. Table 4.4 contains the data for all subjects summarizing the CM heights and CM impact velocities, and Table 4.5 presents the times associated with peak CM deflection and 2% settling times.

The upper traces in Figure 4.10 show the vertical ground reaction force (GRF) following impact. These traces depict two different types of jump landing, as classified from the GRF data. In the Type 1 landing (dashed line, average of 4 jumps), the GRF increases to a maximum of 4 times body weight (BW) approximately 50 ms after

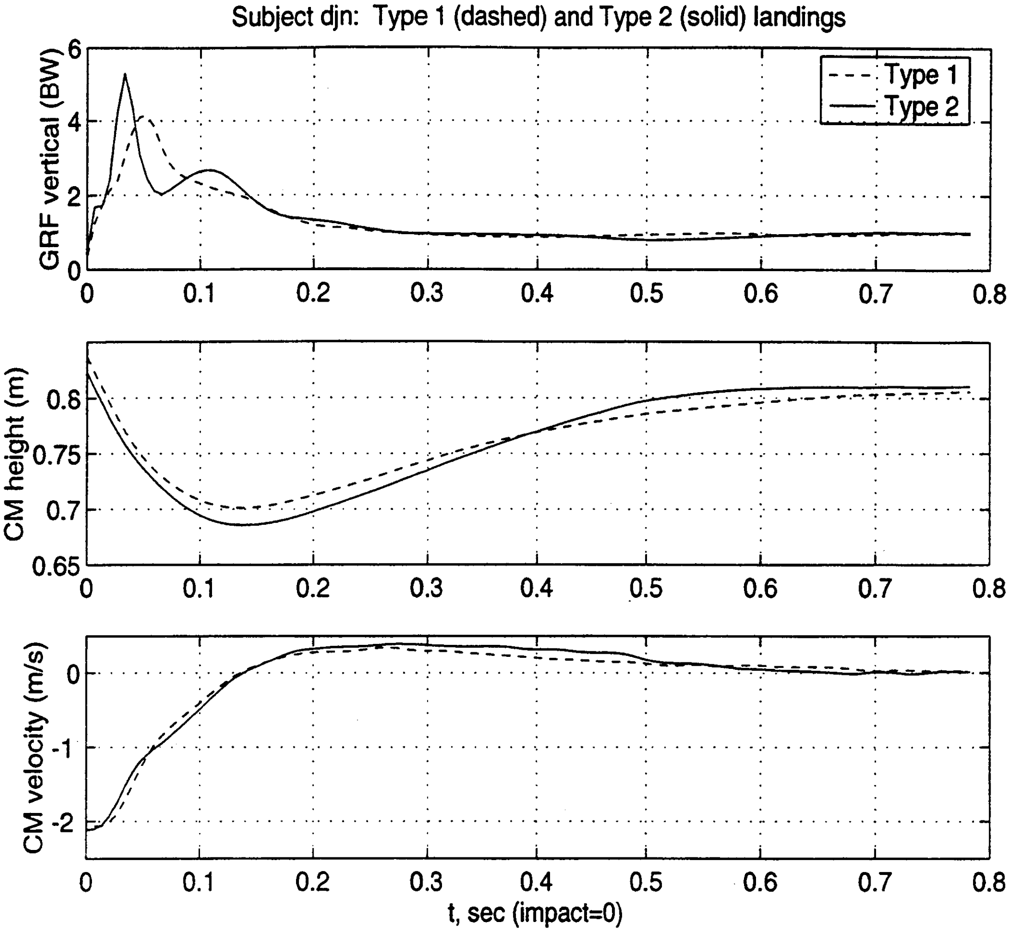

Figure 4.10. P jump vertical ground reaction forces and CM motion. Multiple-jump averages, aligned at impact. Impact is shown as t=0. Upper plot describes vertical ground reaction forces; middle plot shows CM vertical position; lower plot gives CM vertical velocity. Two apparently different landing patterns are seen: Type 1 and Type 2.

landing. The GRF then decreases monotonically, crossing the level of one BW and reaching a minimum of approximately 0.75 BW at 500 ms after impact. The drop of the GRF below 1 BW is associated with the deceleration of the CM at the end of the upward recovery to equilibrium.

In the Type 2 landings the GRF peaks earlier, at approximately 40 ms after impact. This peak is both higher and sharper than that seen in the Type 1 landings, and the GRF decreases rapidly to a local minimum of 2 times BW or less. This dip in the GRF occurs approximately 75 ms after impact. The GRF then increases to a second, lower peak level averaging 2.5 BW at 120 ms after impact, before decreasing again to follow the rest of the pattern observed in the Type 1 landings. The CM kinematics for the Type 1 and Type 2 landings reflect the force plate data. The lower plot in Figure 4.10 shows the vertical velocity of the CM after impact. The trace for the Type 2 landing shows initially more rapid deceleration than the Type 1 record, corresponding to the higher early force peak for the Type 2 landing. However, the velocity trace for the Type 1 jumps crosses the Type 2 graph at approximately 50 ms after impact, matching a reduction in the Type 2 deceleration as the Type 2 force dips sharply below the broad peak in the Type 1 force. Figure 4.11 depicts the magnitude of the GRF for all subjects for each of the 4 events: initial peak, first minimum, second peak, and the overall minimum. The timing of these events is included in Table 4.6.

Table 4.4. Summary of CM vertical motion for platform (P) trials.
Height and CM vertical rate are shown for the time of impact, and minimum CM height after impact is included. CM height is referencedto the final ankle position, and is shown as an absolute distance and a percentage of the final resting CM height.

	CM Height at Impact			CM rate at Impact		CM Height at Minimum		
Subject	Mean (%)	Mean (cm)	S.E.M (cm)	Mean (m/s)	S.E.M. (m/s)	Mean (%)	Mean (cm)	S.E.M (cm)
djn	102	1.75	0.28	-2.02	0.03	84	-12.75	0.50
aqk	102	1.38	0.18	-1.85	0.03	83	-13.03	0.41
mjg	101	0.83	0.39	-2.20	0.02	81	-15.12	0.45
czl	102	1.35	0.28	-2.11	0.05	82	-14.40	0.44
yak	96	-3.21	0.64	-2.00	0.04	78	-17.14	0.44
ssy	100	0.22	0.26	-1.69	0.05	72	-22.41	0.75
SUBJECTS GROUPED	**101**	**0.41**	**0.21**	**-1.97**	**0.02**	**80**	**-16.01**	**0.38**

Table 4.5. Timing of CM vertical trajectory events.
Time to reach CM minimum and time to recover to within 98% of the final CM height are referenced to the time of impact.

	CM minimum		CM reaches 98%	
Subject	Mean (ms)	S.E.M. (ms)	Mean (ms)	S.E.M. (ms)
djn	149	6	531	30
aqk	147	5	545	18
mjg	167	5	671	22
czl	159	5	495	14
yak	159	6	830	40
ssy	241	8	867	94
SUBJECTS GROUPED	**174**	**4**	**663**	**24**

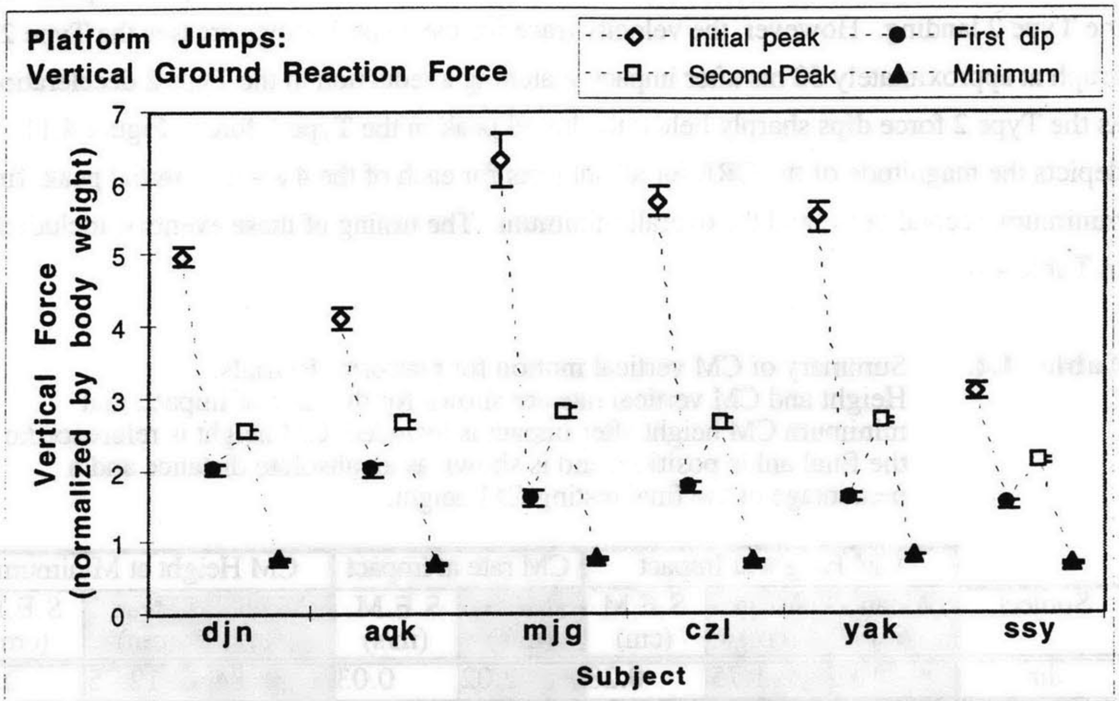

Figure 4.11. Magnitude of vertical ground reaction force for Type 2 jumps. For each subject, the average GRF is shown for four sequential features: (1) peak force; (2) first dip; (3) second peak; and (4) minimum. Error bars indicate ±1 standard error of the mean.

Table 4.6. Timing of vertical ground reaction force events. Means and standard errors for Type 2 jumps.

	Initial Peak		First Dip		Second Peak		Minimum	
Subject	Mean (ms)	S.E.M. (ms)	Mean (ms)	S.E.M. (ms)	Mean (ms)	S.E.M. (ms)	Mean (ms)	S.E.M. (ms)
djn	40	3	76	4	115	6	497	30
aqk	40	1	78	2	119	4	400	20
mjg	32	2	72	4	107	5	445	19
czl	38	2	73	2	115	2	480	25
yak	17	3	46	2	94	2	449	36
ssy	44	2	88	2	144	3	668	28
SUBJECTS GROUPED	**36**	**1**	**73**	**2**	**117**	**2**	**496**	**13**

Figure 4.12 shows the distribution of Type 1 and Type 2 jumps within the jump sequence for all subjects. The great majority (84%) of the jump landings are of Type 2. Most Type 1 landings occur early in the jump sequence, although scattered Type 1 landings are observed later. For all subjects combined, 53% of the Type 1 jumps occur during the baseline jumps, and 70% occur before the first NO-P jump. This means that 47% of the baseline jumps are of Type 1, while only 9% of the remaining jumps are of Type 1. The two jump landing types will be compared more extensively in the modeling and discussion sections.

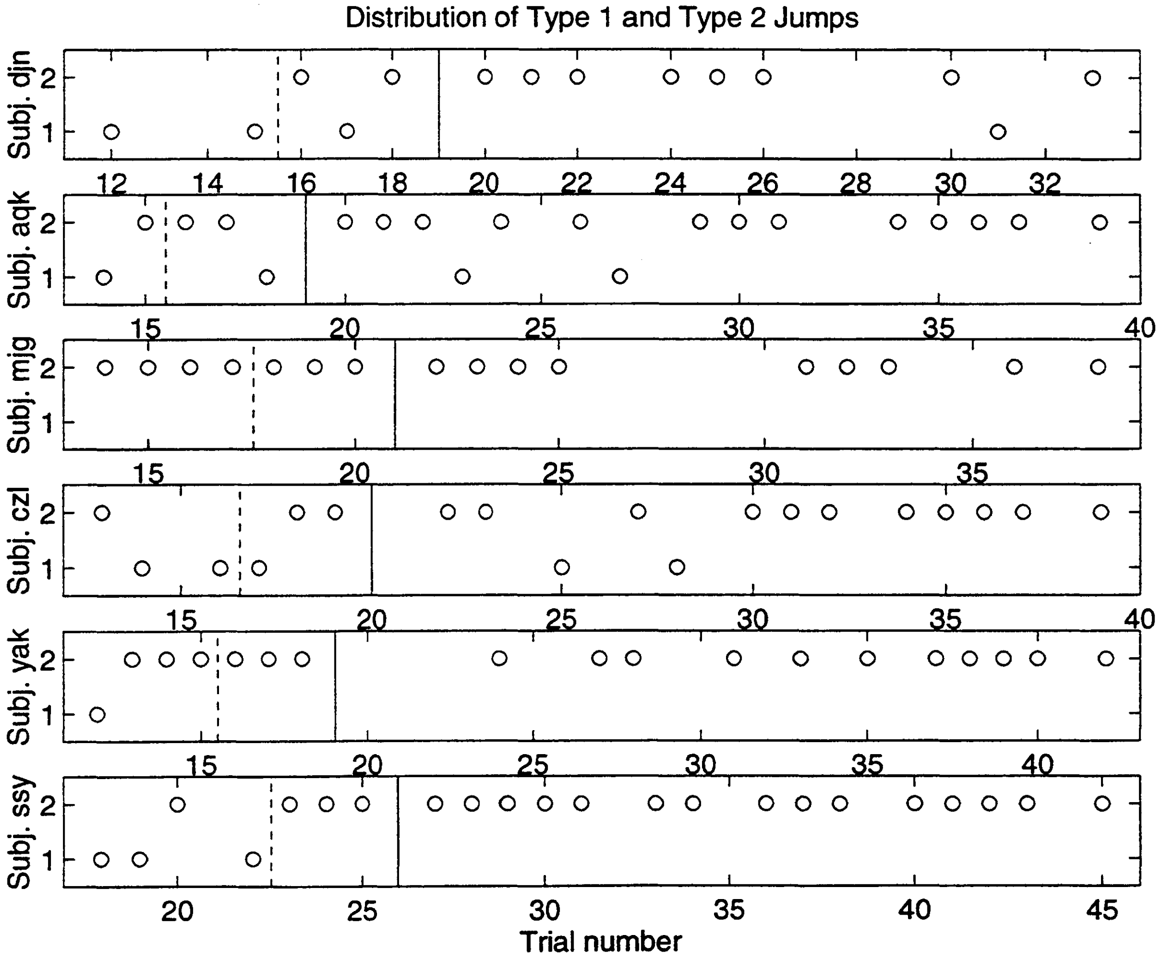

Figure 4.12. Distribution of Type 1 and Type 2 jump landings for all subjects. Jump type is shown by trial number. Dashed vertical line indicates the end of the baseline jumps. Solid vertical line is the first NO-P jump.

4.3.2. No-Platform Jumps

Figure 4.13 shows the leg length and joint angle trajectories for the NO-P jumps for a typical subject (*aqk*), including the free trajectory between nominal and actual impact. The general pattern observed during the time prior to and following the nominal impact, when the subject's feet pass through the paper, can be described in three stages. First, the subject extends the legs during the flight phase of the jump. However, the legs reach peak extension prior to expected impact (actual impact for the P jumps), and approximately 20 ms prior to impact the subject begins to flex the legs. Flexion continues until peak flexion is reached an average of 50 ms following the expected time of impact. In the third stage, re-extension of the limbs is seen, and continues until the subject actually impacts the ground 100 ms after the nominal impact time.

Figure 4.13a show the leg length for *aqk* during this sequence, as measured from the ankle to the body CM. Likewise, Figure 4.13b-d display hip, knee and ankle traces for *aqk* during this time period. The minimum in the leg length corresponds to the peak flexion of the joints. Each of these figures shows the individual traces for each NO-P landing at left, with each trial offset vertically for clarity. The pattern described above is seen consistently in all the landings. In each figure, the individual traces are also superimposed for comparison (top right), and an average trajectory with a confidence interval representing ±1 standard error of the mean is included (bottom right). The ankle traces vanish approximately 30 ms after nominal impact time, as the paper folds up to obscure the foot LED array. Thus, little can be said about the ankle angle after this time, although the first 30 ms appear to indicate a change from plantarflexion to dorsiflexion of the foot, consistent with the results seen for the knee and hip angles.

Figure 4.14a-d show the same ankle-CM length and joint angle data for all of the subjects. In these figures, only average traces for the NO-P trials are included. The NO-P trajectories are aligned with the corresponding averages of the P landing trials. The results for all subjects replicate the pattern seen for *aqk*. A summary of the ankle-CM length and joint angle data is shown for all subjects in Figure 4.15. These results indicate flexion of approximately 10°-15° for the knee and 5° for the hip from the peak extension prior to nominal impact to the maximum flexion during the 100 ms following nominal impact. The ankle results are unreliable, due to missing data points and poor signal quality for the foot array during this time period. Table 4.7 contains data on the timing of the leg extension/flexion pattern during the NO-P jumps for each of the 3 leg angles as well as the ankle-CM length. Part (a) gives the timing of maximum extension prior to impact, while part (b) records the timing of peak flexion following nominal impact.

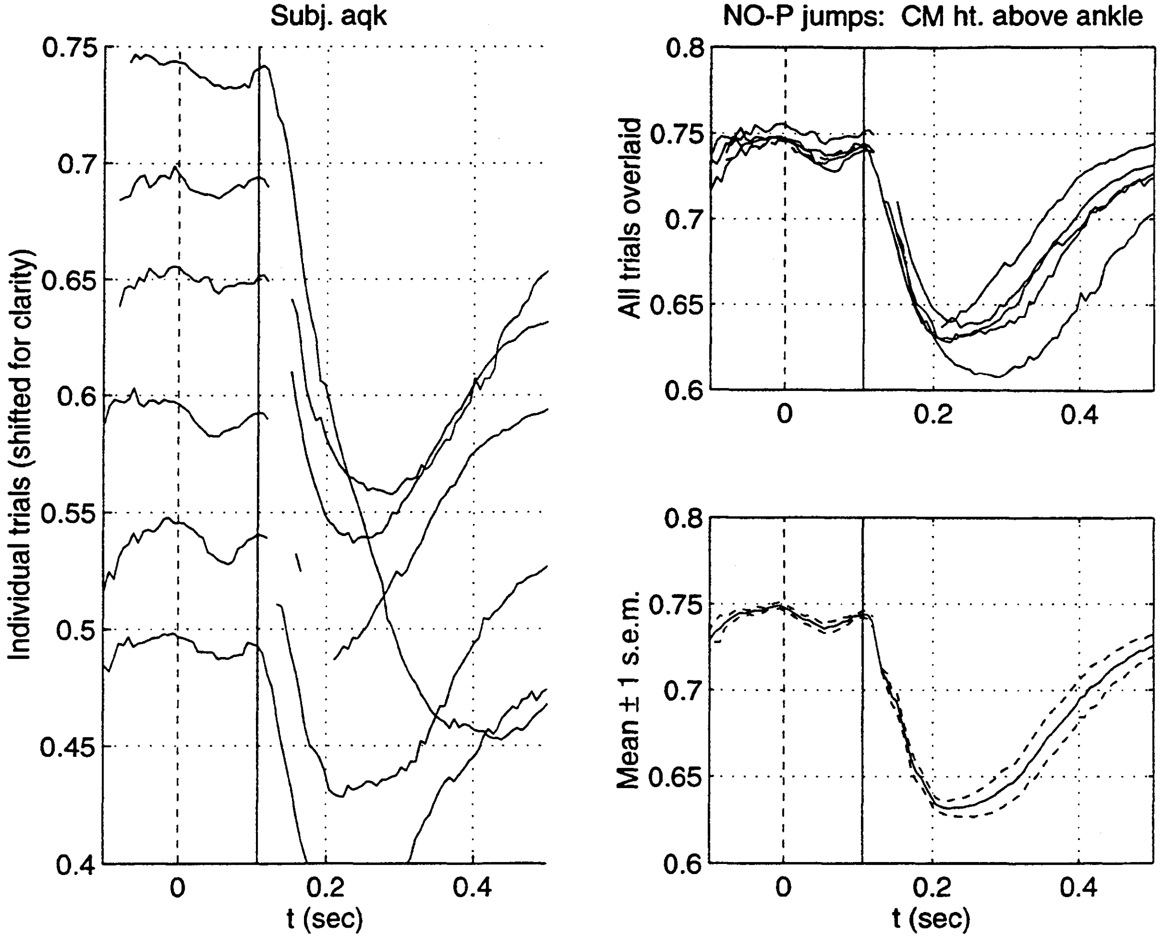

Figure 4.13. Typical NO-P leg length and joint angle trajectories, subject *aqk*.
a. NO-P leg length (m, measured from ankle joint to CM). Nominal impact occurs at t=0; actual impact occurs at solid vertical line. Individual trials are shown aligned at actual impact in raster format (left) and overlaid (upper right). Mean trajectory ±1 standard error shown in lower right.

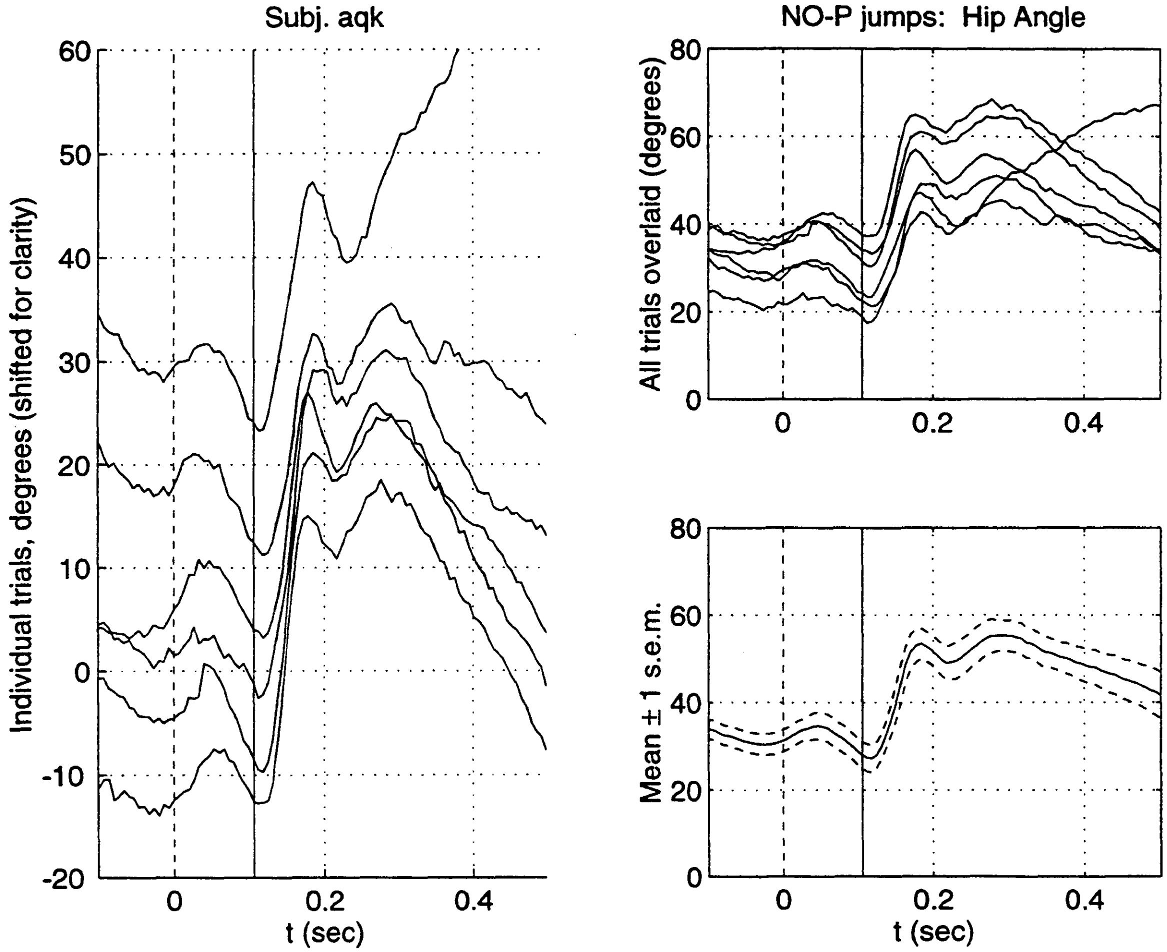

Figure 4.13b. NO-P hip joint angle. Nominal impact occurs at t=0; actual impact occurs at solid vertical line. Individual trials are shown aligned at actual impact in raster format (left) and overlaid (upper right). Mean trajectory ±1 standard error shown in lower right.

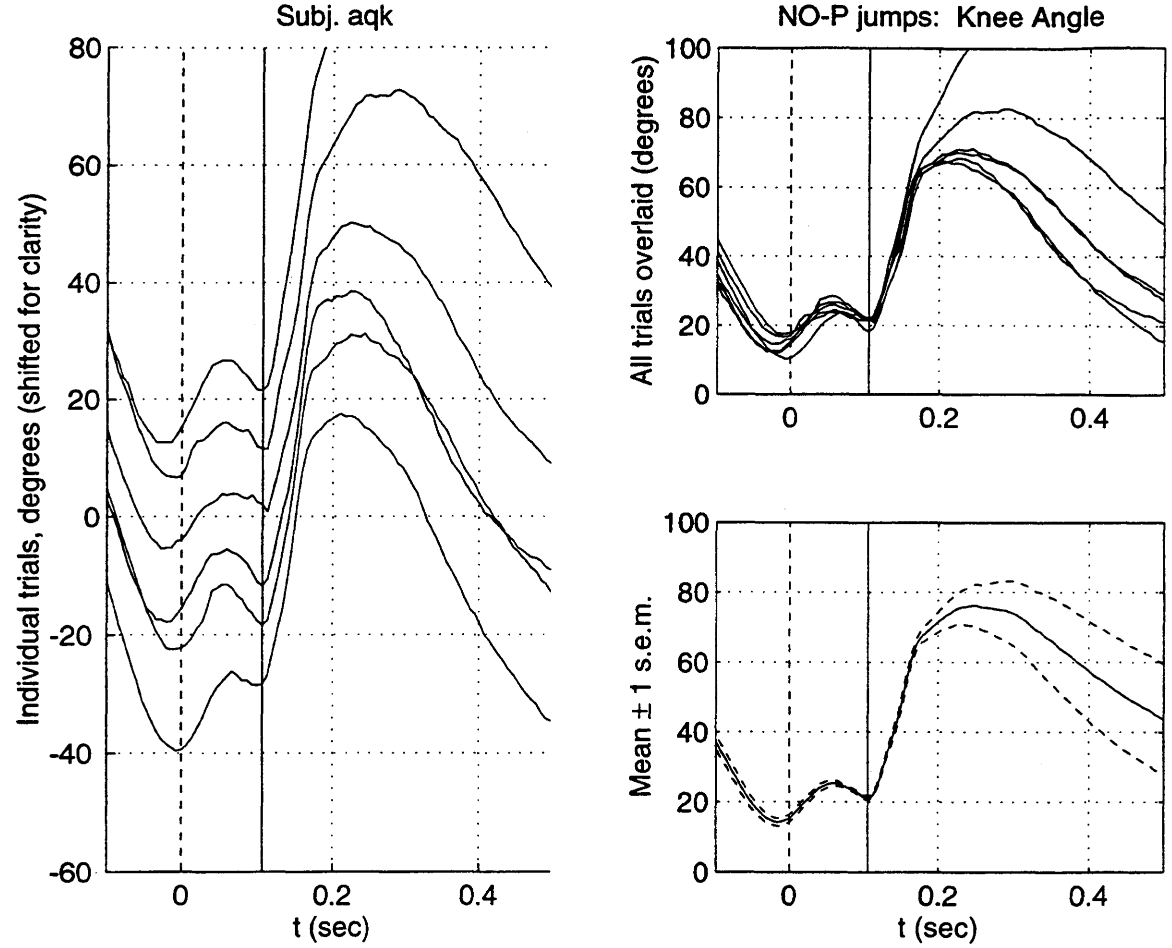

Figure 4.13c. NO-P knee joint angle. Nominal impact occurs at t=0; actual impact occurs at solid vertical line. Individual trials are shown aligned at actual impact in raster format (left) and overlaid (upper right). Mean trajectory ±1 standard error shown in lower right.

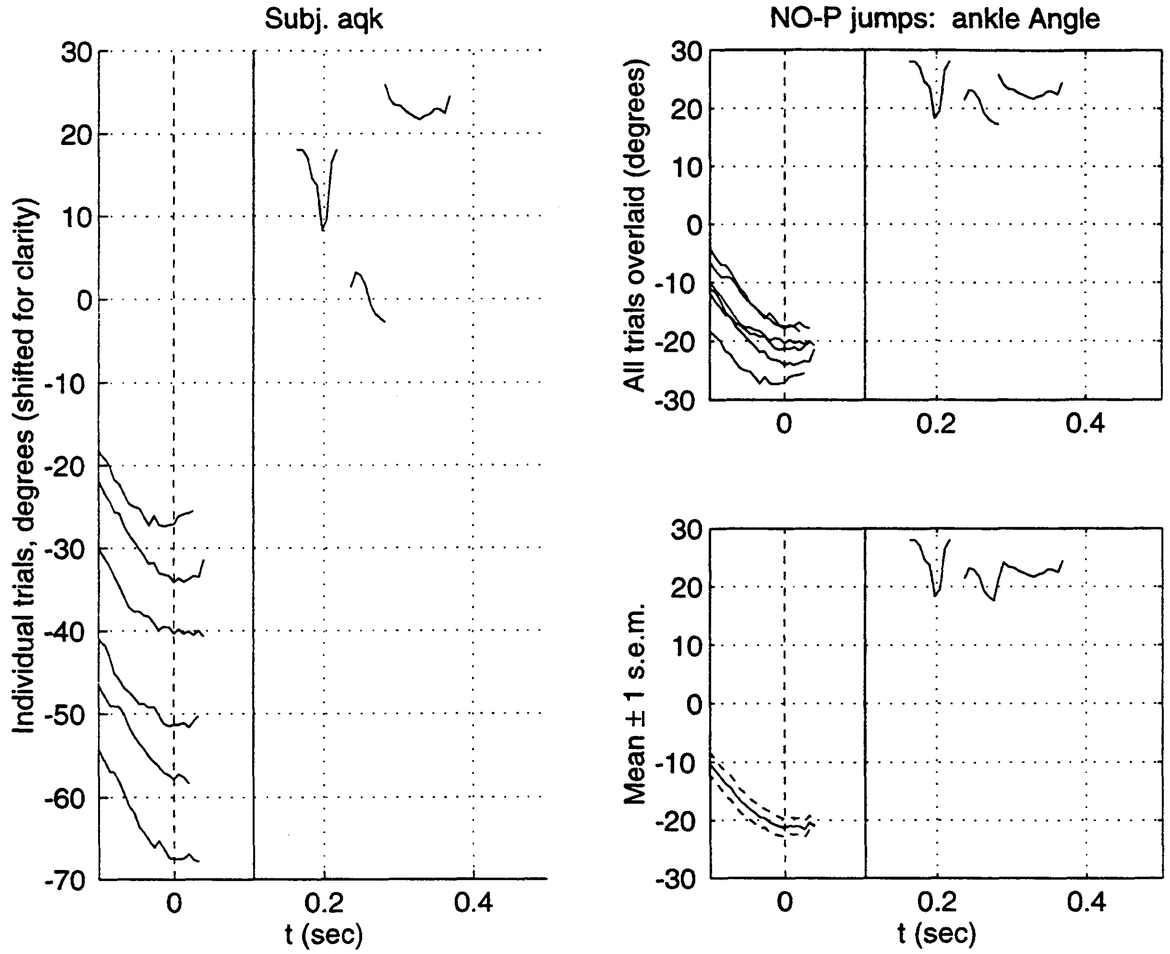

Figure 4.13d. NO-P ankle joint angle. Nominal impact occurs at t=0; actual impact occurs at solid vertical line. Individual trials are shown aligned at actual impact in raster format (left) and overlaid (upper right). Mean trajectory ±1 standard error shown in lower right. Missing regions are due to the paper target folding up and covering the foot arrays.

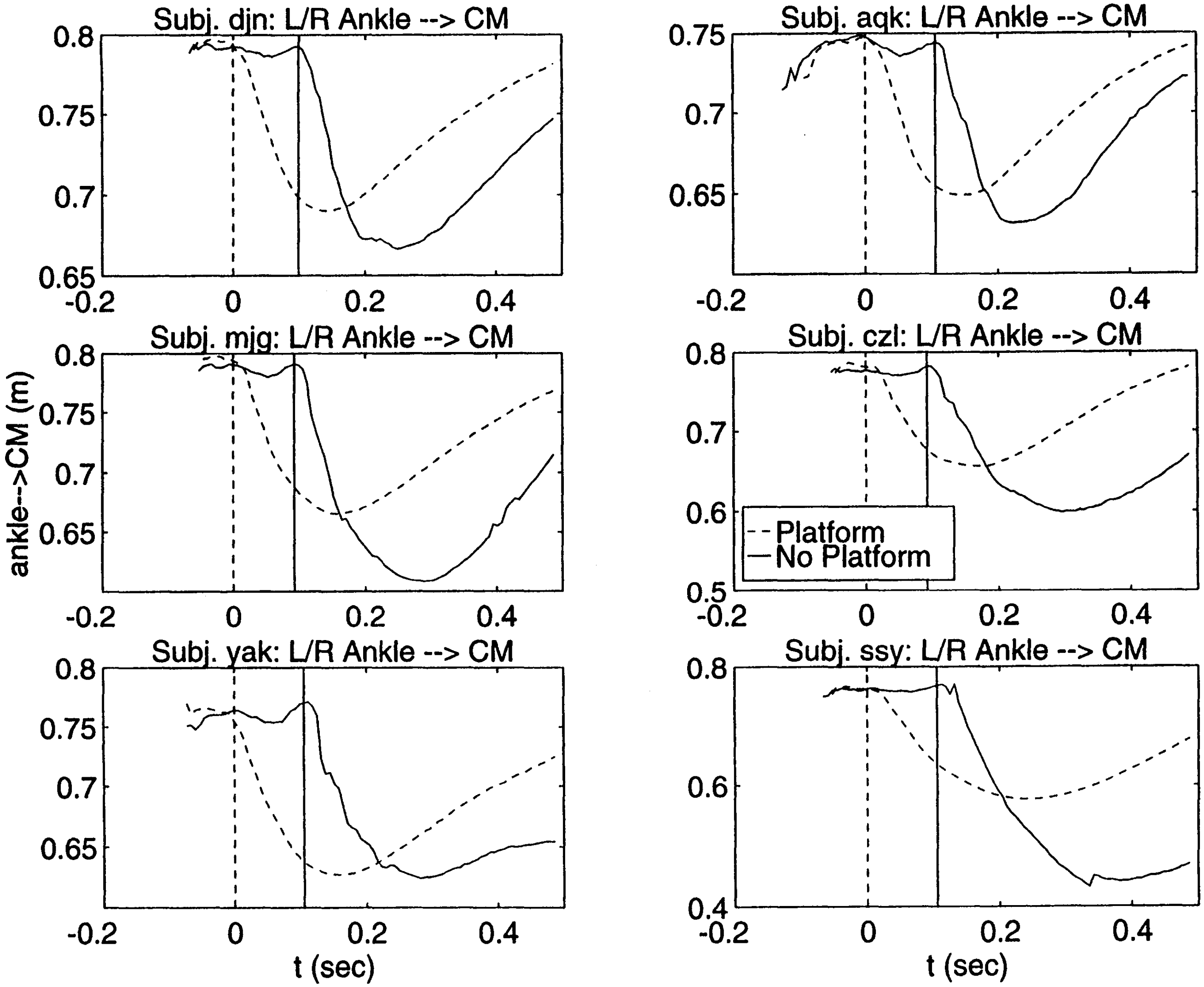

Figure 4.14. Average NO-P and P leg length and joint angle trajectories, all subjects.
a. Leg length (ankle-CM). Nominal impact at t=0 (dashed vertical line); actual impact at solid vertical line.

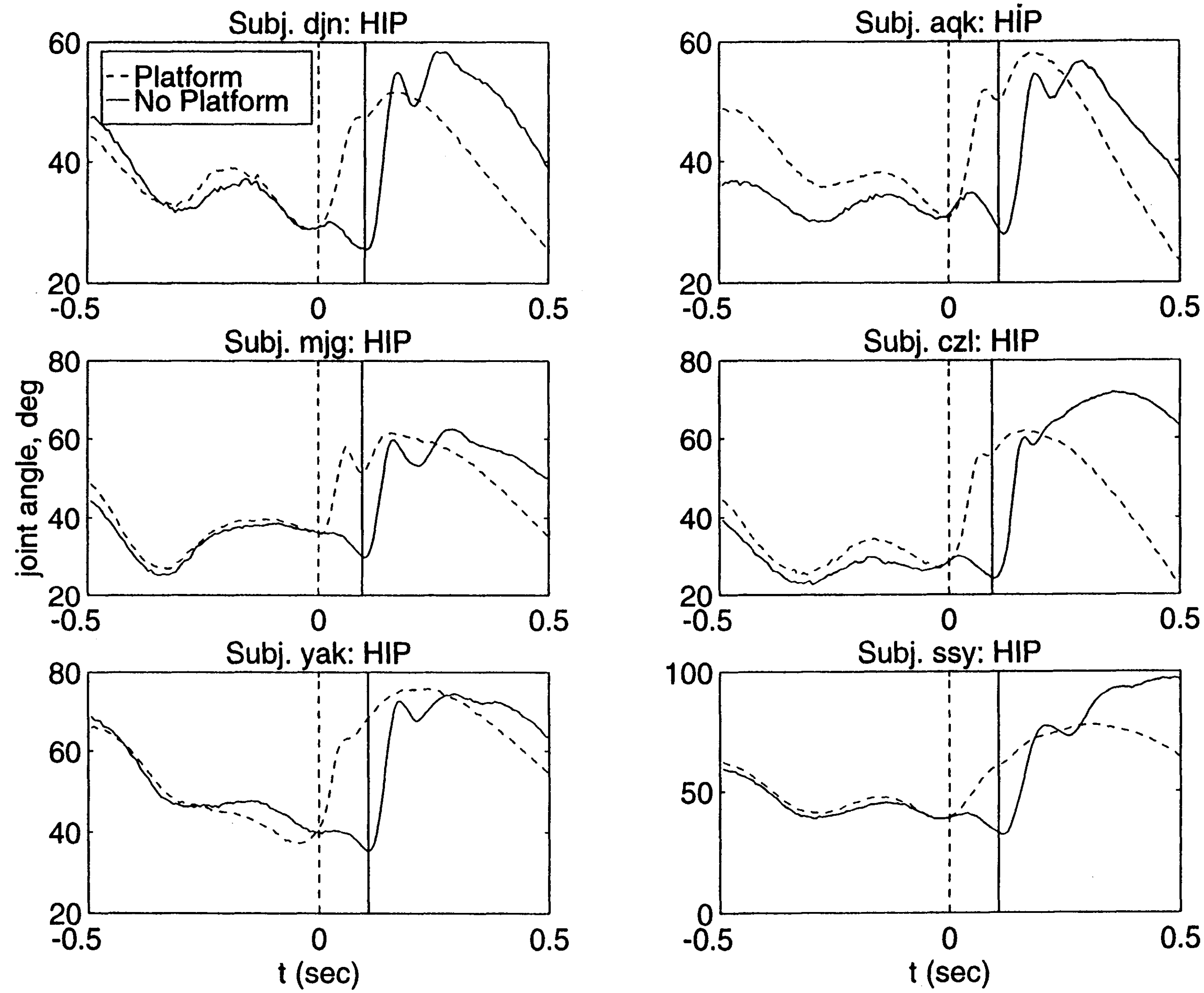

Figure 4.14b. Hip joint angle NO-P and P average trajectories. Nominal impact at t=0 (dashed vertical line); actual impact at solid vertical line.

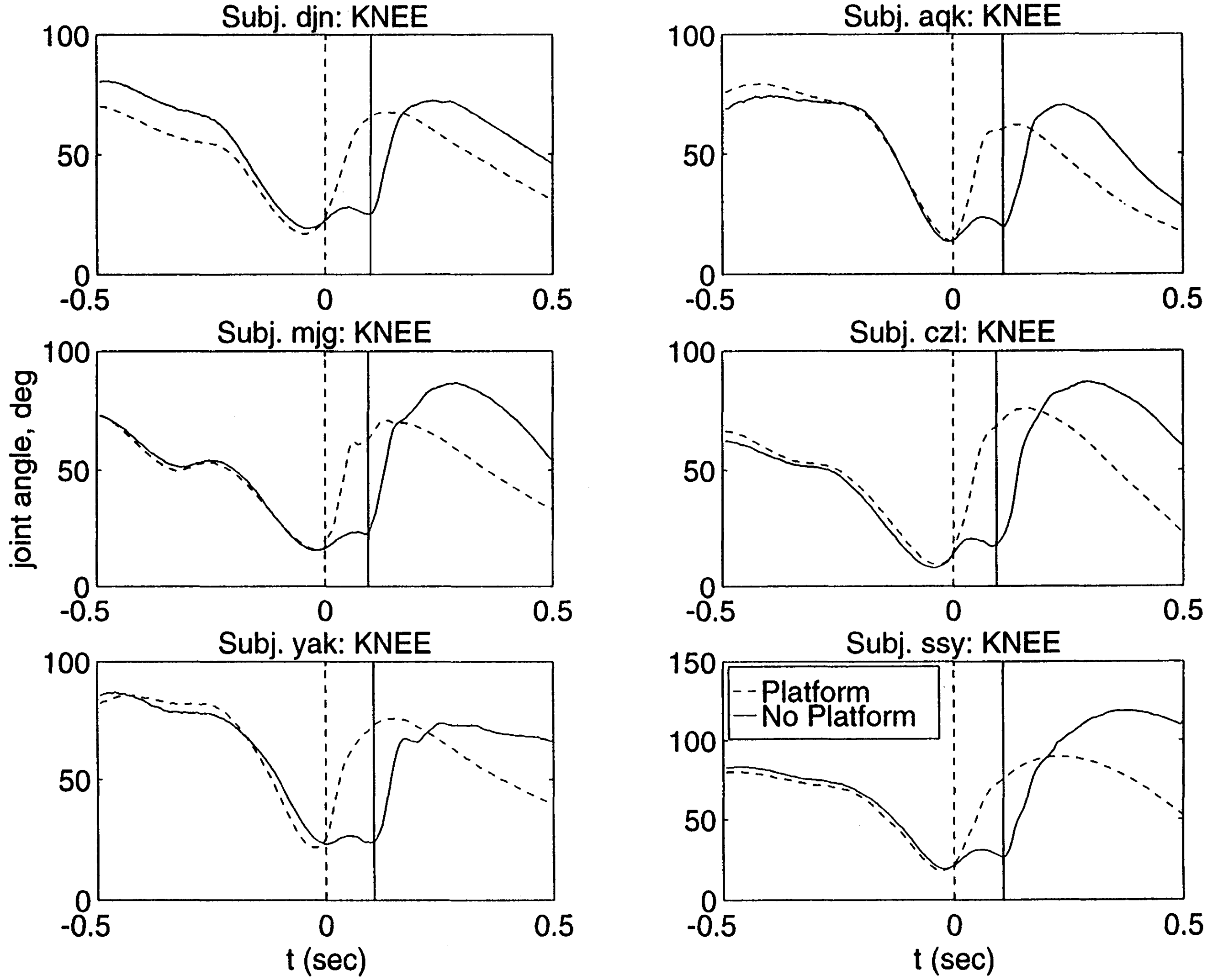

Figure 4.14c. Knee joint angle NO-P and P average trajectories. Nominal impact at t=0 (dashed vertical line); actual impact at solid vertical line.

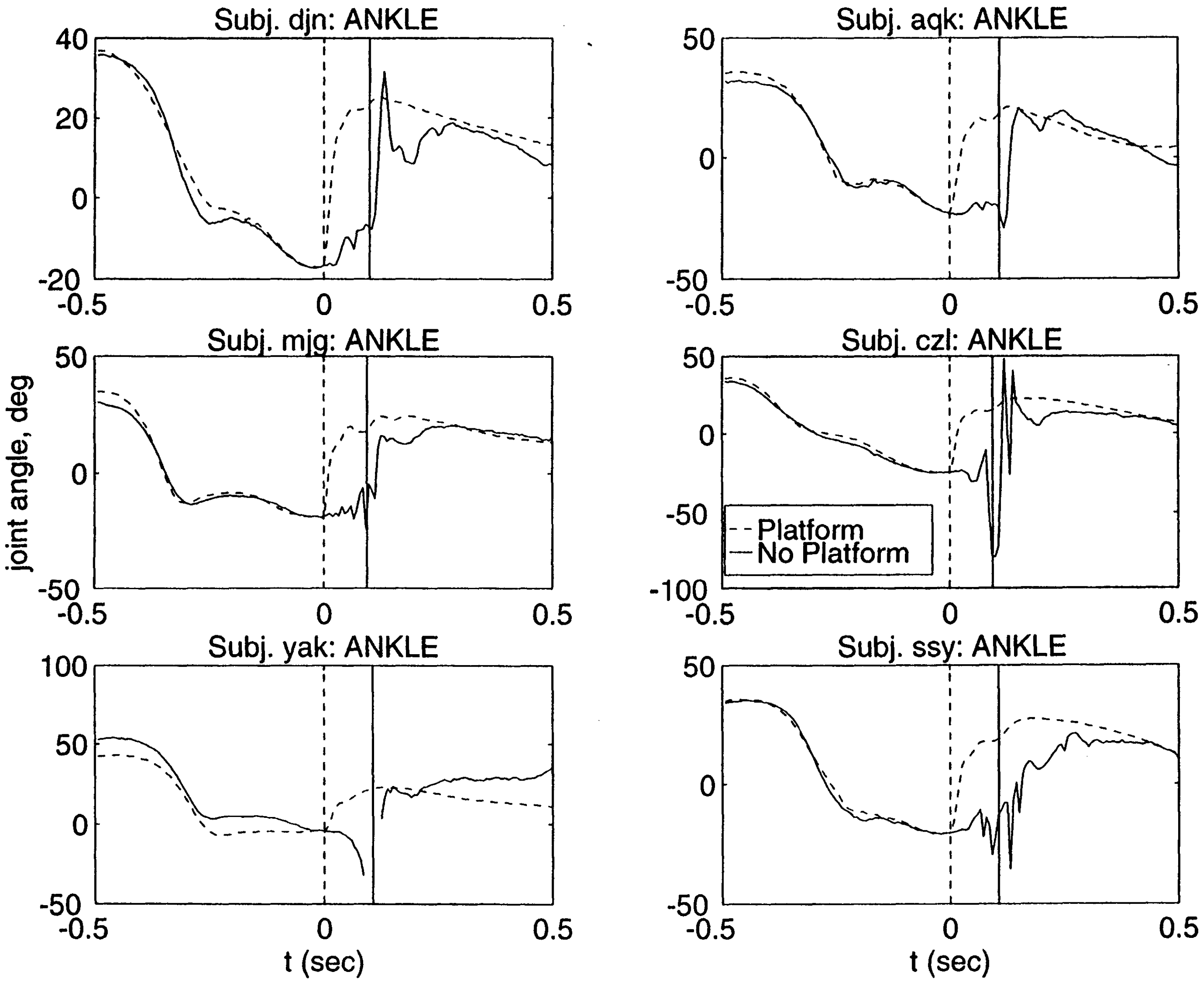

Figure 4.14d. Ankle joint angle NO-P and P average trajectories. Nominal impact at t=0 (dashed vertical line); actual impact at solid vertical line. Noisy and missing segments due to paper target folding up and covering foot arrays.

a. Leg length (ankle-CM)

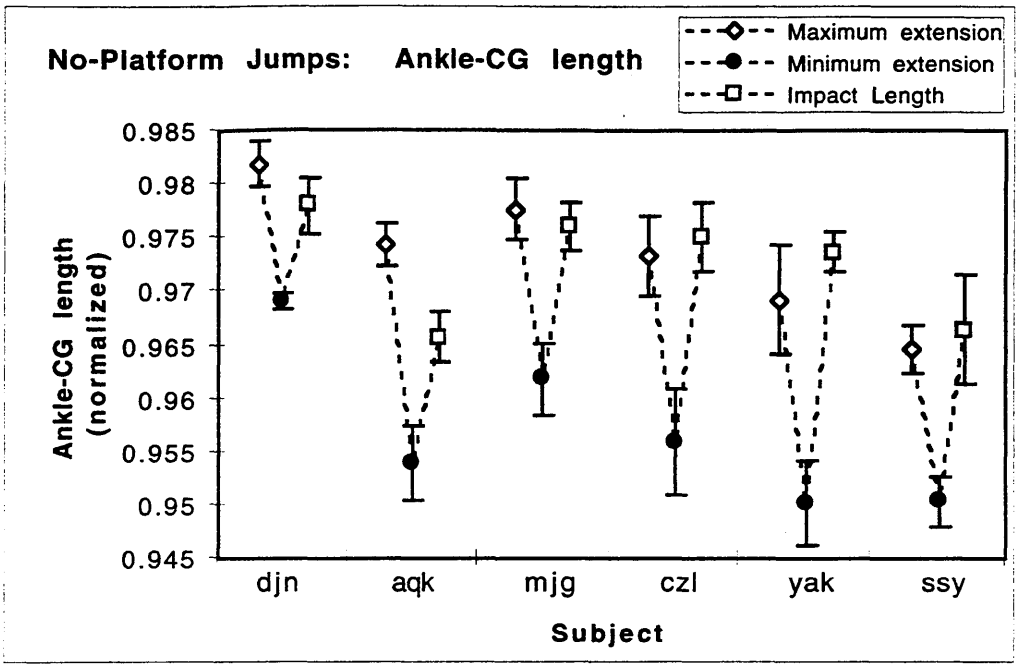

b. Hip angle

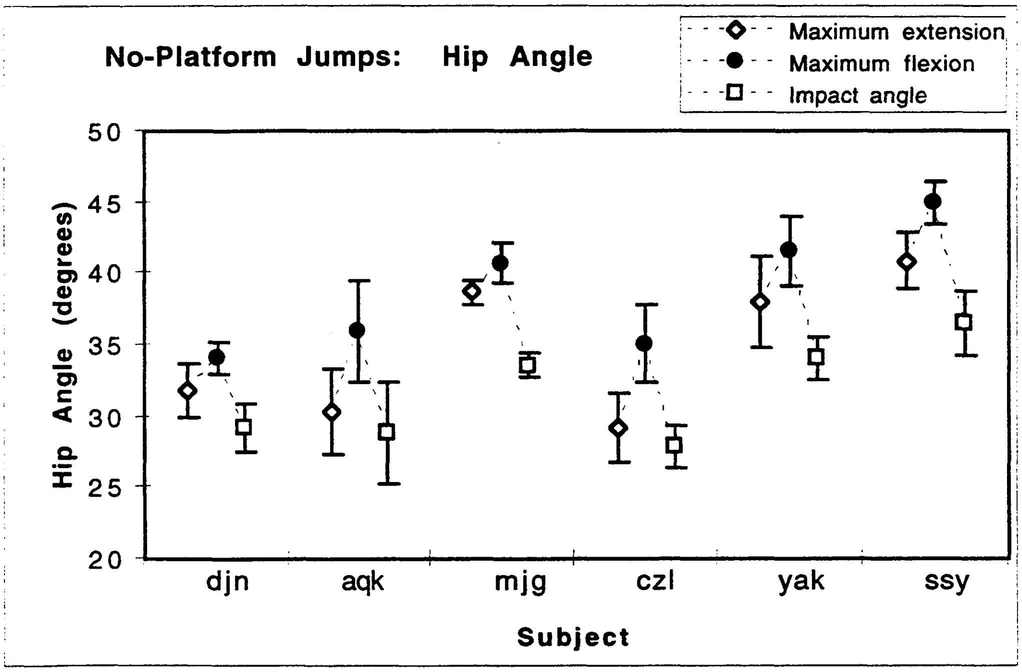

Figure 4.15. NO-P free trajectory leg configuration measurements. Peak pre-impact leg extension, maximum leg flexion between nominal and actual impact, and configuration at impact. (a) Leg length (ankle-CM). (b) Hip angle. Error bars indicate one standard error of the mean.

c. Knee angle

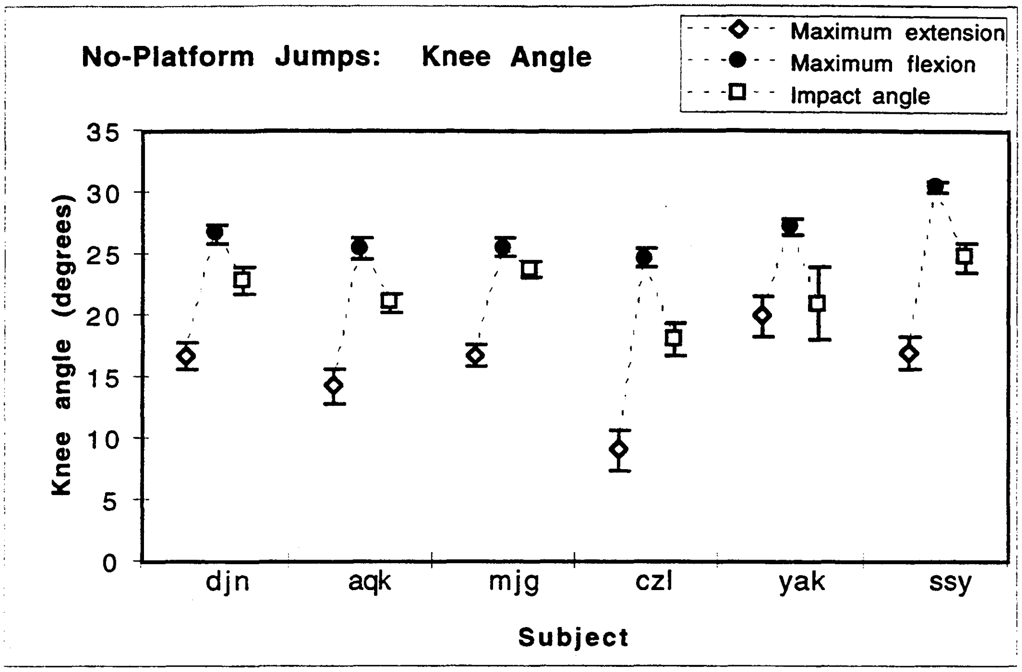

d. Ankle angle

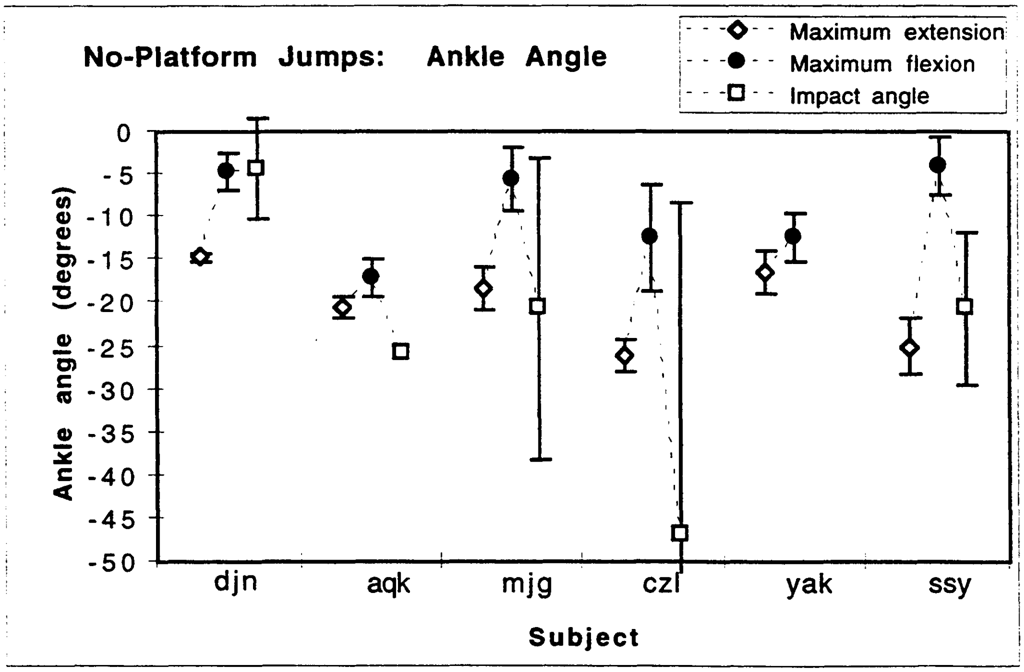

Figure 4.15. NO-P peak pre-impact leg extension, maximum leg flexion between nominal and actual impact, and configuration at impact. (c) Knee angle. (d) Ankle angle. Error bars indicate one standard error of the mean.

Table 4.7. NO-P timing of body configuration events about nominal impact.
(a) Timing of maximum leg extension (negative values indicate that maximum leg extension occurs prior to the nominal impact time.)
(b) Timing of maximum leg flexion following the nominal impact time, but prior to the actual impact.

	Ankle-CM Length		Ankle Angle		Knee Angle		Hip Angle	
Subject	Mean (ms)	S.E.M. (ms)	Mean (ms)	S.E.M. (ms)	Mean (ms)	S.E.M. (ms)	Mean (ms)	S.E.M. (ms)
djn	-16	12	-10	12	-33	10	-18	4
aqk	-18	10	14	6	-14	4	-29	8
mjg	-22	7	-39	36	-23	4	-23	20
czl	-16	14	18	15	-45	5	-50	9
yak	-14	10	-36	40	-1	8	-13	7
ssy	-12	8	-18	40	-16	4	-13	7
SUBJECTS GROUPED	**-17**	**4**	**-13**	**12**	**-22**	**3**	**-25**	**5**

a. Time of Maximum Leg Extension Prior to Nominal Impact

	Ankle-CM Length		Ankle Angle		Knee Angle		Hip Angle	
Subject	Mean (ms)	S.E.M. (ms)	Mean (ms)	S.E.M. (ms)	Mean (ms)	S.E.M. (ms)	Mean (ms)	S.E.M. (ms)
djn	39	11	61	15	53	7	18	6
aqk	55	3	33	7	59	2	36	5
mjg	54	4	55	11	70	7	23	7
czl	52	7	50	13	45	8	30	7
yak	57	4	26	6	54	9	26	9
ssy	46	10	64	11	57	6	27	9
SUBJECTS GROUPED	**51**	**3**	**48**	**5**	**56**	**3**	**27**	**3**

b. Time of Maximum Leg Flexion Following Nominal Impact

4.3.3. False Platform Electromyograms

The EMG results for 4 muscles in the right leg (gastrocnemius, tibialis anterior, hamstrings, and quadriceps) are presented in this section. The pre-impact timing of activity in the gastrocnemius and tibialis anterior is described. The activity in all four muscles in the time period following nominal impact is compared for the P and NO-P jumps.

4.3.3.1. Pre-Impact EMG Timing

Figure 4.16 shows the patterns of activation for the four right leg muscles examined (gastrocnemius, tibialis anterior, hamstrings and quadriceps) for a typical P jump by subject *czl*. All four muscles are activated prior to impact in all subjects. The timing of EMG activity onset prior to impact in the gastrocnemius is shown in Figure 4.17. The gastrocnemius onset timing is considerably different across subjects, varying between approximately 130 and 300 ms prior to impact. Since the flight phase of the jump is generally less than 300 ms, this indicates that the gastrocnemius is continually active through most or all of the flight phase in subjects *djn, aqk, czl.* Figure 4.18 gives a similar presentation of the pre-impact EMG onset times for the tibialis anterior (TA) muscle. The TA activity begins later than the gastrocnemius activity, and average pre-impact onset times for the TA range from 54 to 113 ms.

Some trends are noted in the pre-impact EMG onset timing. First, the onset in the muscles appears to occur earlier for the first few trials. For this reason, the onset times for the baseline jumps are not included in the computation of the means and standard deviations. Also, the mean and standard deviation calculations exclude the NO-P trials, permitting comparison of the EMG timing for the P and NO-P cases. Because the EMG onsets are presumably timed to the expected moment of impact [McKinley and Smith, 1983; Dyhre-Poulsen and Laursen, 1984], the EMG onset may be delayed in the NO-P trials if the subject expects that the landing platform is missing. For subject *yak*, TA onset in two NO-P trials is delayed past one standard deviation following the average P onset time. This is also true for the TA in one NO-P jump for subject *ssy*. In general, however, the data show that the NO-P onsets occur earlier than one standard deviation past the mean P onset time, and indicate that the subjects were not able to anticipate the NO-P trials.

The onset timing for the P jumps that immediately follow NO-P jumps is also of interest, as the subjects' performance may be influenced by the previous NO-P jump. The TA onset times for subjects *djn*, *czl*, and *ssy* indicate that the beginning of activity is delayed for some of the jumps after NO-P trials. The same pattern is noted for the gastrocnemius onset in subject *ssy*.

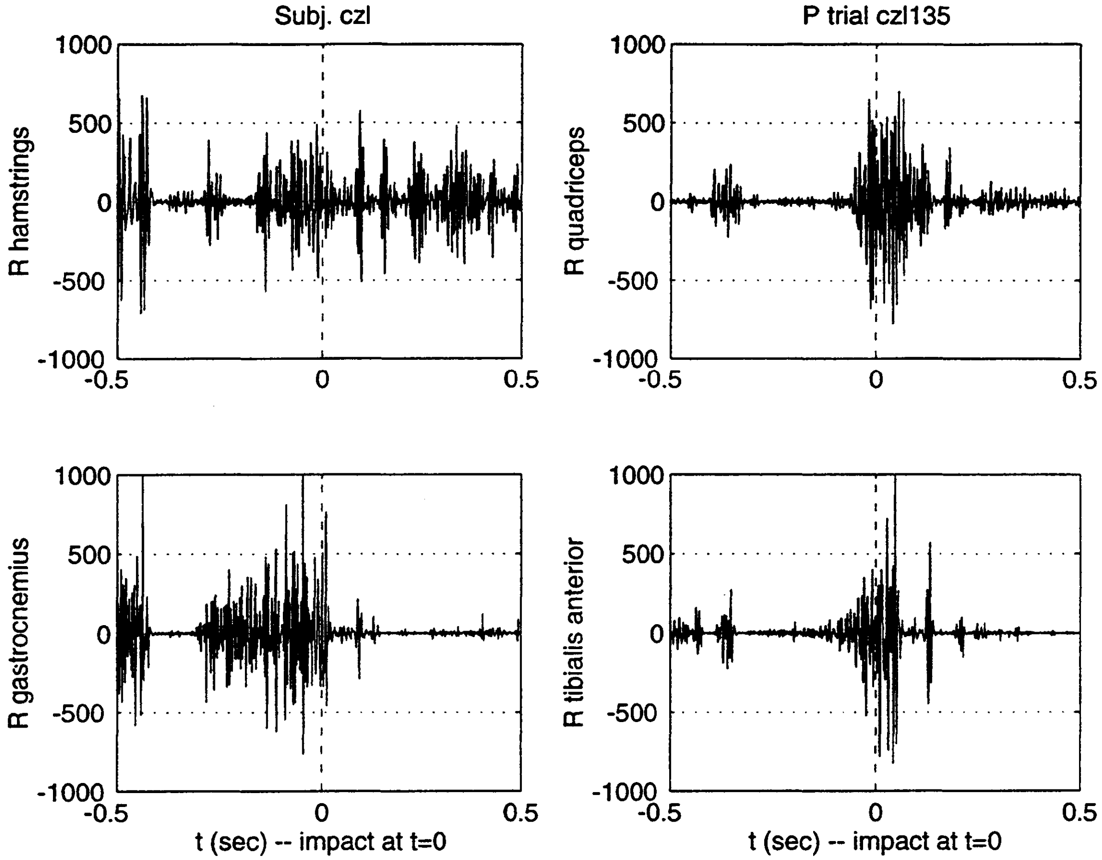

Figure 4.16. Typical P jump leg muscle EMG patterns
Raw EMG data for hamstrings, quadriceps, gastrocnemius and tibialis anterior. Impact occurs at t=0 (dashed vertical line).

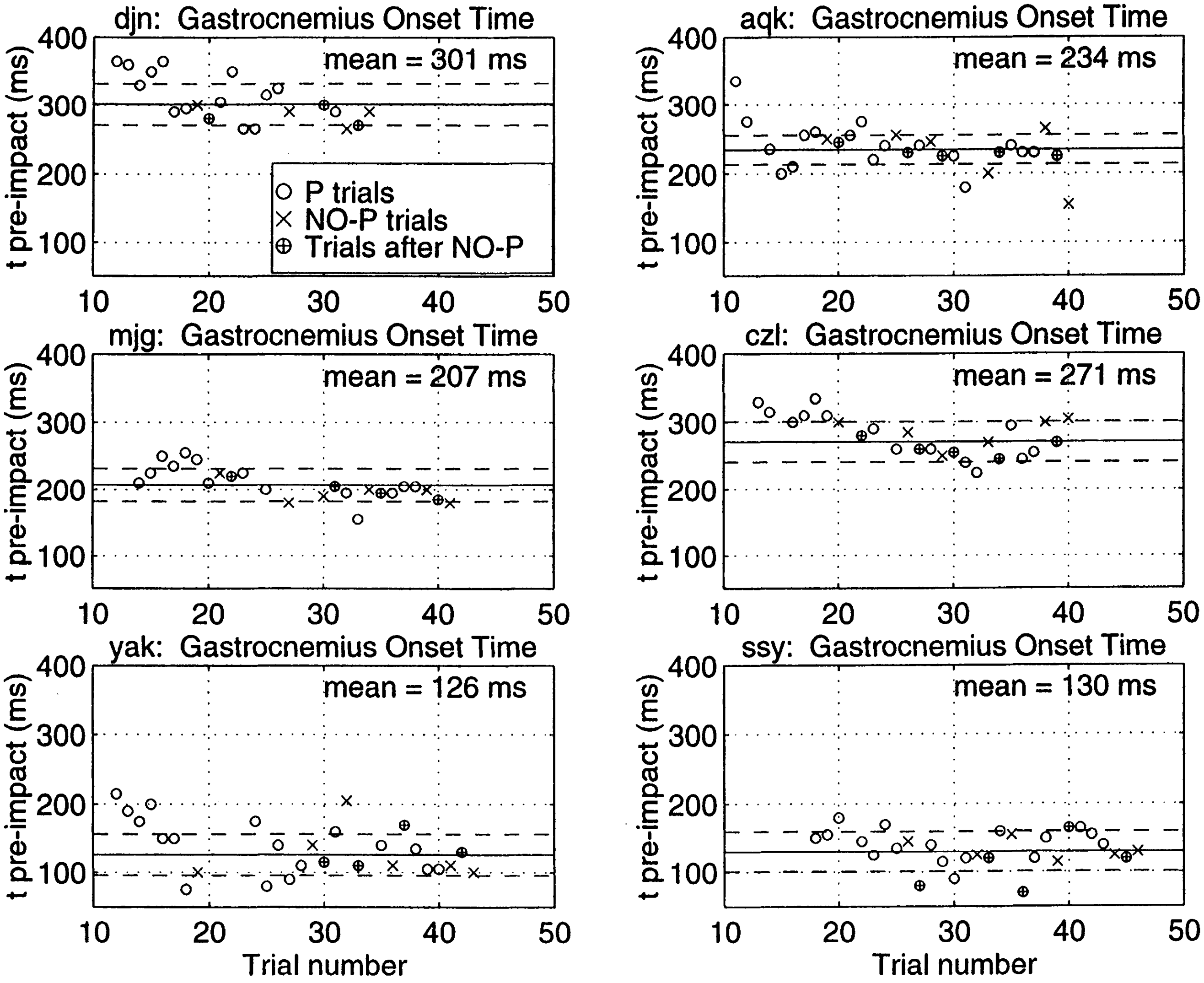

Figure 4.17. Gastrocnemius onset time prior to impact, all subjects.
Mean (solid line) ±1 standard deviation (dashed lines) shown for P jumps.

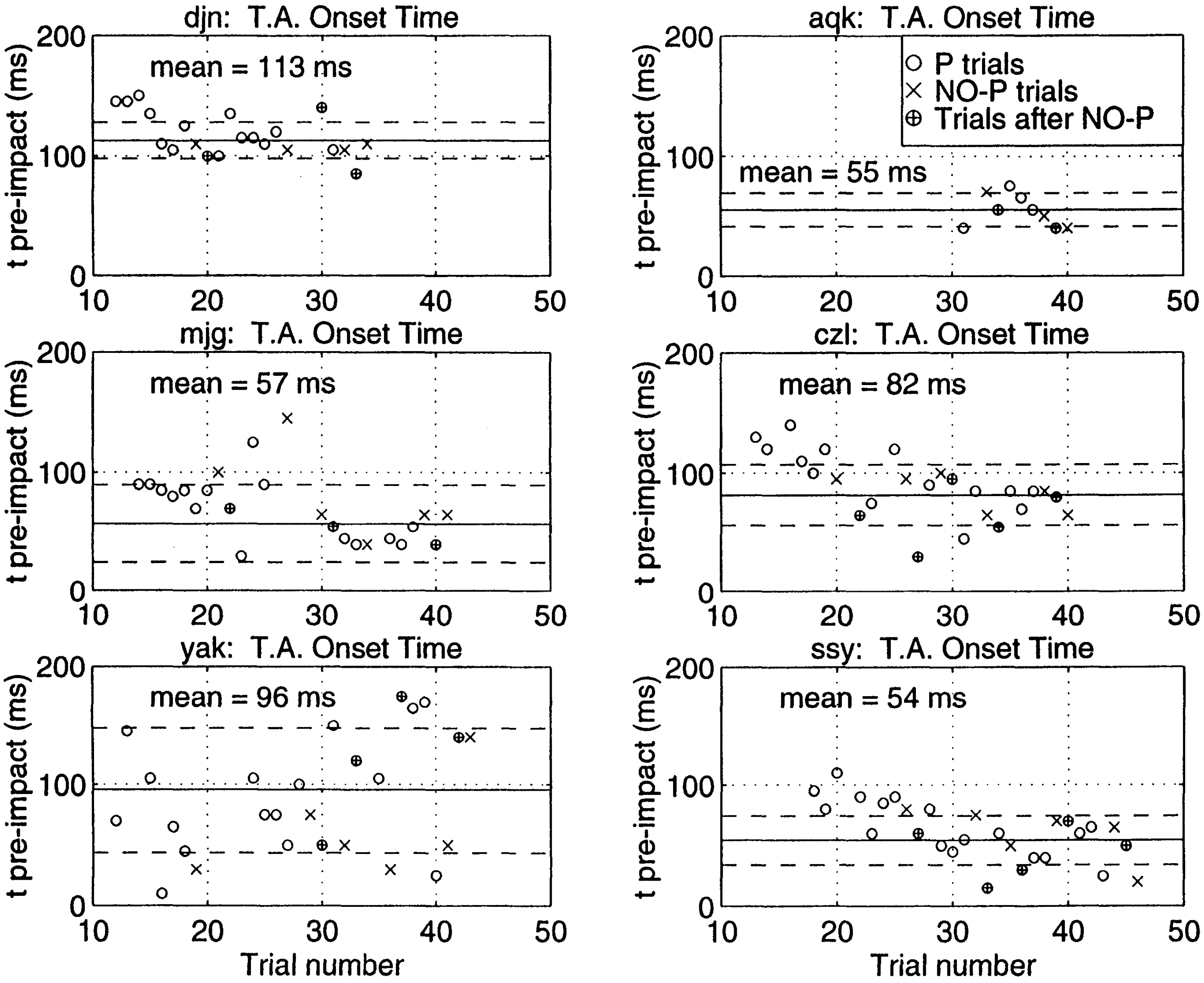

Figure 4.18. Tibialis anterior onset time prior to impact, all subjects. Mean (solid line) ±1 standard deviation (dashed lines) shown for P jumps.

4.3.3.2. Comparison of P and NO-P EMG after Nominal Impact

Figure 4.19 through Figure 4.22 show superimposed ensemble averages of the RMS EMG data for the P and NO-P trials. Generally, the P and NO-P data match well prior to the nominal impact time. However, in the 100 ms following nominal impact (prior to the actual impact for the NO-P jumps) differences are observed between the P and NO-P jumps.

In the gastrocnemius (Figure 4.19), the EMG activity in the P jumps is generally quite low during the period following impact, in contrast to the substantial activation prior to impact. In subjects *djn*, *mjg*, *yak* and *aqk*, a sharp peak in the gastrocnemius signal is seen in the first 20 ms following impact in the P jumps. Because this peak is absent in the NO-P jumps, it it is believed to result from high frequency remnants of the movement artifact associated with impact. In the NO-P jumps, the activation of the gastrocnemius in the 100 ms after nominal impact is considerably higher than the activity seen during the same interval in the P jumps. This heightened gastrocnemius activity is observed in all subjects.

A comparable result is obtained for the hamstrings during the period following nominal impact (Figure 4.20). All subjects show elevated EMG activity in the hamstrings for the NO-P trials when compared to the post-impact interval in the P jumps. The ensemble average comparisons for the TA and quadriceps are shown in Figure 4.21 and Figure 4.22 respectively. Although some individual differences are observed between the P and NO-P jumps in some subjects, no consistent patterns are readily apparent in these muscles.

In order to quantify the extent of the difference between the EMG in P and NO-P jumps after nominal impact, the RMS activity is integrated over the time period between P impact (nominal impact for the NO-P trials) and the time of actual impact for the NO-P trials. The integration period is started 35 ms after P impact to avoid including the effects believed to be associated with impact motion artifact.

The results for gastrocnemius and hamstrings are shown at the top of Figure 4.23. In the gastrocnemius, the integrated activity is 2.5 - 7 times greater in the NO-P jumps than in the P jumps. The difference is significant for all 6 subjects (Student's *t*-test). The results for the hamstrings are comparable to the gastrocnemius data. All 6 subjects exhibit statistically significant increases in the NO-P hamstring activity compared to the P jumps. The bottom of Figure 4.23 presents integrated EMG results for the TA and quadriceps. The trends for the anterior leg muscles are less consistent than the posterior muscle results.

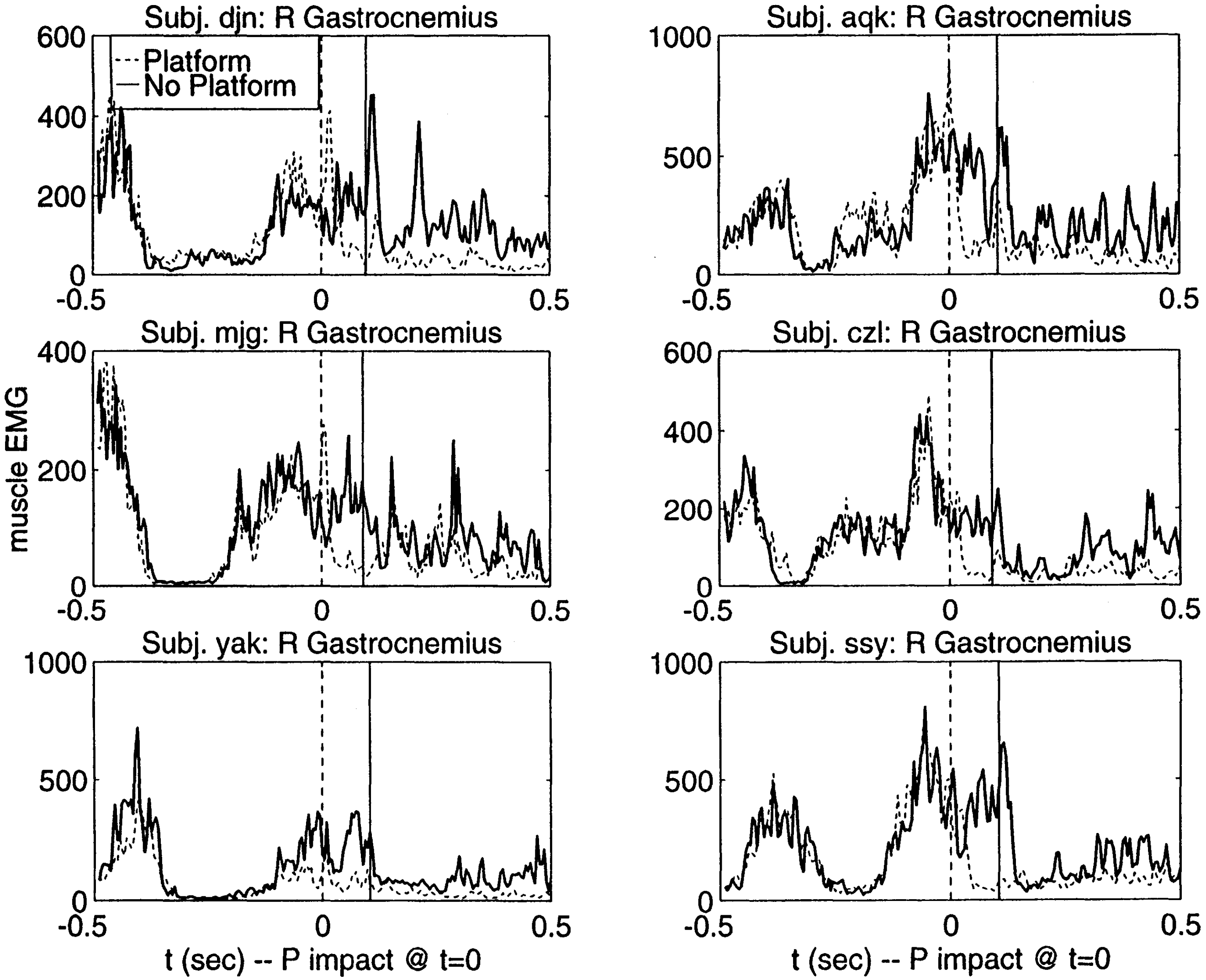

Figure 4.19. Average gastrocnemius P and NO-P activation, all subjects.
Ensemble averages of P and NO-P RMS activation. P impact at t=0; actual NO-P impact at solid vertical line.

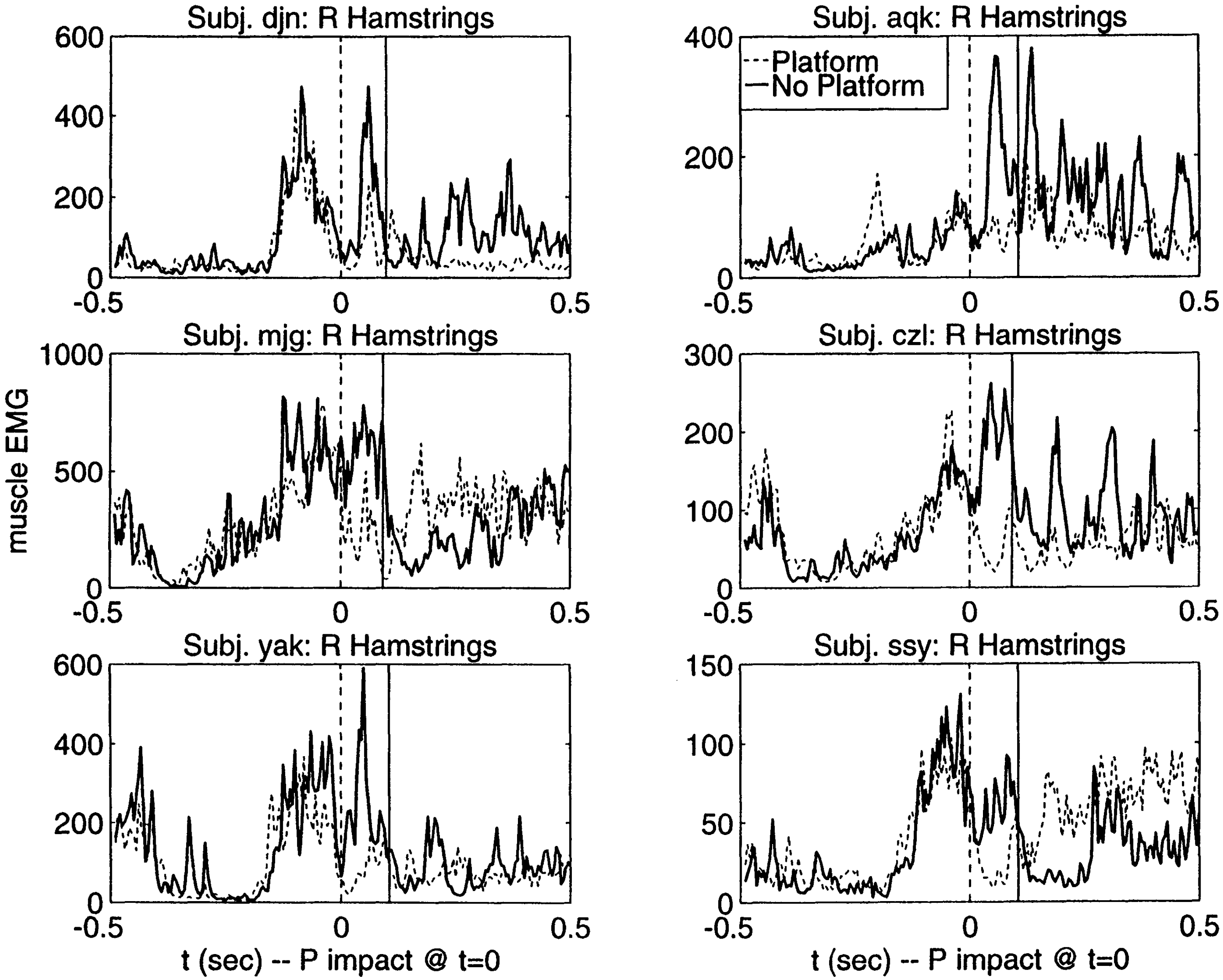

Figure 4.20. Average hamstrings P and NO-P activation, all subjects.
Ensemble averages of P and NO-P RMS activation. P impact at t=0; actual NO-P impact at solid vertical line.

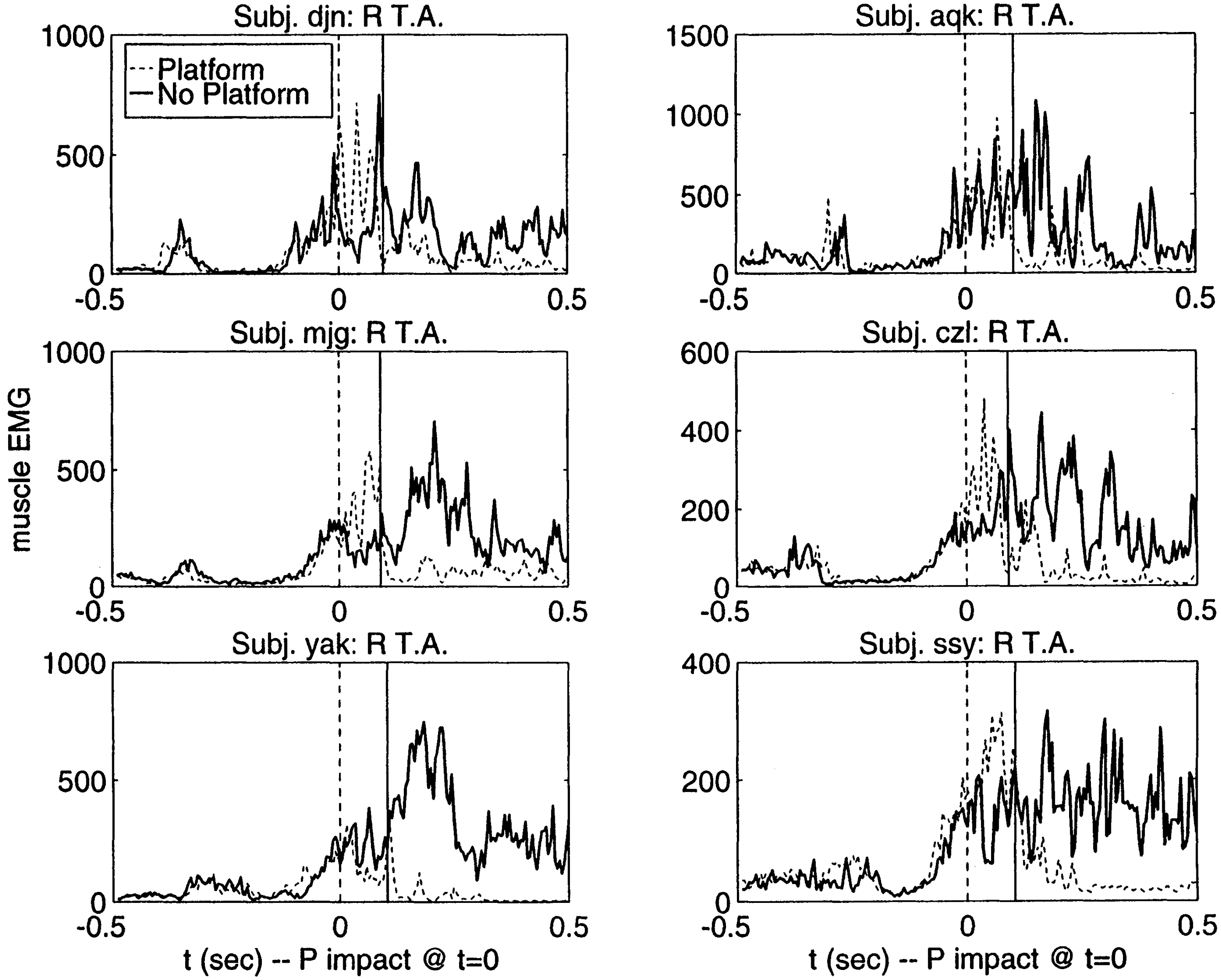

Figure 4.21. Average tibialis anterior P and NO-P activation, all subjects.
Ensemble averages of P and NO-P RMS activation. P impact at t=0; actual NO-P impact at solid vertical line.

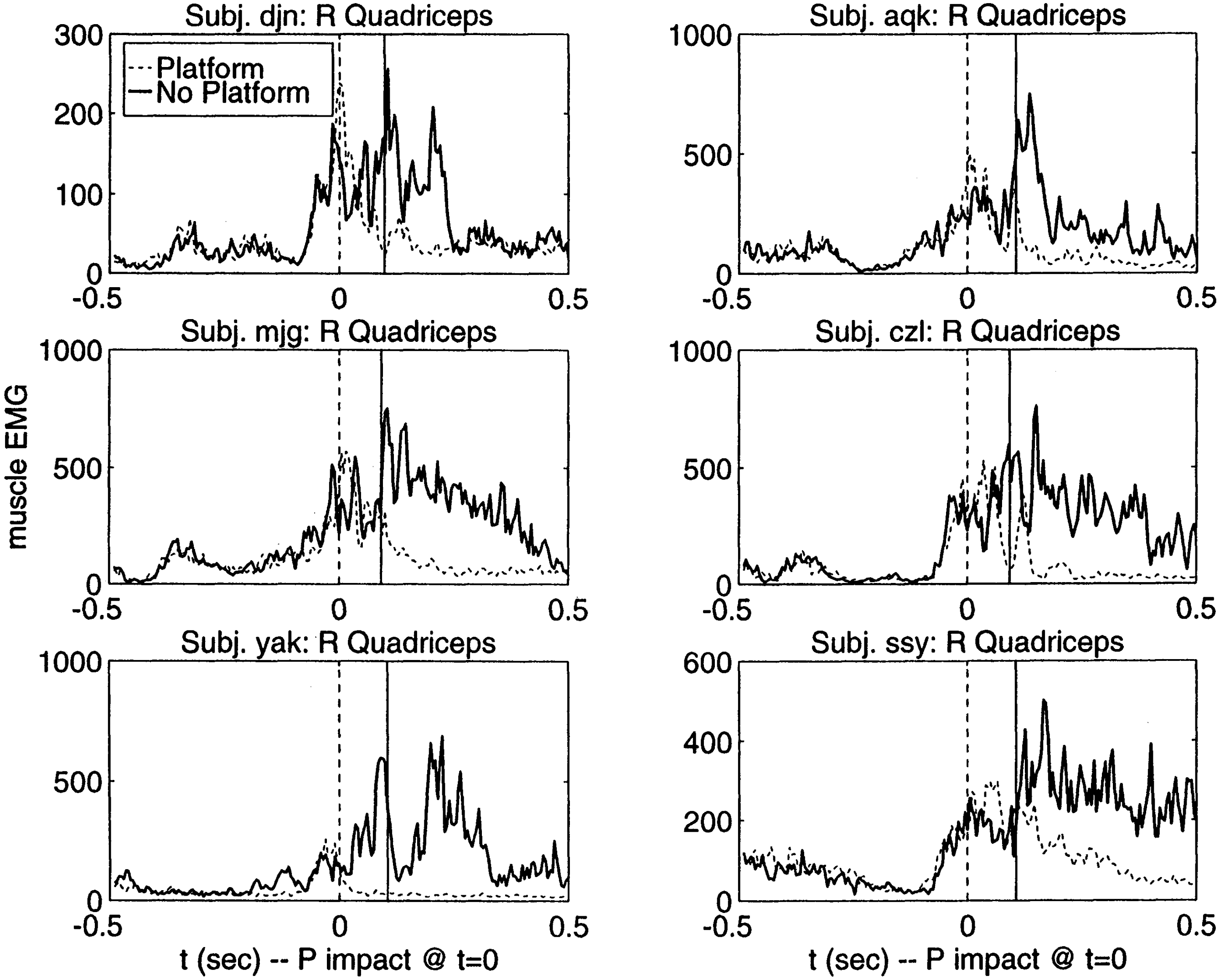

Figure 4.22. Average quadriceps P and NO-P activation, all subjects.
Ensemble averages of P and NO-P RMS activation. P impact at t=0; actual NO-P impact at solid vertical line.

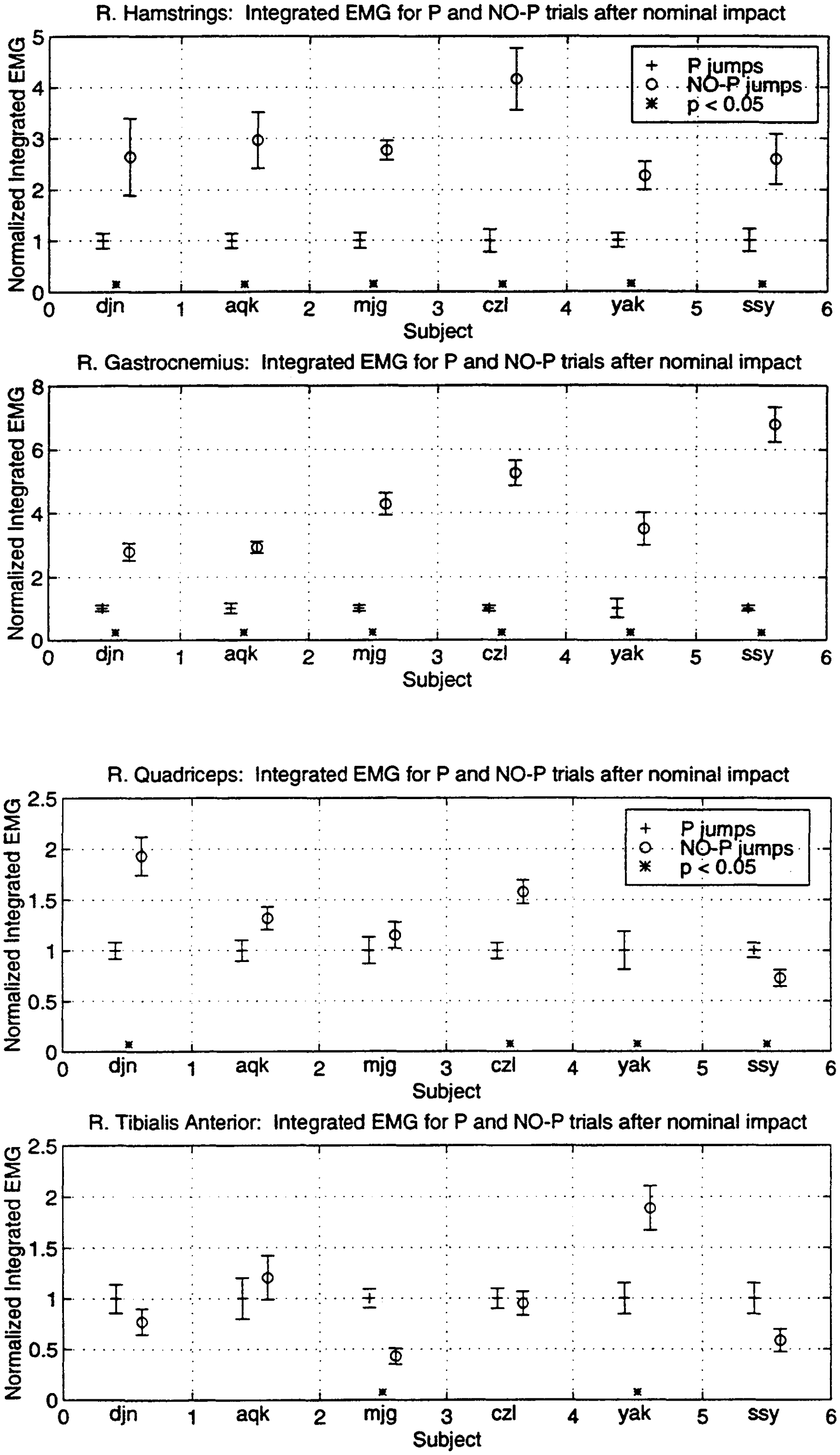

Figure 4.23. P and NO-P integrated EMG for leg muscles.
Activity integrated in period between nominal NO-P impact (P impact time) and actual NO-P impact. "*" indicates significant difference between P and NO-P using *t*-test.

Average TA activity is reduced in the NO-P trials compared to the P-jumps for 4 of the 6 subjects, but the difference is only significant for subject *mjg*. In contrast, subject *yak* exhibits a significant increase in TA activity during this time frame for the NO-P jumps. The results for *aqk* are questionable, because TA data is missing for most of the jumps. For the quadriceps, 3 of 6 subjects (*djn*, *czl*, *yak*) demonstrate significantly increased quadriceps activity in the NO-P jumps, while subject *ssy* shows a significant decrease in integrated EMG for the NO-P jumps when compared to the P results.

The NO-P activity in the gastrocnemius and hamstrings often appears burst-like in the 100 ms following nominal impact (Figure 4.24). For trials with distinguishable bursts in these muscles, the burst latency after nominal impact is determined. The results are shown for the gastrocnemius and hamstrings in Figure 4.25. For both muscles, the bursts occur an average of approximately 38 ms following the nominal impact time.

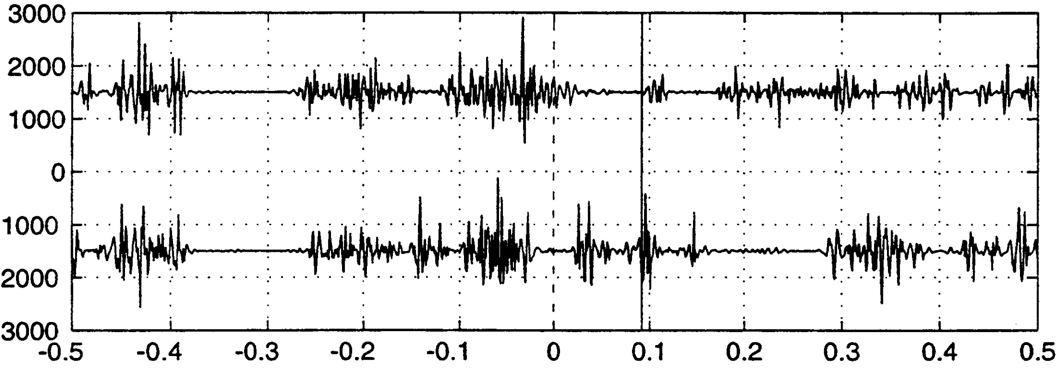
a. R. Gastrocnemius: P (upper) and NO-P (lower) -- Subj. czl

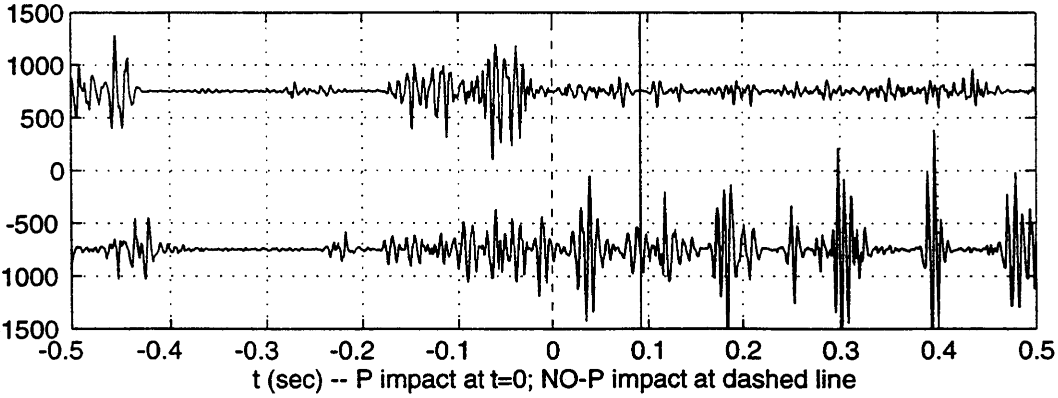
b. R. Hamstrings: P (upper) and NO-P (lower) -- Subj. czl

Figure 4.24. EMG activity after nominal impact in gastrocnemius and hamstrings. Activity appears burst-like in NO-P jumps after nominal impact. P impact (NO-P nominal impact) at t=0. Actual NO-P impact occurs at solid vertical line.

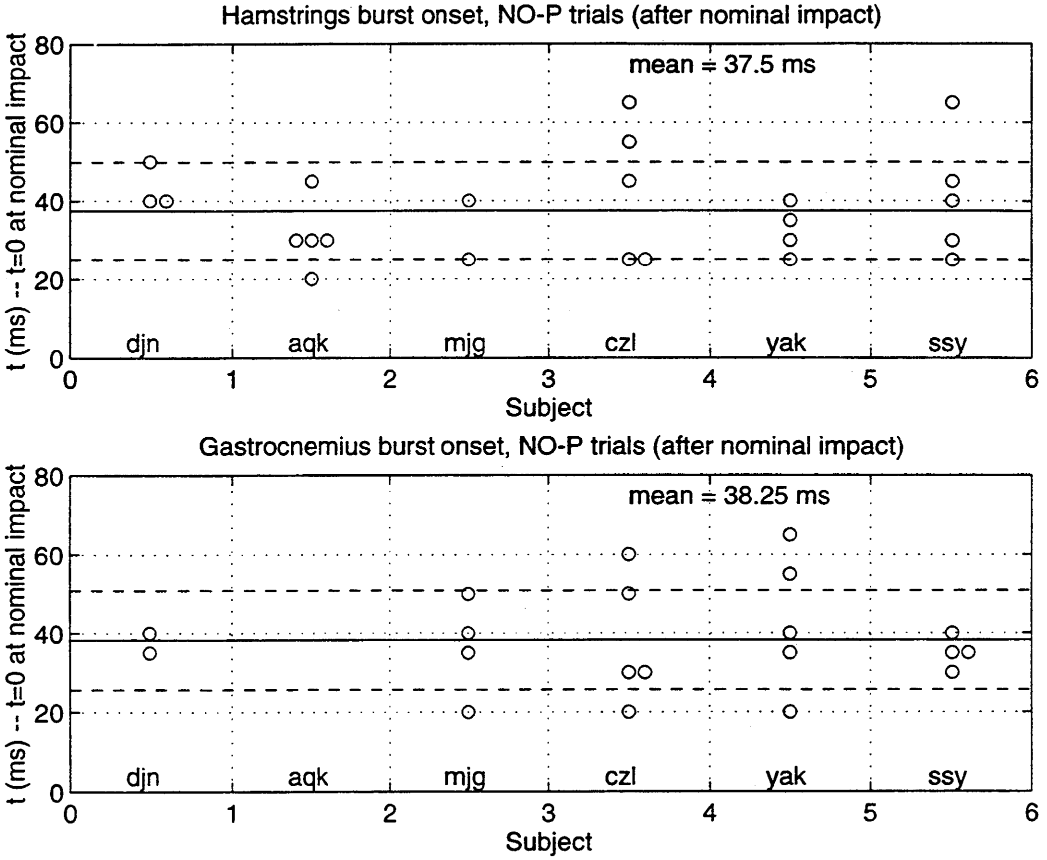

Figure 4.25. Timing of NO-P EMG bursts after nominal impact.
Onset times after nominal impact for trials exhibiting clear burst-like activity in gastrocnemius and hamstrings. All-subject means (solid lines) ± 1 standard deviation (dashed lines).

4.4. DISCUSSION OF FALSE PLATFORM RESULTS

The false platform data provide the highest fidelity data collected for this thesis, in terms of both spatial and temporal resolution. Furthermore, the NO-P trials make up a unique data set describing, at least for the first 100 ms following impact, the trajectory of the body that is actually commanded by the CNS during a jump landing, without the overriding perturbation imposed by the impact. In considering the implications for motor control in jumping, some basic issues must be addressed. First, the consistency and stationarity of the data set are important, especially because the uncertainty associated with the false platform protocol may cause subjects to adopt strategies for performing the jump landings. These points are addressed in the context of the force plate records.

Next, the question is addressed of how the commands to the muscles are generated in activities such as jump landings. Time delays in feedback loops are clearly a critical issue for events that take place in 150 ms or less. The EMG results are reviewed in the context of previous studies by other authors. The evidence for preprogramming of the motor commands in jump landings is reviewed, and the role of reflex activity in the leg musculature during impact absorption is discussed. The lambda model of the equilibrium point hypothesis is used to interpret the NO-P EMG results.

The meaning of the free trajectories from the NO-P jumps is also considered. If the equilibrium point hypothesis is correct, and the commanded stiffnesses are sufficiently large, the free trajectories may provide an approximate measurement of the virtual trajectories used to control the limbs during the jump impact absorption phase. The false platform data form the basis for testing the viability of the equilibrium point hypothesis as a model for the control of jump landings, and the potential applicability of the free trajectories is discussed.

4.4.1. Force Plate Results

The observation of two distinct patterns in the vertical ground reaction forces deserves comment. The Type 1 jumps appear largely in the baseline and early P jumps, while the great majority of later jumps are of Type 2. This raises two possibilities regarding the relationship between the types of jumps. First, the Type 1 jumps may prevail as the subject is learning the jump task, and hence the Type 2 jumps would indicate a refined landing style which the subject has perfected over the course of several trials. Alternatively, the Type 2 jump landing may form a response to the uncertainty associated with the possibility of NO-P jumps. The latter possibility must be considered seriously, because the Type 1 jumps are clustered in the early portion of the protocol, while the NO-P jumps are largely bracketed by Type 2 jumps.

Examination of the force traces for the Moonwalker partial gravity suspension experiment shows that 4 of the 7 subjects exhibit Type 2 jumping patterns, while the other three subjects perform Type 1 landings. Hence, the Type 2 landings are not necessarily related to the possibility of falling associated with the NO-P jumps. However, all of the false platform subjects adopt Type 2 jumps, while almost half of the moonwalker subjects do not. Therefore, the relationship is unclear, and the Type 2 landings may in fact provide some advantage when the height of the landing surface is uncertain.

The difference in footwear between the two experiments must be considered as well. In the moonwalker experiments, the subjects are barefoot, while they wear athletic shoes in the false platform experiments. The peak forces are seen to be higher in the Type 2 jumps, although of shorter duration. The lack of shoes to provide some shock attenuation in the moonwalker experiments may cause the subjects to avoid the higher forces associated with the Type 2 landings.

4.4.2. Pre-programmed Activity in the Leg Musculature

Considerable evidence exists that the events which occur prior to and during the impact absorption phase of jump landings are pre-programmed, rather than the result of reflex activity. Dyhre-Poulsen and Laursen [1984] investigate voluntary jumps down from various heights in monkeys, and find that the EMG activity is precisely timed to the expected moment of impact. Pre-impact activity in the triceps is initiated about 80 ms prior to expected impact, and this initial burst lasts until about 20 ms after impact, then is followed by successive bursts of declining amplitude. Use of a collapsible platform to trick the monkey shows that this activity is linked to the expected rather than the actual impact time, and hence is not of reflex origin. By extinguishing the lights after takeoff in some jumps, the investigators show that the landing sequence appears to be programmed before takeoff.

Similar tests are performed by McKinley and Smith [1983] in cats. They show that the EMG pattern is timed to impact by blindfolding the animals and then shifting the jump heights unexpectedly. Extensor activity begins 73 ms prior to the anticipated impact time, while flexor activity is minimal prior to impact. When tricked by a platform shift, the cats demonstrate EMG timing appropriate to the previously experienced jump. McKinley and Smith also show that even though visual input may normally regulate the timing of the pre-landing extensor sequence, the pre-impact motor sequence may be programmed even without visual information. The ability to predict the jump height, rather than visual information, is the important factor in the timing of the muscle activation sequence.

In humans, most of the muscular activity appears pre-programmed as well. Dyhre-Poulsen *et al.* [1991] find a stereotyped pattern of pre-landing muscular activation for downward jumps of 60 cm, consisting of a burst beginning about 150 ms before impact in the soleus and gastrocnemius, and tibialis anterior activity beginning 170 ms before impact. McKinley and Pedotti [1992] also report continuous activity in the soleus and gastrocnemius from the time the CM reaches maximum height in the flight phase, and observe onset of activity in the TA within 150 ms prior to impact. In this study, they find that the muscles in the upper leg become active shortly before impact as well. These results are consistent with the activity seen prior to impact in all four leg muscle groups measured in the false platform experiments (see Figure 4.16). Simultaneous activation of antagonist muscles acting about a joint generally increases the mechanical stiffness about the joint [Hogan, 1984a], and the concurrent activity in the anterior and posterior muscle groups observed prior to impact in the present study may indicate stiffening of the legs in preparation for landing.

After impact, Dyhre-Poulsen *et al.* [1991] consistently observe two peaks in the soleus activity and report similar results for the gastrocnemius. They suggest that these are preprogrammed rather than reflexive bursts. Interestingly, they report that the initial soleus burst begins approximately 45 ms after impact, yet no corresponding burst of comparable latency in the gastrocnemius is observed for the P jumps in the present study. Melvill Jones and Watt [1971a] cite results for downward stepping in man showing that the ankle extensor EMG activity begins 140 ms before ground contact, and becomes silent 130 ms after contact. They state that the muscular deceleration associated with landing is brought about by a preprogrammed pattern of activity which is "inaccessible to reflex activity."

In fact, all of the authors cited here provide evidence for the suppression of post-impact reflex activity. Melvill Jones and Watt base their argument on the functional stretch reflex, which normally exhibits strong sustained extensor activity beginning approximately 120 seconds after forcible rotation of the ankle. Since this is the time during which the gastrocnemius becomes inactive, the FSR appears to be suppressed. Based on their demonstration that the FSR rather than the monosynaptic stretch reflex is the source of useful force generation at the ankle, it appears that the events during the majority of the landing are preprogrammed.

Dyhre-Poulsen *et al.* [1991] argue that the two post-impact peaks seen in the soleus activity are unlikely to be reflexive in nature due to the strong suppression of the H-reflex prior to and throughout much of the ground contact time. Both McKinley *et al.* [1983] (in cats) and Dyhre-Poulsen and Laursen [1984] (in monkeys) found little evidence for landing stretch reflexes in their studies. Hence, as observed by Melvill Jones and Watt [1971a], the evidence shows the importance of pre-programming complex muscular contraction patterns in order to oppose sudden, passive stretching forces, and moreover indicates the need to initiate these programs prior to the onset of forces.

In the current study, no evidence for stretch reflex activity is observed in the gastrocnemius in the P jumps. Rather, significantly heightened activity is detected in the gastrocnemius and hamstrings in the NO-P jumps in the period following the expected moment of impact. This result is somewhat surprising, since the NO-P activity occurs in the *absence* of an external mechanical input to the legs. Furthermore, the difference in activity between the P and NO-P jumps argues against a consistent pre-programmed set of commands for these muscles. The average latency of burst-like activity with respect to nominal impact in the NO-P jumps is estimated at 38 ms for both gastrocnemius and hamstrings, a result that is essentially identical to the latency of monosynaptic reflex responses to ankle perturbation found by Melvill Jones and Watt [1971a].

Thus, the current results indicate substantial activity with the latency of a stretch reflex in the posterior muscles of the leg when the impact perturbation is absent. This finding can be interpreted in the context of the lambda model of the equilibrium point hypothesis [Feldman, 1986], which states that motor activity is achieved through modulation of the threshold level of the muscular stretch reflex. In the present experiment, the two muscles (gastrocnemius and hamstrings) that consistently exhibit increased NO-P activity are both knee flexors. Activity in these muscles occurs when the subject does *not* impact the landing platform, meaning that the legs are less flexed than they would normally be if the subject had actually landed. As a consequence, the knee flexors are more extended than they would be in the normal jump landing.

If the stretch reflex threshold is set dynamically for the "expected" muscle lengths in the jump landing, and the knee flexor muscles are stretched relative to this expected length, then the burstlike activity in the knee flexors could result from stretch reflex activity in these muscles after failure to impact the platform. Figure 4.26 shows a simple feedback model

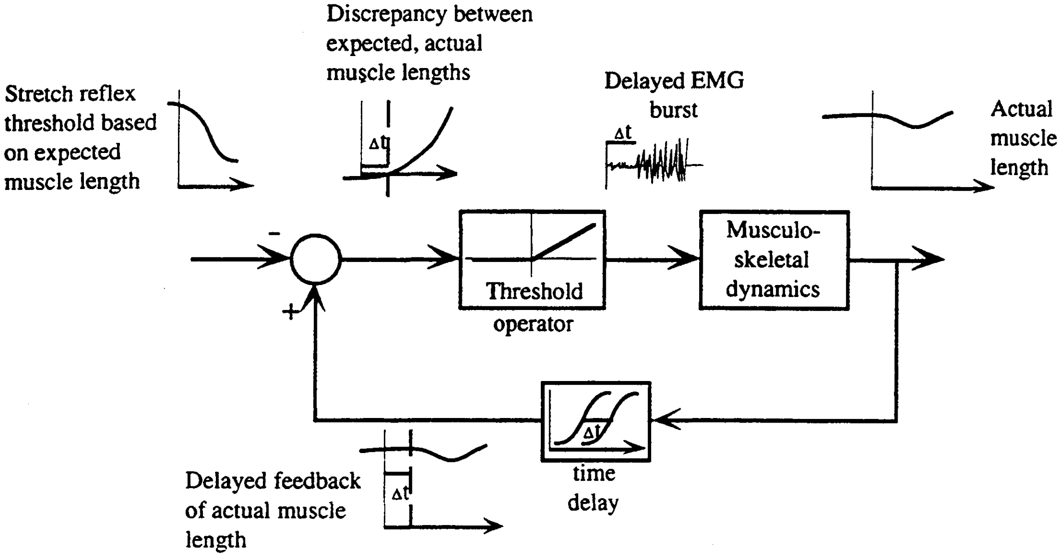

Figure 4.26. NO-P activity model based on control of stretch reflex threshold level. CNS sets activation threshold based on expected muscle length. Expected length is compared with spindle encoding of actual length that is delayed by Δt. Discrepancy results in muscle activation.

of the reflex loop. According to this model, the CNS sets the knee flexor stretch reflex threshold based on the flexion of the knee expected from the landing. Removing the impact results in less flexion than expected. The spindle feedback of the actual muscle length is delayed by the monosynaptic reflex latency, and comparison of the expected and actual muscle lengths at the spinal cord results in muscle activity in the knee flexors which is delayed by the same amount.

Based on this interpretation using a lambda equilibrium point model, the stretch reflex is not actually suppressed during the impact absorption phase, as conjectured by Dyhre-Poulsen *et al.* [1991]. Rather, the stretch reflex threshold activation threshold levels are set by descending commands to track the expected movement, implying that reflex activity occurs only when the actual motion deviates from the expected or intended motion. The results suggest that the CNS utilizes active, pre-programmed control of the stretch reflex thresholds, and that the thresholds are set based on an internal model of the expected body trajectory and muscles lengths. Further, the stretch reflexes may serve to correct for deviations from the intended or expected nominal trajectory in jump landings.

4.4.3. Joint Kinematics in the NO-P Jumps

The kinematic behavior immediately prior to and following the nominal time of impact is of particular interest. Extension is observed at all joints during the free fall portion of the jump. However, this extension does not continue until impact. Rather, the joints reach maximum extension about 20 ms prior to impact, then begin to flex again. The pattern observed here corroborates the work of McKinley and Pedotti [1992], who find that the limb reaches its largest extension prior to landing, and is already slightly flexed at the moment of impact. The functional significance of this behavior may be a reduction in the high impulsive forces associated with impact by removing the body from the singular joint position that occurs in perfectly upright posture. Further impact force reductions may be achieved as a result of partial matching of the foot velocity to the relative velocity of the upcoming landing surface (in a frame fixed at the hip, for instance).

The NO-P jumps provide a direct measure of the free trajectory of the limbs following the nominal impact time. The pattern seen in all subjects consists of a continuation of the joint flexion initiated immediately prior to the expected time of impact. This flexion phase ends approximately 50 ms after the expected impact time, and is followed by re-extension of the limb up to the point of actual impact with the foam mat. Based on the evidence reviewed above, this consistent pattern is most likely the result of a sequence of motor events which is pre-programmed during the flight phase or even prior to takeoff. Given the latency of the segmental stretch reflexes in the legs, the joint accelerations needed to effect the reversal from flexion to extension within 50 ms after nominal impact must result from a pre-programmed sequence of commands, rather than arising from feedback information.

The limb motions observed in NO-P jumps of the present experiment represent the previously unobserved free limb motions associated with these preprogrammed muscular contractions. An important question, then, concerns how these muscular contractions are commanded. One possibility is that they are, in fact, the result of a series of explicitly predefined muscle activations. Alternatively, the free trajectories may closely match virtual trajectory commands to the limbs, according to the equilibrium point hypothesis for motor control. Using this model, several researchers [Flash, 1987; McIntyre and Bizzi, 1993] have calculated virtual trajectories for unconstrained planar reaching movements which lie close to the actual observed motions.

It has often been suggested that the stability properties inherent in the virtual trajectory formulation provide a simple, yet effective means of solving the problem of tasks where the limb must exert force stably on the environment [Bizzi *et al.*, 1992a]. The same process that controls unconstrained motion can equally well control the force exerted on the environment by modulating the depth of the penetration of the virtual trajectory into the surface. In a normal jump landing, the legs contact the surface and the actual jump landing trajectory is observed. In the NO-P jumps, the landing surface is unexpectedly removed, and the limbs may freely follow the hypothesized equilibrium trajectory.

Thus, if the actual trajectory truly does follow the equilibrium trajectory closely, the free trajectories in the NO-P trials may actually provide a measurement of a virtual trajectory designed to modulate the environmental interaction associated with a jump landing. On the surface, this possibility seems plausible based on the measured free trajectories: the early flexion helps to decrease high impact forces, while the re-extension portion will bring the body back to an upright posture by making use of the spring-like properties of the neuromuscular system. Based on the kinematics of the NO-P trials, this line of reasoning appears feasible, and the question will be addressed in more detail in the context of the dynamic models of the system.

5 JUMP LANDING MODELS

Dynamic models of the human body provide a framework for rigorous appication of the physical laws of motion to the mechanics of the jump landing problem. The models give further insight into the measured jumping kinematics and ground reaction forces, and are needed to test the applicability of the equilibrium point hypothesis to the control of jump landings. Three models of varying complexity are formulated for the dynamics of the impact absorption and recovery phase of the jump landing. These models are used to estimate stiffness and damping parameters for the legs based on the difference between the measured P and NO-P trajectories. The significance of the estimated impedance parameters is discussed in the context of the equilibrium point hypothesis. The first model is the simplest, and the next two add higher levels of fidelity.

The first two models consider only vertical motion of the center of mass (CM). In Model 1, the CM is supported by a linear spring and dashpot. In Model 2, the CM is still constrained to move along the vertical, but the linear leg spring and damper are replaced by a massless leg with a torsional spring and damper at the knee joint. Model 3 is a three link planar model of the human body that incorporates lumped rigid bodies representing the shank, thigh, and upper body (head, arms and trunk, or HAT). In this three link model, the segments are connected by frictionless pin joints at the ankle, knee and hip.

5.1. MODEL 1: CM VERTICAL MOTION: SECOND ORDER LINEAR

5.1.1. Model Derivation and Parameter Estimation

Figure 5.1 shows the simplest mechanical model for jump landings. The body mass is lumped at the mass center, which is supported by a linear spring and a linear dashpot element. The equation of motion for this system is:

$$m\ddot{y}(t) = -k[y(t) - y_0(t)] - b\dot{y}(t) + mg \qquad (5\text{-}1)$$

where $y(t), \dot{y}(t), \ddot{y}(t)$ = CM position, velocity and acceleration
$y_0(t)$ = spring unloaded equilibrium length
m = body mass
k = stiffness
b = damping
g = gravitational acceleration = $-9.8\ \mathrm{m/s^2}$

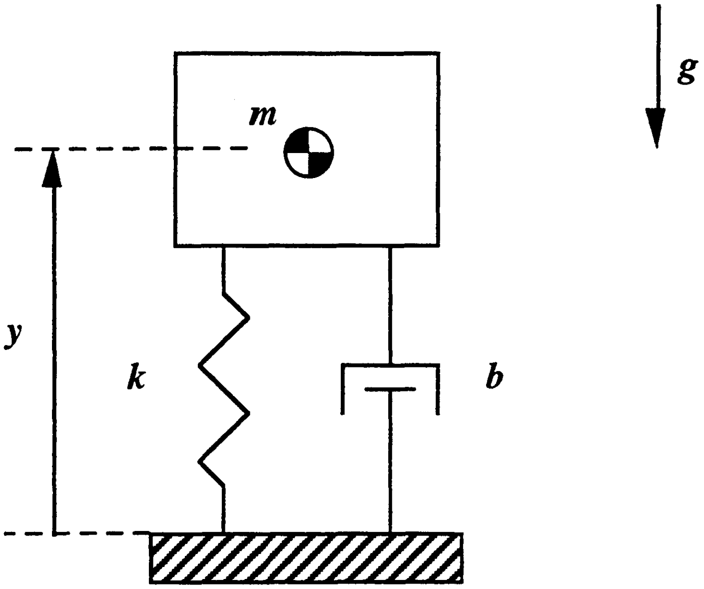

Figure 5.1. Model 1: Second order linear model of CM vertical motion. The body mass *m* is lumped at the mass center, which is supported by a leg spring of stiffness *k*. Damping is provided by a viscous damper *b*.

Dividing Equation (5-1) through by the body weight *mg* and collecting terms gives the standard damped harmonic oscillator:

$$\ddot{y}(t) + B\dot{y}(t) + K[y(t) - y_0(t)] = 1 \tag{5-2}$$

where $\ddot{y}(t)$ = CM acceleration (normalized by gravity)
K = spring stiffness (normalized by body weight)
B = damping (normalized by body weight)

The stiffness K and damping B are estimated from the NO-P and P CM trajectories and the P vertical forceplate data. In this model, the force on the CM by the spring/dashpot system is given by:

$$\overline{F}(t) = -K[y(t) - y_0(t)] - B\dot{y}(t) \tag{5-3}$$

where $\overline{F}$ = force normalized by body weight
= forceplate output

and $\overline{F}$, y, $\dot{y}$ are known. The unloaded spring length $y_0(t)$ represents the hypothesized virtual trajectory in this model, and is assumed to be the same as the average time history of the ankle-CM distance in the NO-P trials. Although use of the toe-CM distance would be preferable as the toe normally impacts the landing surface before the ankle, the toe position could not be estimated for much of the period following nominal impact because the foot array was obscured by the paper. However, the ankle position can still be estimated during this time from the shank array. For consistency, the CM position y is referenced to the final height of the ankle joint in the P trials. The first 5 samples following impact are excluded from the analysis, as the ankle is undergoing rapid vertical motion during this time.

Equation 5-3 can be rewritten as a system of equations, where each individual equation corresponds to a single sample. In matrix form,

$$\begin{bmatrix} \vdots & \vdots \\ (y_i - y_{0_i}) & \dot{y}_i \\ \vdots & \vdots \end{bmatrix} \begin{bmatrix} K \\ B \end{bmatrix} = \underline{C} \begin{bmatrix} K \\ B \end{bmatrix} = \begin{bmatrix} \vdots \\ -\overline{F}_i \\ \vdots \end{bmatrix} \qquad (5\text{-}4)$$

where $\underline{C}$ represents the matrix of coefficients multiplying K, B
i = sample number

With two unknowns (K and B), the system is overdetermined when more than 2 samples are used. The equations can be solved for the best fitting K and B in a least squares sense by computing the pseudoinverse of the coefficient matrix $\underline{C}$ and premultiplying both sides of the equation:

$$\begin{bmatrix} \hat{K} \\ \hat{B} \end{bmatrix} = (\underline{C}^T \underline{C})^{-1} \underline{C}^T \begin{bmatrix} \vdots \\ -\overline{F}_i \\ \vdots \end{bmatrix} \qquad (5\text{-}5)$$

where $\hat{K}$ = best fit stiffness
$\hat{B}$ = best fit damping

In order to quantify the model goodness of fit for the stiffness and damping estimates, the fraction of the variance in the GRF data that is accounted for by the model GRF (Equation 5-3) is computed. This fraction, R^2, is the ratio of the regression sum of squares (Reg SS) to the total sum of squares (Total SS) as shown in Equation 5-6.

$$\begin{aligned} \text{Total SS} &= \sum_i (F_i - \underline{F})^2 \\ \text{Reg SS} &= \sum_i (\hat{F}_i - \underline{F})^2 \\ R^2 &= \frac{\text{Reg SS}}{\text{Total SS}} \end{aligned} \tag{5-6}$$

where

$$\underline{F} = mean(F_i)$$

$$\hat{F}_i = -\hat{K}_i[y_i - y_{0_i}] - \hat{B}_i \dot{y}_i$$

Using calculated values for $\hat{K}$ and $\hat{B}$, a virtual trajectory (VT) for the spring equilibrium length can be estimated for the remainder of the jump landing after actual NO-P impact by solving Equation 5-3 for $y_0(t)$.

$$\hat{y}_0(t) = y(t) + \hat{K}^{-1}[\overline{F} + \hat{B}\dot{y}(t)] \tag{5-7}$$

where $\hat{y}_0(t)$ = estimated ankle-CM length virtual trajectory

5.1.2. Model Fits to Experimental Data

Ten samples of $y_0(t)$ are available for estimation of K and B (15 samples of the free trajectory from nominal to actual impact, less the first 5 due to rapid ankle motion). Using Equation 5-5, the stiffness and damping are estimated at each of samples 7-14 following impact, using 3 samples centered about the current sample of interest. Figure 5.2 shows the results for subject *djn*. The plots on the left side show Type 1 jump landings (average of 4 jumps), while the right plots depict Type 2 landings (average of 5 jumps). The same trajectory for $y_0(t)$ is used in each case. For each landing type, the estimated stiffness and damping are aligned with the corresponding averaged vertical ground reaction force.

In the Type 1 landings, the ground reaction force is increasing for the initial samples (numbers 7-9). The estimated stiffness is positive, and decreases from a large initial value to a minimum corresponding to the most rapid rate of force decrease. At the same time, the damping estimate is initially small and increases to peak at the same time the stiffness estimate is minimized. As the rate of decrease of the force diminishes, the stiffness estimate increases slightly, while the damping estimate decreases.

The Type 2 landings demonstrate a contrasting pattern. Here, the force is decreasing rapidly during the first few samples (7-10). The estimated stiffness is negative, accompanied by large positive damping values. As the force begins to increase toward the second peak, the stiffness becomes positive and the damping estimate decreases sharply toward zero.

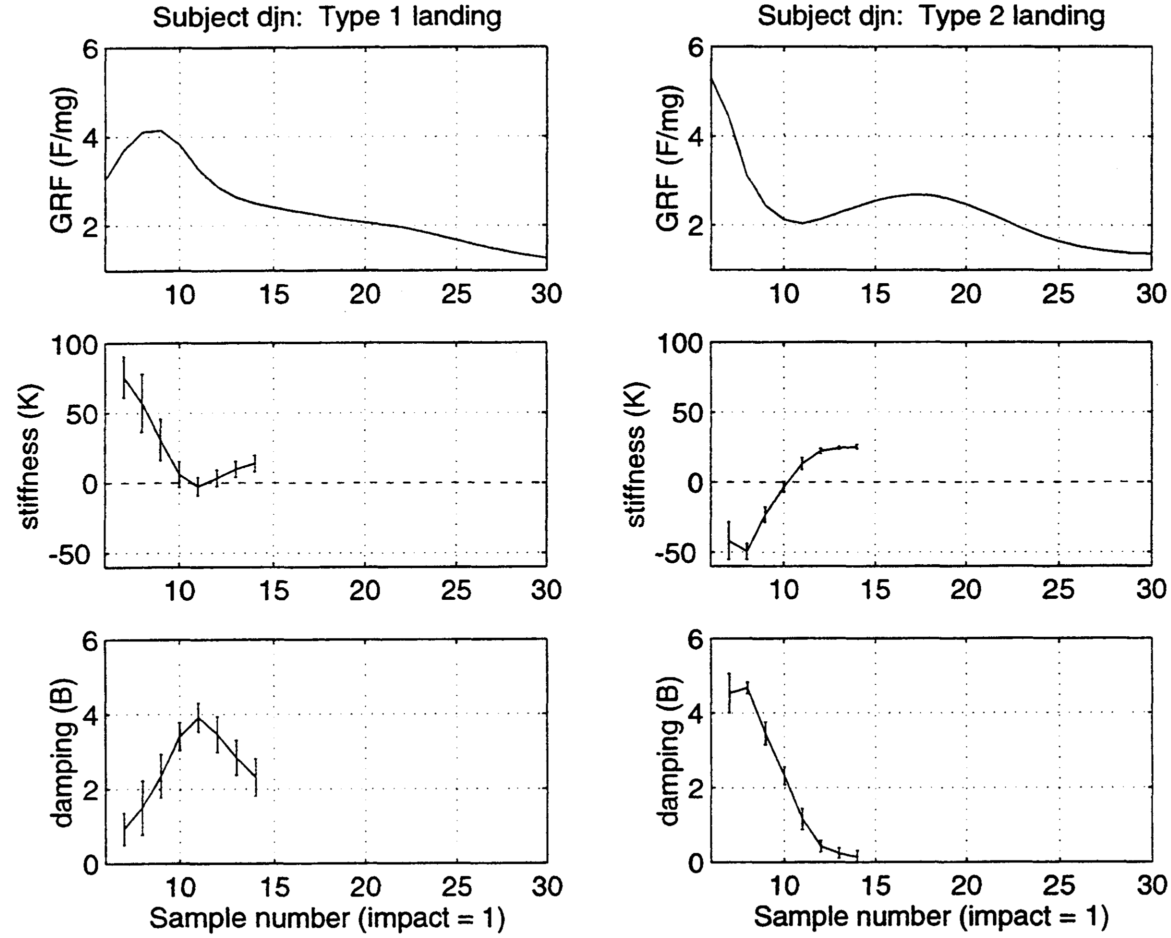

Figure 5.2. Impedance estimates for landing Types 1 and 2, subject *djn*. Force, stiffness and damping all normalized by body weight. Error bars indicate one standard error of the mean.

Figure 5.3 shows the stiffness and damping estimates for each subject. Only Type 2 landings are used in these calculations, as the Type 2 landings greatly predominate after the baseline jumps. Stiffness and damping are calculated using averages of the CM trajectory and force data. The solid horizontal line in each plot denotes the stiffness or damping estimate found when all 10 available samples are used to estimate $\hat{K}$ and $\hat{B}$, and represents an average value over this time period. Table 5.1 shows the SS and R^2 values for each subject for the model fits. The model fits are generally quite good, with all R^2 values greater than 0.83.

Table 5.1. Goodness of fit measures for Model 1.

Subject	*djn*	*aqk*	*mjg*	*czl*	*yak*	*ssy*
Total SS	9.73	4.43	12.20	15.50	0.78	2.86
Reg SS	9.31	3.67	11.57	15.36	0.66	2.65
R^2	0.96	0.83	0.95	0.99	0.85	0.93

The model fit results for the individual subjects follow the pattern seen for subject *djn*'s Type 2 jumps. The estimated stiffness is negative during the sharp decline in vertical force toward the initial minimum. As the force begins to increase again, the stiffness estimates become positive. Damping estimates look like inverted plots of the stiffness values. Low or negative stiffness values correspond to high damping estimates, while increasingly positive stiffness values match decreases in the damping. This pattern is quite clear in Figure 5.4, where the average stiffness and damping estimates for all subjects are aligned with the averaged vertical force.

Interestingly the stiffness estimates are *negative* for all subjects for a portion of the landing phase. Considering the vertical force data, this is not surprising, as the restoring force is expected to *increase* as a spring with positive stiffness is compressed. In the Type 2 landings, the ground reaction force *decreases* sharply during the time period examined, even as the leg is compressed further from the NO-P trajectory (Figure 5.5). It appears that the damping properties of the leg system are most important in the early deceleration of the CM, while the stiffness properties become significant later in the deceleration phase. The large variation in the stiffness and damping estimates over the short time period examined (70 ms) is also noteworthy.

a. Stiffness (normalized by body weight)

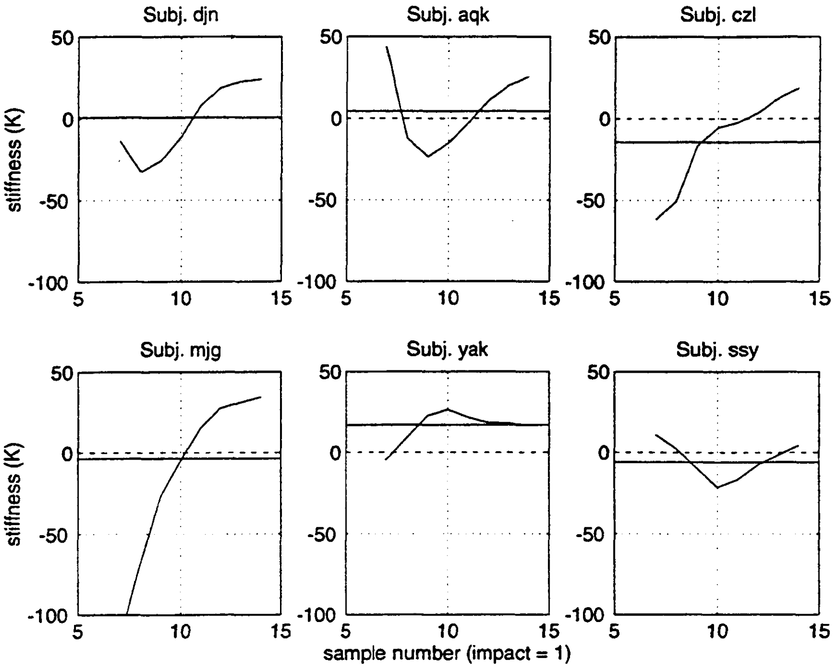

b. Damping (normalized by body weight)

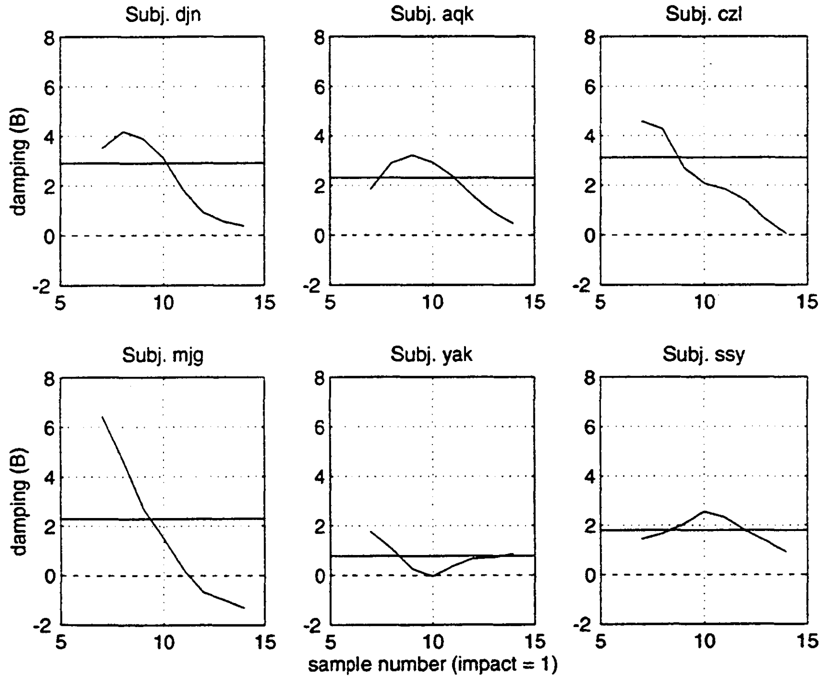

Figure 5.3. Individual subject stiffness and damping for Model 1. Values are normalized by subject's body weight. Solid horizontal lines indicate mean stiffness and damping values using all 10 samples.Negative stiffnesses are estimated for some samples in all subjects.

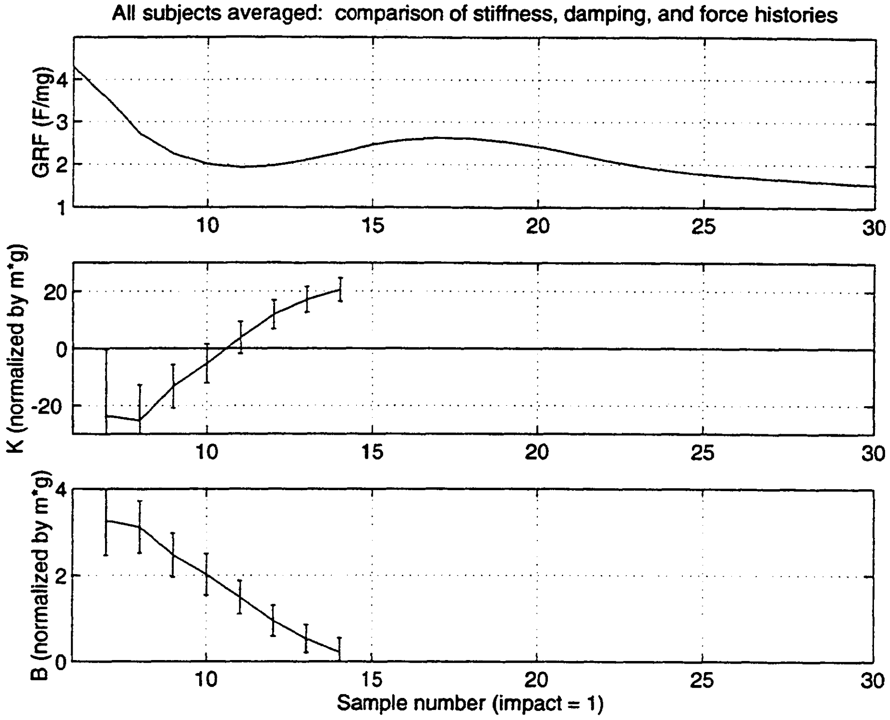

Figure 5.4. Stiffness and damping for Model 1 averaged across all subjects. Stiffness and damping are normalized by body weight. Error bars indicate 1 standard error of the mean. Vertical ground reaction force (top) is provided for timing reference.

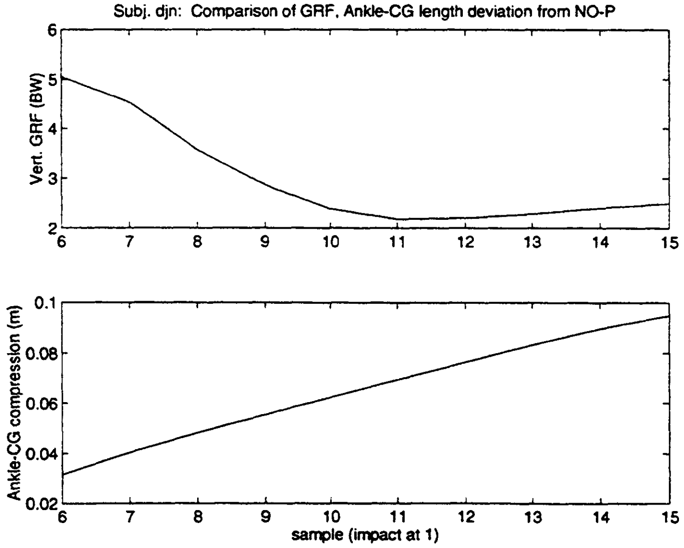

Figure 5.5. GRF decreases with increasing leg compression relative to NO-P. Rapid decrease in vertical ground reaction force (top) is seen as the leg is being compressed away from the NO-P free trajectory (bottom, difference between P and NO-P trajectories).

The shape of the VTs for the remainder of the landing phase (based on the impedance estimates) is of interest. The VTs for the spring equilibrium length are estimated using the values of $\hat{K}$ and $\hat{B}$ determined from the last 3 available samples of $y_0(t)$, and assume constant stiffness and damping values. Average trajectories for all subjects combined are shown in Figure 5.6, aligned with the average GRF trace. Figure 5.7 shows each subject's estimated VT; in each case, the VT is superimposed on the actual P ankle-CM trajectory and the corresponding NO-P results that provided $y_0(t)$. For each subject, the VT follows a similar pattern that replicates the features of the ground reaction force: a dip in the VT matches the first trough in the GRF, followed by a temporary increase in the VT length corresponding to the second peak in the GRF. The VT then decreases again to a minimum length at the time when the GRF reaches its minimum value, before recovering to a final length. This final equilibrium length is much larger than the maximum physiologically feasible distance between ankle and CM because of the finite spring stiffness K.

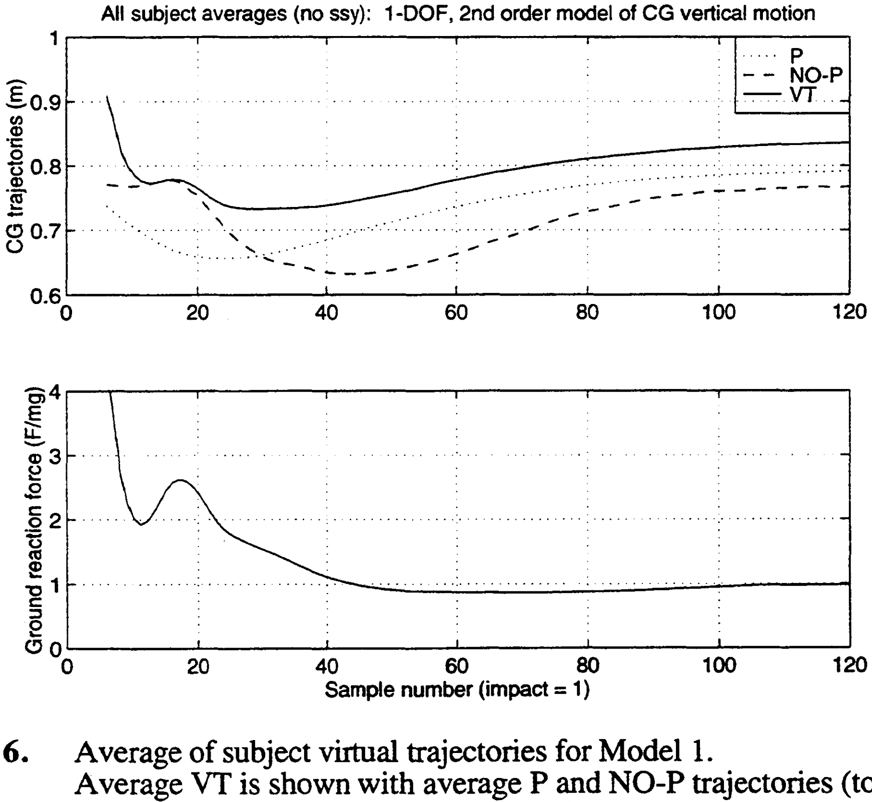

Figure 5.6. Average of subject virtual trajectories for Model 1.
Average VT is shown with average P and NO-P trajectories (top), and average vertical GRF is shown below for reference. Subject *ssy* data are excluded because her comparatively low stiffness estimates results in a VT that is considerably different from the other subjects.

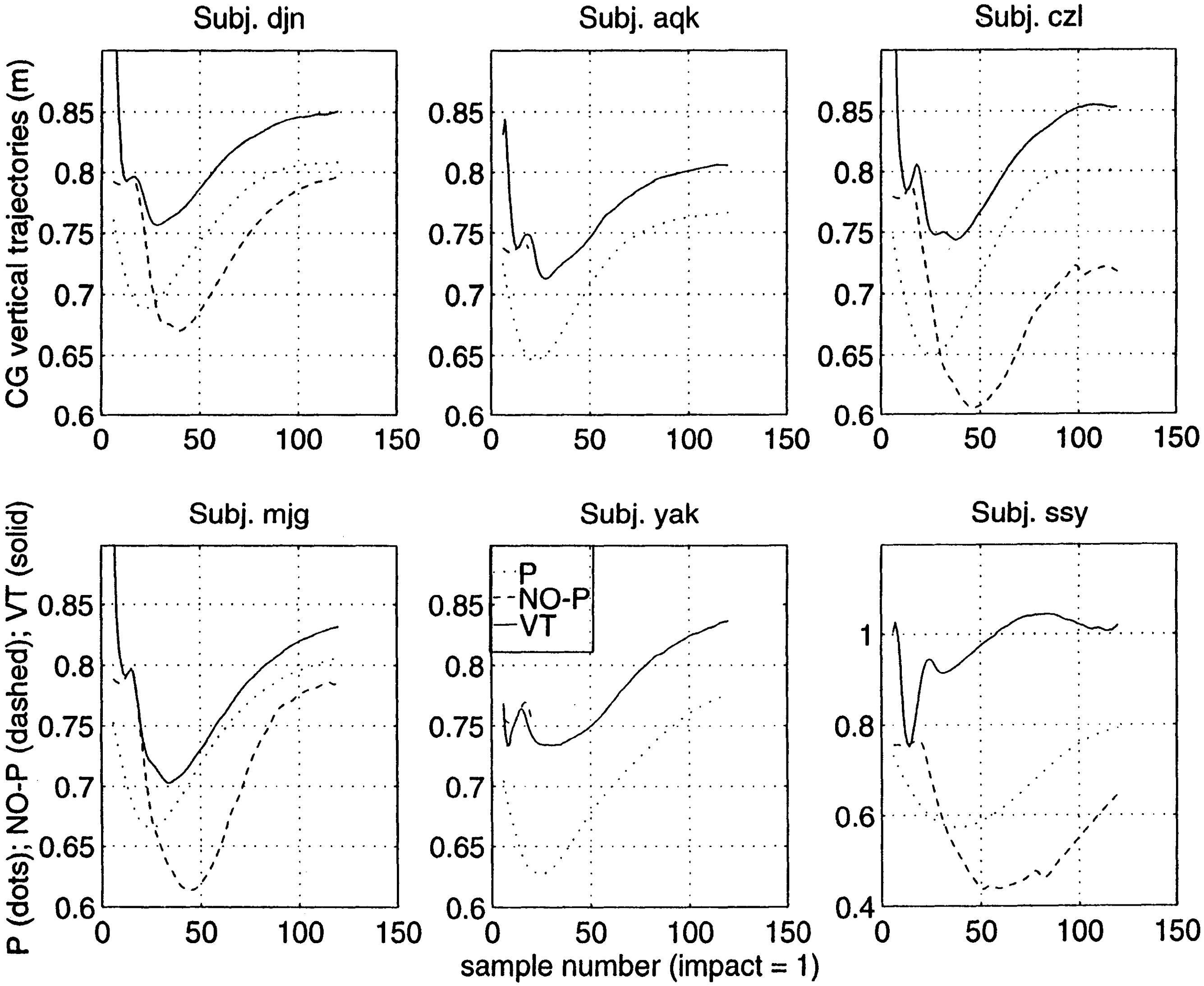

Figure 5.7. Individual subject estimated VTs for Model 1.
VTs are shown superimposed on average P and NO-P trajectories.

5.2. MODEL 2: CM VERTICAL MOTION: SECOND ORDER WITH KNEE

5.2.1. Model Derivation and Parameter Estimation

The linear spring and damper in the first model have the advantage of simplicity, but fail to account for the fact that the vertical stiffness of the body increases substantially as the posture changes from a crouch to upright standing [Greene and McMahon, 1979]. If the body were in fact a series of rigid links connected by pin joints, the stiffness would become infinite in the singular configuration of upright standing. Model 1 cannot account for stiffness variations as a function of posture, and results in VTs for the leg spring that reach physiologically infeasible lengths. The second model, pictured in Figure 5.8, retains the simplicity of the vertical CM motion in the first model, but incorporates a knee joint to account for the dependence of body stiffness on posture.

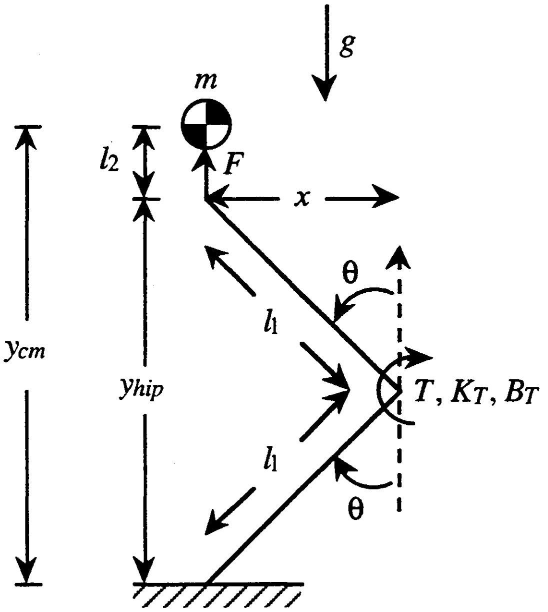

Figure 5.8. Second order model of vertical CM motion with knee joint. The CM is constrained to move only along the vertical, and is supported by a massless leg consisting of equal shank and thigh segments of length l_1. Linear torsional stiffness (K_T) and damping (B_T) provide a torque (T) about the knee.

Once again, the CM is constrained to vertical motion only. The leg is modeled as shank and thigh segments of equal length connected at the knee by a pin joint. A linear torsional spring and damper generate torque at the knee. The CM is a constant distance l_2 above the hip. The angle θ represents the rotation of the thigh segment with respect to the vertical; for this geometry, the angle of the shank with respect to the vertical is also θ.

The distance l_2 is found by averaging the vertical distance from the hip to the CM over the first 120 samples following impact. The leg segment length l_1 is set to one half of the ankle-hip distance in upright standing. This assumption of equal segment lengths (also used by Greene and McMahon [1979]) is a simplification of the actual limb geometry; Young *et al.* [1983] report average thigh and shank lengths of 41 cm and 36 cm respectively for their study of female subjects. As in the first model, the distance y_{cm} is defined to be the height of the CM above the final ankle position. In order to replicate the motion of the center of mass, the angle θ is calculated as shown in Equations 5-8:

$$\begin{aligned} y_{hip} &= y_{cm} - l_2 \\ \theta &= \cos^{-1}\left(\frac{y_{hip}}{2l_1}\right) \end{aligned} \tag{5-8}$$

The equation of motion for this model is

$$m\ddot{y}_{cm}(t) = F(t) + mg \tag{5-9}$$

where

$$\begin{aligned} T(t) &= -K_T[2\theta(t) - 2\theta_0(t)] - B_T \cdot 2\dot{\theta}(t) \\ F(t) &= -\frac{T(t)}{x(t)} = -\frac{T(t)}{l_1 \sin\theta(t)} \end{aligned} \tag{5-10a,b}$$

In this case, the equilibrium trajectory is expressed as the equilibrium knee angle $\theta_0(t)$. The velocity of the mass center is related to the joint rate by:

$$\dot{y}_{cm}(t) = \frac{d}{dt}[2l_1 \cos\theta(t)] = -2l_1 \sin\theta(t) \cdot \dot{\theta}(t) \tag{5-11}$$

and Equation 5-9 can be written as a set of coupled first order nonlinear equations:

$$\begin{bmatrix} \dot{z}_1 \\ \dot{z}_2 \end{bmatrix} = \begin{bmatrix} -\dfrac{z_2}{2l_1 \sin z_1} \\ \dfrac{F}{m} + g \end{bmatrix} \tag{5-12}$$

where $\begin{bmatrix} z_1 \\ z_2 \end{bmatrix} = \begin{bmatrix} \theta \\ \dot{y}_{cm} \end{bmatrix}$

Given the vertical ground reaction force and knee angle histories, the knee torques T_i can be computed at each sample from Equation 5-10b. Then, in a manner analogous to Equation 5-5, the knee stiffness and damping can be estimated from the P and NO-P data as follows:

$$\begin{bmatrix} \hat{K}_T \\ \hat{B}_T \end{bmatrix} = (\underline{C}^T \underline{C})^{-1} \underline{C}^T \begin{bmatrix} \vdots \\ -T_i \\ \vdots \end{bmatrix} \tag{5-13}$$

where $\underline{C} = \begin{bmatrix} \vdots & \vdots \\ 2(\theta_i - \theta_{0_i}) & 2\dot{\theta}_i \\ \vdots & \vdots \end{bmatrix}$

$\hat{K}_T$, $\hat{B}_T$ = estimated stiffness, damping
i = sample index
θ_{0_i} = NO-P knee angle

Again, this linear system of equations in two unknowns is overdetermined when more than two samples are used. Goodness of fit measures are again calculated using Equation 5-5, in the same manner as for Model 1. In this case, however, the model force estimates $\hat{F}_i$ for the regression SS calculation are given by:

$$\begin{aligned} \hat{F}_i &= -\frac{\hat{T}_i}{x_i} = -\frac{\hat{T}_i}{l_1 \sin \theta_i} \\ \hat{T}_i &= -\hat{K}_{T_i}[2\theta_i - 2\theta_{0_i}] - \hat{B}_{T_i} \cdot 2\dot{\theta}_i \end{aligned} \tag{5-14}$$

After estimating the stiffness and damping coefficients, the knee angle equilibrium trajectory is found by rewriting Equation 5-10a:

$$\hat{\theta}_0(t) = \theta(t) + \frac{1}{2\hat{K}_T}[T(t) + \hat{B}_T \cdot 2\dot{\theta}(t)] \tag{5-15}$$

where $\hat{\theta}_0(t)$ = estimated knee angle equilibrium trajectory

An additional point of interest is the minimum knee stiffness necessary to return the system to the upright posture, $\theta = 0$. Allowing the system to come to rest, with the equilibrium joint angle $\theta_0 = 0$, gives

$$F_{\theta\to 0} = \lim_{\theta\to 0} \frac{K_T \cdot 2\theta}{l_1 \sin\theta} = \frac{2K_T}{l_1} \tag{5-16}$$

The requirement that the system return to upright can be expressed by the inequalities

$$\begin{aligned} F_{\theta\to 0} &\geq -mg \\ K_T &\geq \frac{-mgl_1}{2} \end{aligned} \tag{5-17}$$

5.2.2. Model 2 Fits to Experimental Data

The knee torsional stiffness and damping coefficients are estimated in the same manner as the linear stiffness and damping in the first model. Figure 5.9 depicts the knee stiffness and damping, averaged across subjects. In this case, the stiffness and damping estimates are normalized by body mass. The pattern for the stiffness and damping during the same 10 sample window discussed earlier is similar to that seen in the results for Model 1. In the early samples, the joint stiffness estimates are low and the damping is high, when the knee torque is high but decreasing rapidly. Over the course of the time interval, the average knee stiffness increases while the damping decreases, as the knee torque diminishes more slowly and then begins to rise again.

Although the average stiffness and damping estimates are all greater than zero using this model, examination of the results for the individual subjects (Figure 5.10) shows that the stiffness in the region of rapidly falling torques is estimated to be negative for 3 of the 6 subjects (*czl, mjg, ssy*). Of these 3, subjects *czl* and *mjg* are the two subjects with the largest negative stiffnesses, as estimated from the linear spring/damper model. As the stiffness increases, the damping drops toward zero. In some cases (*mjg, yak,* and *aqk*), the estimated best-fit damping values actually become negative. Goodness of fit is high for Model 2, as shown in Table 5.2.

Table 5.2. Goodness of fit measures for Model 2.

Subject	*djn*	*aqk*	*mjg*	*czl*	*yak*	*ssy*
Total SS	9.73	4.43	12.20	15.50	0.78	2.86
Reg SS	9.30	3.66	11.62	15.39	0.67	2.64
R^2	0.96	0.83	0.95	0.99	0.86	0.92

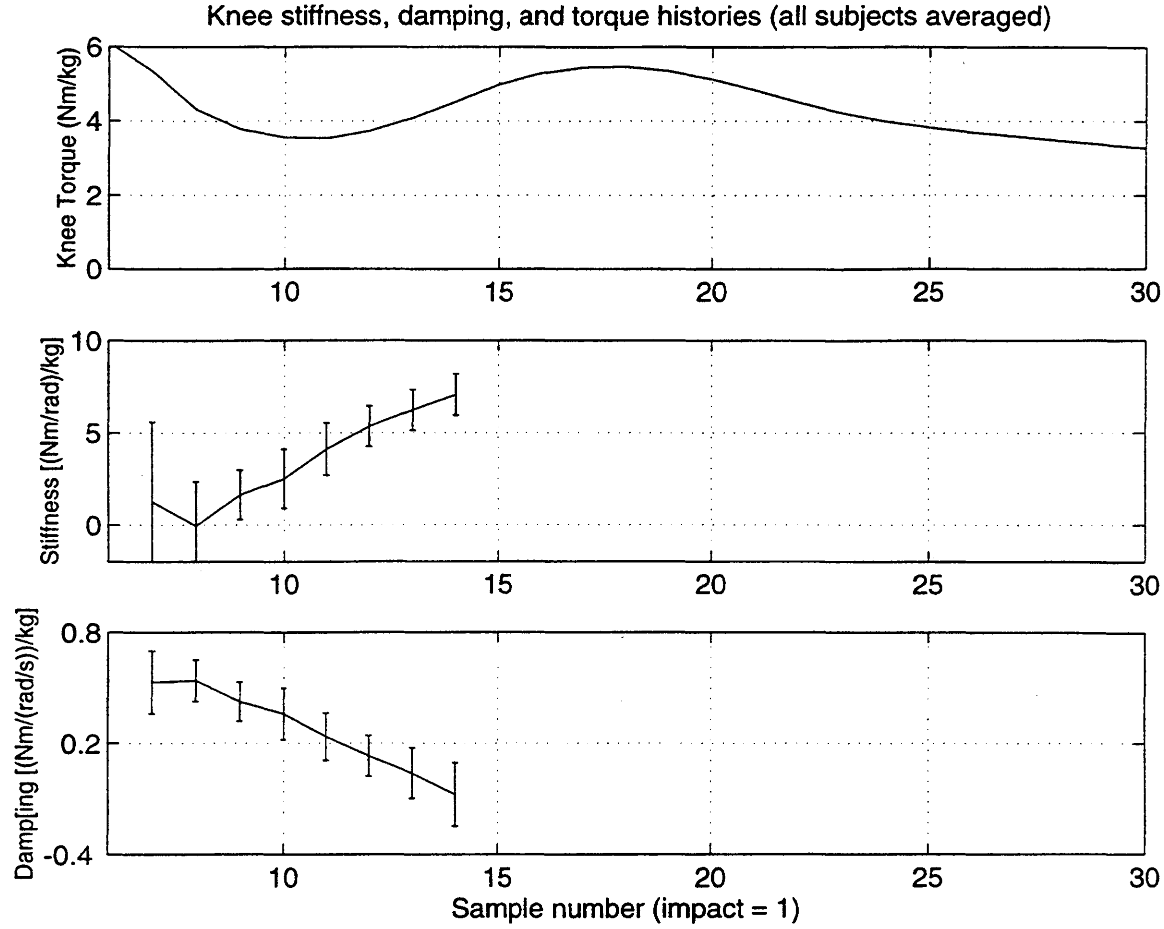

Figure 5.9. Model 2 stiffness and damping estimates, all subjects averaged. Average estimates of knee stiffness (middle) and damping (bottom) are shown with the vertical GRF (top) for reference. Stiffness and damping are normalized by subject body mass.

Using the stiffness and damping values estimated from the last 3 available samples, knee angle equilibrium trajectories are estimated. Again, constant stiffness and damping throughout the trajectories are assumed. These trajectories are shown averaged across subjects in Figure 5.11, and for each subject individually in Figure 5.12. The general pattern for the knee virtual trajectories is comparable to that of the ankle-CM length VTs seen for the linear spring/damper model. The equilibrium knee angle must increase during the time associated with the early decrease in the knee torque, that matches the initial trough in the ground reaction force. As the knee torque increases again, the equilibrium angle decreases until the time of the second maximum in the GRF. At this point, the estimated equilibrium angle increases again, reaches a maximum approximately 250 ms after impact and then decreases gradually toward zero.

a. Normalized knee stiffness estimates [(Nm/rad)/kg]

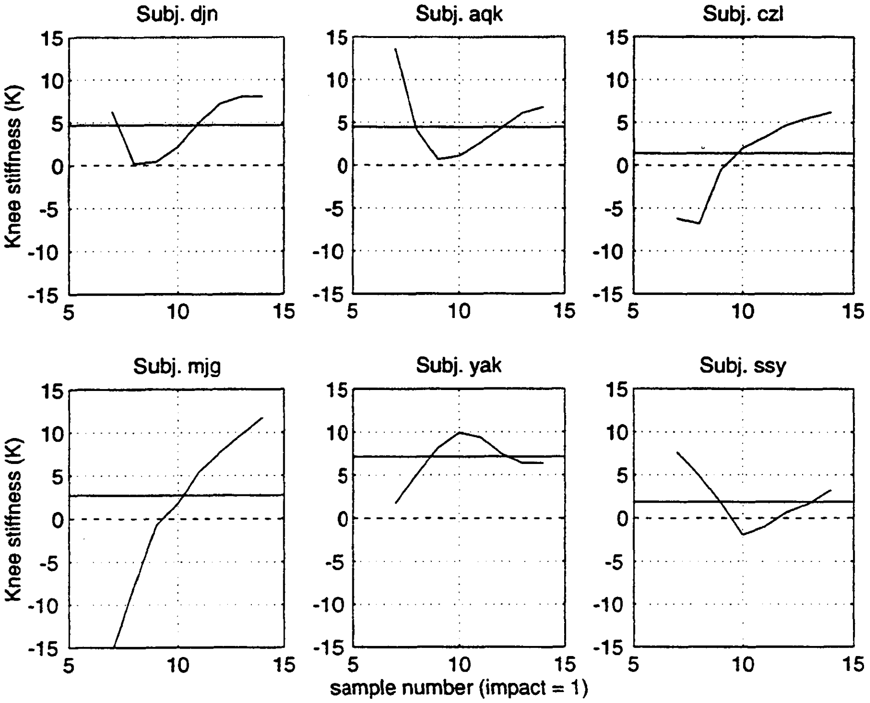

b. Normalized knee damping estimates [(Nm/(rad/s))/kg]

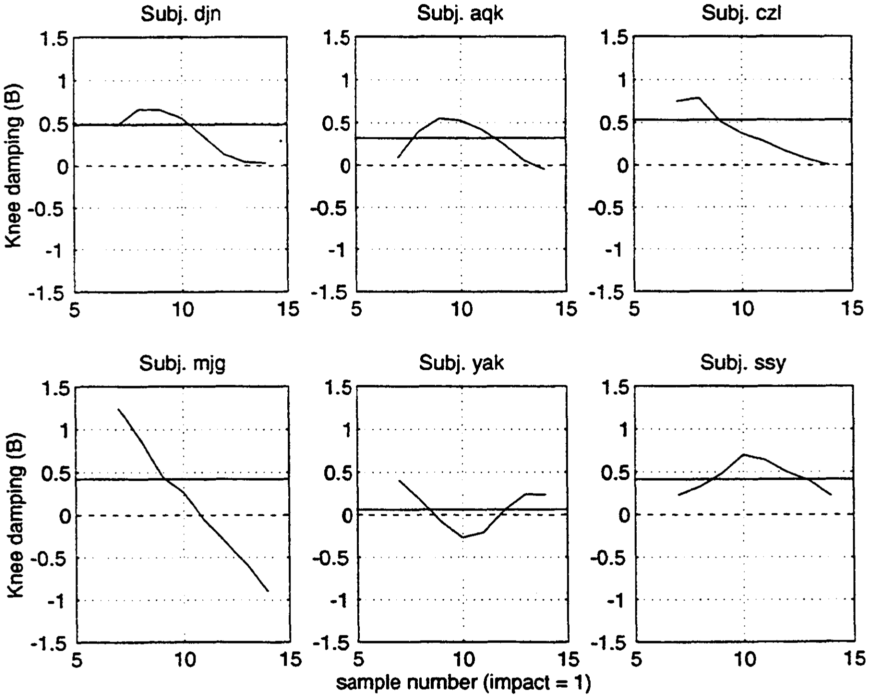

Figure 5.10. Individual subject knee stiffness and damping for Model 2. Values are normalized by body mass. Horizontal solid lines indicate average stiffness and damping for the complete 10 sample period.

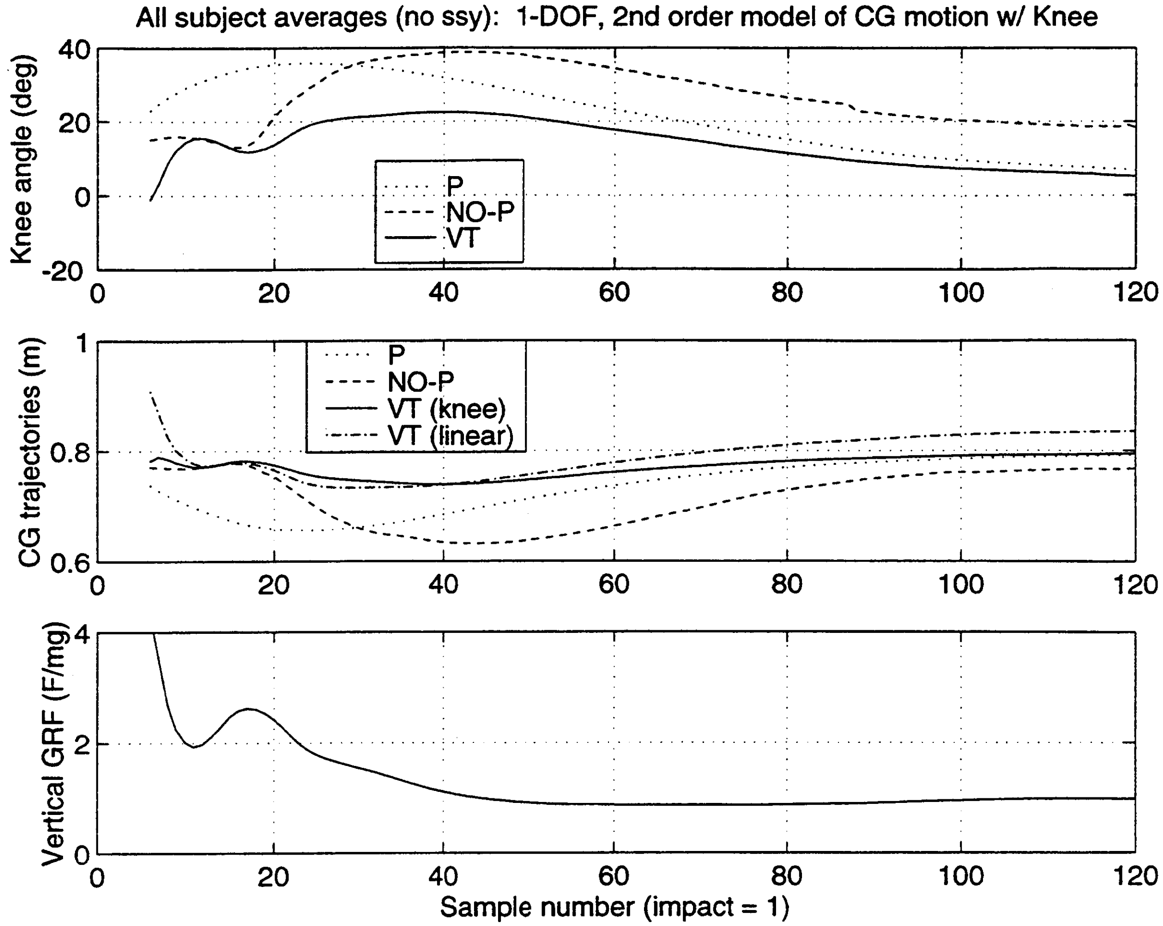

Figure 5.11. Virtual trajectories for Model 2, all subjects averaged. Knee angle VTs (top) and corresponding CM vertical position VTs (middle) are shown with average P and NO-P results. The CM VT for Model 1 (linear) is included for comparison with Model 2 (knee). Vertical GRF (bottom) is shown for reference. Subject *ssy* data are excluded because her comparatively low stiffness estimates results in a VT that is considerably different from the other subjects.

Figure 5.11 (middle) also shows the same average VT for the knee model, transformed from the knee angle trajectory into the corresponding ankle-CM length. For comparison, it is superimposed on the same trajectory calculated for the linear spring/damper model. Because the effective vertical stiffness in the second model approaches infinity for upright stance, the virtual trajectory simply approaches the upright ankle-CM length. In contrast, the VT for the linear constant stiffness spring (Model 1) must surpass physiologically meaningful limits as the system approaches upright posture. Nevertheless, for the stiffnesses estimated here, the VTs for both models observe the same basic shape, most notably in the time interval associated with the early trough and second peak in the vertical ground reaction forces (the first 120 ms after impact).

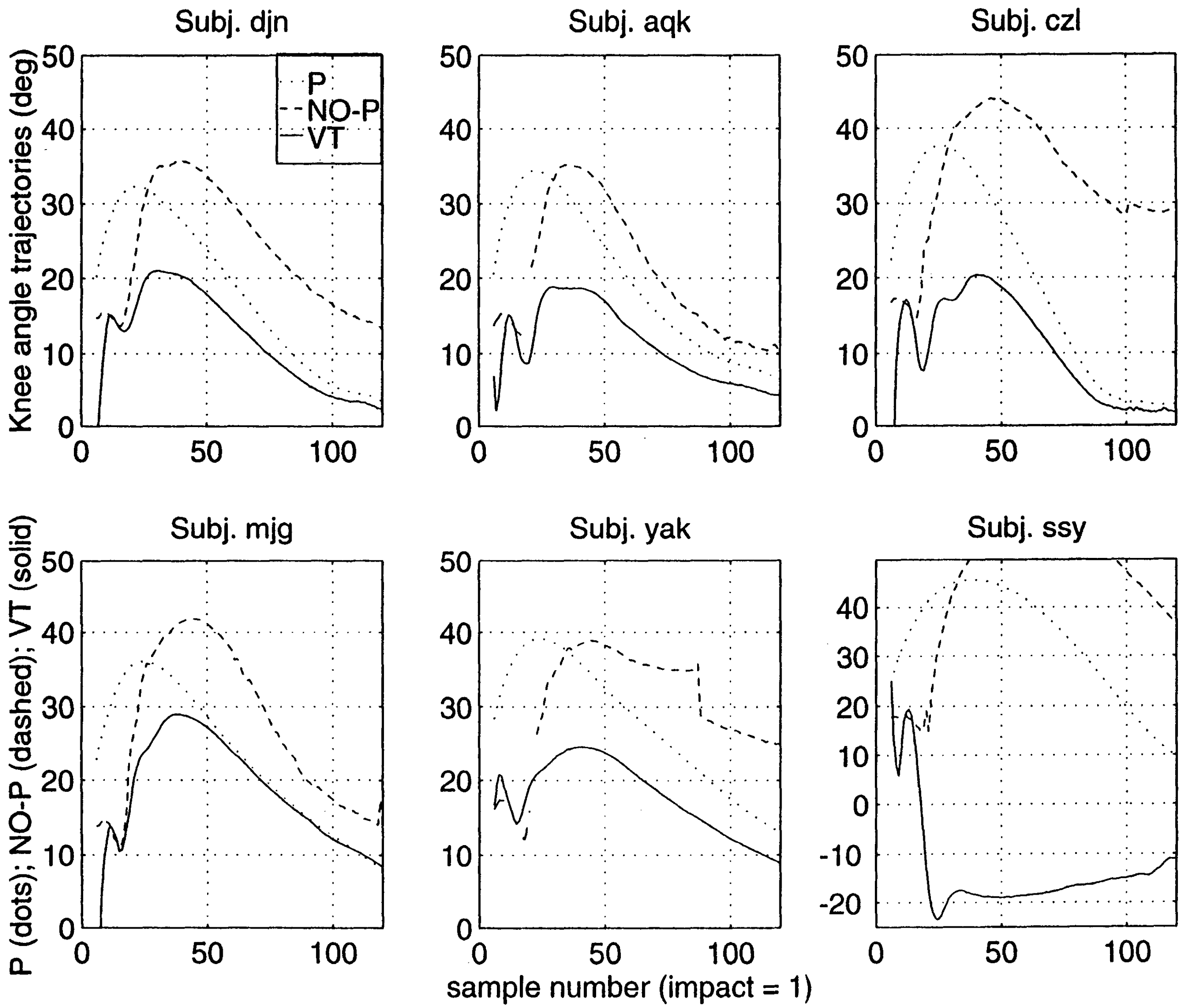

Figure 5.12. Individual subject knee angle virtual trajectories for Model 2. VTs are shown superimposed on average P and NO-P knee trajectories.

5.3. MODEL 3: THREE LINK PLANAR

While the first two models capture gross measures of the body motion and leg impedance properties, their simplifications ignore the fact that the body mass is actually distributed among the body segments. Furthermore, the CM models omit the horizontal component of the motion as well as the dynamic complexity associated with the multilink structure of the human body. The third model, while still a considerable simplication of the body mechanics, goes beyond describing the motion of the full body CM. It uses a three segment description of the human body with a more realistic mass distribution. The segments represent (1) the shanks, (2) the thighs, and (3) the upper body, or "HAT" (for Head, Arms and Trunk).

This section describes the formulation of the model, the equations of motion, and the procedure for estimating joint stiffness and damping matrices using an equilibrium point control model. The resulting impedance fits are presented next. Estimation of virtual trajectories for this model is discussed, and the virtual trajectories found for a single subject are described. The incorporation of rate information into the virtual trajectory is also evaluated.

5.3.1. Description of the Three Link Model

The three link planar model, shown in Figure 5.13, is constrained to move in the sagittal plane, and has three degrees of freedom corresponding to the ankle, knee and hip joints. The segments are connected by frictionless pin joints.

Each segment is modeled as a rigid body. The shank, thigh and HAT segments have masses m_1, m_2, and m_3, respectively. Likewise, the respective centroidal moments of inertia are I_1, I_2, and I_3. The shank and thigh segments combine the left and right sides of the body. The trunk segment inertial properties are determined using the parallel axis theorem and the estimated inertial properties of the individual upper body segments.

The shank and thigh segment CMs are assumed to lie along the lines between the proximal and distal joints. In reality, the CMs of these segments lie approximately 1-2 cm posterior to the lines connecting the joints. However, simulation shows that this simplification has negligible effect on the full-body CM estimate or the estimated torques and forces.

As shown in Figure 5.13, two different angular conventions can be used to describe the configuration of the linkage. The two conventions consist of absolute angles

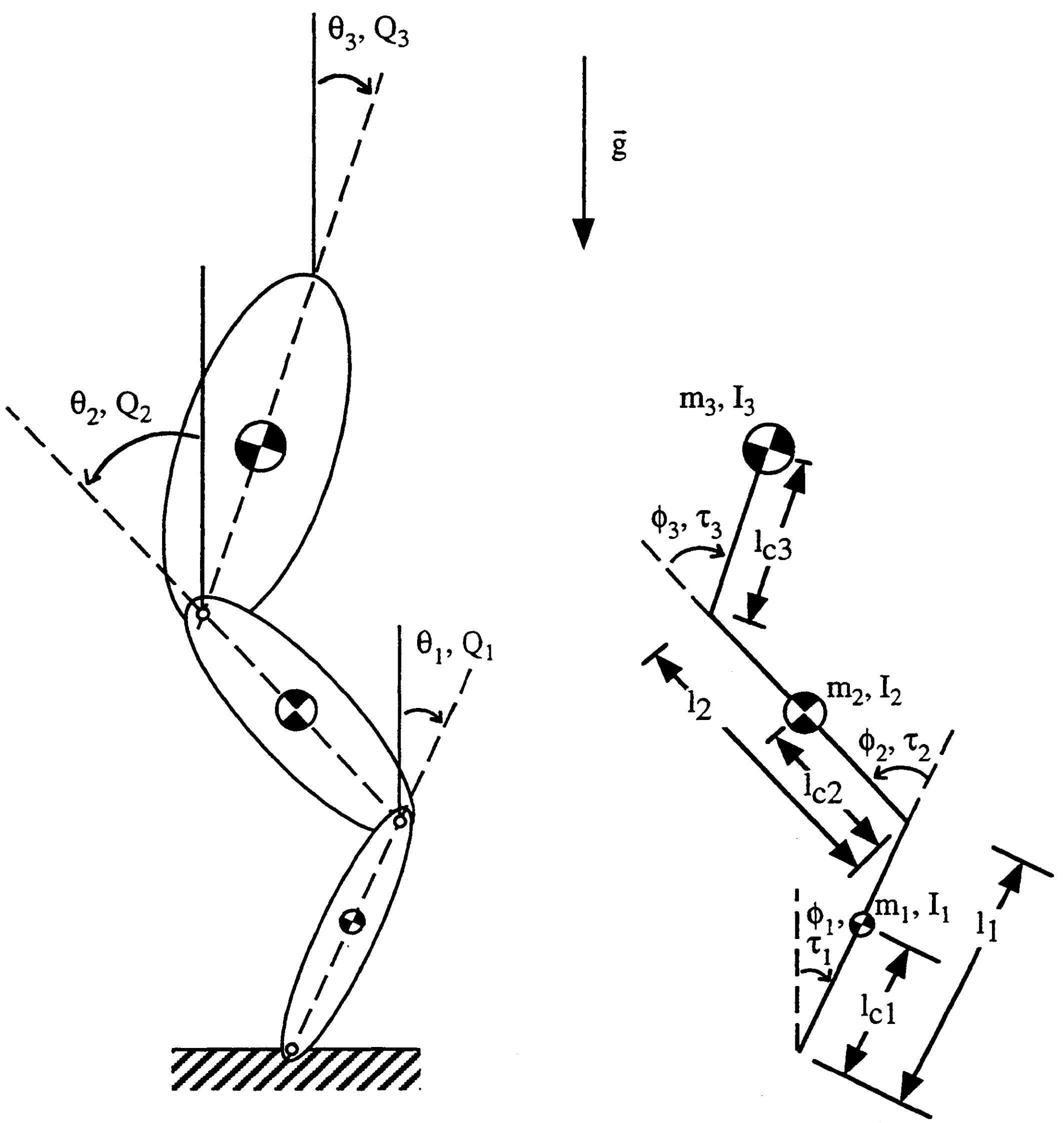

Figure 5.13. Three link planar human body model. The segments are connected by frictionless pin joints. The shank, thigh and HAT segments are designated 1, 2 and 3, respectively. Lengths l_1 and l_2 denote the shank and thigh lengths. Lengths l_{c1}, l_{c2} and l_{c3} represent the distances from the distal joints to the segment CMs. On the left, segment angles are described by the generalized coordinates Θ, defined with respect to the gravitational vertical. On the right, joint angles Φ are defined by the relative angles of the proximal and distal segments. Generalized forces Q correspond to the generalized coordinates Θ, while the joint torques T correspond to the relative joint angles Φ. The segments masses and centroidal moments of inertia are given by m_i and I_i respectively, where the subscript i denotes the segment number.

Θ and relative angles Φ. [Note that in the remainder of this chapter, capital greek letters (Θ and Φ) are used to denote the vectors of all three joint angles, while small letters (θ and ϕ) refer to the individual joint angles. Likewise, T indicates the vector of joint torques, while τ refers to the torque at an individual joint.] The first set uses the absolute segment angles Θ, which are defined with respect to the gravitational vertical. The knee angle sign convention is defined opposite to that for the ankle and hip. For the shank and HAT angles in Figure 5.13, clockwise rotations with respect to the vertical are positive, while a positive thigh angle corresponds to a counterclockwise rotation of this segment with respect to the vertical. This set of generalized coordinates corresponds to a set of generalized joint forces Q.

The other angular convention Φ defines relative joint flexion between adjacent segments. The ankle angle ϕ_1 is defined with respect to the gravitational vertical, because no foot segment is used. In this angle convention, joint flexion is positive and hyperextension is negative. Thus, in Figure 5.13 a clockwise rotation of the shank with respect to the vertical and of the HAT with respect to the thigh are positive, while a counterclockwise rotation of the thigh with respect to the shank is considered positive. The joint torques corresponding to these joint angles are denoted by T, and flexional torques are positive.

Both angle conventions are useful in different situations. The absolute angles Θ are more convenient for deriving the dynamic equations describing the model motion, while the relative angles Φ correspond to the physical joint moments and prove more useful in describing virtual trajectories for the model. The two angle conventions are related by Equations 5.18.

$$\begin{bmatrix}\phi_1\\ \phi_2\\ \phi_3\end{bmatrix} = J\begin{bmatrix}\theta_1\\ \theta_2\\ \theta_3\end{bmatrix}$$

$$J = \begin{bmatrix}1 & 0 & 0\\ 1 & 1 & 0\\ 0 & 1 & 1\end{bmatrix} \tag{5.18}$$

where J = Jacobian relating the derivatives $\dot{\phi}_i$ and $\dot{\theta}_i$

Similarly,

$$\begin{aligned} \dot{\Phi} &= J\dot{\Theta} \\ \ddot{\Phi} &= J\ddot{\Theta} \end{aligned} \qquad (5\text{-}19)$$

where $\dot{\Phi}$, $\ddot{\Phi}$ = vectors of 1st, 2nd derivatives of the relative joint angles
$\dot{\Theta}$, $\ddot{\Theta}$ = vectors of 1st, 2nd derivatives of the absolute joint angles

The generalized forces corresponding to the two sets of generalized coordinates are related by:

$$\begin{bmatrix} \tau_1 \\ \tau_2 \\ \tau_3 \end{bmatrix} = \left(J^{-1}\right)^T \begin{bmatrix} Q_1 \\ Q_2 \\ Q_3 \end{bmatrix} \qquad (5\text{-}20)$$

5.3.2. Three Link Model Dynamic Equations

The dynamic equations governing the motion for this model are derived using a Lagrangian approach [Asada and Slotine, 1986], then checked for correctness with AutoLev™, a software package for symbolic manipulation and dynamic equation derivation (Online Dynamics, Inc.; Sunnyvale, CA). The AutoLev and Matlab scripts containing the three link model equations are included in Appendix C. The general form for the dynamic equations is given by Equation 5-21:

$$H(\Theta)\ddot{\Theta} + h(\Theta,\dot{\Theta}) + G(\Theta) = Q \qquad (5\text{-}21)$$

where $H(\Theta)$ = configuration dependent inertia tensor
$h(\Theta,\dot{\Theta})$ = rate dependent terms
$G(\Theta)$ = gravitational terms

The specific equations for the three link model can be written:

$$\begin{aligned} H_{11}\ddot{\theta}_1 + H_{12}\ddot{\theta}_2 + H_{13}\ddot{\theta}_3 + h_{122}\dot{\theta}_2^{\,2} + h_{133}\dot{\theta}_3^{\,2} + G_1 &= Q_1 \\ H_{21}\ddot{\theta}_1 + H_{22}\ddot{\theta}_2 + H_{23}\ddot{\theta}_3 + h_{211}\dot{\theta}_1^{\,2} + h_{233}\dot{\theta}_3^{\,2} + G_2 &= Q_2 \\ H_{31}\ddot{\theta}_1 + H_{32}\ddot{\theta}_2 + H_{33}\ddot{\theta}_3 + h_{311}\dot{\theta}_1^{\,2} + h_{322}\dot{\theta}_2^{\,2} + G_3 &= Q_3 \end{aligned} \qquad (5\text{-}22a)$$

The symmetric inertia tensor elements are:

$$\begin{aligned}
H_{11} &= m_1 l_{c1}^2 + m_2 l_1^2 + m_3 l_1^2 + I_1 \\
H_{22} &= m_2 l_{c2}^2 + m_3 l_2^2 + I_2 \\
H_{33} &= m_3 l_{c3}^2 + I_3 \\
H_{12} &= H_{21} = -\left(m_2 l_1 l_{c2} + m_3 l_1 l_2\right)\cos(\theta_1 + \theta_2) \\
H_{13} &= H_{31} = m_3 l_1 l_{c3}\cos(\theta_1 - \theta_3) \\
H_{23} &= H_{32} = -m_3 l_2 l_{c3}\cos(\theta_2 + \theta_3)
\end{aligned} \qquad \text{(5-22b)}$$

The velocity dependent gyroscopic torques have coefficients:

$$\begin{aligned}
h_{122} &= h_{211} = l_1\left(m_2 l_{c2} + m_3 l_2\right)\sin(\theta_1 + \theta_2) \\
h_{133} &= -h_{311} = m_3 l_1 l_{c3}\sin(\theta_1 - \theta_3) \\
h_{233} &= h_{322} = m_3 l_2 l_{c3}\sin(\theta_2 + \theta_3)
\end{aligned} \qquad \text{(5-22c)}$$

The gravity terms are given by:

$$\begin{aligned}
G_1 &= g\left(m_1 l_{c1} + m_2 l_1 + m_3 l_1\right)\sin\theta_1 \\
G_2 &= g\left(m_2 l_{c2} + m_3 l_2\right)\sin\theta_2 \\
G_3 &= g m_3 l_{c3}\sin\theta_3
\end{aligned} \qquad \text{(5-22d)}$$

where $g = -9.8 \text{ m/s}^2$

Note that use of the absolute angles Θ means that the Coriolis terms $(h_{ijk}\dot{\theta}_j\dot{\theta}_k ,\, i \neq j \neq k)$ drop out.

The ground reaction forces for this model, defined as the forces exerted by the first link on the environment at the fixed ankle joint, are given by:

$$\begin{aligned}
Fy = {} & [l_{c1}m_1 + l_1(m_2 + m_3)]\sin\theta_1\ddot{\theta}_1 + (l_2 m_3 + l_{c2}m_2)\sin\theta_2\ddot{\theta}_2 + l_{c3}m_3\sin\theta_3\ddot{\theta}_3 \\
& + [l_{c1}m_1 + l_1(m_2 + m_3)]\cos\theta_1\dot{\theta}_1^2 + (l_2 m_3 + l_{c2}m_2)\cos\theta_2\dot{\theta}_2^2 + l_{c3}m_3\cos\theta_3\dot{\theta}_3^2 \\
& + g(m_1 + m_2 + m_3)
\end{aligned}$$

(5-23a)

$$\begin{aligned}
Fx = {} & -[l_{c1}m_1 + l_1(m_2 + m_3)]\cos\theta_1\ddot{\theta}_1 + (l_2 m_3 + l_{c2}m_2)\cos\theta_2\ddot{\theta}_2 - l_{c3}m_3\cos\theta_3\ddot{\theta}_3 \\
& + [l_{c1}m_1 + l_1(m_2 + m_3)]\sin\theta_1\dot{\theta}_1^2 - (l_2 m_3 + l_{c2}m_2)\sin\theta_2\dot{\theta}_2^2 + l_{c3}m_3\sin\theta_3\dot{\theta}_3^2
\end{aligned}$$

(5-23b)

5.3.3. Estimation of Joint Stiffness and Damping Properties

The procedure for estimating linear stiffness and damping properties in the CM motion models is extended to determine joint impedance properties for the three link model. This section describes the steps taken to apply the model to the body motion data, including estimation of joint angles for the P and NO-P jumps. The body segment position and orientation data from the 11 tracked segments are reduced to a form that gives joint trajectories appropriate for the three link model, and the impact of the lack of useful ankle data from the NO-P trials is discussed.

Next, the stiffness and damping properties at the leg joints are estimated from the free trajectories determined from the NO-P jumps. In addition to using the virtual position formulation that includes only position information (applied to the CM models above), an extension is made to the three link model to accomodate a version of the equilibrium point hypothesis that includes an additional velocity command [McIntyre and Bizzi, 1993].

5.3.3.1. *Estimation of Joint Trajectories for Three Link Models*

In order to apply Equations 5-22 to the inverse dynamic calculations for the three link model, estimates of the joint angles and the first and second derivatives must be obtained. Two different methods for estimating the model joint angles are attempted; the first is found to be inadequate, requiring development of the second method.

Initially, the joint flexion angles are estimated directly from the segment array orientations. The shank angle $\phi_1 = \theta_1$ is given by the flexion of the shank segment with respect to the vertical, and the relative knee angle ϕ_2 is set equal to the knee flexion angle as determined from the procedure described in Section 4.2.1.4. Left and right side angle data are averaged for the shank and knee angles. The hip flexion determined using the 11 segment model is not used here, because it gives the angle of the thigh relative to the pelvis, and therefore cannot account for the actual configuration of the upper body segments. Instead, the absolute hip angle θ_3 is determined by estimating the CM position of the HAT segment, then computing the vector from the center of the line joining the two hip joints to the HAT CM. The angle made by this vector with the vertical gives the absolute hip angle.

Unfortunately, when the three link model ground reaction forces are computed from Equation 5-23 using these angles, then compared to the actual forceplate data, the results prove substantially different (Figure 5.14). Further investigation shows that when the full body CM trajectory is re-estimated (using these joint angles in the three link model) and compared to the CM estimate from the 11 segment model, the two estimates differ by as much as 5 cm at some points in the trajectory. The discrepancies are believed to result from a combination of factors: (1) out-of-plane motion due to abduction and external rotation at the leg joints; (2) variation in the distance from the hip joint to the HAT CM over the course of a jump; and (3) vertical motion of the ankle due to lifting of the heel during impact absorption.

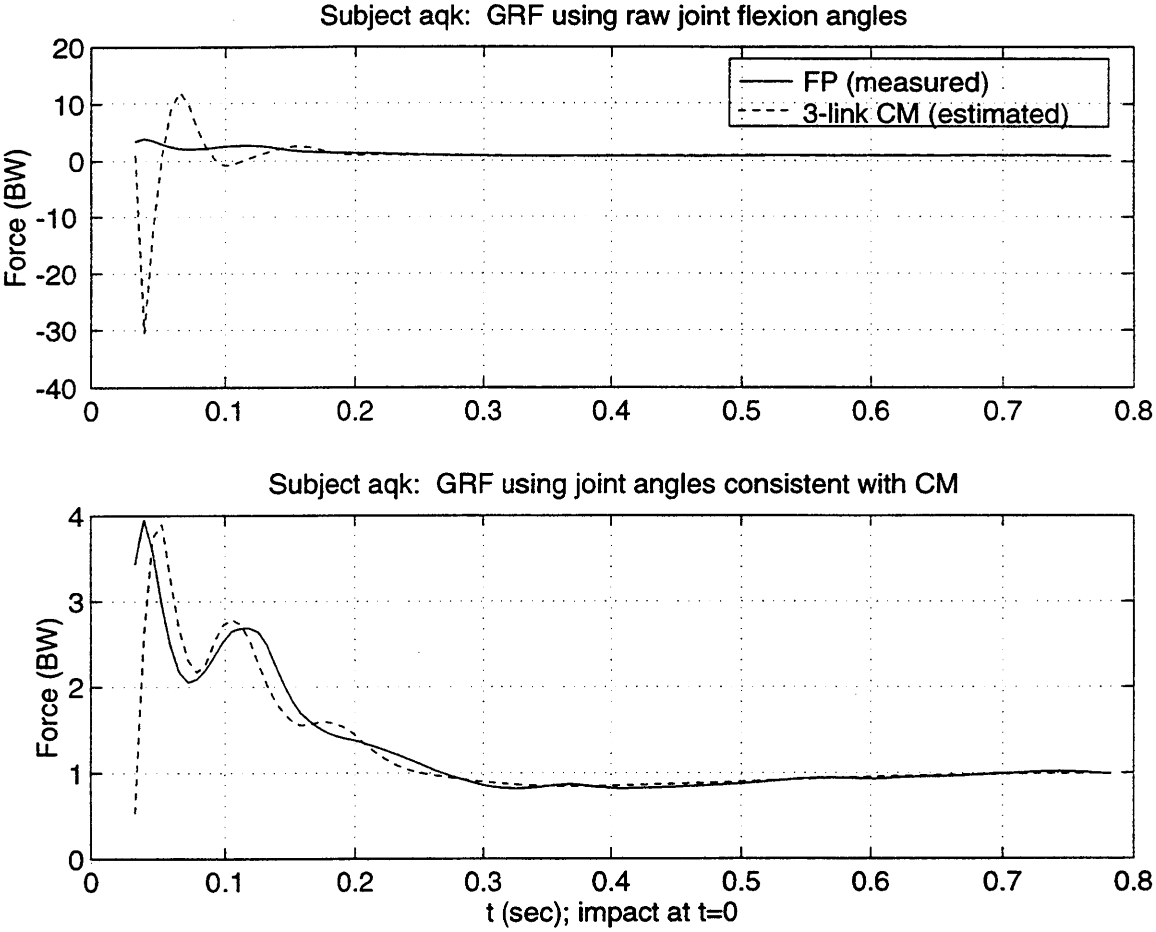

Figure 5.14. GRF results for three link model for two different joint angle estimates. Vertical GRFs estimated using the equations for the three link model are shown in comparison to the actual measured GRFs. The match is poor using the joint flexion angles from the 11 segment model; use of a second method results in much improved correspondence between model and data.

For this reason, another method of estimating the joint angles for the three link model is designed to match better the motion of the full body CM. The full body CM estimate is believed to be quite good, based on excellent matches between the measured ground reaction forces and the forces predicted from the CM acceleration (see Figure 4.8). This second method uses the CM estimates from the 11 segment model based on the link geometry shown in Figure 5.15.

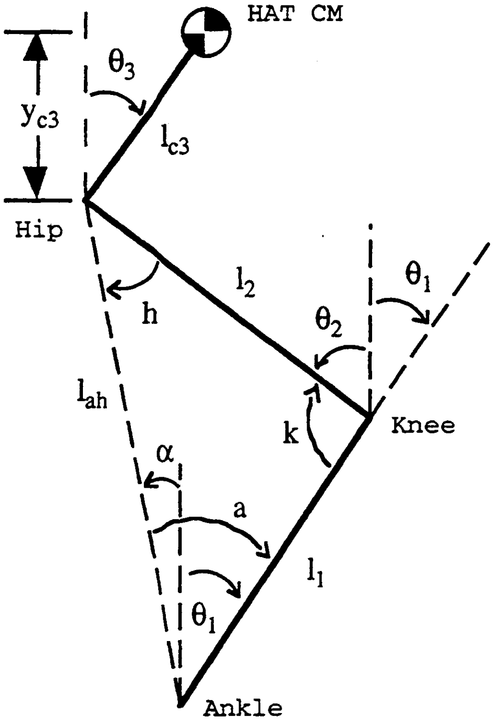

Figure 5.15. Limb geometry used to estimate joint angles for three link planar model.

The ankle coordinates are fixed at the final ankle location, using the average of the data between 300 and 350 samples following impact. At each sample, the hip location (based on the average of the left and right hips) is known, and the distance from ankle to hip (l_{ah}) is calculated. Using the known shank and thigh lengths, the interior angles of the triangle formed by the ankle, knee and hip are calculated using the law of cosines.

$$\begin{aligned} a &= \cos^{-1}\left(\frac{l_{ah}^2 + l_1^2 - l_2^2}{2 l_{ah} l_1}\right) \\ k &= \cos^{-1}\left(\frac{l_1^2 + l_2^2 - l_{ah}^2}{2 l_1 l_2}\right) \end{aligned} \tag{5-24}$$

The angle made by the vector from ankle to knee with respect to the vertical (α) is calculated from the known locations of the ankle and hip. With this information, the shank and thigh angles can be determined:

$$\begin{aligned} \theta_1 &= a - \alpha \\ \theta_2 &= \pi - k - \theta_1 \end{aligned} \tag{5-25}$$

The angle of the HAT segment is found using the vertical distance from the hip to the HAT CM. Because the estimated distance from the hip to the HAT CM varies somewhat over the course of the jump, the average length during the first 80 post-impact samples is used.

$$\theta_3 = \cos^{-1}\left(\frac{y_{c3}}{l_{c3}}\right) \tag{5-26}$$

After determining the joint angle trajectories, the angles are smoothed and differentiated using a quintic spline fit [Woltring, 1986]. Because of the high frequency content of the angle trajectories immediately following the moment of impact, the knot spacing for the spline fits is set at 5 samples for the first 30 samples after impact; the knot spacing is increased to 20 samples after this point (the knots are the values of the independent variable [sample number] used in fitting the piecewise polynomials).

5.3.3.2. *Three Link Model Stiffness and Damping Estimates*

The equilibrium point control model is extended to the three link case. The joint control torques result from deviations of the actual trajectory from the equilibrium point trajectory, based on linear stiffness and damping properties. Equation 5.27 gives the joint torques as a function of the actual and equilibrium point trajectories.

$$\begin{aligned} \mathrm{T} &= -K(\Phi - \Phi_0) - B\dot{\Phi} \\ K &= K^T = \begin{bmatrix} k_{11} & k_{12} & 0 \\ k_{21} & k_{22} & k_{23} \\ 0 & k_{23} & k_{33} \end{bmatrix} \\ B &= B^T = \begin{bmatrix} b_{11} & b_{12} & 0 \\ b_{21} & b_{22} & b_{23} \\ 0 & b_{23} & b_{33} \end{bmatrix} \end{aligned} \tag{5.27}$$

where T = vector of joint torques τ_i
$\Phi,\ \dot{\Phi}$ = vector of joint angles and rates
Φ_0 = vector of equilibrium point joint angles
K = joint stiffness matrix
B = joint damping matrix

The stiffness and damping matrices are constrained to be symmetric, meaning that the restoring forces are strictly springlike in the model and the relationship between displacement vectors and restoring force vectors is without curl. This assumption of symmetric stiffness has been tested in arm posture by Mussa-Ivaldi *et al.* [1985]; they find that the conservative components of the elastic force field are much larger than the non-conservative components. While no such tests have been performed for the lower limbs, it seems reasonable to assume that common mechanisms apply to both arm and leg posture.

The off-diagonal terms represent the interjoint coupling provided by biarticular muscles that span two joints. For example, the gastrocnemius crosses the knee and ankle joints, and the hamstrings span the hip and knee joints. Because no muscles cross all three leg joints, zero coupling between the ankle and hip joints is assumed and the terms k_{13}, k_{31}, b_{13}, b_{31} are set to zero.

Based on the symmetry of the matrices and the zero elements, 5 independent stiffness elements and 5 independent damping elements must be estimated. The joint torques T are estimated using the inverse dynamic solution given by Equation 5.22 and the coordinate transformation in Equation 5.20. Then, Equation 5.27 gives 3 simultaneous equations in 10 unknowns at each sample. Equation 27 can be rewritten in a form conducive to a least squares estimate of the unknown elements:

$$\left[\begin{array}{ccccc:ccccc} & & & & \vdots & & & & & \\ & & & & \vdots & & & & & \\ & & & & & & & & & \\ \Delta\phi_{1_p} & 0 & 0 & \Delta\phi_{2_p} & 0 & \dot{\phi}_{1_p} & 0 & 0 & \dot{\phi}_{2_p} & 0 \\ 0 & \Delta\phi_{2_p} & 0 & \Delta\phi_{1_p} & \Delta\phi_{3_p} & 0 & \dot{\phi}_{2_p} & 0 & \dot{\phi}_{1_p} & \dot{\phi}_{3_p} \\ 0 & & \Delta\phi_{3_p} & 0 & \Delta\phi_{2_p} & 0 & 0 & \dot{\phi}_{3_p} & 0 & \dot{\phi}_{2_p} \\ & & & & & & & & & \\ & & & & \vdots & & & & & \\ & & & & \vdots & & & & & \end{array}\right] \begin{bmatrix} k_{11} \\ k_{22} \\ k_{33} \\ k_{12} \\ k_{23} \\ b_{11} \\ b_{22} \\ b_{33} \\ b_{13} \\ b_{23} \end{bmatrix} = -\begin{bmatrix} \vdots \\ \\ \tau_{1_p} \\ \tau_{2_p} \\ \tau_{3_p} \\ \\ \vdots \end{bmatrix}$$

(5-28a)

where $\Delta\phi_i = \phi_i - \phi_{i0}$
ϕ_{i0} = equilibrium joint angle for joint i
p = sample number

Let the matrix quantities in Equation 5.3.11a be denoted by

$$C \cdot X = \mathrm{T} \tag{5-28b}$$

where C = matrix of joint angle deviations and joint rates
X = vector of unknown stiffness and damping elements
T = vector of joint torques

Then the best estimates of the stiffness and damping elements in a least-squares sense may be estimated by

$$\hat{X} = \left(C^T C\right)^{-1} C^T \mathrm{T} \tag{5-29}$$

where $\hat{X}$ = vector of estimated stiffness and damping elements

Each sample provides three independent equations, so at least 4 data samples are needed to estimate the 10 independent elements.

5.3.3.3. Rate Command in the Virtual Trajectory

McIntyre and Bizzi [1993] suggest a variation of the equilibrium point control hypothesis that includes the desired velocity waveform in addition to the desired position in the equilibrium trajectory used to generate muscle torques. In this variation, Equation 5-27 is rewritten to include the desired joint rates:

$$\mathrm{T} = -K(\Phi - \Phi_0) - B\left(\dot{\Phi} - \dot{\Phi}_0\right) \tag{5-30}$$

where $\dot{\Phi}_0$ = joint rate vector in equilibrium point trajectory

Likewise, the coefficient matrix C in Equation 5-28 must be altered to account for the new rate term in estimating the stiffness and damping.

$$C = \left[\begin{array}{ccccc:ccccc} & & & & & \vdots & & & & \\ & & & & & \vdots & & & & \\ \Delta\phi_{1_p} & 0 & 0 & \Delta\phi_{2_p} & 0 & \Delta\dot{\phi}_{1_p} & 0 & 0 & \Delta\dot{\phi}_{2_p} & 0 \\ 0 & \Delta\phi_{2_p} & 0 & \Delta\phi_{1_p} & \Delta\phi_{3_p} & 0 & \Delta\dot{\phi}_{2_p} & 0 & \Delta\dot{\phi}_{1_p} & \Delta\dot{\phi}_{3_p} \\ 0 & & \Delta\phi_{3_p} & 0 & \Delta\phi_{2_p} & 0 & 0 & \Delta\dot{\phi}_{3_p} & 0 & \Delta\dot{\phi}_{2_p} \\ & & & & & \vdots & & & & \\ & & & & & \vdots & & & & \end{array}\right] \tag{5-31}$$

where $\Delta\dot{\phi}_i = \dot{\phi}_i - \dot{\phi}_{i0}$

$\dot{\phi}_{i0}$ = joint rate in equilibrium point trajectory

Once again, the pseudo-inverse solution of Equation 5-29 is applied to estimate the best stiffness and damping elements.

The lack of usable free trajectory data from the ankle joint during the NO-P trials introduces a potentially serious deficiency into the stiffness and damping estimation procedure. While free trajectories are available for the knee and hip, a trajectory must be assumed for the ankle during the 100 ms following the fall through the paper. For lack of better information, the ankle equilibrium trajectory is assumed to remain constant during this time period. This assumption is considered further in the presentation of the results of the stiffness and damping fits.

5.3.3.4. Goodness of Fit for the Three Link Model

An approach similar to that used in the CM model fits defines goodness of fit measures for the three link model. In this case the correspondence between joint torques and the predicted torques from the model fits is extremely close. Therefore, the residual differences between the torques and model fits are used to enable better comparison between the two formulations of the virtual trajectory considered here (with and without rate information). The total sum-of-squares (Total SS) and residual sum of squares (Res SS) are given by:

$$
\begin{aligned}
[\text{Total SS}]_i &= \sum_s (\tau_{i_s} - \underline{\tau}_i)^2 \\
[\text{Res SS}]_i &= \sum_s (\hat{\tau}_{i_s} - \tau_{i_s})^2
\end{aligned}
\qquad (5\text{-}32)
$$

where

s = sample number
i = joint number (1=ankle, 2=knee, 3=hip)

$$
\begin{bmatrix} \hat{\tau}_{1_s} \\ \hat{\tau}_{2_s} \\ \hat{\tau}_{3_s} \end{bmatrix} = \hat{\mathrm{T}}_s = \begin{cases} -\hat{K}_s\left(\Phi_s - \Phi_{0_s}\right) - \hat{B}_s\dot{\Phi}_s & \text{(position - only VT)} \\ -\hat{K}_s\left(\Phi_s - \Phi_{0_s}\right) - \hat{B}_s(\dot{\Phi}_s - \dot{\Phi}_{0_s}) & \text{(rate in VT)} \end{cases}
$$

The goodness of fit is summarized by the term D^2, which is the squared residual error in the model fit joint torques scaled by the variance in the actual torque data. D^2 is defined here for the individual joints and for all torques combined:

$$
\begin{aligned}
D_i^2 &= \frac{[\text{Res SS}]_i}{[\text{Total SS}]_i} \\
D_{SUM}^2 &= \frac{\sum_i [\text{Res SS}]_i}{\sum_i [\text{Total SS}]_i}
\end{aligned}
\qquad (5\text{-}33)
$$

5.3.3.5. Cartesian Endpoint Impedance at the HAT CM

The joint stiffness and damping matrices can be transformed into Cartesian stiffness and damping matrices for an "endpoint" at the HAT CM. The eigenvalues and eigenvectors of the endpoint stiffness and damping matrices give the scaling and orientation of the force fields due to the elastic and viscous components at the HAT CM. This information can be presented in graphical format using ellipses to show the orientation of the eigenvectors and the scaling of the eigenvalues [Mussa-Ivaldi *et al.*, 1985].

The transformation to endpoint properties requires the Jacobian relating infinitesimal changes in joint angles to infinitesimal changes in CM HAT position:

$$\begin{bmatrix}\delta x\\ \delta y\end{bmatrix} = \begin{bmatrix} l_1\cos\theta_1 & -l_2\cos\theta_2 & l_{c3}\cos\theta_3 \\ -l_1\sin\theta_1 & -l_2\sin\theta_2 & -l_{c3}\sin\theta_3\end{bmatrix}\begin{bmatrix}\delta\theta_1\\ \delta\theta_2\\ \delta\theta_3\end{bmatrix}$$
$$\begin{bmatrix}\delta x\\ \delta y\end{bmatrix} = J_{CM_{HAT}}\begin{bmatrix}\delta\theta_1\\ \delta\theta_2\\ \delta\theta_3\end{bmatrix} \tag{5-34}$$

The Jacobian is written in terms of absolute segment angles Θ for simplicity. The endpoint compliance and endpoint stiffness are given in 5-33, after Asada and Slotine [1986].

$$C_{CM_{HAT}} = J_{CM_{HAT}} J^{-1} K^{-1} \left(J^{-1}\right)^T J_{CM_{HAT}}{}^T$$
$$K_{CM_{HAT}} = C_{CM_{HAT}}{}^{-1} \tag{5-35}$$

where $C_{CM_{HAT}}$ = Cartesian compliance matrix
$K_{CM_{HAT}}$ = Cartesian stiffness matrix
J = Jacobian matrix relating θ, ϕ coordinates

Likewise, a similar transformation may be performed to produce the endpoint damping:

$$B_{CM_{HAT}} = \left[J_{CM_{HAT}} J^{-1} B^{-1} \left(J^{-1}\right)^T J_{CM_{HAT}}{}^T\right]^{-1} \tag{5-36}$$

5.3.3.6. Estimation of Virtual Trajectories for the Three Link Model

In the case where no rate information is included in the equilibrium point muscle torque formulation, Equation 5-27 is solved for the equilibrium joint angles:

$$\Phi_0 = \Phi + \hat{K}^{-1}\left(T + \hat{B}\dot{\Phi}\right) \tag{5-37}$$

However, when the joint rates associated with the virtual trajectory are included in the muscle torque equation (5-30), an algebraic solution is not available. Equation 5-30 is a set of first order linear differential equations in Φ_0, and can be rewritten as:

$$B\dot{\Phi}_0 + K\Phi_0 = B\dot{\Phi} + K\Phi + \mathrm{T} \tag{5-38a}$$

$$\dot{\Phi}_0 = -B^{-1}K\Phi_0 + \dot{\Phi} + B^{-1}K\Phi + B^{-1}\mathrm{T} \tag{5-38b}$$

Putting Equation 5-38b in the standard state space form and replacing K and B with their respective estimates gives

$$\dot{\Phi}_0 = A_{VT}\Phi_0 + B_{VT}u \tag{5-39}$$

where

$$\begin{aligned} A_{VT} &= -\hat{B}^{-1}\hat{K} \\ B_{VT} &= \left[I_{3x3} \;\vdots\; \hat{B}^{-1}\hat{K} \;\vdots\; \hat{B}^{-1} \right] \end{aligned}$$

$$u = \begin{bmatrix} \dot{\Phi} \\ -- \\ \Phi \\ -- \\ \mathrm{T} \end{bmatrix}$$

Equation 5-39 is easily solved in Matlab, using the free trajectory joint angles from the NO-P jumps as the initial conditions for Φ_0.

5.3.4. Three Link Model Results

The impedance estimates for the three link model are based on the estimated torques at the leg joints following impact, and these torque estimates are presented first. Next, the stiffness and damping fits based on the free trajectory data from the NO-P jumps are shown. The selection of the ankle virtual trajectory is discussed in this context. The joint stiffness and damping estimates are transformed into corresponding HAT CM endpoint stiffness and damping matrices, and the results are presented. Virtual trajectories are estimated for the single subject whose data give positive definite stiffness and damping.

5.3.4.1. Estimated Joint Torques

The joint torque histories at the ankle, knee and hip are estimated using the inverse dynamic solution to Equation 5.22. Figure 5.16 shows the average joint torques found by combining the data from all 6 subjects. The average measured vertical ground reaction force is included for comparison. The ankle and hip torque histories are very similar in shape, with high extensional torques immediately following impact. These extensional torques decrease rapidly, approaching zero and even becoming slightly flexional at the hip.

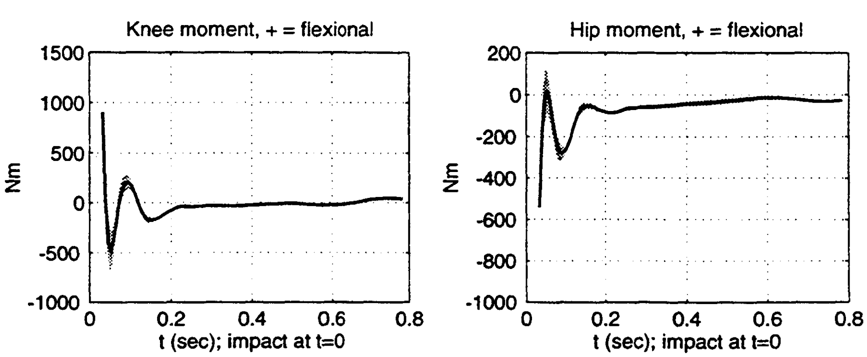

Figure 5.16. All-subject average of three link model joint torques after landing. Means are shown (solid line) within a shaded area indicating ±1 standard error of the mean. Positive torques are flexional.

Based on this model, the ankle torques at this point become strongly flexional for a short time. The high level of ankle flexion torque found here are probably not realistic for the actual subject, because the maximum available torque at the ankle is constrained by the length of the foot. This is especially true for flexional ankle torques, because the short distance between the ankle and the back of the foot results in lifting of the toes when moderate ankle flexion torques are applied. However, in this model the ankle is pinned to the floor and no constraints are placed on the ankle torque.

Following the peak in the hip and ankle torques, the torques at these joints again become extensional, increasing to a maximum then decreasing toward zero through the rest of the recovery phase. The knee pattern is almost exactly opposite that seen at the other two joints. Initially, a high flexion torque is exerted at the knee, which decreases quickly and becomes extensional. Peak extensional torque is reached at the time of peak flexional torque at the ankle and knee. From this level, the torque decreases and becomes flexional again, reaching a new high point at the time when the ankle and hip extension torques are maximized. The knee torque then becomes extensional and remains so for the remainder of the recovery period.

The pattern seen in the joint torques reflects the vertical GRF history. The flexional peaks at the ankle and hip, together with the extensional peak at the knee, correspond to the initial dip in the ground reaction force. Likewise, the subsequent extensional torque maxima at the ankle and hip together with the peak in knee flexional torque correspond to the second peak in the vertical GRF.

5.3.4.2. Joint Impedance Estimates (Position-Only Virtual Trajectory)

Using the joint torque estimates, best fit joint stiffness and damping matrices are estimated first for the version of the equilibrium point hypothesis that uses only position information in the virtual trajectory. In order to perform the impedance fits, an equilibrium trajectory for the ankle must be assumed. A constant value is used here for the ankle angle equilibrium trajectory. In order to determine what this constant should be, fits are performed using several different ankle equilibrium angles. Ten samples are used for the stiffness and damping fits. Because the equations are overdetermined for 4 or more samples, the joint torques predicted by the best fit stiffness and damping differ somewhat from the torques estimated directly from the data. A torque error term is constructed by summing the squared difference between the predicted and estimated torques.

The torque error is assessed for each of the equilibrium ankle angles, and is plotted for subject *djn* in Figure 5.17. The torque error exhibits a fairly broad minimum centered at approximately 3° of ankle flexion, indicating that using this value for the impedance fits predicts joint torques that are the most consistent with the actual estimated torques. Similar assessments for the other subjects also show error minima for ankle angles near zero degrees, so the ankle equilibrium trajectory is set to zero for the stiffness and damping estimates for all subjects.

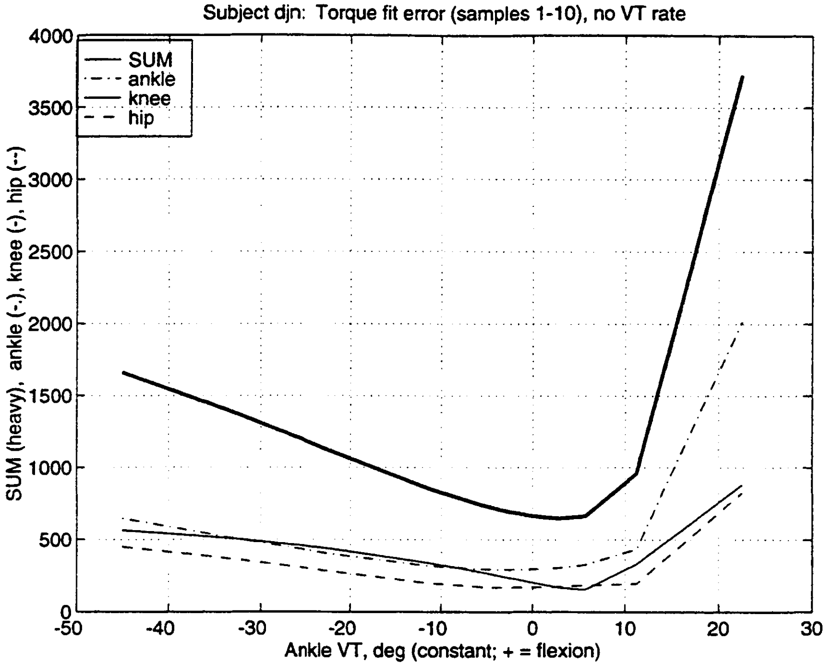

Figure 5.17. Torque fit error for different assigned ankle equilibrium angles. Summed squared errors are shown for each joint individually as a function of the value set for the ankle equilibrium, as well as for all joints combined (SUM). Best fit for this subject corresponds to the minimum at 3° ankle flexion.

Joint stiffness and damping matrices are estimated over the 10 samples available from the NO-P free trajectories. Five samples are used in each least-squares fit; a centered fit is performed for each sample in the range 8-13 using data from samples 6-15 (~30-90 ms after impact; sample 1 corresponds to impact). The eigenvalues of the stiffness and damping matrices are calculated for each fit. The stiffness eigenvalues are shown in Figure 5.18a for each subject. For 5 of the 6 subjects, one or more of the stiffness eigenvalues is negative throughout the range of samples fit. A negative eigenvalue corresponds to a negative stiffness in the direction of one of the eigenvectors of the stiffness matrix. In 4 of these 5 subjects, the minimum eigenvalue is most negative at the beginning of the samples fit, and increases toward zero over the course of the next 5 samples. Only one subject's data (*ssy*) gives a positive definite stiffness matrix (all eigenvalues positive). In this case, the stiffness is positive definite over the entire range of samples fit.

a. Joint stiffness eigenvalues

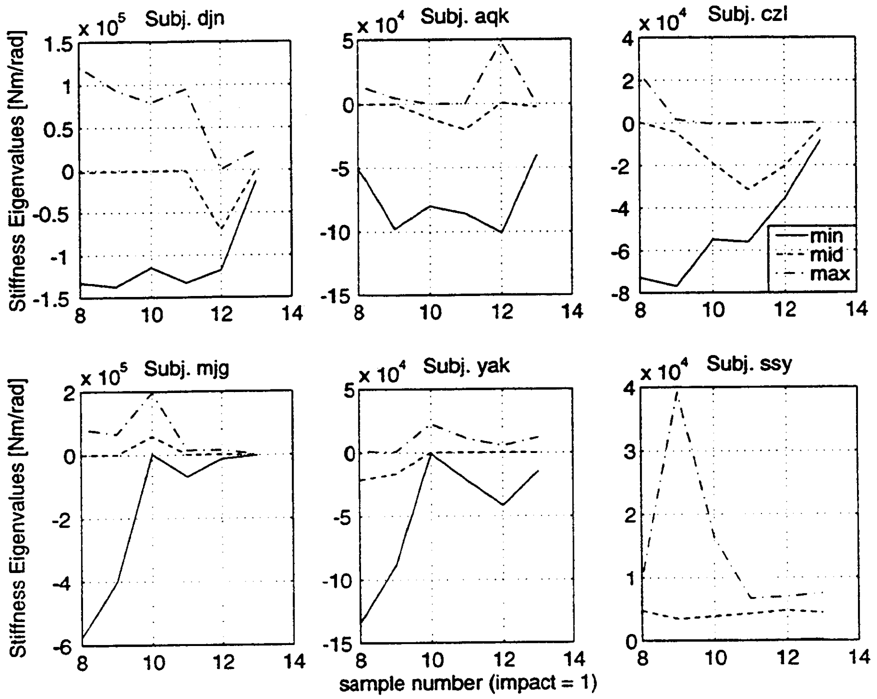

b. Joint damping eigenvalues

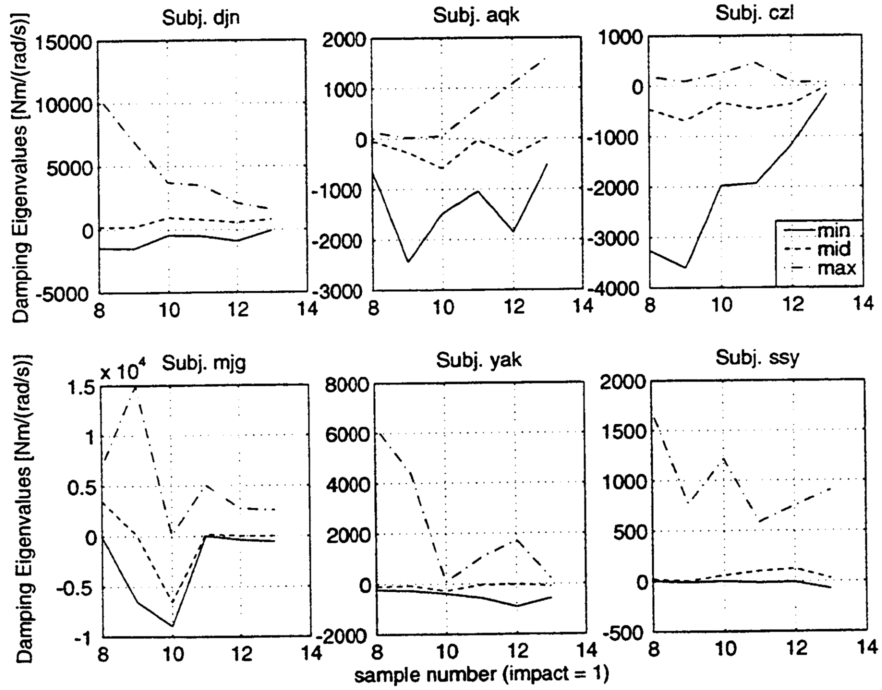

Figure 5.18. Joint impedance estimates for three link model, all subjects. Eigenvalues for the 3x3 stiffness (a) and damping (b) matrices are shown.

A corresponding plot of the damping matrix eigenvalues for each subject is found in Figure 5.18b. As with the stiffness, all subjects except *ssy* are found to have one or more damping eigenvalues that remain negative throughout the fit period. Even subject *ssy* 's damping matrix has an eigenvalue that becomes negative at some samples in this period. In 4 of the 6 subjects (*djn, mjg, yak, ssy*) the maximum damping eigenvalue tends to decrease over the course of the fit period.

Table 5.3 shows the goodness of fit measures for each subject for the joint torques, as computed from Equations 5-32 and 5-33. The scaled residual SS is shown for the individual joint torques and for all torques combined. The residual error is quite small, and is generally only a fraction of a percent of the variance in the joint torques.

Table 5.3. Goodness of fit measures for three link model fits (position-only VT). The ratio D^2 indicates the size of the residual errors in proportion to the variance in the torque data. Goodness of fit is shown for the individual joint torques and all three torques combined.

	Subject	***djn***	***aqk***	***mjg***	***czl***	***yak***	***ssy***
Ankle	Total SS	8.19e+6	4.94e+6	2.55e+7	1.41e+7	2.55e+6	6.28e+5
	Res SS	4.28e+3	2.97e+3	1.56e+5	1.14e+3	7.08e+2	6.49e+1
	D^2	0.05%	0.06%	0.61%	0.01%	0.03%	0.01%
Knee	Total SS	3.23e+6	1.57e+6	1.03e+7	5.94e+6	8.78e+5	6.02e+5
	Res SS	1.66e+3	4.72e+2	9.25e+4	1.88e+3	6.62e+2	6.74e+1
	D^2	0.05%	0.03%	0.90%	0.03%	0.08%	0.01%
Hip	Total SS	4.99e+5	2.46e+5	2.04e+6	1.58e+6	1.49e+5	3.90e+5
	Res SS	1.55e+3	2.42e+3	1.05e+5	3.27e+3	3.15e+2	7.82e+1
	D^2	0.31%	0.99%	5.14%	0.21%	0.21%	0.02%
All Joints	Total SS	1.19e+7	6.75e+6	3.79e+7	2.16e+7	3.58e+6	1.62e+6
	Res SS	7.49e+3	5.87e+3	3.53e+5	6.29e+3	1.69e+3	2.10e+2
	D^2_{SUM}	0.06%	0.09%	0.93%	0.03%	0.05%	0.01%

Figure 5.19 presents averages over all subjects of the minimum, middle and maximum stiffness and damping eigenvalues. These averages show more clearly the trends observed in the individual subjects. The minimum stiffness and damping eigenvalues are negative throughout, although they tend to be most strongly negative early in the period tested, then increase toward zero. Averages of the diagonal terms in the

stiffness and damping matrices are presented as well; each diagonal element represents the torque-angle relationship at an individual joint due only to motion about that joint. The trends in the diagonal terms generally match the eigenvalue results.

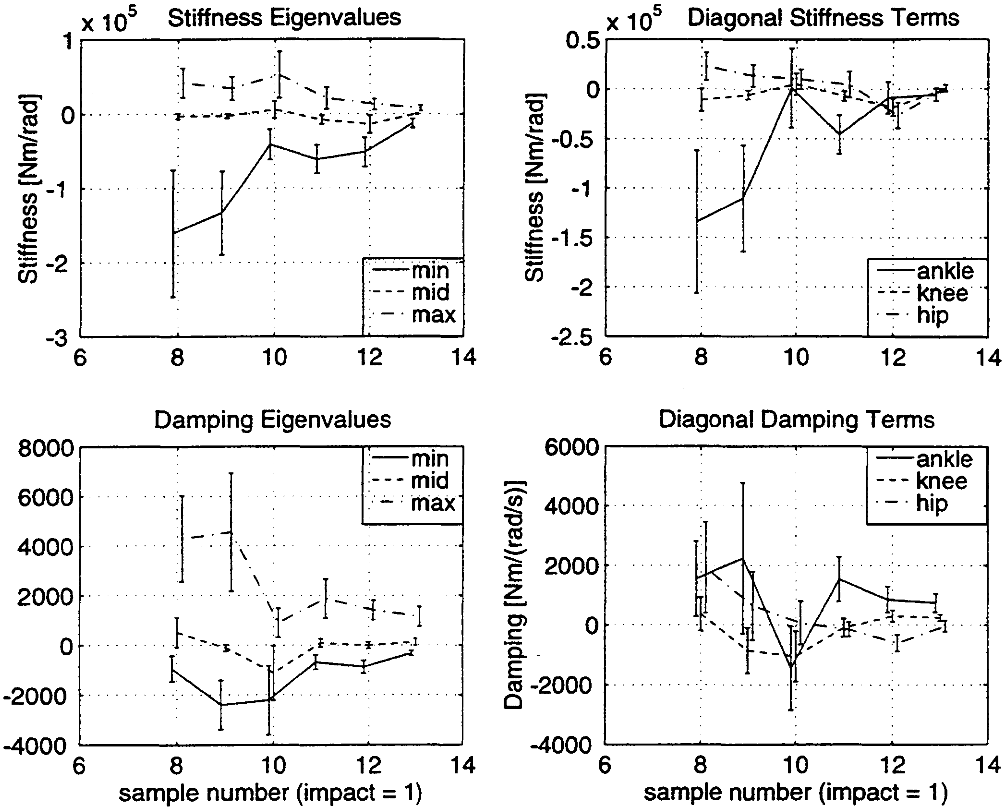

Figure 5.19. All-subject averages of joint stiffness and damping estimates. Averages of the stiffness and damping eigenvalues (left) are shown with error bars indicating one standard error of the mean. Averages of the diagonal terms in the stiffness and damping matrices are shown at right.

5.3.4.3. Cartesian Impedance at the HAT CM (Position-Only VT)

Using the results of Equations 5-35 and 5-36, the Cartesian stiffness and damping properties at the HAT CM are calculated from the joint stiffness and damping estimates. The Cartesian impedance properties depend on the link configuration as well as the joint impedance. Figure 5.20 shows the Cartesian stiffness and damping at the HAT CM graphically for subject *ssy* for the samples immediately following impact. The major and minor axes of the ellipses correspond to the directions of the eigenvectors associated with the maximum and minimum eigenvalues respectively.

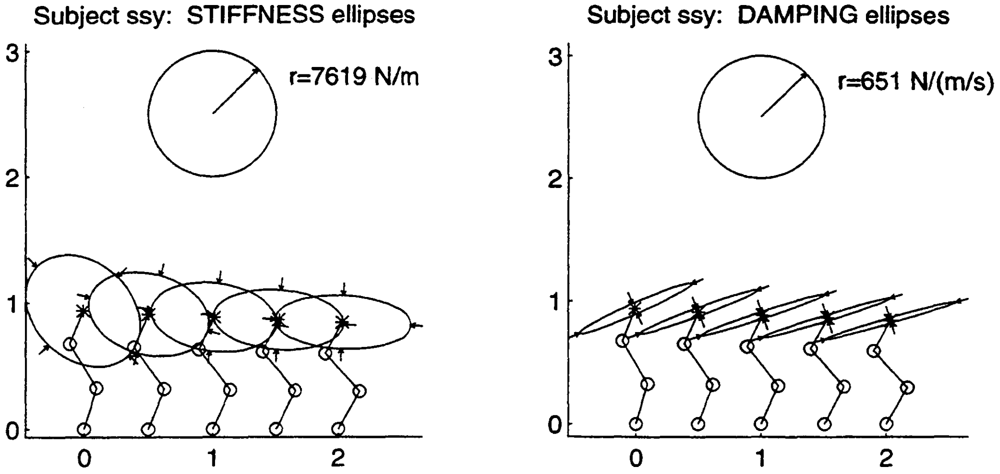

Figure 5.20. HAT CM cartesian endpoint stiffness and damping ellipses. Ellipses are shown for the estimated joint stiffness and damping at samples 7, 9, 11, 13 and 15 after impact. Ellipses are centered at the HAT CM, and the scale for the ellipses are shown by the circles above. The configuration of the three links at each sample is shown as well. Inward-pointing arrows indicate positive endpoint stiffness and damping eigenvalues.

The stiffness is greatest in the direction along the major axis, and least in the perpendicular direction. The arrows pointing inward at the endpoints of the major and minor axes indicate that the stiffness and damping are positive. A positive stiffness implies that a perturbation of the endpoint will resort in a restoring force. Likewise, positive damping generates a force that resists the velocity of the endpoint. The restoring force is only aligned with the direction of the perturbation if the perturbation is along the major or minor axis of the ellipse.

In the case of subject *ssy*, the positive definite endpoint stiffness and damping matrices are expected because her joint stiffness and damping matrices were also positive definite. Note, however, that even if the Cartesian stiffness and damping are positive definite, horizontal and vertical motion of the HAT CM only describe two of the three degrees of freedom of the model. The third degree of freedom is associated with the rotation of the HAT segment about its CM. Even though the translational stiffnesses and damping may be positive, the impedance properties related to this third degree of freedom will be negative if the joint stiffness and damping matrices are not positive definite.

The vertical stiffness and damping estimates for the HAT CM correspond to the k_{yy} elements of the Cartesian HAT CM stiffness and damping matrices. These vertical impedance values are averaged across subjects and shown in Figure 5.21. They are plotted together with the averaged vertical GRF to show the relative timing of the changes. The vertical stiffness average is negative during the period of decline toward the early dip in the vertical GRF, and becomes positive for the samples during which the GRF is increasing toward the second peak.

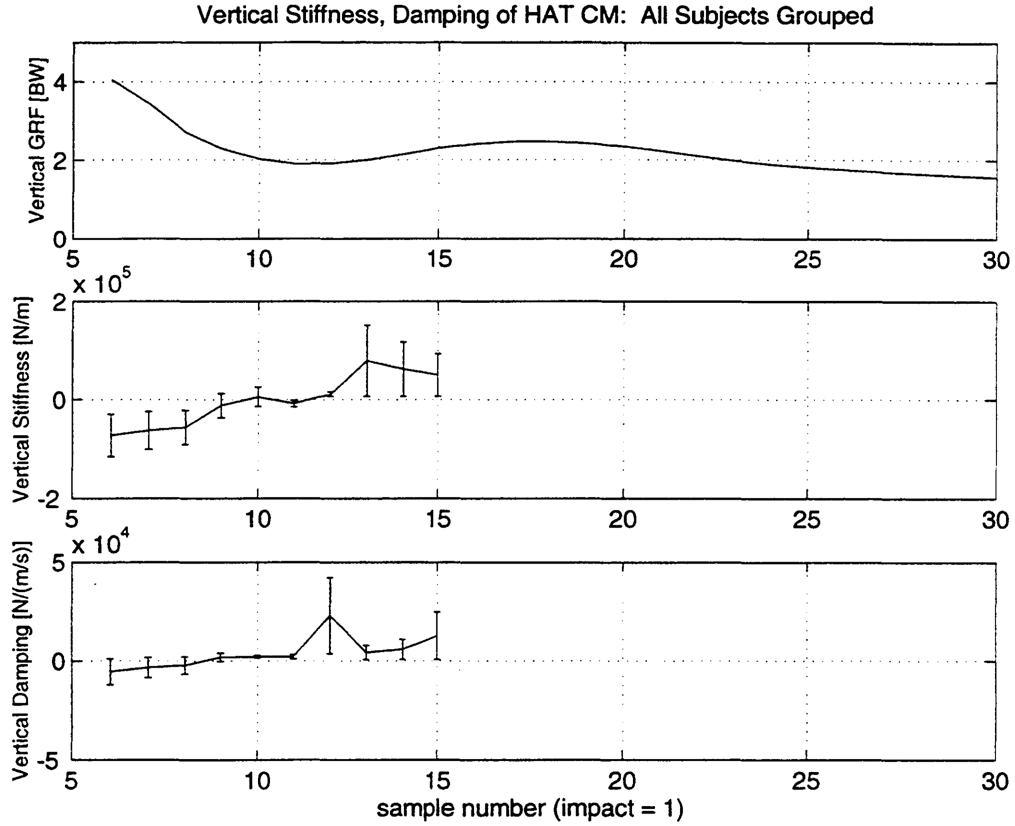

Figure 5.21. All-subject averages of the HAT CM vertical endpoint impedance. Vertical components of the HAT CM endpoint Cartesian stiffness (middle) and damping (bottom) are shown with the vertical GRF (top). Error bars indicate ±1 standard error of the mean.

Figure 5.22a presents the vertical stiffness estimates at the HAT CM for the individual subjects. Four of the subjects (*djn, aqk, czl, mjg*) have negative vertical stiffness in the early samples that become positive toward the end of the interval. The vertical stiffnesses for *yak* and *ssy* are positive throughout. The vertical damping estimates for the HAT CM are shown in Figure 5.22b. No trends are readily apparent, although negative vertical damping estimates are observed for subjects *djn, czl, mjg,* and *yak.*

a. HAT CM vertical endpoint stiffness

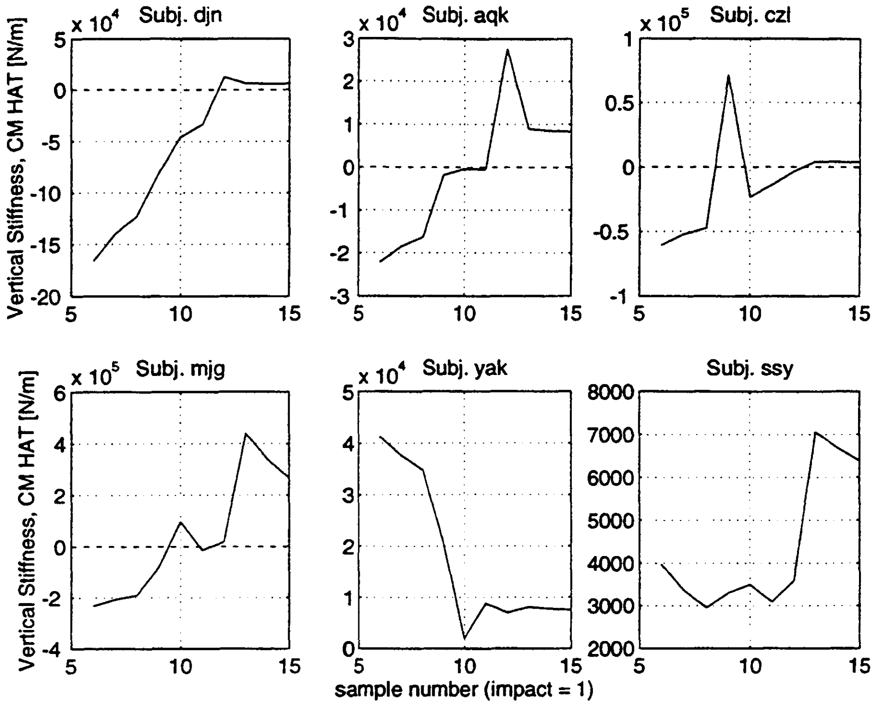

b. HAT CM vertical endpoint damping

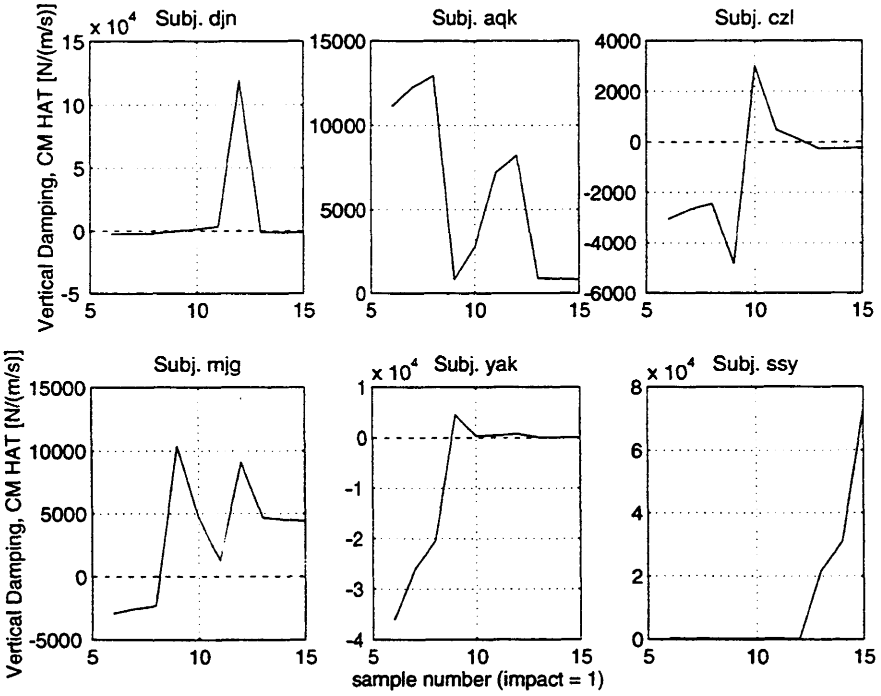

Figure 5.22. Individual subject HAT CM endpoint vertical impedances.
a. Vertical component of the Cartesian endpoint stiffness at the HAT CM.
b. Vertical component of the Cartesian endpoint damping at the HAT CM.

5.3.4.4. Estimated Joint VTs for Subject ssy *(Position-Only VT)*

Subject *ssy* is the only subject for whom positive definite stiffness and damping matrices are found, and hence is the only subject for whom meaningful virtual trajectories may be computed. First, virtual trajectories are computed using the formulation of the equilibrium point control hypothesis (Equation 5-27) that uses only the position of the equilibrium point. Constant joint stiffness and damping matrices are assumed throughout the trajectory. Figure 5.23a shows the equilibrium point trajectories in relative joint angle coordinates, plotted against the P and NO-P joint trajectories.

For each of the joints, the virtual trajectory exhibits a brief period of extension, with the minimum flexion point corresponding to the time of the peak in the vertical GRF. At the knee, the VT is actually hyperextended briefly, reaching a peak angle of 20°. Each angle VT then exhibits a period of rapid flexion lasting approximately 80 ms, followed by a slow extension toward zero flexion angle. In the case of the ankle and knee, the VT actually crosses zero, reaching approximately 5° of extension at the ankle and 25° of hyperextension at the knee. It is clear that the virtual trajectories in joint space are not simple monotonic functions that return to the upright standing position. The equilibrium trajectory transformed into HAT CM translation is shown in Figure 5.23b. The VTs are not simple in this coordinate system either, exhibiting multiple peaks and valleys.

5.3.4.5. Virtual Trajectories Incorporating Rate Commands

An analysis comparable to that of the proceeding sections is performed for the extension of the equilibrium point hypothesis that postulates the incorporation of rate information into the virtual trajectories, as described in Section 5.3.3.3. Figure 5.24a shows the average stiffness and damping matrix results for all subjects combined using the stiffness and damping estimation procedure from Equations 5-29 and 5-31. Likewise, the estimated stiffness eigenvalues for this formulation of the equilibrium point hypothesis are presented in Figure 5.24b for the individual subjects. As in the case where the VT uses only a position command, negative stiffness and damping eigenvalues are found for all subjects except *ssy*. Much more variability among subjects is observed for this formulation, as judged from the error bars in Figure 5.24b.

The goodness of fit measures for this version of the equilibrium point model are contained in Table 5.4. As before, the ratio of the residual squared errors in the model joint torques to the variance of the torque data is computed. The results indicate that the residual errors are very small compared to the variance in the joint torques, demonstrating that the torque fits are generally very good for this model.

a. Virtual trajectory in joint coordinates

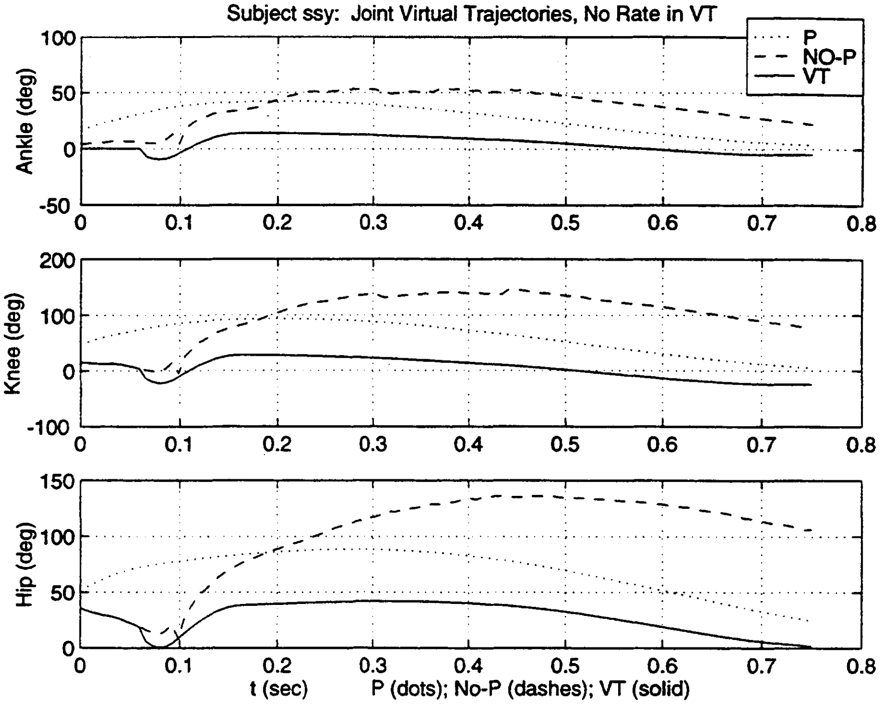

b. Virtual trajectory in HAT CM Cartesian coordinates

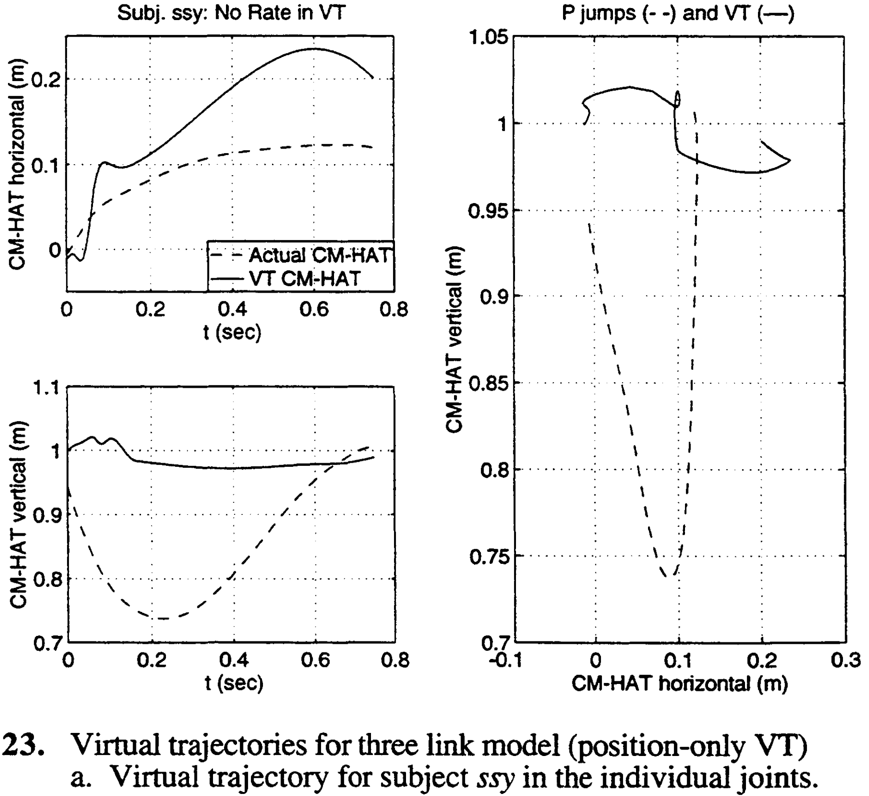

Figure 5.23. Virtual trajectories for three link model (position-only VT)
a. Virtual trajectory for subject *ssy* in the individual joints.
b. Virtual trajectory for *ssy* transformed into HAT CM Cartesian coordinates.

a. impedance properties averaged across subjects

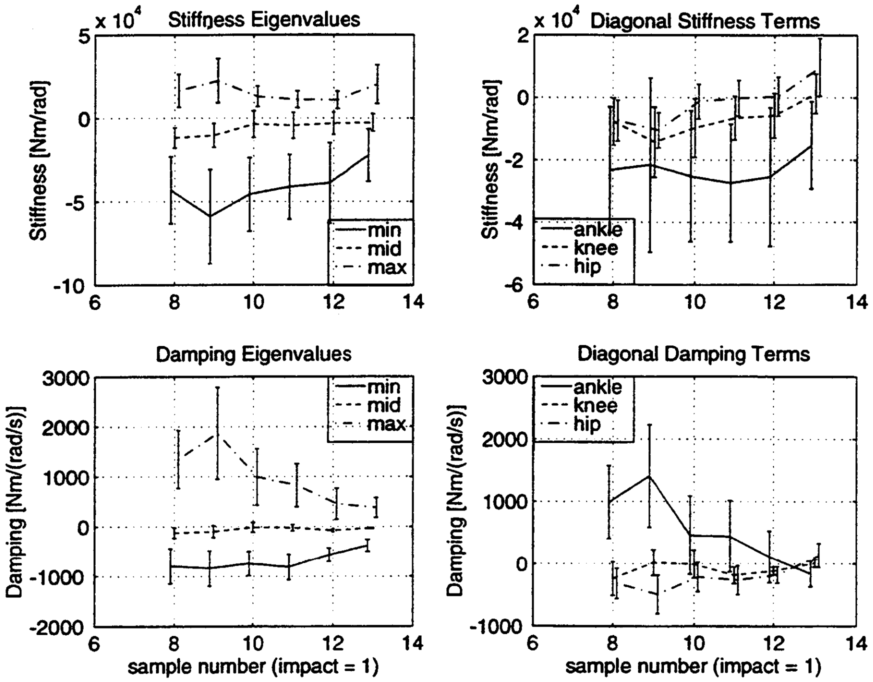

b. Stiffness eigenvalues for individual subjects

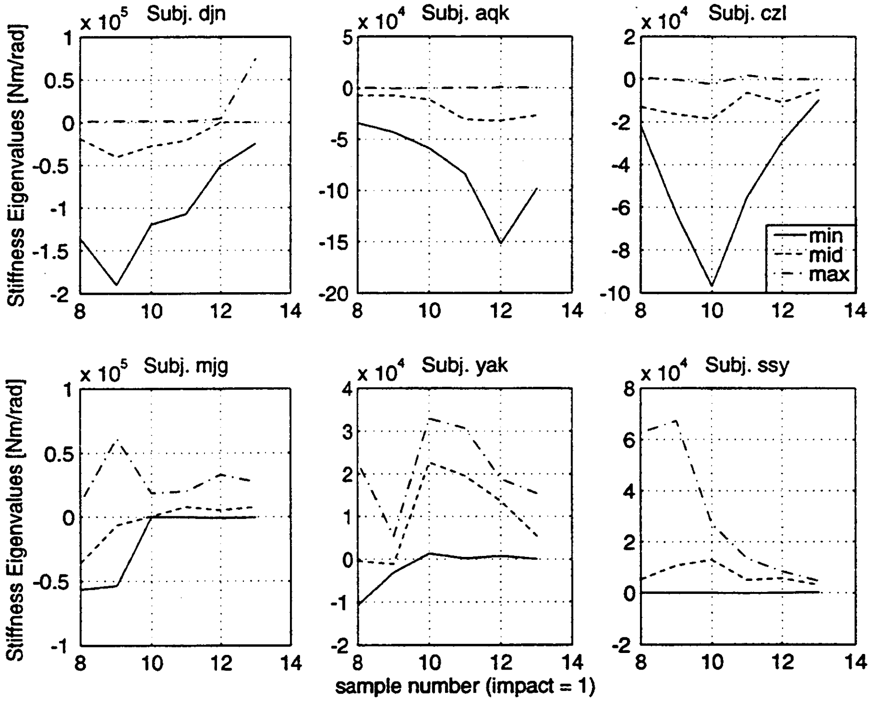

Figure 5.24. Impedance estimates for VT incorporating joint rates
a. Stiffness and damping eigenvalues and matrix diagonal elements averaged across all subjects. b. Stiffness eigenvalues for individual subjects.

Table 5.4. Goodness of fit measures for three link model fits (rate command in VT). The ratio D^2 indicates the size of the residual errors in proportion to the variance in the torque data. Goodness of fit is shown for the individual joint torques and all three torques combined.

	Subject	***djn***	***aqk***	***mjg***	***czl***	***yak***	***ssy***
Ankle	Total SS	8.19e+6	4.94e+6	2.55e+7	1.41e+7	2.55e+6	6.28e+5
	Res SS	6.87e+3	5.08e+3	1.43e+5	1.21e+4	2.58e+3	5.72e+2
	D^2	0.08%	0.10%	0.56%	0.09%	0.10%	0.09%
Knee	Total SS	3.23e+6	1.57e+6	1.03e+7	5.94e+6	8.78e+5	6.02e+5
	Res SS	1.35e+3	3.30e+3	2.33e+5	1.06e+3	8.57e+2	2.77e+2
	D^2	0.04%	0.21%	2.26%	0.02%	0.10%	0.05%
Hip	Total SS	4.99e+5	2.46e+5	2.04e+6	1.58e+6	1.49e+5	3.90e+5
	Res SS	9.94e+2	1.02e+3	1.04e+6	1.94e+2	1.27e+3	1.74e+2
	D^2	0.20%	0.41%	51.12%	0.01%	0.85%	0.04%
All Joints	Total SS	1.19e+7	6.75e+6	3.79e+7	2.16e+7	3.58e+6	1.62e+6
	Res SS	9.21e+3	9.39e+3	1.42e+6	1.33e+4	4.71e+3	1.02e+3
	D^2_{SUM}	0.08%	0.14%	3.75%	0.06%	0.13%	0.06%

Equilibrium point trajectories are estimated using the joint torque formulation (Equation 5-30) that incorporates the joint rates in the equilibrium trajectory. Figure 5.25a presents the VTs derived using this variation of the equilibrium point hypothesis. The results are considerably different than in the case where the angles alone are used. At each joint, an initial hyperextension is seen in the VT, although the motion is less abrupt than that seen in the position-only VT case above. The ankle extension reaches approximately 10°, while the knee VT hyperextension reaches almost 30°. The hyperextension in the hip VT is less than 10°. Following maximum (hyper)extension, the ankle and knee angles show a period of slow flexion and re-extension, before declining slowly toward zero. The joint angles are hyperextended past zero throughout. At the hip, a slow flexion of the joint takes place, reaching a maximum flexion of approximately 20° before decreasing slowly toward zero. The equilibrium point trajectory of the HAT CM is shown in Figure 5.25b. The horizontal and vertical range of the equilibrium points is smaller in extent than seen for the no-rate case; in general, the VTs that incorporate the joint rates are more highly damped.

a. Virtual trajectory in joint coordinates

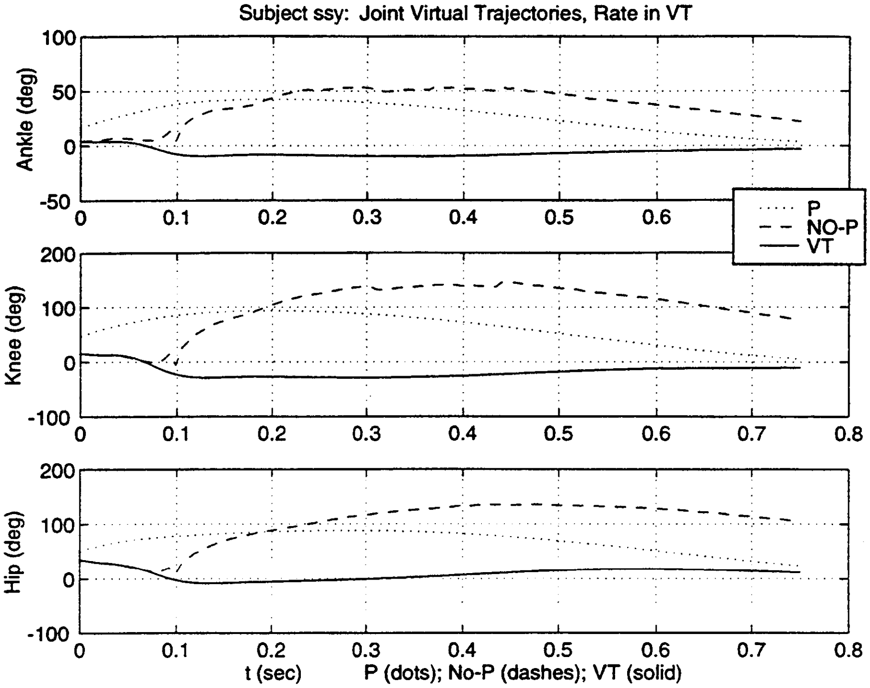

b. Virtual trajectory in HAT CM Cartesian coordinates

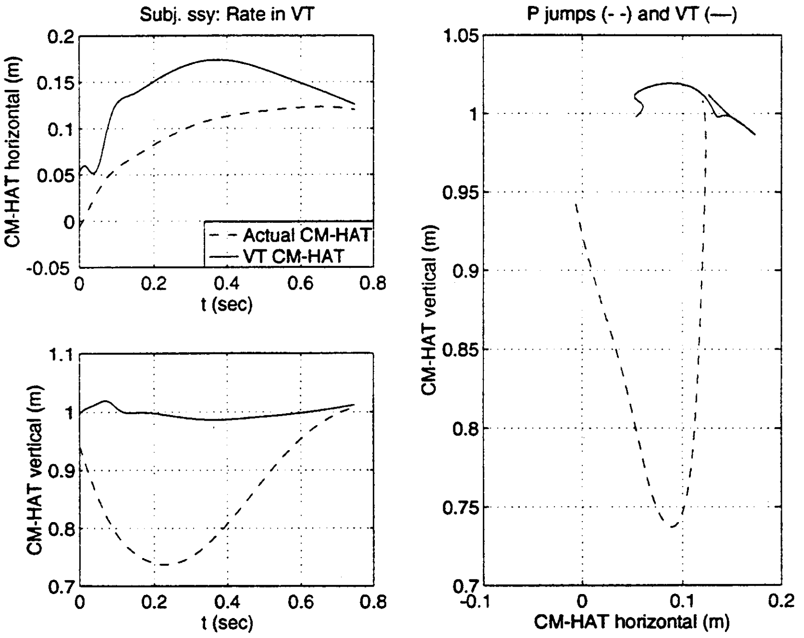

Figure 5.25. Virtual trajectories for three link model (rate incorporated in VT)
a. Virtual trajectory for subject *ssy* in the individual joints.
b. Virtual trajectory for *ssy* transformed into HAT CM Cartesian coordinates.

5.4. DISCUSSION OF JUMP LANDING MODELS

Three different models of the dynamics of human jump landings have been presented here. Each model represents the human body at a different degree of complexity, and the equilibrium point hypothesis is used in each case to estimate impedance properties in the context of the model. The implications of the model fits are discussed in the following sections. First, the relative merits of the two models of vertical CM motion (Models 1 and 2) are considered. Next, the distinction between formulation of the VT with and without rate command is evaluated for Model 3. Finally, the most interesting finding from the model fits is discussed: the prevalence of estimated negative stiffness for all three models.

5.4.1. Two Models of CM Vertical Motion

Model 1 describes the restoring force generation in the legs as the action of a linear spring. The results of the astronaut jumping experiments indicate that fixing the equilibrium spring length and spring stiffness at constant values can provide good fits to the transient impact response or to the final resting position, but not both (see Figure 3.10). Stiffnesses that give good fits to the early portion of the impact response, during which the legs are flexed, predict final CM rest positions that lie below the experimental results. A related difficulty is seen in the VT estimates using this model: in order to replicate the measured CM trajectories using the estimated stiffnesses, the final equilibrium spring length reaches a level considerably longer than the physical height of the CM above the feet (see Figure 5.7).

Both of these limitations appear to result from the assumption of a constant force spring. As a compound linkage, the human body approaches a singular position near upright posture. Theoretically, the stiffness along the axis from the head to the feet should increase to infinity as the singular position is reached. Experimentally, Greene and McMahon [1979] do observe a substantial variation in the vertical body stiffness for different amounts of leg flexion. A nonlinear spring that softens with increasing compression should help to remedy the shortcomings associated with Model 1.

Greene and McMahon [1979] use a model incorporating a linear spring about the knee joint to fit their data; Model 2 in the current study is a simplification of their model. In Model 2, the CM VT estimates cannot require physiologically unrealistic leg lengths (see Figure 5.11). Moreover, the joint angle VTs (see Figure 5.12) show that the knee joint VT remains well within physiological extension limits for all subjects but *ssy*. In this respect, Model 2 improves on Model 1.

Model 2 effectively provides a nonlinear spring that softens with increasing compression. Fits to the experimental data for subject *mjg*'s P jumps are compared in Figure 5.26a for Model 1 and Model 2 using constant stiffness, constant equlibrium point springs (linear in Model 1; torsional in Model 2). In this test constant stiffness, damping and equilibrium spring setting parameters are estimated for each model using a procedure comparable to that described for the astronaut jumping experiments. The result observed for astronaut jumping for Model 1 also appears to hold for Model 2: stiffness values that allow good fits to the final rest position in upright standing results in substantial deviations from the actual CM trajectories during the transient portion of the impact response.

The differences between the model responses and actual trajectories for each model are shown in Figure 5.26b. This plot shows that the fit deviations from the jump data are very similar for the two models, while the summed squared errors (shown on the plot for each jump) are generally slightly larger for Model 2. However, examination of the difference between the fits and the actual trajectories shows that the steady-state position for Model 1 consistently lies below the actual CM rest position, while such a difference is not observed in Model 2. (The dashed horizontal line shown for each trace in Figure 5.26b indicates perfect correspondence between the model and the data.) Thus, Model 2 does appear to provide somewhat better steady-state results than Model 1. Although this test of one subject's results is not exhaustive, it suggests that the effective nonlinear vertical spring of Model 2 cannot fully resolve the conflict between transient and steady-state performance seen for Model 1 with a constant stiffness, constant equilibrium length spring.

The systematic damped sinusoidal nature of the discrepancies between the model fits and actual jump data indicates that the models fail to capture a mode of the actual system. It appears that a higher order model of the system dynamics would better represent the actual impact responses. Models 1 and 2 for the human body are in fact gross simplifications of a truly high order system. Even the dynamics of individual muscles are known to have higher than second order dynamics [Hill, 1922]. Greene and McMahon [1979] add a second spring to their model in series with the leg, because they find that the vertical stiffness of the body in upright standing is only about 4 times greater than with the knees flexed 90° (rather than becoming infinite in the fully extended posture). The additional series spring compliance allows them to fit their experimentally measured stiffness data, and also introduces a second vibratory mode for the system. A similar addition to the CM motion models derived here could conceivably help to match the jump landing responses. Nevertheless, given their extreme simplicity, the capability of Models 1 and 2 to represent the CM jump landing dynamics as well as they do is quite impressive.

a. CM trajectories and model fits

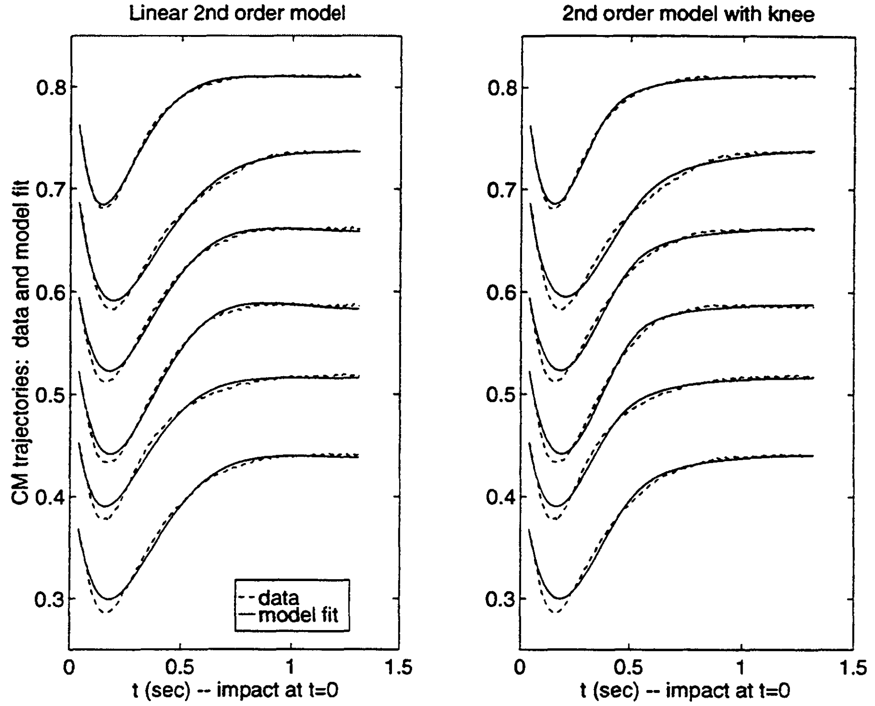

b. Residual differences between model fits and data

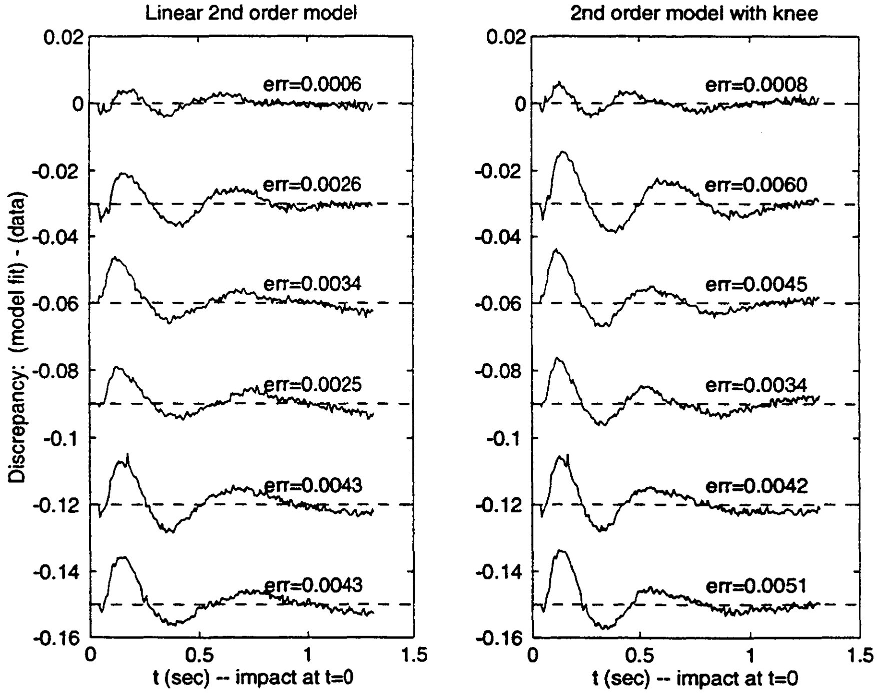

Figure 5.26. Comparison of Models 1 and 2 for constant-parameter fits.
a. Model 1 (left) and Model 2 (right) fits to P jump CM trajectories.
b. Discrepancies and summed squared error values for Models 1 and 2.

5.4.2. Control of Velocity in the Virtual Trajectory

McIntyre and Bizzi [1993] have suggested that the equilibrium point hypothesis be extended to include desired velocity information in the formulation of the VT. This proposal appears plausible, and they show that it can help to explain the control of fast arm movements. Furthermore, robotic trajectory tracking control algorithms generally make use of the desired velocity and even acceleration to improve tracking performance [Asada and Slotine, 1986].

This modification of the VT is evaluated here using the three link model. Figure 5.27 compares the goodness of fit measures for VTs with and without rate information, plotting the ratio of the residual SS for the rate-supplemented VT to the residual SS for the position-only VT. Values greater than one indicate poorer performance for the rate-supplemented VT. Although both models provide torque estimates that match closely with the experimental data, the quality of the fits is generally worse for the version of the equilibrium point hypothesis that includes the term for the velocity of the virtual trajectory. The overall performance of the rate-supplemented VT version is worse for all subjects than the comparable position-only VT result, and the total errors are more than twice as large in 4 of the subjects for the rate-supplemented VT. The individual joint torque results show that the position-only VT provides better model fits for 5 of 6 subjects at the ankle, 4 of 6 subjects at the knee and 3 of 6 subjects at the hip. Hence, at least for this model the addition of rate information to the VT does not improve the fidelity of the model fits.

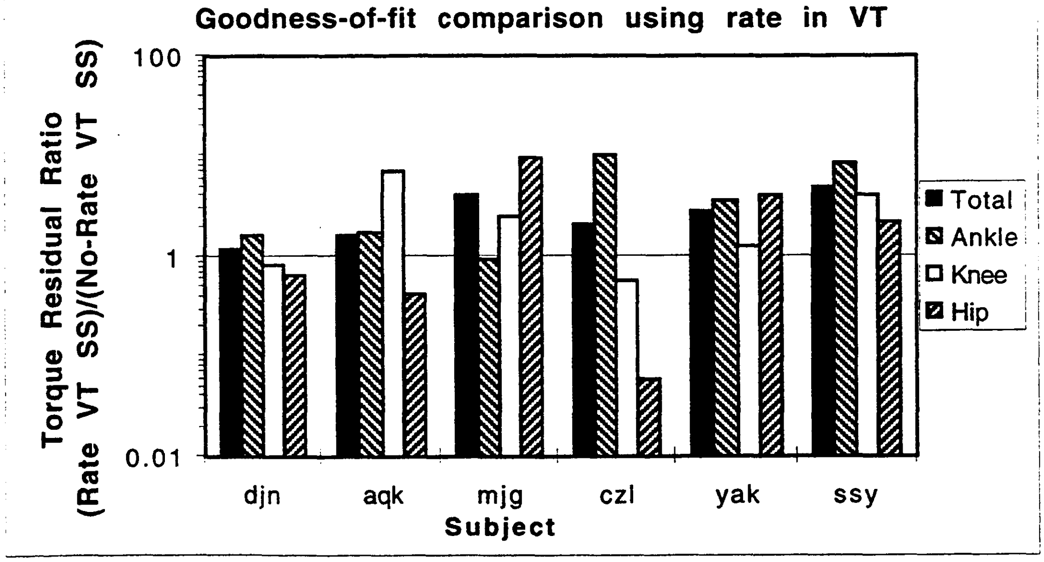

Figure 5.27. Goodness of fit for VTs with and without rate information. Ratio of residual SS for models with and without the rate in the VT. Values greater than 1 denote worse fits for the rate-supplemented VT.

The original position-only VT formulation produces estimated stiffness and damping matrices that generally are not positive definite. Since positive definite results are required for stable control under the equlibrium point hypothesis, one reason for testing incorporation of the rate term into the VT is to determine whether this extension can generate positive definite stiffness and damping estimates. The outcome of the model fits using the rate-supplemented VT formulation shows that negative stiffness and damping eigenvalues still result, so no improvement over the original position-only formulation is observed in this regard for the three link model.

5.4.3. Negative Stiffness and the Equilibrium Point Hypothesis

The most surprising and puzzling result from the various models is the prevalence of negative stiffness estimates. Using the simple linear second order model (Model 1), all of the subjects exhibit negative stiffnesses over some range of samples in the region examined. For three of the six subjects, the average stiffness over the whole region (10 samples) is negative. However, the negative stiffnesses are generally confined to the time corresponding to the sharp initial drop in the vertical GRF. The stiffness estimates are found to be positive at the end of the region tested for all subjects, indicating that the negative stiffness is of limited temporal duration, at least using this model.

Using the three link model, however, the situation appears much worse. When the joint stiffness matrix is transformed into an endpoint stiffness at the HAT CM, the diagonal vertical component k_{yy} shows the same behavior as the vertical stiffness for the CM vertical model: negative stiffness over the early portion of the region corresponding to the decreasing region of the vertical GRF, followed by gradually increasing positive stiffness values as the GRF starts to rise again. Unfortunately, looking only at this single component of the endpoint stiffness hides a deeper problem with the joint stiffnesses: for 5 of the 6 subjects, at least one of the joint stiffness eigenvalues is negative throughout the region examined.

When the stiffness is negative in the equilibrium point formulation used here, the system becomes unstable. The equilibrium trajectory is no longer a stable attractor. Rather, a force is exerted along the direction of the eigenvector corresponding to the negative eigenvalue that tends to magnify any perturbation in that direction. Clearly, though, the real system must be stable in a global sense. The stiffness estimates correpond to a time segment ending 100 ms after impact. The body obviously recovers to an stable upright stance and remains there. Models of CM vertical motion that fit a constant equilibrium spring position give positive stiffness and damping values, and replicate the main features of the CM trajectory. Nevertheless, the combination of the measured NO-P trajectory and the measured forceplate or estimated joint torques stubbornly produces negative stiffness estimates over the 100 ms interval following impact.

In the following sections, three implications of the negative stiffness estimates are considered. First, the negative stiffnesses may simply be the erroneous results of inadequate models, poor equilibrium point estimates, or errors introduced by the numerical fits. However, the negative stiffnesses may in fact accurately represent the mechanical properties of the system, and evidence from other studies is introduced to support this view. Finally, the implications of negative stiffness for stable trajectory control via the equilibrium point hypothesis are discussed.

5.4.3.1. Potential Sources of Error in Impedance Estimates

At least two major criticisms of the methods used to estimate stiffness and damping can be made: (1) the models are inadequate to capture the important dynamics of the system, and (2) the assumption that the equilibrium point follows the free trajectories of the NO-P jumps may be invalid. The first complaint may strike hardest at the weaknesses of the three link model. Although this model does manage to replicate faithfully the CM motions and GRFs, the method used to determine the joint angles for this model is somewhat questionable, as it relies largely on the position of three points: the hip joint, the ankle joint and the HAT CM. Matches to the actual joint angles are not exact, and the discrepancies may introduce errors into the inverse dynamics calculations as the joint angles are differentiated twice.

The unrealistically high ankle flexor torques computed from this model provide an example of the potential errors that might be introduced. Furthermore, since the estimated torques are used in the stiffness and damping calculations, these calculations may also be compromised. In comparison, the relatively simple CM vertical motion model incorporating a linear spring and damper is probably less susceptible to these sorts of modeling errors. The model fit does not require a double differentiation of the position data because the actual vertical GRFs are measured, and the virtual trajectory is estimated from the ankle joint and the body CM, a calculation less dependent on the types of assumptions made to provide kinematic data for the three link model.

Aside from issues regarding numerical limitations, the validity of using of low-order, time-varying linear models of force and torque generation to describe the dynamics of a nonlinear system of unknown but high order is questionable. The shape of the vertical

GRF traces in the Type 2 jump landings cannot be replicated by a passive linear system of second order (see Figure 4.9). Similarly, the systematic damped sinusoid pattern of the residual errors between the actual CM trajectory and the fits for Models 1 and 2 (see Figure 5.26) indicates that higher order models are needed to capture the behavior of the system. The use of a second order model of force generation to estimate impedance properties for a system of higher order may have unpredictable consequences.

Furthermore, the time-varying linear models of force and torque generation used in the present models ignore the known nonlinearities in the length-dependent and velocity-dependent behavior of passive and active muscle. While such simplified models have been used successfully to model free arm reaching motions under the equilibrium point hypothesis [Flash, 1987; Bizzi *et al.*, 1992], the current results show that these models may well prove inadequate for the considerably different dynamics associated with full-body motion and ground contact during jump landings. Winters *et al.* [1988] use a physiologically based, nonlinear 8th order antagonistic muscle model of elbow joint motion under various conditions. They conclude that incorporation into the model of nonlinearities in parallel and series elasticity and in the position- and velocity-dependent behavior of the contractile tissue is necessary to simulate adequately a number of different tasks.

Their work suggests that higher order models incorporating fundamental nonlinearities are required for sufficient representation of the actual functioning of muscle-joint systems. Likewise, a recent study by Gribble *et al.* [1997] finds that simple straight-line equilbrium trajectories in the lambda equilibrium point version can be used to generate realistic arm motions for a model that incorporates nonlinearities associated with muscle moment arm variations, muscle force-length and force-velocity dependence, and graded development of muscle force. They also show that attempts to reconstruct the virtual trajectory using simplified models of force and torque generation result in virtual trajectory estimates that are substantially different from the actual trajectory used to drive the model. The authors conclude that inferences about the form of control signals depend strongly upon the nature of the representation of the neuromuscular plant. Like Winters *et al.* [1988], they stress that results regarding impedance properties and equilibrium point control obtained from overly simple models must be treated with caution.

The assumption made here that the equilibrium point trajectory is close to the NO-P jump free trajectory is also questionable. If the equilibrium point trajectory is in fact far from the free trajectory of the limbs, the stiffness and damping estimates will be in error and may even change sign, resulting in negative estimates of positive quantities. However, the assumption is probably valid if the limb stiffness is high enough that the difference between the free trajectory and the equilibrium trajectory is small relative to the difference between the free trajectory and the P impact trajectory. The question should be explored further, and forms the basis for one of the concluding recommendations for future work.

This question is also difficult to address in the context of the CM motion models. Because the lumped CM sits on ideal springs that have no internal dynamics, the virtual trajectory is equal to the free trajectory by definition. Of course, this model effectively ignores the actual dynamics of the legs, and this omission my have serious consequences for a realistic estimate of the virtual trajectory.

5.4.3.2. Supporting Evidence for Negative Stiffness in Jump Landings

In spite of the difficulties discussed above, the possibility that the estimated negative stiffnesses are representative of the true situation should not be dismissed. Negative stiffness has been observed at the individual muscle level and at the joint level. Other researchers reports negative muscle, joint and full body stiffness for jump landings in both monkeys and humans.

First, negative muscle stiffness has been described in submaximally contracted muscles subjected to high velocity stretch [Rack, 1981]. In these experiments, the stiffness of a muscle stretched by a muscle puller depends on initial length, stretch velocity and stimulus frequency in a complex manner. An *et al.* [1989] show as well that many muscles under a fixed activation level exhibit negative stiffness over much of the physiological length range. At the joint level, Winters *et al.* [1988] build a convincing case against incautious application of an equilibrium point formulation dependent on antagonistic springs characterized by activation-dependent length-tension curves. They find that (1) the parallel elastic stiffness is small in the primary joint operating range, and (2) the torque-angle relation at various joints has a low and often negative slope over large segments of the operating range, especially for major extensors.

Dyhre-Poulsen and Laursen [1984] study monkeys landing on their arms from downward jumps. They find that the incremental muscle stiffness in the triceps increases to a high initial value over the first 10 ms following impact, then decreases and becomes negative for the remainder of the landing. In a later study, Dyhre-Poulsen *et al.* [1991] find a similar result in humans jumping down. Again, the muscle stiffness in the ankle joint increases over the first 10 ms, then decreases and became negative for the remainder of the impact. In both monkeys and humans, the investigators attribute the initial high positive stiffness (as well as part of the initial sharp rise in vertical ground reaction force) to the short-range stiffness [Rack and Westbury, 1974] before cross-bridges are broken. The total body stiffness is also estimated for the human study, and the calculation shows that the total body stiffness is very low or negative in the region when ankle stiffness is negative.

Dyhre-Poulsen and his colleagues suggest that the negative stiffnesses are generated intentionally based on the deceleration requirements for a jump landing. They contrast the pattern seen for jump landings with the results seen for repetitive hopping [Dhyre-Poulen *et al.*, 1991]. In repetitive hopping, undamped spring-like properties in the leg are desireable. The ground reaction forces resemble those that would be expected for a mass dropped onto a spring, with the peak force occurring simultaneously with the maximum downward CM deflection. Conversion of kinetic energy into elastic energy stored in tendon and muscle is desirable, so that the upward hop can make use of the stored potential energy. In the hopping tests, they perform the same stiffness calculations, and estimate positive stiffnesses throughout the ground contact time.

In jump landings, however, the goal is to dissipate the kinetic energy rather than store it as elastic potential energy. The vertical GRF traces are very different from those seen in hopping, with the sharp early peaks that match the high velocity portion of the jump rather than the peak deflection. Thus, true spring-like behavior would be far from ideal in jump landings. Dyhre-Poulsen *et al.* [1991] hypothesize that the negative stiffness is in effect designed to convert the muscles into damping units.

Indirect support for this hypothesis is provided by the postulated inhibition of post-impact extensor reflex activity in different species. Evidence exists that the segmental stretch reflexes act to maintain muscle stiffness at relatively constant level [Houk, 1979]. Inhibition of the stretch reflex would therefore prevent the feedback needed to restore positive stiffness in the muscles, sustaining the low or negative muscle stiffness levels. In their human study, Dyhre-Poulsen *et al.* [1991] show that the H-reflex is strongly inhibited prior to and during ground contact for jump landings. In contrast, the H-reflex excitability in repetitive hopping increases before touchdown and remains relatively high during the stance phase. The H-reflex excitability level is believed to represent the efficacy of transmission from Ia afferents to α motoneurons, and hence a measure of stretch reflex potentiation. Thus, the investigators conclude that the H-reflex results in landing reflect stretch reflex suppression, while the hopping data indicate that the stiffness regulation effected by stretch reflexes is desirable in that task.

The H-reflex results are consistent with findings by Melvill Jones and Watt [1971a] that the FSR appears to be inhibited during downward steps, while preferred hopping frequencies seem to favor timing that makes the best use of the FSR. In monkeys [Dyhre-Poulsen and Laursen, 1984] and in cats [McKinley and Smith, 1983], the post-landing extensor activity appears to be suppressed as well, in agreement with the human data. In sum, these data provide a strong circumstantial case for the importance of negative stiffness properties in the impact absorption phase of jumps.

5.4.3.3. Implications of Negative Stiffness for Equilibrium Point Control

The requirement for positive definite stiffness in the neighborhood of an attractor point has been the focus of some criticism of the equilibrium point control hypothesis [Adamovich, 1992; Hasan, 1992]. Indeed, as Bizzi *et al.* [1992a] admit, "... the equilibrium-point hypothesis makes the assumption that during movement as well as posture the limbs exhibit stability. Note that this is not a requirement for the motion of a mechanical system. Nor is it a fundamental requirement for a biological system ...."

The negative stiffness results obtained in the present false platform study indicate that for the current models the equilibrium point hypothesis alone does not suffice to explain the control of jump landings. In fact, the attractive simplicity obtained through formulation of the equilibrium point hypothesis as a servomechanism [McIntyre and Bizzi, 1993] may limit the utility of the hypothesis. By requiring a virtual trajectory of the same form as the desired trajectory, the controller must ignore the dynamics of the system. However, there is considerable evidence that the motor control system does in fact take into account known dynamic properties of the body [Flanagan and Wing, 1993; Shadmehr and Mussa-Ivaldi, 1994]. Anticipatory postural reactions in advance of fast arm movements provide a ready example [Gurfinkel, 1994].

Other authors suggest that the equilibrium trajectory may account for limb dynamics by assuming a form that deviates from the desired trajectory, giving "N-shaped" virtual trajectories for single joint movements [Latash and Gottlieb, 1991]. Variations on feedforward control strategies have been postulated [Kuo and Zajac, 1992b; Gutman and Gottlieb, 1992]. Gottlieb *et al.* [1996] and Lackner and DiZio [1994] argue that voluntary motion explicitly accounts for expected movement dynamics and externally imposed forces, and may actually plan movements in terms of muscle activation patterns.

5.5. OPTIMALITY CONSIDERATIONS IN JUMP LANDINGS

One goal of this thesis is to show that an optimization procedure based on a set of physically and biomechanically plausible variables can reproduce important features of the experimentally observed trajectories for jump landings. Specific optimization criteria to be examined include center of mass excursions, joint motion, joint torques and impact forces. Optimality of the jump landing trajectories is considered in the context of two models. First, vertical motion of the full body CM is examined using a linear quadratic regulator (LQR) approach. Next, the optimal control problem for the three link model is formulated in terms of a parameter optimization problem. Effects of variations in the cost functionals for the optimizations are discussed.

5.5.1. Vertical Motion of the Full Body Mass Center

The simplest model of the jump landing phase consists of the vertical motion of fully body CM. Two forces act on the CM: gravity and the force exerted by the legs. The differential equation governing the CM motion can be written

$$\begin{aligned} m\ddot{y}_{cm} &= F + mg \\ \ddot{y}_{cm} &= u = \frac{F}{m} + g \end{aligned} \tag{5-40}$$

where y_{cm} = vertical deviation of the CM from the final rest position (0)
F = leg force on CM
u = acceleration of the CM
g = gravitational acceleration = $-9.8\ \mathrm{m/s^2}$

Equation 5.40 can be written in state space form:

$$\begin{aligned} \begin{bmatrix} \dot{y}_{cm} \\ \ddot{y}_{cm} \end{bmatrix} &= A \begin{bmatrix} y_{cm} \\ \dot{y}_{cm} \end{bmatrix} + Bu \\ A &= \begin{bmatrix} 0 & 1 \\ 0 & 0 \end{bmatrix} \\ B &= \begin{bmatrix} 0 \\ 1 \end{bmatrix} \end{aligned} \tag{5-41}$$

A simplistic description of the control objective in landing from a jump might be: "Return the CM to the upright stance position while limiting the forces exerted by the legs." The tradeoff between the amount of deviation of the mass center from the final position and the magnitude of the CM acceleration can be expressed mathematically as an objective function to be minimized. An objective function where the cost is quadratic in the state variables $(y_{cm}, \dot{y}_{cm})$ and the control variable (u) is given in Equation 5-42:

$$J = \int_{t=t_0}^{\infty} \left(\begin{bmatrix} y_{cm} & \dot{y}_{cm} \end{bmatrix} Q \begin{bmatrix} y_{cm} \\ y_{cm} \end{bmatrix} + Ru^2 \right) dt \tag{5-42}$$

$$Q = \begin{bmatrix} Q_p & 0 \\ 0 & Q_v \end{bmatrix}$$

where R = scalar force weight
Q_p = position weight
Q_v = velocity weight

The optimal control law for this linear quadratic regulator (LQR) problem [Kwakernaak and Sivan, 1972] is given in steady state by

$$\begin{aligned} u &= -G \begin{bmatrix} y_{cm} \\ y_{cm} \end{bmatrix} \\ G &= R^{-1} B^T K \end{aligned} \tag{5-43}$$

where G is the vector of optimal state feedback gains and K is the unique positive definite solution to the algebraic Ricatti equation

$$Q + KA + A^T K - KBR^{-1} B^T K = 0 \tag{5-44}$$

The approach taken here is to determine nominal cost weights $\overline{Q}, \overline{R}$ that give the best match to the experimental jump data, then vary the weights about the nominal to examine the effects on the CM trajectory and control forces. Nominal weights are found using a Nelder-Meade simplex search method. At each step in the search, the optimal gains are calculated using the current weights, and the model response is simulated. An objective function is constructed from the sum of the squared differences between the model CM position response and the experimental data points at each integration step. The numerical search algorithm attempts to minimize this objective function.

This procedure is performed using a representative subject, *djn*. The CM trajectory used in the model fit is the average of selected P jumps (the selection procedure is described in Section 4.2.1.6). Likewise, the vertical GRF shown throughout is the average for these same P jumps. Based on the simplex search, the nominal weights are determined to be:

$$\begin{aligned} \overline{Q} &= \begin{bmatrix} \overline{Q}_p & 0 \\ 0 & \overline{Q}_v \end{bmatrix} = \begin{bmatrix} 1 & 0 \\ 0 & 0.0165 \end{bmatrix} \\ \overline{R} &= 2.804 \times 10^{-4} \end{aligned} \tag{5-45}$$

The closed-loop poles found using the optimal feedback gains are located at -6.3±4.4i, resulting in a natural frequency and damping ratio of

$$\begin{aligned} \omega_n &= 7.73\, s^{-1} \\ \varsigma &= 0.82 \end{aligned} \tag{5-46}$$

Figure 5.28 shows the model fit compared to the experimental data using the feedback gains determined from the nominal weights $\overline{Q}, \overline{R}$. The LQR solution gives a reasonable fit to the experimental CM trajectory. As expected, however, the vertical GRF predicted by the simple model only replicates the gross behavior of the experimentally measured GRF. The second order LQR model predicts a smooth decay of the GRF, and cannot account for the dip and second peak seen in the actual experimental data.

Effects of variations in the cost function weights on the CM vertical trajectory are shown in Figure 5.29. The plots on the left describe the effect of changes on the relative weighting of CM position deviation and CM acceleration. The bold traces indicate the nominal weights that best fit the experimental data. As CM deviation is penalized more heavily relative to the CM force, the CM position deviates less from zero, and returns more quickly to the zero position. The time from impact to maximum downward deflection of the CM decreases, as does the settling time toward the final equilibrium position. Consequently, the peak ground reaction force is seen to increase, and the GRF drops sharply due to the faster response in the CM trajectory. The GRF also exhibits a larger undershoot below the 1 body weight level, corresponding to the higher deceleration as the CM moves upward toward the final position.

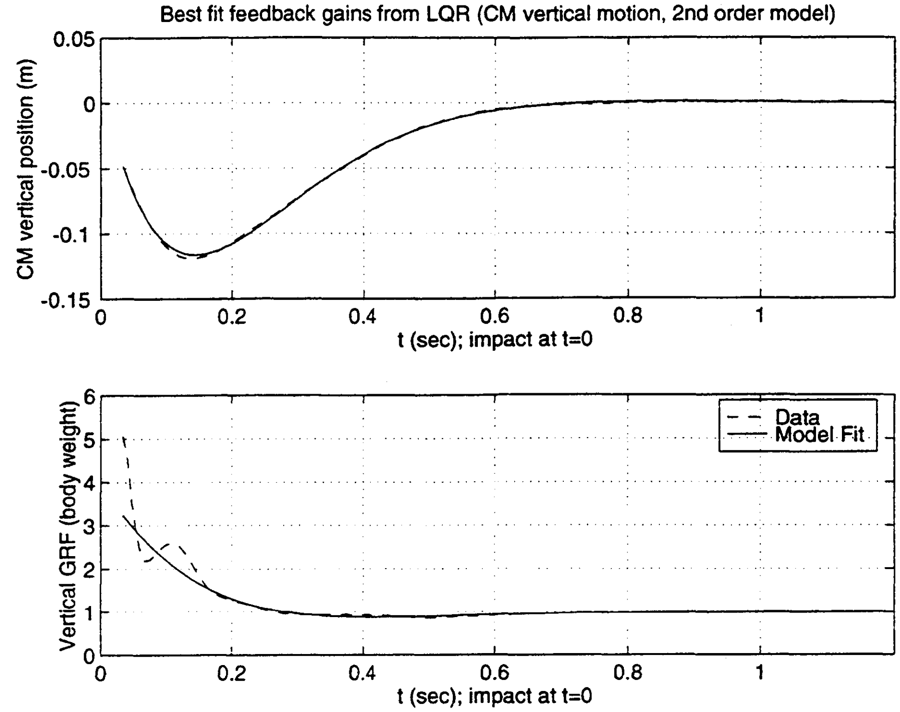

Figure 5.28. Comparison of data and model simulation for best-fit LQR weights. CM trajectory (top) and vertical ground reaction force (bottom) for model simulation using LQR weights that give the best fit to experimental data.

Alterations in the relative costs on CM deviation and CM acceleration largely affect the natural frequency of the response. In contrast, change in the relative cost on CM deviation relative to CM velocity greatly affects the damping ratio of the closed loop system. The plots on the right in Figure 5.29 show the effect of changes in the relative costs on position and velocity. As velocity is penalized more heavily relative to position deviation, two effects are seen. First, the maximum downward deflection of the CM is reduced, reflecting the large penalty associated with high downward velocities, and the time to reach the CM minimum decreases. The higher penalty associated with CM velocity also causes a slower return to the equilibrium position, resulting in a more heavily damped response. With an increase in the relative velocity penalty, the peak ground reaction force in increased, reflecting the more abrupt deceleration of the CM downward motion. In this case, however, the increased peak GRF is associated with a smaller undershoot below the 1 body weight level, corresponding to the more highly damped response.

Figure 5.30 summarizes the main effects of the variation in the relative costs of CM position, velocity, and force. The CM position deviates less from zero as position is weighted more heavily relative to force; however, smaller deviation of the CM from zero is also seen when position is penalized less relative to CM velocity. Smaller CM deviations from zero correspond to shorter times from impact to peak CM deflection; reduced times to CM minimum result from increased penalty on CM position deviation relative to force, or increased penalty on CM velocity relative to position.

Smaller CM deviations and shorter times to CM minimum require larger peak GRFs, and an increase in peak GRF may result from a higher penalty on CM deviation relative to force. Alternatively, the increase in force may result from a higher cost placed on the CM vertical velocity relative to the position deviation. However, these two cases exhibit different patterns for the GRF undershoot below 1 body weight. In the more heavily damped response, corresponding to the increased relative penalty on CM velocity, the undershoot is less pronounced. In contrast, increase in the CM position cost relative to force results in a less damped response with a more prominent undershoot in the GRF.

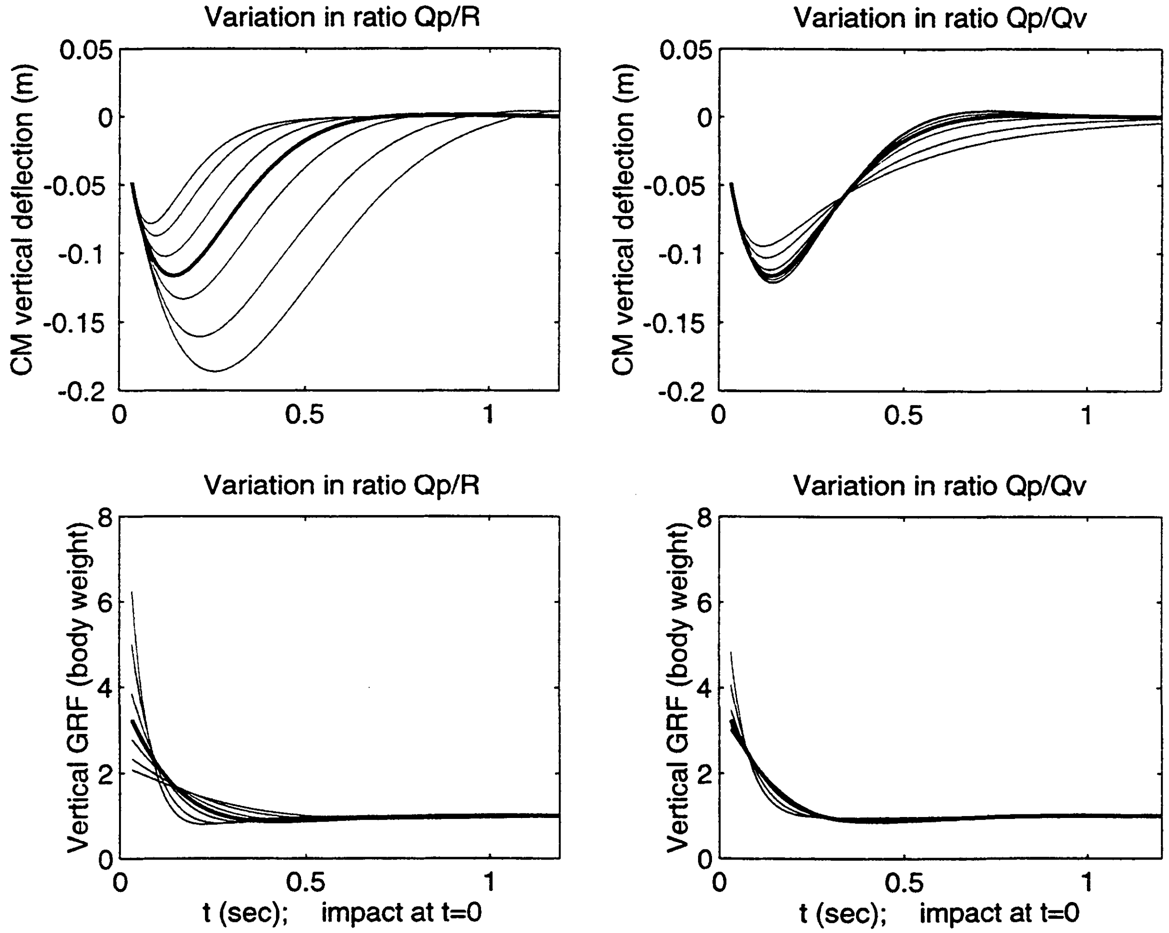

Figure 5.29. Effects of variation in relative LQR weights on model simulations. Relative variation of position and force weights (left) and position and velocity weights (right); CM (top) and vertical GRFs (bottom). Bold traces represent baseline weights that best fit experimental data.

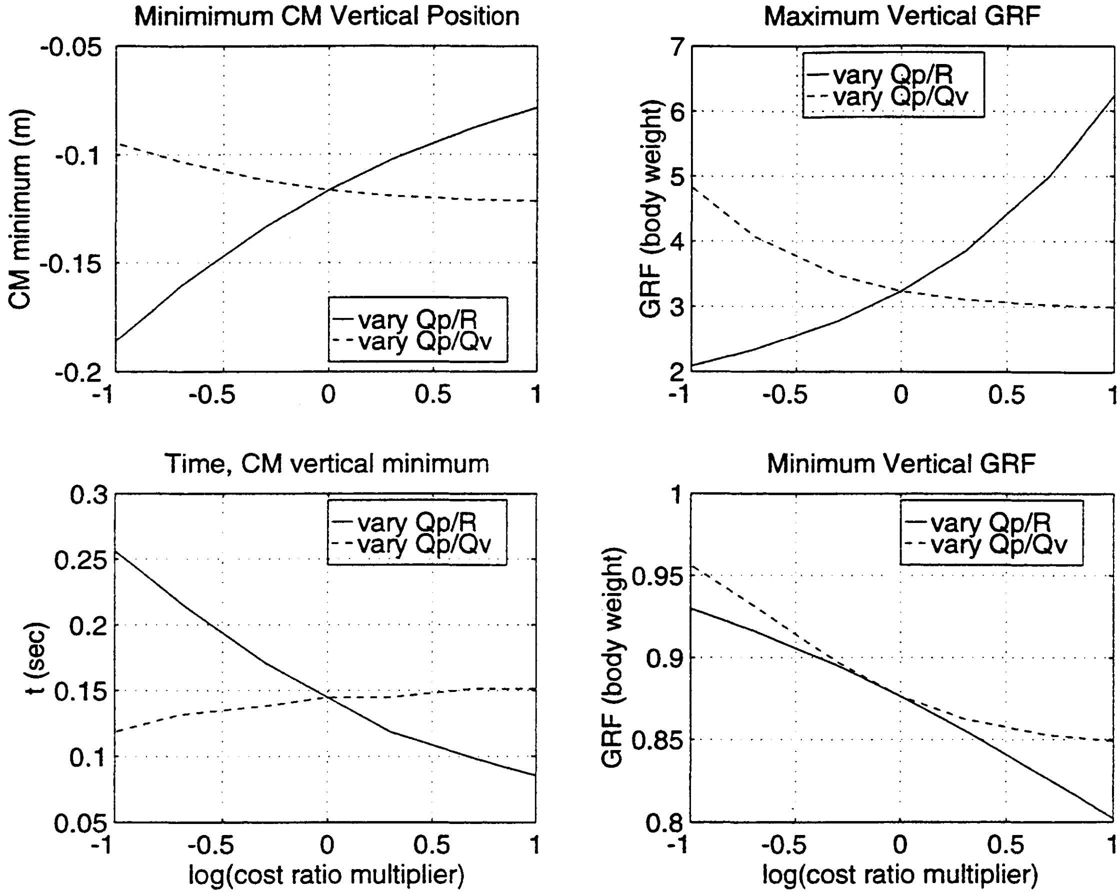

Figure 5.30. Summary of LQR weight variations on CM and GRF behavior. Effects of relative variation of the weights on minimum CM vertical position (upper left), the time to reach CM minimum (lower left), maximum vertical GRF (upper right), and minimum GRF (lower right).

5.5.2. Optimal Landing Trajectories for the Three Link Planar Model

As with the CM vertical motion model, the goal is to show that the important features of the experimental data can be replicated in trajectories of the more realistic three link model that are optimal according to an objective function based on physiologically plausible variables. In a manner analogous to the approach used for the CM vertical motion model, an objective function is constructed based on the states and control inputs for the three link model.

In this case, determination of the trajectory for the three link model that optimizes the given cost function is more complex, because the nonlinear dynamic equations prevent the use of methods like the LQR described above. A standard approach in solving an optimal control problem is to convert it to a parameter optimization problem, where the optimal parameters are determined using a nonlinear programming method [Hull, 1997]. The conversion to a parameter optimization is performed by splitting the time interval of the optimal control problem into a set of subintervals. The times at the endpoints of the subintervals are called nodes. The states and/or controls at the nodes are the unknown parameters to be optimized, and the full state and control histories are formed by interpolation between the nodes.

For the three link model, the joint angles are taken to be the unknown parameters in the problem. In order to keep the optimization problem reasonably small, the time period of interest (samples 6-115 following impact) is divided into 7 subintervals. The initial joint angles and rates are fixed, using the actual experimental data. At the remaining seven nodes, the joint angles are unconstrained, giving a total of 21 parameters (3 angles at each of 7 nodes) to be optimized. The node locations are set somewhat arbitrarily at samples 6, 12, 19, 27, 40, 70 and 115, where impact occurs at sample 1 and the node at sample 6 represents the fixed initial conditions for the problem. The nodes are spaced more closely at the beginning of the interval because of the higher frequency content of the movement immediately following the impact.

The complete joint angle histories are interpolated between the nodes using a cubic spline fit. From the spline fits, the first and second derivatives of the joint angle trajectories are determined. Using the angles and derivatives, the joint control torques required to generate the joint trajectories are computed from the inverse dynamic Equations 5-22. Likewise, the ground reaction forces are calculated using Equations 5-23. An appropriate objective function is evaluated based on the state histories, and a Nelder-Meade simplex search algorithm is used to find the node parameters that minimize the objective function.

The objective function is formulated on a somewhat *ad hoc* basis, and is given in Equation 5-47.

$$J = \sum_{s=6}^{115} \left[\tilde{\Phi}_s{}^T K_\Phi \tilde{\Phi}_s + \dot{\Phi}_s{}^T K_{\dot{\Phi}} \dot{\Phi}_s + \mathrm{T}_s^T K_\mathrm{T} \mathrm{T}_s + k_x \tilde{x}_s^2 + k_F (F_{y_s} - w)^2 \right] \tag{5-47}$$

where s = sample number (impact occurs at $s = 1$)
$\tilde{\Phi}_s = \Phi_s - \Phi_f$
Φ_s = vector of joint angles
Φ_f = vector of final joint angles
K_Φ = diagonal matrix of weights on joint angle deviations
$\dot{\Phi}_s$ = vector of joint angular rates
$K_{\dot{\Phi}}$ = diagonal matrix of weights on joint rates $k_{\dot{\phi}_i}$, $i=1,2,3$

$$k_{\dot{\phi}_i} = \begin{cases} k_{\dot{\phi}_i}{}^+ & \forall \quad \dot{\phi}_i > 0 \\ k_{\dot{\phi}_i}{}^- & \forall \quad \dot{\phi}_i < 0 \end{cases}$$

T_s = vector of joint torques
K_T = diagonal matrix of weights on joint torques
$\tilde{x}_s = x_{CM(HAT)_s} - x_{CM(HAT)_f}$
$x_{CM(HAT)_s}$ = horizontal position of HAT CM
$x_{CM(HAT)_f}$ = final horizontal position of HAT CM
k_x = scalar weight on HAT CM horizontal deviation
F_{y_s} = vertical ground reaction force
w = body weight
k_F = scalar weight on vertical ground reaction force

The weights in the objective function can be chosen to penalize five quantities independently: (1) joint angle deviations from the final position, (2) joint rates, (3) joint torques, (4) horizontal HAT CM deviations from the final position, and (5) vertical ground reaction forces.

Initially, a cost function is chosen based only on the states (joint angles and rates) and the control inputs (joint torques). Interestingly, such a cost function favors very rapid decelerations of the initial joint velocities. In this case, the costs associated with joint angles and rates are decreased because of the smaller joint angle deviations and shorter duration of the time associated with flexional joint rates. Interestingly, the necessary control inputs are reduced as well, because the reduced joint flexion also reduces the mechanical advantage of forces acting relative to the joints. Thus, smaller torques are required to effect the deceleration of the body mass and its restoration to upright posture.

However, the rapid deceleration of the body's downward motion does result in extremely high forces at the ground and at the joints. Since high forces at the joints may damage the joint tissues or conceivably the bones through which the forces are transmitted, the landing strategy employed by the CNS may attempt to limit the magnitude of these forces. Hence, the term penalizing vertical GRFs is added to the cost function. At first, the squared absolute magnitude of the GRF was penalized. However, this resulted in "pathological" behavior near the end of the simulated movement, characterized by high joint rates that created centrifugal forces to reduce the vertical GRF to near zero. Although the costs associated with the joint rates increased, they were more than offset by the reduced costs associated with the GRF. For this reason, the GRF cost is changed to the form shown in Equation 5-47, and the deviation of the GRF from one body weight is penalized instead. This effectively places a cost on the acceleration of the CM, and is equivalent to the cost on CM acceleration used in the analysis of the CM vertical motion model above.

Two other alterations are made to the cost function. First, a term penalizing deviations of the horizontal CM position is included. Optimizations using the cost function without this term produce "uncoordinated" joint angle trajectories that cause large horizontal movements of the CM ranging outside the base of support of the foot. Introduction of the cost on CM deviation forces coordinated angle trajectories that maintain the CM within narrower horizontal bounds. Also, the cost function is modified to place different penalties on the joint rates depending on whether the joint motion is flexional or extensional. This modification improves the ability of the optimization to match better both the flexional and extensional phases in the landing trajectory. This asymmetric weighting of extensional and flexional joint rates may be physiologically significant when the asymmetry of the muscle force-velocity relationship in lengthening and shortening is considered.

The different weights in the cost function are adjusted using a trial and error method to find a nominal combination that results in joint angle trajectories similar to those observed experimentally. Again, *djn* is chosen as the representative subject. Figure 5.31shows the trajectories found to optimize the nominal cost function, superimposed on the experimental average trajectories. Although an effort is made to determine cost weights that result in good trajectory correspondence with the experimental data, the nominal weights do result in some clear differences between the "optimal" and actual trajectories. For example, the early portion of the hip angle trajectory does not match well, and the corresponding portion of the GRF history shows discrepancies as well.

The slow convergence of the numerical search routine makes adjustment of the cost weights an extremely time consuming process. Since the goals of the optimization procedure are to show that a cost function based on physiologically plausible objectives can match the important features of the data, and to assess the effect of variations about the nominal cost weights, the nominal trajectories shown in Figure 5.31 are deemed adequate. No claims are made that the nominal trajectory found represents a global minimum of the nominal cost function. However, the parameter optimization is repeated several times from different initial parameters to show that the search does converge to a consistent, stable local minimum.

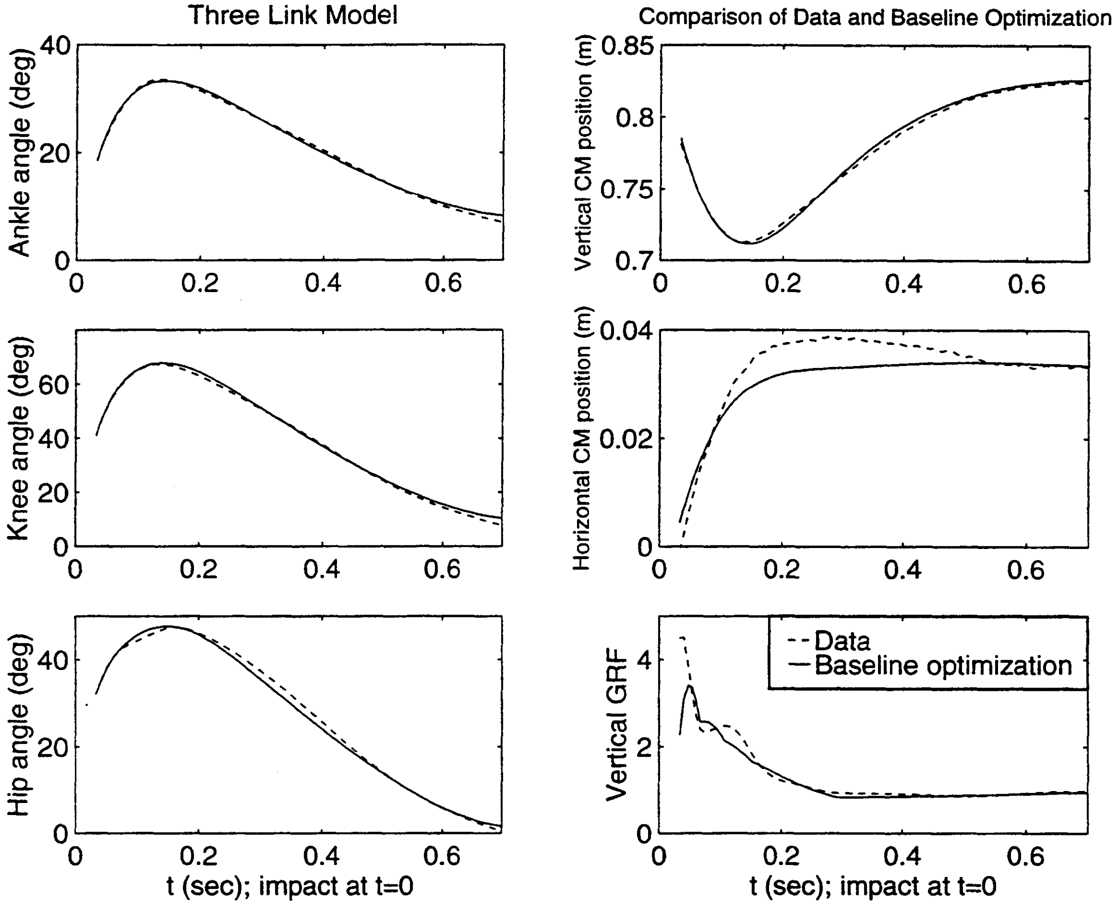

Figure 5.31. Optimal three link trajectories for nominal cost function weights. Nominal weights are selected to give optimal trajectories close to the observed experimental data. Optimal joint trajectories (left) and CM trajectories (right top and middle) are shown compared to actual data. Optimal GRF for nominal weights is shown at lower right.

Having found a nominal set of weights for the cost function, the different weights are systematically varied about the nominal values to determine the effects on the joint trajectories, torques, CM motion and GRF. Figure 5.32 shows the results of altering the cost weight on vertical GRF. When k_F is reduced by half, the results are quite similar to those observed for a comparable variation in the CM vertical motion model. The peak ground reaction force increases and the undershoot below the one body weight level becomes more pronounced. Peak joint flexion is reduced, as is deviation of the CM, and the system returns more quickly to the upright equilibrium position.

The opposite effects are observed when the weight on k_F is doubled. Interestingly, the GRF traces do not exhibit the smooth decay seen when only the CM vertical motion is considered. Instead, the GRF decreases rapidly, then increases slightly before continuing to decay, in a manner similar to the pattern in the actual Type 2 GRF data. As the weight on the GRF in the cost function is increased, this second peak in the GRF becomes more prominent.

The result of variation in the cost weight on joint angle deflections is shown in Figure 5.33. Decreasing the cost on joint angle deflections has effects similar to those seen when the cost on vertical GRF is increased. The peak angle deflections increase, and occur later. The downward deflection of the CM increases, and the peak vertical GRF decreases. Because decreasing the joint angle cost effectively increases the relative cost on joint rates, the joint angles exhibit a more heavily damped return to the upright stance.

Figure 5.34 presents the effects of variations in the cost weights associated with joint rates. As the joint rates are penalized more heavily, deceleration of the joint flexion occurs more rapidly, and the peak joint flexion is decreased. A slower return of the system to the upright also results. Corresponding changes are seen in the CM vertical motion, including smaller downward CM deflection and slower return to the upright position. The peak GRF increases, reflecting the more rapid deceleration of the downward CM motion.

In Figure 5.35, the impact of changing the weights on the joint torques is displayed. Interestingly, the change in torque weights relative to the other cost weights has an almost imperceptible effect on the CM vertical motion and vertical GRF. The knee trajectory is virtually unchanged, and the only readily apparent results are opposing changes in the ankle and hip angle histories, with corresponding changes in the joint torques.

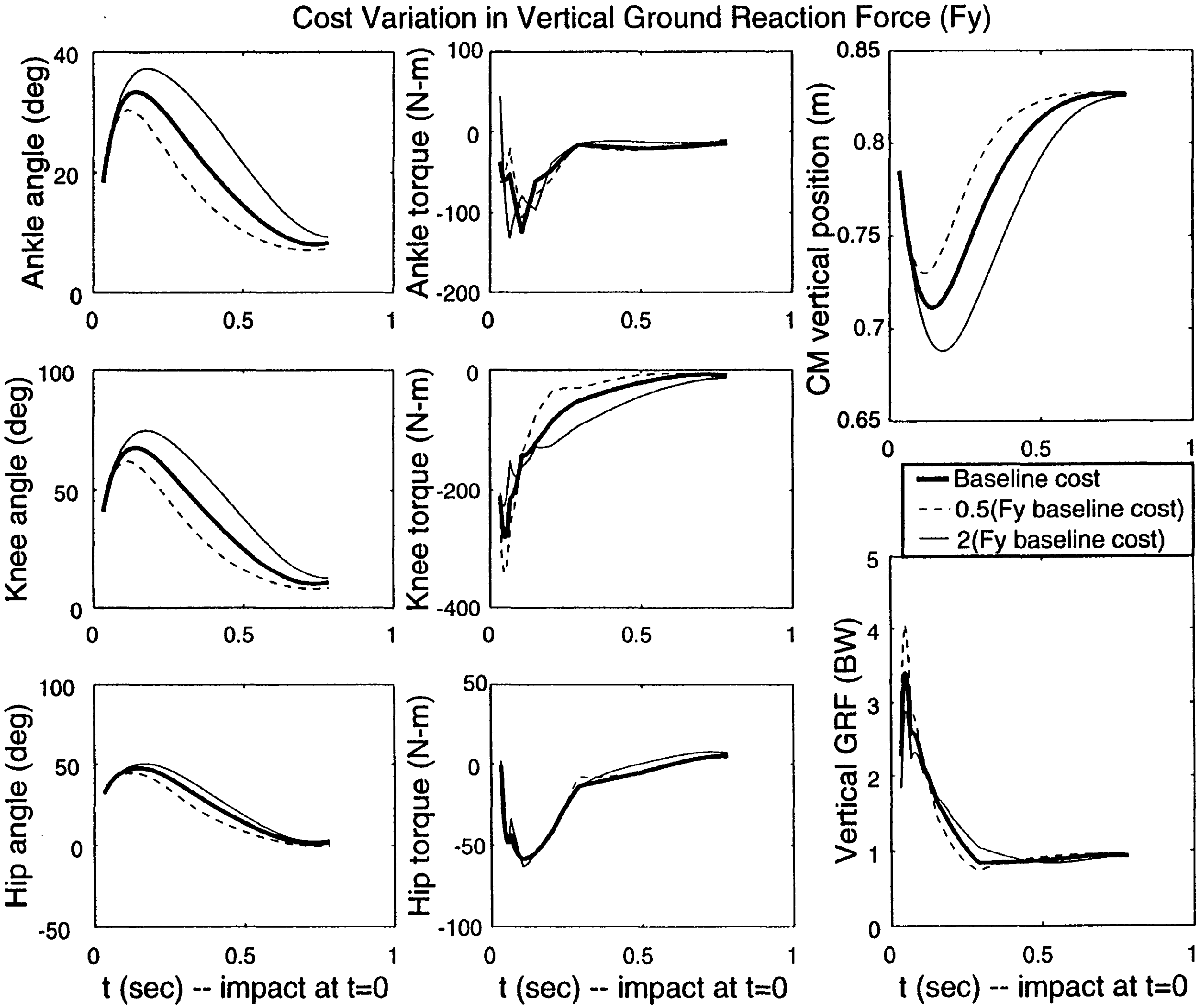

Figure 5.32. Effects of variations in vertical GRF cost weight for three link optimization.

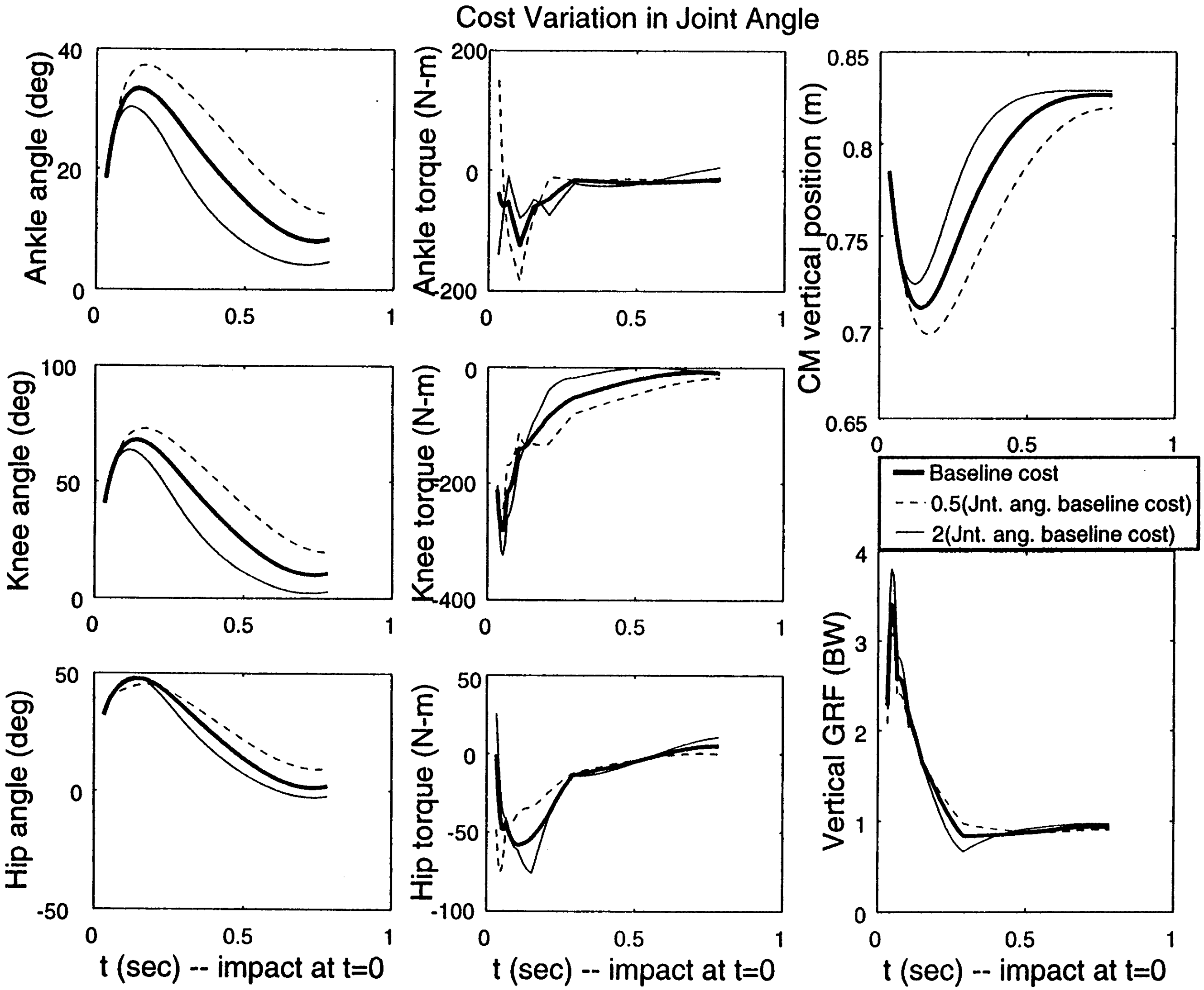

Figure 5.33. Effect of variations in joint angle cost weights for three link optimization.

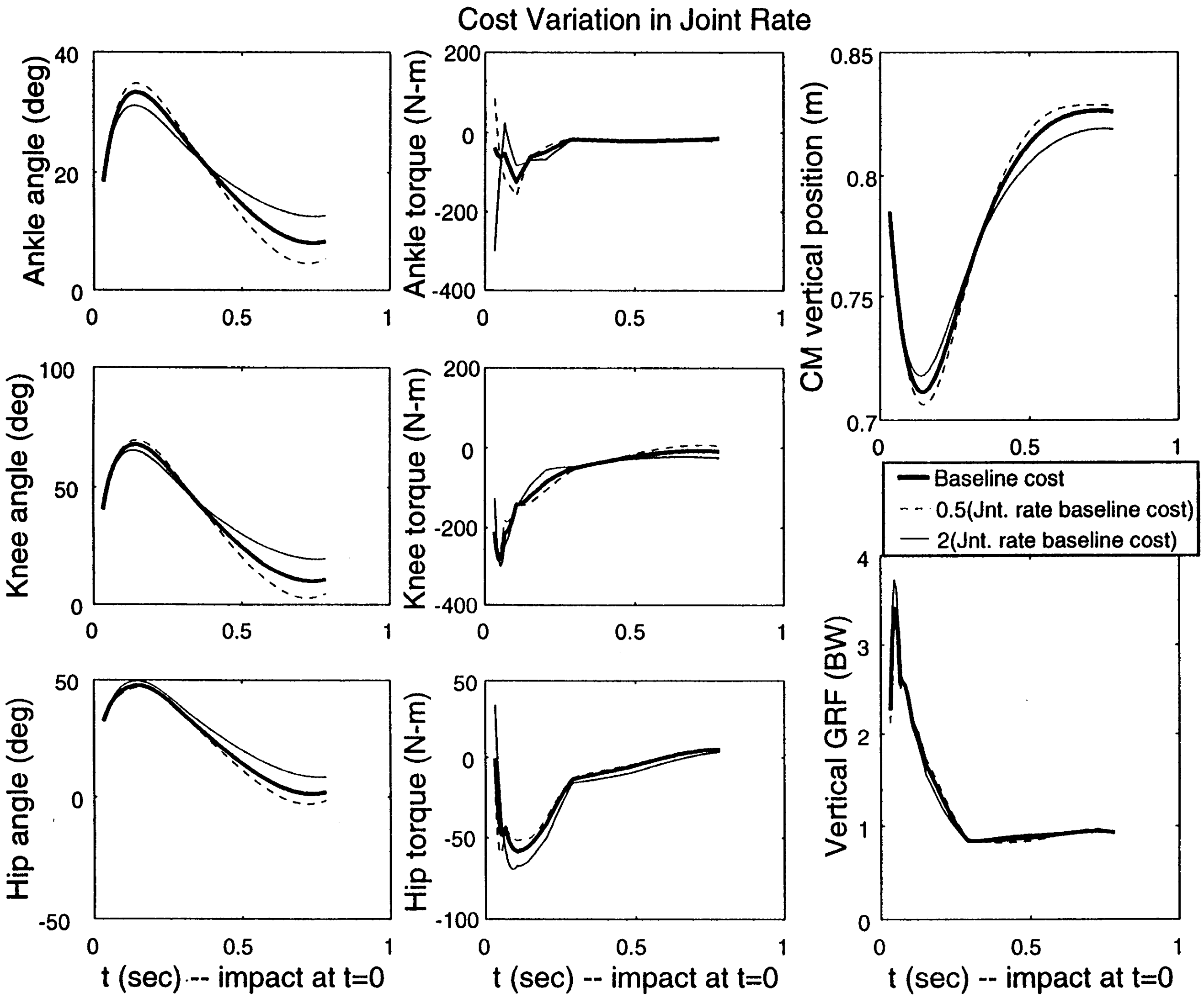

Figure 5.34. Effect of variations in joint rate cost weights for three link optimization.

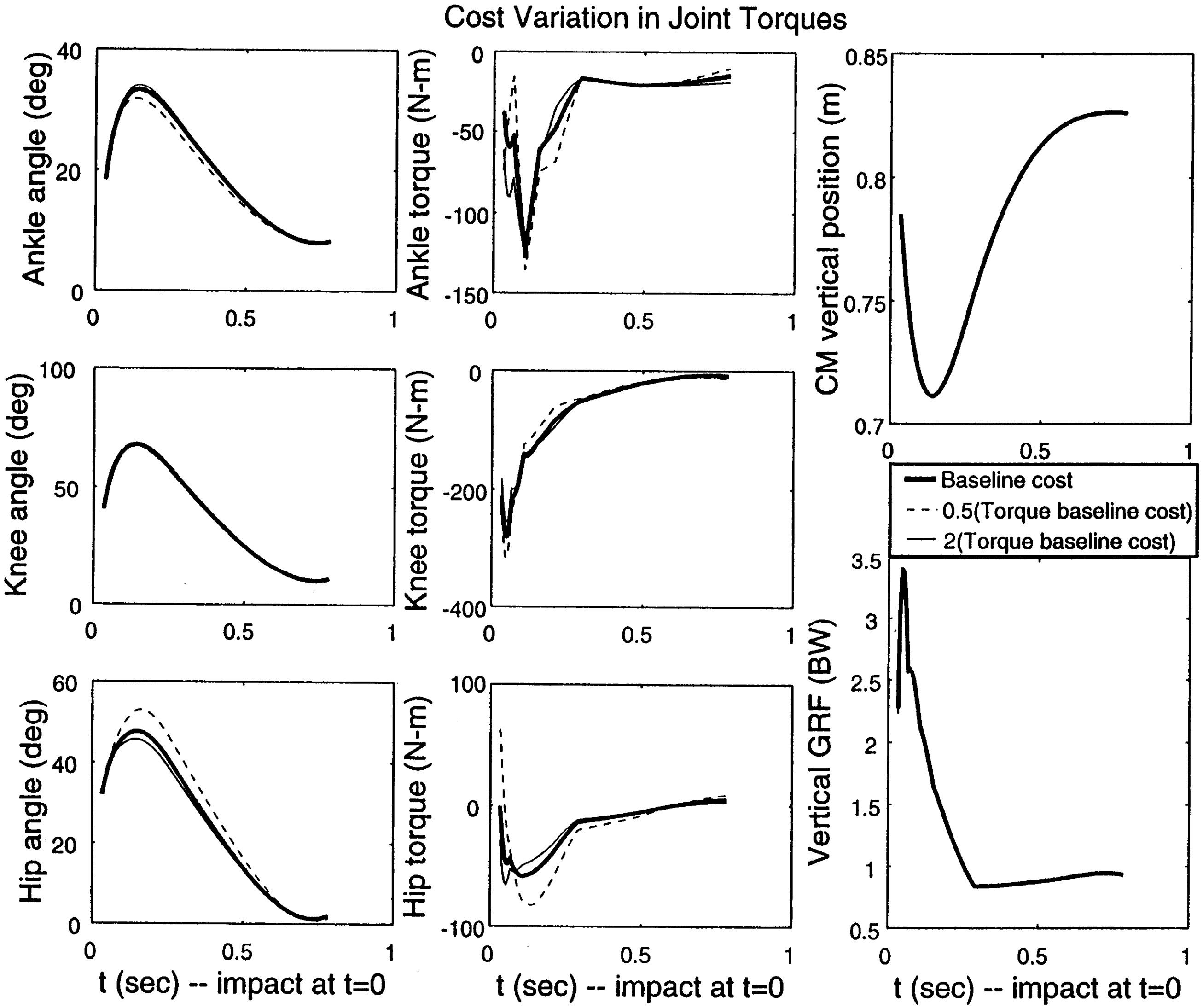

Figure 5.35. Effect of variations in joint torque cost weights for three link optimization.

5.5.3. Variation of Costs Weights to Explore Trajectory Tradeoffs

The optimizations undertaken here represent, at some level, curve fits to the data. There is no assurance that the results seen using the selected objective function cannot be replicated or improved upon with a different set of variables. However, the effort shows that the jump landing trajectories can in fact be represented as the optimal solutions to the control problem posed by an objective based on a relatively small number of physiologically reasonable variables. Furthermore, variation of the cost weights from the nominal values gives some insight into the considerations that may drive the control strategy used by the central nervous system.

For instance, the relative unimportance of the joint control torques in the objective function indicates that the control authority of the system is not the limiting factor in rapidly returning the body to an upright posture. Rather, it is the need to limit the impact forces that results in greater joint flexion, deeper deflection of the CM, and slower return to upright. posture. In addition, the optimimum trajectories in the three link model result in vertical GRF traces that bear some resemblance to the Type 2 landing responses. Specifically, the force does not decrease monotonically from the peak value. Rather, the GRF decay is interrupted by a second, smaller peak before continuing to decline. This feature becomes more prominent as the penalty on vertical GRF is increased, indicating that the Type 2 response may result from an attempt by the CNS to reduce the duration of high-magnitude reaction forces.

The importance of the weight on horizontal CM deviation is also quite interesting. It emphasizes the need for coordinated joint motion, because motions of the CM outside the base of support will result in stepping, and control torques available at the ankle are limited by the foot length. Horstmann and Dietz [1990] have argued that direct control of the position of the CM is an explicit goal of the postural control system. The need to penalize the CM deviation here provides some support for this contention. This result is comparable to the findings of Kuo [1992], who shows that the best match to experimental data for an linearized multilink model of postural control is provided by a cost function that penalizes both joint angle deviations from upright and motion of the CM.

6 CONCLUSIONS AND RECOMMENDATIONS FOR FUTURE WORK

The goal of this thesis is to corroborate or refute each of three hypotheses. The outcome of the experiments with respect to these hypotheses is summarized here. Based on the conclusions reached, additional research directions are suggested.

6.1. MICROGRAVITY ADAPTATION ALTERS CONTROL OF LEG STIFFNESS

The first hypothesis states that changes in astronaut jumping performance postflight can be explained on the basis of altered limb impedance as the result of microgravity adaptation. A simple model of CM vertical motion indicates that the observed kinematic changes in astronaut jump landings postflight are best explained by changes in the lumped leg stiffness after microgravity exposure. It is conjectured that the astronauts adapt to the reduced postural demands in microgravity by reducing the stiffness in the legs. The "moonwalker" partial weight unloading experiment provides support for this conjecture by demonstrating rapid adaptation of the leg stiffness during brief reductions in the load bearing requirements on the legs.

From an operational standpoint, the results of the astronaut study are important for understanding how microgravity exposure might impair astronauts' abilities to perform tasks such as an emergency egress from the Space Shuttle, or even locomotion on another planet following an extended duration space flight. The postflight changes in the kinematics of astronaut jump landings reported here have been attributed to changes in the control of the lower limb impedance due to exposure to the microgravity conditions of space flight. The decreased stiffness of the posture control system observed in the P-C group of subjects may reflect inflight adaptation to the reduced requirements for posture control in the absence of gravitational forces. On the ground, the nature of the body's compound inverted pendulum structure requires the maintenance of a certain minimum stiffness for stability in an upright position. In space, the body need not be stabilized against gravity, and the control bandwidth and stiffness may therefore be reduced without compromising postural stability. Inflight, an overall reduction in postural stiffness may be observed as reduction in extensor tone and decreases in stretch reflex gain, and may be related to the loss of drop-induced H-reflex potentiation.

Compliant postflight behavior may result from a residual decrement in the stiffness of the postural control system following return to earth. In contrast, stiff postflight behavior may indicate overcompensation for reduced inflight stiffness upon return to earth, similar to the "rebound" effect observed by Reschke *et al.* (1986) for the H-reflex. Thus, stiff responses postflight may be related to the observation by Young *et al.* (1986) that some subjects were able to maintain balance only within a narrow "cone of stability" postflight, especially with the eyes closed. By using a stiffening strategy postflight, the subject minimizes deviations from equilibrium to avoid approaching the boundaries of the cone of stability. Such stiffening in turn requires a commensurate increase in postural control bandwidth.

In summary, the astronaut study provides evidence for adjustment of lower limb impedance in response to microgravity exposure in space flight. The results reported here, interpreted in light of other studies, indicate that this impedance modulation may result from a combination of altered tonic muscular activity and changes in the pre-programmed neuromuscular activity observed prior to and during impact absorption. Simulations using a simple mechanical model of the CM vertical motion indicate that changes in the lumped leg stiffness cause the differences in postflight jumping performance seen in the joint and CM kinematics. The reduced requirements for maintenance of posture under microgravity conditions probably contribute to the changes seen postflight, in concert with decrements in limb proprioception and altered interpretation of otolith acceleration cues.

The results of the moonwalker experiment strengthen the conjecture that the reduced postural demands in space flight contribute most to altered performance postflight. The partial weight unloading protocol is not believed to affect stretch reflexes, descending vestibular effects on muscle tone, or interpretation of vestibular acceleration signals. Hence, the significant changes seen after moonwalker adaptation most likely result from altered open-loop modulation of the limb trajectories and stiffness during the flight and impact phases of the jumps.

6.2. EQUILIBRIUM POINT CONTROL IS NOT SUPPORTED BY FALSE PLATFORM RESULTS

The simple second order models evaluated in the astronaut and moonwalker jumping experiments indicate that the overall system dynamics can be adequately characterized by passive stiffness and damping elements that bring the body to rest in the upright standing position. This result is consistent with experiments in running and hopping that show good agreement with models of the leg in these tasks as an undamped linear spring [Alexander and Vernon, 1975; McMahon and Cheng, 1990; He *et al.*, 1991;

Farley and González, 1996]. Equilibrium point motor control models hypothesize that spring-like properties of the neuromuscular system are not merely a descriptor of the gross mechanical behavior, but also provide a plausible detailed model for the neural control of posture and movement. In these models, the CNS commands a "virtual" or "equilibrium" trajectory, and relies on the inherent elastic and dissipative properties of skeletal muscle in concert with the stiffness and damping provided by spinal stretch reflexes to cause the actual limb trajectory to approximate the commanded trajectory.

It is hypothesized that a control model based on the equilibrium point hypothesis can explain the experimentally observed characteristics of human downward jumps. The false platform experiment is designed to provide access to free limb trajectories after the nominal impact time, which may give good approximations to the hypothesized virtual trajectories. The data obtained for the no-platform (NO-P) jumps comprise the first description of the unperturbed trajectories during the nominal impact absorption phase that result from the motor commands generated during the flight and impact segments of the landing. These results show a stereotyped pattern of leg flexion that is initiated immediately prior to the expected moment of impact and continues for approximately 50 ms following nominal impact. The legs then re-extend from this time until the actual impact with the ground (approximately 100 ms after nominal impact).

The initial flexion probably reduces impulsive impact forces by partially matching the foot velocity to the relative speed of the landing platform while removing the body from a near-singular joint configuration. The muscle activation leading to subsequent re-extension of the legs in the NO-P case may function to provide the required extensional forces to arrest the downward body motion in the platform (P) jumps. This NO-P trajectory is clearly the result of preprogrammed neuromuscular activity, as the flexion sequence is initiated prior to the expected time of impact. Moreover, the transition from flexion to re-extension occurs in a time span after nominal impact that is shorter than the time in which significant muscular torques could be generated by the fastest spinal reflexes.

While the NO-P trajectories are unlikely to be affected substantially by reflex feedback during the majority of the 100 ms interval following nominal impact, the false platform experiment provides evidence that the stretch reflexes in the leg are active during the impact absorption phase. The present data indicate that the activity in the gastrocnemius and hamstrings is significantly enhanced in the NO-P jumps in comparison to the P jumps, and that the apparent latency of muscle activation following nominal impact is consistent with the timing of a spinal stretch reflex. This result contrasts with the supposition by Dyhre-Poulsen and Laursen (1983) and Dyhre-Poulsen *et al.* (1991) that the stretch reflex is suppressed during the jump landing. Rather, it appears that the stretch reflex is triggered when the leg trajectory deviates from the configuration expected during normal jump landings.

This apparent adjustment of the threshold length for activation of the stretch reflex to reflect the expected leg motion during impact is conceptually similar to Feldman's lambda model of equilibrium point control, in which the CNS establishes threshold muscle lengths for alpha motoneuron recruitment and relies on afferent feedback from muscle spindles. If, as suggested by the present results, reflex activity is triggered only when the body configuration diverges from the nominal jump landing trajectory, it is not surprising that other investigators [Dyhre-Poulsen and Laursen, 1984; Dyhre-Poulsen *et al.*, 1991; McKinley and Smith, 1983] conclude that the stretch reflex plays a minor role during normal jump landings. The knee flexor activity seen in the NO-P trials seemingly should return the legs to the normal post-impact trajectory. The equilibrium point hypothesis proposes that the stretch reflexes enhance the position-dependent properties tending to restore the limbs to the equilibrium trajectory. Therefore, it is possible that the NO-P trajectory does not meet the criteria defining a virtual trajectory according to the equilibrium point hypothesis.

Three dynamic models of various fidelity levels are considered using the NO-P trajectories as candidate virtual trajectories. However, the measured free trajectories, combined with measured GRFs and estimated joint torques, result in negative stiffness estimates in most cases. This result indicates that the NO-P trajectories do not represent stable attractors in these models. While the model analysis does not support the existence of a stable attractive trajectory for the system during the time segment within 100 ms following impact, the data are insufficient to disprove the existence of a stable attractor in the actual system. The fact that the subjects recover to an upright standing position implies that this final position is a stable attractive configuration. At least three possibilities must be considered: (1) the NO-P trajectory does represent a stable attractor, but the simplistic formulation of the models results in erroneous negative stiffness estimates; (2) a stable attractive trajectory does exist, but the NO-P trajectory is not close to this attractor and erroneous impedance estimates are due to use of an inappropriate estimate of the virtual trajectory; or (3) a stable attractive trajectory does not exist in the period immediately following impact.

The first two potential explanations of the current data must be considered in the context of studies of arm motions that use comparable models of joint torque production and also estimate impedances about the unperturbed limb trajectory [Gomi and Kawato, 1996; Flash, 1987]. These studies estimate positive stiffness values and show that the equilibrium point hypothesis is competent to describe arm movements given appropriate virtual trajectories. The false platform experiments do not disprove the equilibrium point hypothesis, but do show that the simple models used in these studies cannot explain the control of jump landing. The third possibility listed above implies that the equilibrium point hypothesis is not a viable description for the control of this phase of jump landings. Further analysis is required to address these issues.

Regardless of the existence of a stable attractor, the observed force-position relationship during impact absorption appears to have some functional significance for jump landings. The negative stiffness estimates for the simple linear models used here result from decreasing vertical force during continued downward deflection of the body, and other studies [Dyhre-Poulsen *et al.*, 1991; Dyhre-Poulsen and Laursen, 1984] also report negative stiffnesses in jumping. These authors theorize that low or even negative stiffnesses are appropriate to the goals of jump landings, because these tasks require energy dissipation rather than storage of elastic energy for rebound. Their conjecture that the negative stiffness estimates reflect the task requirements is supported by consistently positive stiffness estimates during repetitive hopping where spring-like behavior is appropriate.

6.3. OPTIMIZATION EFFORT PROVIDES PLAUSIBLE OBJECTIVE FUNCTIONS

The first two hypotheses deal with how altered environments change jump performance, and how jump landings might be controlled. However, the tradeoffs that underlie the selection by the CNS of particular landing trajectories is not explicitly addressed. Therefore, optimization methods are applied to two jump landing models to derive objective functions that can be used to generate optimal trajectories consistent with experimental data. The results for both models indicate that cost functions incorporating a small number of physiologically plausible variables (that are probably accessible to the CNS) generate optimal trajectories that are quite similar to measured jump landings. Two main limitations of the approach are noted. First, there is no evidence that the cost functions selected here are unique, and similar results might be found using a somewhat different set of variables. Second, the procedure applied to the three link model generates optimal open-loop trajectories based on the cost function and model dynamics, but provides little insight into how a closed-loop control algorithm could reproduce these trajectories.

Use of an LQR approach for the linear second order model of CM vertical motion demonstrates that a quadratic penalty on vertical force CM position and velocity can give optimal trajectories that capture the overall shape of the CM trajectory, but cannot replicate the Type 2 behavior seen immediately following impact. Relative costs on vertical force and position deviation govern how rapidly the subject returns to the upright position. Similarly, the relative costs on CM position and velocity govern the damping of the response.

Application of a parameter optimization method to the three link model shows that joint and CM trajectories approximating the experimental results minimize a cost function based on joint angles, rates and torques, vertical ground reaction forces, and CM horizontal deviation. Variation of the cost weights shows that joint torques are relatively unimportant in the optimal control problem, while reducing impact forces appears to be of central importance. In contrast with the optimization for the linear model, an inflection in the vertical ground reaction force appears that qualitatively resembles the Type 2 force traces. This second peak in the optimized force becomes more prominent as the cost on vertical ground reaction force increases, indicating that the experimentally observed results may reflect a strategy to reduce the impact forces. A cost on horizontal CM motion is also introduced to force the CM to follow a realistic path, emphasizing the importance of interjoint coordination in keeping the CM above the base of support.

6.4. RECOMMENDATIONS FOR FUTURE WORK

Recommendations for future work include proposed improvements to the experimental protocols, additional modeling work to clarify the results found here, and additional studies to build on the foundation laid by this thesis.

Modifications to Experimental Protocols

The astronaut and moonwalker experiments strongly suggest that adaptive changes in preprogrammed activity during the flight and impact phases of the jumps lead to altered leg stiffness properties. EMG data in the current false platform experiment and other studies cited previously support the hypothesis that muscle activation is programmed prior to impact, and significant co-contraction of antagonist muscles may set impedance properties before landing. EMG data could provide further insight into how leg stiffness is set differently after exposure to reduced load bearing demands. EMG data are available for a small number of astronaut subjects, and should be examined for muscle activation patterns that correlate with the P-C and P-S performance patterns. Likewise, EMG data could be easily collected to supplement the moonwalker studies, while force plate data from astronauts jumping would be very useful in interpreting both the astronaut kinematic data and the moonwalker force plate results.

Some improvements to the moonwalker experiment can be made. First, a higher ceiling would permit a greater cable length between the subject attachment point and the overhead pulleys, decreasing the resultant horizontal forces for a given movement away from the point beneath the overhead attachment. A higher ceiling would also allow the use of longer, less stiff springs, effectively reducing the variation in vertical force as the subject moves vertically. Alternatively, a negator spring arrangement might be designed to provide a constant vertical force. A redesigned harness could place the suspension point closer to the mass center, provide greater mobility and remove the horizontal strap forces that tend to force the subject into a slightly forward-inclined position while suspended.

Some additions to the false platform experiment would provide better data. A significant difficulty with the current arrangement is the loss of foot data when the paper target folds up to hide the foot array in the NO-P jumps. A better design would supply useful foot and ankle data throughout the free-fall portion of the NO-P jumps, improving the estimates of the NO-P trajectory for the equilibrium point control analysis. Improved EMG recording techniques could reduce or eliminate the substantial movement artifacts associated with landing and allow reliable analysis of the muscle activation data immediately after impact. A more extensive series of baseline jump data could clarify the time course associated with reaching a "steady-state" jumping pattern, and increase insight into the relationship between the "Type 1" and "Type 2" landings. More baseline jumps could also distinguish whether the higher prevalence of the "Type 2" landings is related to the uncertainty in landing surface location in the false platform series.

Further Modeling Approaches

The assumption that the NO-P trajectories provide good estimates of the hypothesized equilibrium trajectories should be considered more carefully in future work. If dynamic effects due to inertial and velocity dependent terms are not negligible during the time following nominal impact in the NO-P jumps, the difference between the postulated equilibrium trajectory and the measured NO-P trajectory might be significant, leading to erroneous estimates of stiffness and damping. First, the magnitude of the torques needed to replicate the free trajectory kinematics should be assessed relative to the actual impact-related torques. If the joint torques are significant in the NO-P jumps, an iterative technique might be employed to estimate stiffness and damping matrices and a virtual trajectory that fit both the P and NO-P data. If positive definite stiffness and damping matrices can be found along with a virtual trajectory to match both sets of data, the apparent inconsistency of the current results with the equilibrium point hypothesis will be resolved.

The models examined in this thesis could also be extended the examine the influence of more realistic representations of force and torque generation. First, the effects of system order on the estimated stiffness and damping values could be examined in the context of the linear model. The vertical ground reaction forces are difficult to explain with a passive second order model, especially for "Type 2" landings. The possibility should be tested that a third or higher order model of force generation might better match the vertical CM motion data and provide non-negative stiffness and damping estimates. Similarly, higher order torque generation models could be evaluated in the three link case. A more ambitious effort could address some of the known nonlinearities in the torque generation by explicitly accounting for muscle passive length-tension characteristics, force-velocity relationships, and graded force development in the muscle [Winters *et al.*, 1988; Gribble *et al.*, 1997]. Likewise, time delays in stretch reflex feedback could be explicitly taken into account.

More complex multilink models could also be considered The addition to the three-link model of a foot segment would add considerably to the model verisimilitude, as the ankle is known to lift off of the floor during the impact absorption phase of landings. While additional degrees of freedom such as abduction and external rotation of the leg segments could be included, care should be taken to ensure that model complexity does not rise to the point where useful insight is prevented by excessive detail.

Additional Experiments

The results of this thesis indicate several avenues for additional exploration. First, the demonstration that adaptation to reduced load bearing requirements can result in decreased leg stiffness suggests a number of experiments that would determine the range of leg stiffness properties when different environmental conditions are varied. Tests should be performed to determine if the effective leg stiffness can be increased by temporary adaptation while supporting extra weight. Furthermore, the leg stiffness during partial weight unloading and during increased load bearing could be evaluated for comparison with the adapted cases under normal loading, and the time course of readaptation after exposure could be addressed. Extension of the trajectory optimization techniques introduced in this thesis might be used to predict optimal values of leg stiffness for jump landings during or after increased or decreased load bearing.

An interesting experiment would measure the effective limb stiffness after a sudden change in loading during the flight phase of the jump. In the moonwalker experiment described here, the subjects' leg stiffness probably begins to adjust to a level appropriate for normal weight bearing as soon as the suspension cables are released. An electrically controlled cable brake similar to that used by Wicke and Oman [1982] could be used to release the weight borne by the suspension harness after takeoff. Such an experiment might help to evaluate separate contributions of pre-programmed and reflex activity to the effective leg stiffness. Furthermore, the contribution of otolith sensing of downward acceleration to the stiffness of the legs in landing could be assessed, using a variable downward acceleration comparable to the protocol devised for sudden falls by Wicke and Oman [1982].

The apparent task-dependent differences in leg stiffness modulation seen in comparisons of jumping with hopping or running could be investigated. In repetitive hopping or running, it appears that spring-like behavior and elastic energy storage is much more important than in jump landings. Two experimental results in the literature prompt further experimentation: (1) In contrast to the results found for jumping in this thesis, the effective leg stiffness during running appears to be unaltered during partial weight unloading [He *et al.*, 1991]; and (2) Dyhre-Poulsen *et al.* [1991] find positive incremental leg stiffness in repetitive hopping that contrasts with the negative incremental stiffness they observe during jump landings. The first result suggests that the leg stiffness during repetitive hopping may be unaltered under extra weight carrying or partial weight unloading conditions. The second finding would be interesting to investigate further using a test similar to the false platform experiments that allows the landing platform to be lowered abruptly while the subject is airborne between hops. It is hypothesized that an analysis similar to that performed for the jumps in this thesis would reveal positive stiffness and relatively small damping estimates about the NO-P hopping trajectory. An appropriately controlled platform could also be used to deliver measured perturbations during jump landings or the ground contact phase of hopping, permitting better controlled estimates of leg stiffness and damping.

The optimization analysis indicates that the CNS balances the competing requirements of quick recovery to upright with low impact and joint forces. Since landing on more compliant surfaces could reduce impact loads even for stiff landings, it would be interesting to investigate how the controlled leg stiffness varies with the expected compliance of the landing surface. Studies by McKinley and Pedotti [1992] show that ankle range of motion is reduced during jump landings on more compliant surfaces, potentially indicating higher stiffness about the ankle joint. However, tuned track designs are based on the assumption of constant leg stiffness independent of the surface compliance [McMahon and Greene, 1979]. Extension of the model optimization could be used to predict leg stiffness as a function of surface compliance, and the predictions could be tested on landing surfaces of different compliance.

6.5. SUMMARY OF CONTRIBUTIONS

This thesis describes the results of three experiments related to the control of downward jump landings in humans. The first two experiments test the effect of microgravity exposure and partial weight unloading on jumping performance. They show that adaptation to reduced load bearing requirements results in changes in the leg impedance during jump landings. Furthermore, the leg impedance appears to be preprogrammed prior to impact. Changes in the lumped leg stiffness adequately explain the key changes in body kinematics after adaptation. The moonwalker experiments also demonstrate that short term partial weight unloading can provide a useful terrestrial analogue for certain adaptation effects in motor control induced by microgravity exposure.

The false platform tests described here provide a unique set of data showing the pattern of flexion and re-extension in the free limb trajectories that is commanded by the CNS during the 100 ms following nominal impact. The EMG results from the NO-P trials show that the stretch reflex is active in jump landings, rather than suppressed as reported by other investigators. The false platform experiment also provides the first test of the equilibrium point hypothesis for control of a lower limb or full body trajectories during contact with the environment. Model fits using the NO-P trajectories as estimates of virtual trajectories result in negative stiffness values. Hence, the model fits do not support the existence of a stable attractive trajectory for the time period immediately following impact. This result is especially intriguing, and merits further investigation using more realistic models of force and torque generation.

Trajectory optimization using dynamic models of jump landings indicate that cost functions based on physiologically plausible variables are sufficient to replicate important features of measured landing data. Results indicate that impact forces rather than required joint torques limit the speed of return to upright posture. The apparent need for a cost weight on the CM horizontal position indicates that explicit control of this variable may be important for coordinated movement in Earth's gravity field.

APPENDIX A. EXPERIMENTAL SUBJECT CONSENT FORMS

A copy of the experimental subject informed consent statement is signed by each subject before beginning the test. Signed forms are kept on file. Sample consent forms for the experiments performed at M.I.T. and MGH are contained below.

A.1. CONSENT FORM FOR MOONWALKER EXPERIMENT

EXPERIMENTAL SUBJECT CONSENT FORM

Adaptive effects of exposure to simulated partial gravity on downward jump landings

Principal Investigator:	Co-Investigator:
D. Keoki Jackson[1]	Prof. Dava J. Newman[2]

I. VOLUNTARY PARTICIPATION, RIGHT TO WITHDRAW

Participation in this experiment is voluntary and the subject may withdraw consent and discontinue participation in this experiment at any time without prejudice.

II. PURPOSE AND OBJECTIVE OF EXPERIMENT

Upon returning to Earth's gravity, astronauts demonstrate altered performance in landing from small downward jumps. The goal of this experiment is to examine the effects of short-term exposure to simulated partial gravity to permit better understanding of the effects seen in astronauts following space flight.

The experiment in which I will be participating consists of measuring body segment kinematics and ground reaction forces in a series of jumps performed before and after exposure to simulated partial gravity. Partial gravity simulation is accomplished using the "moonwalker" suspension apparatus, which consists of a climbing-style harness suspended from the ceiling. The amount of weight unloaded by the harness can be adjusted using a battery powered winch.. Body segment kinematics are measured using a video camera viewing markers placed at the subject's joints. Ground reaction forces are recorded using an instrumented forceplate.

III. EXPERIMENTAL PROTOCOL

I will be asked by the investigator about the general condition of my health, and specifically about any orthopedic or musculoskeletal conditions relevant to the jump experiment. I agree to inform the test operator of any prior or persistent bone, joint or muscle injuries which might be aggravated by the test procedure.

I will perform several downward jumps from a 1 ft (30 cm) high step onto an instrumented force platform. After performing pre-exposure baseline jumps, I will perform multiple repetitions of the following sequence:

(1) Several "adaptation" jumps under simulated partial gravity, while suspended in the "moonwalker" apparatus so that I am supporting approximately 40% of my body weight.

---

[1] Ph.D. Candidate, Dept. of Aeronautics and Astronautics, MIT 37-219.

[2] Assistant Professor of Aeronautics and Astronautics, MIT, 33-119.

(2) A single jump under normal loading conditions, in which I am unhooked from the "moonwalker."

Following the sequence of partial-gravity adaptation jumping, I will perform post-exposure baseline jumps under normal loading conditions. Throughout the tests, my body segment kinematics will be recorded using a video camera. I will wear black tights on my legs and arms, on which white markers will be placed to facilitate joint angle measurement.

IV. FORESEEABLE INCONVENIENCE, DISCOMFORT, AND RISKS TO THE SUBJECT

A. Delayed-onset muscle soreness may occur due to physical exercise performed as part of the experiment.

B. Hoisting the subject on a suspended harness may cause minor discomfort during the period of locomotion.

C. Standard risks associated with small voluntary jumps.

V. RISK MINIMIZATION

A. Treatment for sore muscles and other injuries incurred from participation in this experiment will be available through the M.I.T. Medical Department, at the expense of the subject's insurance carrier where applicable.

B. It will be possible for the experimenter to release the suspension at any point in the experiment without danger to the subject. All subjects will be familiarized with the equipment before beginning the experiment.

VI. REMEDY IN THE EVENT OF INJURY

In the unlikely event of physical injury resulting from participation in this research, the subject understands that medical treatment will be available from the MIT Medical Department, including first aid emergency treatment and follow-up care as needed, and that his/her insurance carrier may be billed for the cost of such treatment. However, no compensation can be provided for medical care apart from the foregoing. The subject further understands that making such medical treatment available, or providing it, does not imply that such injury is the investigator's fault. The subject also understands that by his/her participation in this study he/she is not waiving any of his/her legal rights.[*] .

VII. VIDEOTAPED AND PHOTOGRAPHED IMAGES OF SUBJECTS

Permission for the investigator to use videotaped or photographed images of the subject is granted voluntarily by the subject, and may be withdrawn at any time without prejudice. The subject may be videotaped or photographed during the experimental process, and such images may be used in the analysis of data and the presentation of experiment results.

VIII. COMPENSATION

The subject will receive no compensation for participating in this experiment.

IX. ANSWERS TO QUESTIONS

The subject may receive answers to any questions related to this experiment by contacting the Principal Investigator at (617) 253-5487.

X. IN THE EVENT OF UNFAIR TREATMENT

The subject understands that he/she may also contact the Chairman of the Committee on the use of Humans as Experimental Subjects, M.I.T. (617) 253-6787, if the subject feels that he/she has been treated unfairly as a subject.

---

[*] Further information may be obtained by calling the Institute's Insurance and Legal Affairs Office at (617) 253-2822.

XI. SIGNATURE

I, ______________________________, have read and understand the information contained
(Subject's Printed Name)
in this consent form and agree to participate as a subject in this experiment.

_______________________________________ (Subject's Signature)

__________________________ (Date)

____ (Witness)

A.2. CONSENT FORM FOR FALSE PLATFORM EXPERIMENT

EXPERIMENTAL SUBJECT CONSENT FORM

Limb and body trajectories in jump landings on solid surfaces and false platforms

Principal Investigator:
D. Keoki Jackson[3]

Co-Investigators:
Prof. Dava J. Newman[4], Dr. David Krebs[5]

I. VOLUNTARY PARTICIPATION, RIGHT TO WITHDRAW

Participation in this experiment is voluntary and the subject may withdraw consent and discontinue participation in this experiment at any time without prejudice.

II. PURPOSE AND OBJECTIVE OF EXPERIMENT

The goal of this experiment is to determine the free trajectory of the limbs and body during a small downward jump when the landing surface is removed unexpectedly. The experiment in which I will be participating consists of measuring body segment kinematics, muscular commands and ground reaction forces during a series of voluntary jumps from a small height (1 ft, or 30 cm.) In a few jumps, the landing surface will be removed unexpectedly, such that the subject continues to fall for approximately 100 ms. (an additional 1 ft, or 30 cm) following the normal time of impact. These jumps are readily performed by a healthy person. Some jumps may be performed with the eyes closed. Tests on over 20 astronaut subjects at the NASA Johnson Space Center indicate that subjects have no difficulty performing stable landings with the eyes closed.

Lightweight arrays of light emitting diodes (LEDs) will be strapped to various body segments to enable recording of limb and body kinematics with high speed cameras. A set of electromyographic (EMG) electrodes mounted in plastic capsules containing EMG preamplifiers will furnish EMG signals from my leg and other postural muscles. Ground reaction forces at landing will be recorded using an instrumented forceplate.

III. EXPERIMENTAL PROTOCOL

I agree to be examined by a physician to certify that I am free from any neuro-vestibular defects which might impair my balance, posture control or performance in the tests described below. This examination will include standard clinical testing on a posture platform to check responses to postural perturbations. Caloric testing (irrigation of the ear canal with cold or warm water) will also be performed to verify the vestibulo-ocular reflex. The caloric test may cause mild spatial disorientation, and infrequently may induce nausea.

---

[3] Ph.D. Candidate, Dept. of Aeronautics and Astronautics, MIT 37-219.

[4] Assistant Professor of Aeronautics and Astronautics, MIT, 33-119.

[5] Biomotion Laboratory, Massachusetts General Hospital

I will be asked by the investigator about the general condition of my health, and specifically about any orthopedic or musculoskeletal conditions relevant to the jump experiment. I agree to inform the test operator of any prior or persistent bone, joint or muscle injuries which might be aggravated by the test procedure.

I will perform several downward jumps from a 1 ft (30 cm) high step onto a paper target which conceals the underlying surface. I understand my instructions will be to land normally on the paper target. In the majority of these jumps, a solid landing surface will lie a fraction of an inch beneath the paper. However, in a few randomly selected jumps, the solid landing platform will be removed, and I will fall through the paper target. I understand that I will not know in advance which of the jumps will involve the false platform. Following each jump, I agree to don a blindfold and earphones playing masking noise to permit setup of the next jump without my knowledge of the upcoming landing surface. Some jumps may be performed with the eyes closed.

In the false platform jumps, the actual landing surface will lie a maximum of 1 ft (30 cm) below the paper target. The unexpected nature of the falls in the false platform condition may not allow a landing which is as well controlled as under normal circumstances. Various safety measures have been incorporated to minimize the jolts in case I react inaccurately. The landing surface will consist of an athletic mat to minimize impact forces, and the step from which I jump will be well padded. I will wear close-fitting boots or high-topped athletic shoes to provide ankle support and minimize the possibility of ankle strain.

One of the following methods will be used to prevent potentially dangerous falls: (1) thick foam pads of the type used in high jump landing pits will be placed forward and to the sides of the landing area, or (2) a parachute-style safety harness connected to an overhead anchor point will prevent me from collapsing completely. The harness suspension will normally be slack to prevent interference with the jump. However, it will provide support if I fall more than 4 inches below the level reached in a normally controlled jump landing. Elastic shock cords will be used to minimize jolts upon loading of the harness.

Short (~5 minute) rest periods will be taken between blocks of about 10 jumps.

IV. FORESEEABLE INCONVENIENCE, DISCOMFORT, AND RISKS TO THE SUBJECT

There is a slight risk of fractures, dislocations or sprains, but the design of the safety devices makes such accidents unlikely. If I notice any persistent joint or muscular pain, I should disqualify myself from further testing. Delayed-onset muscle soreness may occur due to the physical exercise performed as part of the experiment. Some apprehension may result from the uncertain nature of the landing surface. I may also experience minor discomfort due to suspension in the safety harness.

V. RISK MINIMIZATION

As described above, care has been taken in the experiment design to prevent injury due to uncontrolled landings. Treatment for sore muscles or other injuries incurred from participation in this experiment will be available through the M.I.T. Medical Department, at the expense of the subject's insurance carrier where applicable.

VI. REMEDY IN THE EVENT OF INJURY

In the unlikely event of physical injury resulting from participation in this research, the subject understands that medical treatment will be available from the MIT Medical Department, including first aid emergency treatment and follow-up care as needed, and that his/her insurance carrier may be billed for the cost of such treatment. However, no compensation can be provided for medical care apart from the foregoing. The subject further understands that making such medical treatment available, or providing it, does not imply that such injury is the investigator's fault. The subject also understands that by his/her participation in this study he/she is not waiving any of his/her legal rights.* .

VII. COMPENSATION

The subject will receive no compensation for participating in this experiment.

VIII. ANSWERS TO QUESTIONS

The subject may receive answers to any questions related to this experiment by asking the test conductor or contacting the Principal Investigator at (617) 253-5487.

IX. IN THE EVENT OF UNFAIR TREATMENT

The subject understands that he/she may also contact the Chairman of the Committee on the use of Humans as Experimental Subjects, M.I.T. (617) 253-6787, if the subject feels that he/she has been treated unfairly as a subject.

X. SIGNATURE

I, ______________________________, have read and understand the information contained
(Subject's Printed Name)
in this consent form and agree to participate as a subject in this experiment.

______________________________ ______________________
(Subject's Signature) (Date)

____
(Witness)

---

* Further information may be obtained by calling the Institute's Insurance and Legal Affairs Office at (617) 253-2822.

APPENDIX B. ATAXIA TESTS FOR JUMPING SUBJECTS

The tests described here are based on the work of Fregly & Graybiel, 1966: "An Ataxia Test Battery Not Requiring the Use of Rails." NASA/NAMI Joint Report NAMI-985.

All tests are performed on a hard linoleum surface. The subjects wear hard-soled shoes with low heels (preferably lace-up shoes with leather or hard rubber soles). No boots or running shoes are permitted. Two tests are performed: (1) the Sharpened Romberg quiet standing test with the eyes closed, and (2) Walking a line with the eyes closed.

Sharpened Romberg (SR)

The subject stands with eyes closed in the "Sharpened Romberg" position (heel-to-toe, with the feet aligned in the anterior-posterior direction). The subject may put either foot in front, based on individual preference. The arms are crossed across the chest in the following position: with the forearms approximately horizontal, one hand is placed on opposite the side, while the other hand holds the opposite arm just above the elbow.

A maximum of 4 trials are administered. The individual trial duration is 60 seconds. Testing is discontinued when the criterion score of 60 seconds standing time is reached on any one trial. The subject may close her eyes at any time after assuming the correct body and foot position. Timing begins when the subject closes her eyes. The trial ends when (1) 60 seconds is reached; (2) the subject takes a step or releases her arms from the crossed position to maintain balance; or (3) the eyes are opened.

The time for each trial is recorded, and the overall test is scored as follows. A score of 60 seconds on the first trial is weighted 4 (60x4 = 240, perfect score). A perfect score on the second trial is weighted 3 (60x3 = 180), and the overall score is 180 plus the number of seconds obtained on the first trial. A perfect score on the third trial is weighted 2 (60x2 = 120) and the overall score is 120 plus the combined number of seconds achieved in the first and second trials. For subjects requiring a fourth trial, the total score is the sum of the individual trial times.

The results of Fregly and Graybiel [1966] indicate that perfect SR scores (240) represent 99th percentile performance for vestibular normal females in the 18-29 year age group. A score of 130 represents ranks at the 18th percentile for normals in the same age group. In contrast, bilateral labyrinthine deficient (LD) subjects had average scores of 18 (standard deviation = 8). Unilateral LDs scored an average of 13.3 (standard deviation = 2.5) and vertigo patients scored an average of 40.8 (standard deviation = 66.7).

Walk a Line Eyes-Closed (WALEC)

The subject walks as straight as possible along a 12-foot line on the floor with the eyes closed. The arms are folded across the chest as described above. Each step is taken heel-to-toe, with the feet placed in tandem so that they are aligned in the anterior-posterior direction.

Trials during which the foot position is violated either by non-tandem alignment of feet or by toe not touching heel are not scored. A maximum of 5 nonscorable trials is permitted. Each scorable trial requires that the subject walk the entire 12-foot distance.

The subject performs 3 scorable trials (unless 5 non-scorable trials are performed, at which point the test is halted). The score on the scorable trials is the number of inches of deviation from the line (measured to the nearest inch from the center of the foot) at the end of the 12-foot length). For each trial (both scorable and non-scorable), the number of steps taken without violating the foot position is recorded. Non-scorable trials are labeled "unable to perform," or UTP.

Two overall measures are derived:

1. Number of successful steps = total of best 3 of 5 trials, where the individual trial measure is the number of successful steps taken after the first two, up to a maximum of 10. (3x10 = 30 is perfect score.)

2. Inches deviation from centerline = total of best 2 of 3 scorable trials.

Fregly and Graybiel [1966] find that none of their unilateral or bilateral LD subjects are able to meet the criterion of a single scorable trial on the WALEC test. All of these LD patients side-step, and attempts to walk without side-stepping invariably result in marked veering and immediate loss of balance, usually within 2 to 5 steps. In contrast, all normal subjects tested to date prove able to achieve perfect scores of 30 steps. Scores of 1, 10, 19 and 30 for the inches from centerline measure correspond to percentile performance levels of 99, 49, 10 and 2 respectively. The authors find that the inches from centerline score is a better measure of spatial orientation than of ataxia.

B.1. MOONWALKER SUBJECT ATAXIA RESULTS

The results of the ataxia tests for the moonwalker subjects are shown for the SR test in Table B.1 and for the WALEC test in Table B.2. All subjects achieved perfect scores on the SR test. All subjects except H also achieved perfect scores for number of successful steps in the WALEC test. All subjects except H clearly perform at a level unachievable by the LD and vertigo patients, and are found to be normal on the basis of these tests.

Subject H performed perfectly in the SR test, but only had one scorable trial in the WALEC test and did not achieve a perfect score for number of successful steps. Based on her SR score and the fact that she was able to complete one WALEC trial, she is believed to perform at a level not achievable by LD patients. However, the subject commented that she had recently suffered a severe case of the flu, and that hearing tests taken before and after the illness indicated a decrement afterward. If these hearing tests were accurate, it is conceivable that the illness also affected her vestibular system, contributing to her poor performance in the WALEC test. As her jumping tests were performed prior to her illness, vestibular complications from the illness would not have affected her performance during the actual moonwalker experiment.

Table B.1. Sharpened Romberg scores for moonwalker experimental subjects. Scores are in seconds. A perfect score is 240.

	Subject Code						
	B	**C**	**D**	**E**	**F**	**G**	**H**
SR TOTAL	**240**	**240**	**240**	**240**	**240**	**240**	**240**
SR #1	60	60	60	60	60	60	60
SR #2	--	--	--	--	--	--	--
SR #3	--	--	--	--	--	--	--

Table B.2. WALEC scores for moonwalker experimental subjects. Number of successful step scores are shown first for each trial (perfect score = 30). Inches from centerline scores follow (in parentheses).

	Subject Code						
	B	**C**	**D**	**E**	**F**	**G**	**H**
Steps (inches)	**30 (27)**	**30 (2)**	**30 (11)**	**30 (16)**	**30 (4)**	**30 (8)**	**24 (UTP)**
Trial #1	12 (UTP)	2 (UTP)	15 (15)	14 (12)	14 (4)	15 (4)	1 (UTP)
Trial #2	13 (23)	14 (2)	10 (UTP)	14 (16)	8 (UTP)	6 (UTP)	1 (UTP)
Trial #3	13 (11)	14 (3)	15 (0)	14 (4)	14 (14)	5 (UTP)	4 (UTP)
Trial #4	13 (16)	3 (UTP)	15 (11)		13 (UTP)	4 (UTP)	14 (11)
Trial #5	--	3 (UTP)	--	--	2 (UTP)	4 (UTP)	12 (UTP)
Trial #6	--	14 (0)	--	--	2 (UTP)	14 (4)	4 (UTP)
Trial #7	--	--	--	--	14 (0)	14 (8)	

B.2. FALSE PLATFORM SUBJECT ATAXIA RESULTS

The scores for the false platform experimental subjects for the SR and WALEC tests are shown in Table B.3 and Table B.4. All subjects achieved perfect scores for number of successful steps in the WALEC test. Three of the subjects also achieved perfect scores on the SR test, while the other three subjects (*mjg, yak, ssy*) performed above the 18th percentile level for SR. Based on these results, all subjects are judged free of abnormality.

Table B.3. Sharpened Romberg scores for false platform experimental subjects. Scores are in seconds. A perfect score is 240.

	Subject Code					
	djn	*aqk*	*czl*	*mjg*	*yak*	*ssy*
SR TOTAL	**240**	**240**	**240**	**186**	**205**	**136**
SR #1	60	60	60	6	25	9
SR #2	--	--	--	60	60	7
SR #3	--	--	--	--	--	60

Table B.4. WALEC scores for false platform experimental subjects. Number of successful step scores are shown first for each trial (perfect score = 30). Inches from centerline scores follow (in parentheses).

	Subject Code					
	djn	*aqk*	*czl*	*mjg*	*yak*	*ssy*
Steps (inches)	**30 (30)**	**30 (7)**	**30 (5)**	**30 (22)**	**30 (17)**	**30 (UTP)**
Trial #1	16 (19)	4 (UTP)	14 (3)	8 (UTP)	15 (13)	12 (UTP)
Trial #2	11 (UTP)	16 (7)	14 (5)	15 (9)	1 (UTP)	3 (UTP)
Trial #3	15 (14)	16 (14)	15 (2)	15 (13)	3 (UTP)	10 (UTP)
Trial #4	15 (16)	16 (0)	--	15 (30)	15 (27)	9 (UTP)
Trial #5	--	--	--	--	4 (UTP)	11 (UTP)
Trial #6	--	--	--	--	15 (4)	--

APPENDIX C. THREE LINK MODEL CODE

C.1. AUTOLEV CODE FOR THREE LINK MODEL

The file below contains the AutoLev commands used to construct the dynamic equations and derive the constraint forces for the three link model. Lines preceded by "->" are AutoLev responses, and all other lines are command inputs. Links A, B and C represent the shank, thigh and HAT segments, respectively. Points O, P and Q represent the ankle, knee and hip respectively. Generalized coordinates U1, U2 and U3 correspond to the angular velocities of the shank, thigh and HAT segments. Generalized coordinates U4 and U5 are the horizontal and vertical velocity components of the (fixed) point O, and are used to define constraint equations to solve for the ground reaction forces. Lines Lines 113 and 115 give the derived expressions for the forces at the ankle. Lines 126, 127 and 128 give the equations of motion for the linkage in terms of the generalized coordinates.

```
   (1) %File:  fb_3link.al
   (2) % For:  fixed-based 3-link inverted pendulum model
   (3) NEWTONIAN N
   (4) BODIES A, B, C
   (5) POINTS O
   (6) POINTS P, Q, R
   (7) %VARIABLES U{3}'
   (8) VARIABLES U{5}'
   (9) VARIABLES THA', THB', THC'
   (10) VARIABLES FA{2}, FB{2}, FC{2}
   (11) CONSTANTS G
   (12) CONSTANTS LA, LB
   (13) CONSTANTS LCA, LCB, LCC
   (14) CONSTANTS MA, MB, MC
   (15) CONSTANTS IA, IB, IC
   (16) MASS A=MA, B=MB, C=MC
   (17) INERTIA A, 0, 0, IA
-> (18) I_A_AO>> = IA*A3>*A3>

   (19) INERTIA B, 0, 0, IB
-> (20) I_B_BO>> = IB*B3>*B3>

   (21) INERTIA C, 0, 0, IC
-> (22) I_C_CO>> = IC*C3>*C3>

   (23) SIMPROT(N,A,3,-THA)
-> (24) N_A = [COS(THA), SIN(THA), 0; -SIN(THA), COS(THA), 0; 0, 0, 1]

   (25) SIMPROT(N,B,3,THB)
-> (26) N_B = [COS(THB), -SIN(THB), 0; SIN(THB), COS(THB), 0; 0, 0, 1]

   (27) SIMPROT(N,C,3,-THC)
-> (28) N_C = [COS(THC), SIN(THC), 0; -SIN(THC), COS(THC), 0; 0, 0, 1]

   (29) %POSITION VECTORS
   (30) P_O_P> = LA*A1>
-> (31) P_O_P> = LA*A1>
```

```
   (32) P_P_Q> = LB*B1>
-> (33) P_P_Q> = LB*B1>

   (34) P_O_Ao> = LCA*A1>
-> (35) P_O_AO> = LCA*A1>

   (36) P_P_Bo> = LCB*B1>
-> (37) P_P_BO> = LCB*B1>

   (38) P_Q_Co> = LCC*C1>
-> (39) P_Q_CO> = LCC*C1>

   (40) %KINEMATIC DIFF. EQS.
   (41) THA' = U1
-> (42) THA' = U1

   (43) THB' = U2
-> (44) THB' = U2

   (45) THC' = U3
-> (46) THC' = U3

   (47) %ANGULAR VELOCITIES
   (48) W_A_N> = -THA'*A3>
-> (49) W_A_N> = -U1*A3>

   (50) W_B_N> = THB'*B3>
-> (51) W_B_N> = U2*B3>

   (52) W_C_N> = -THC'*C3>
-> (53) W_C_N> = -U3*C3>

   (54) %VELOCITIES
   (55) %V_O_N> = 0>
   (56) V_O_N> = U4*N1> + U5*N2>
-> (57) V_O_N> = U4*N1> + U5*N2>

   (58) V2PTS(N,A,O,Ao)
-> (59) V_AO_N> = -LCA*U1*A2> + U4*N1> + U5*N2>

   (60) V2PTS(N,A,O,P)
-> (61) V_P_N> = -LA*U1*A2> + U4*N1> + U5*N2>

   (62) V2PTS(N,B,P,Bo)
-> (63) V_BO_N> = -LA*U1*A2> + LCB*U2*B2> + U4*N1> + U5*N2>

   (64) V2PTS(N,B,P,Q)
-> (65) V_Q_N> = -LA*U1*A2> + LB*U2*B2> + U4*N1> + U5*N2>

   (66) V2PTS(N,C,Q,Co)
-> (67) V_CO_N> = -LA*U1*A2> + LB*U2*B2> - LCC*U3*C2> + U4*N1> + U5*N2>

   (68) %MOTION CONSTRAINTS
   (69) AUXILIARY[1] = DOT(V_O_N>,N1>)     %No base motion in N1>
-> (70) AUXILIARY[1] = U4

   (71) AUXILIARY[2] = DOT(V_O_N>,N2>)     %No base motion in N2>
-> (72) AUXILIARY[2] = U5

   (73) CONSTRAIN(AUXILIARY[U4,U5])        %Solve for U4, U5
-> (74) U4 = 0
-> (75) U5 = 0
-> (76) U4' = 0
-> (77) U5' = 0
```

```
    (78) %ANGULAR ACCELERATION
    (79) ALF_A_N> = DT(W_A_N>, N)
->  (80) ALF_A_N> = -U1'*A3>

    (81) ALF_B_N> = DT(W_B_N>, N)
->  (82) ALF_B_N> = U2'*B3>

    (83) ALF_C_N> = DT(W_C_N>, N)
->  (84) ALF_C_N> = -U3'*C3>

    (85) %ACCELERATIONS OF MASS CENTERS AND POINTS
    (86) A_O_N> = 0>
->  (87) A_O_N> = 0>

    (88) A2PTS(N,A,O,Ao)
->  (89) A_AO_N> = -LCA*U1^2*A1> - LCA*U1'*A2>

    (90) A2PTS(N,A,O,P)
->  (91) A_P_N> = -LA*U1^2*A1> - LA*U1'*A2>

    (92) A2PTS(N,B,P,Bo)
->  (93) A_BO_N> = -LA*U1^2*A1> - LA*U1'*A2> - LCB*U2^2*B1> + LCB*U2'*B2>

    (94) A2PTS(N,B,P,Q)
->  (95) A_Q_N> = -LA*U1^2*A1> - LA*U1'*A2> - LB*U2^2*B1> + LB*U2'*B2>

    (96) A2PTS(N,C,Q,Co)
->  (97) A_CO_N> = -LA*U1^2*A1> - LA*U1'*A2> - LB*U2^2*B1> + LB*U2'*B2> - LCC*
         U3^2*C1> - LCC*U3'*C2>

    (98) %FORCES
    (99) GRAVITY(G*N1>)
-> (100) FORCE_AO> = G*MA*N1>
-> (101) FORCE_BO> = G*MB*N1>
-> (102) FORCE_CO> = G*MC*N1>

   (103) %FORCE_O> = FA1*N1> + FA2*N2>
   (104) %FORCE_P> = FB1*N1> + FB2*N2>
   (105) %FORCE_Q> = FC1*N1> + FC2*N2>
   (106) FORCE_Q> = -MC*G*N1> + MC*A_Co_N>
-> (107) FORCE_Q> = -LA*MC*U1^2*A1> - LA*MC*U1'*A2> - LB*MC*U2^2*B1> + LB*MC*
         U2'*B2> - LCC*MC*U3^2*C1> - LCC*MC*U3'*C2> - G*MC*N1>

   (108) FORCE_P> = FORCE_Q> - MB*G*N1> + MB*A_Bo_N>
-> (109) FORCE_P> = -LA*(MB+MC)*U1^2*A1> - LA*(MB+MC)*U1'*A2> - (LB*MC+LCB*MB)*
         U2^2*B1> + (LB*MC+LCB*MB)*U2'*B2> - LCC*MC*U3^2*C1> - LCC*MC*U3'*C2>
          - G*(MB+MC)*N1>

   (110) FORCE_O> = FORCE_P> - MA*G*N1> + MA*A_Ao_N>
-> (111) FORCE_O> = -(LCA*MA+LA*(MB+MC))*U1^2*A1> - (LCA*MA+LA*(MB+MC))*U1'*A2>
         - (LB*MC+LCB*MB)*U2^2*B1> + (LB*MC+LCB*MB)*U2'*B2> - LCC*MC*U3^2*C1>
          - LCC*MC*U3'*C2> - G*(MA+MB+MC)*N1>

   (112) FA1 = DOT(FORCE_O>,N1>)
-> (113) FA1 = -G*(MA+MB+MC) - LCC*MC*COS(THC)*U3^2 - (LB*MC+LCB*MB)*COS(THB)*
         U2^2 - (LCA*MA+LA*(MB+MC))*COS(THA)*U1^2 - LCC*MC*SIN(THC)*U3' - (LB*
         MC+LCB*MB)*SIN(THB)*U2' - (LCA*MA+LA*(MB+MC))*SIN(THA)*U1'

   (114) FA2 = DOT(FORCE_O>,N2>)
-> (115) FA2 = LCC*MC*SIN(THC)*U3^2 + (LCA*MA+LA*(MB+MC))*SIN(THA)*U1^2 + (LB*
         MC+LCB*MB)*COS(THB)*U2' - (LB*MC+LCB*MB)*SIN(THB)*U2^2 - LCC*MC*COS(
         THC)*U3' - (LCA*MA+LA*(MB+MC))*COS(THA)*U1'
```

```
   (116) FB1 = DOT(FORCE_P>,N1>)
-> (117) FB1 = -G*(MB+MC) - LCC*MC*COS(THC)*U3^2 - LA*(MB+MC)*COS(THA)*U1^2 - (
         LB*MC+LCB*MB)*COS(THB)*U2^2 - LCC*MC*SIN(THC)*U3' - LA*(MB+MC)*SIN(THA
         )*U1' - (LB*MC+LCB*MB)*SIN(THB)*U2'

   (118) FB2 = DOT(FORCE_P>,N2>)
-> (119) FB2 = LCC*MC*SIN(THC)*U3^2 + LA*(MB+MC)*SIN(THA)*U1^2 + (LB*MC+LCB*MB)
         *COS(THB)*U2' - (LB*MC+LCB*MB)*SIN(THB)*U2^2 - LCC*MC*COS(THC)*U3' -
         LA*(MB+MC)*COS(THA)*U1'

   (120) FC1 = DOT(FORCE_Q>,N1>)
-> (121) FC1 = -MC*(G+LA*COS(THA)*U1^2+LB*COS(THB)*U2^2+LCC*COS(THC)*U3^2+LA*
         SIN(THA)*U1'+LB*SIN(THB)*U2'+LCC*SIN(THC)*U3')

   (122) FC2 = DOT(FORCE_Q>,N2>)
-> (123) FC2 = MC*(LA*SIN(THA)*U1^2+LCC*SIN(THC)*U3^2+LB*COS(THB)*U2'-LB*SIN(
         THB)*U2^2-LA*COS(THA)*U1'-LCC*COS(THC)*U3')

   (124) %EQUATIONS OF MOTION
   (125) ZERO = FR() + FRSTAR()
-> (126) ZERO[1] = LA*(LB*MC+LCB*MB)*COS(THA+THB)*U2' + LA*(G*(MB+MC)*SIN(THA)+
         LCC*MC*SIN(THA-THC)*U3^2+(LB*MC+LCB*MB)*SIN(THA+THB)*U2^2+LA*(MB+MC)*
         U1'+LCC*MC*COS(THA-THC)*U3'-(LB*MC+LCB*MB)*COS(THA+THB)*U2') - G*LA*
         MB*SIN(THA) - G*LA*MC*SIN(THA) - G*LCA*MA*SIN(THA) - LA*(LCB*MB*SIN(
         THA+THB)*U2^2+MC*(LB*SIN(THA+THB)*U2^2+LCC*SIN(THA-THC)*U3^2)) - LA*
         LCC*MC*COS(THA-THC)*U3' - (IA+MA*LCA^2+MB*LA^2+MC*LA^2)*U1' - LA*MC*(
         LB*COS(THA+THB)*U2'-G*SIN(THA)-LB*SIN(THA+THB)*U2^2-LCC*SIN(THA-THC)*
         U3^2-LA*U1'-LCC*COS(THA-THC)*U3')

-> (127) ZERO[2] = LB*LCC*MC*COS(THB+THC)*U3' + LA*(LB*MC+LCB*MB)*COS(THA+THB)*
         U1' + LB*MC*(G*SIN(THB)+LA*SIN(THA+THB)*U1^2+LCC*SIN(THB+THC)*U3^2+LB*
         U2'-LA*COS(THA+THB)*U1'-LCC*COS(THB+THC)*U3') - G*LB*MC*SIN(THB) - G*
         LCB*MB*SIN(THB) - LA*LCB*MB*SIN(THA+THB)*U1^2 - LB*MC*(LA*SIN(THA+THB)
         *U1^2+LCC*SIN(THB+THC)*U3^2) - (IB+MB*LCB^2+MC*LB^2)*U2'

-> (128) ZERO[3] = LB*LCC*MC*COS(THB+THC)*U2' - G*LCC*MC*SIN(THC) - LCC*MC*(LB*
         SIN(THB+THC)*U2^2-LA*SIN(THA-THC)*U1^2) - (IC+MC*LCC^2)*U3' - LA*LCC*
         MC*COS(THA-THC)*U1'

-> (129) ZERO[4] = G*MA + G*MB + G*MC + LCA*MA*COS(THA)*U1^2 + MB*(LA*COS(THA)*
         U1^2+LCB*COS(THB)*U2^2) + MC*(LA*COS(THA)*U1^2+LB*COS(THB)*U2^2+LCC*
         COS(THC)*U3^2) + (LA*MB+LA*MC+LCA*MA)*SIN(THA)*U1' - G*(MB+MC) - G*(
         MA+MB+MC) - 2*LCC*MC*COS(THC)*U3^2 - LA*(MB+MC)*COS(THA)*U1^2 - 2*(LB*
         MC+LCB*MB)*COS(THB)*U2^2 - (LCA*MA+LA*(MB+MC))*COS(THA)*U1^2 - LCC*MC*
         SIN(THC)*U3' - LA*(MB+MC)*SIN(THA)*U1' - (LB*MC+LCB*MB)*SIN(THB)*U2'
          - (LCA*MA+LA*(MB+MC))*SIN(THA)*U1' - MC*(G+LA*COS(THA)*U1^2+LB*COS(
         THB)*U2^2+LCC*COS(THC)*U3^2+LA*SIN(THA)*U1'+LB*SIN(THB)*U2'+LCC*SIN(
         THC)*U3')

-> (130) ZERO[5] = 2*LCC*MC*SIN(THC)*U3^2 + LA*(MB+MC)*SIN(THA)*U1^2 + (LCA*MA+
         LA*(MB+MC))*SIN(THA)*U1^2 + MC*(LB*SIN(THB)*U2^2-LA*SIN(THA)*U1^2-LCC*
         SIN(THC)*U3^2) + (LB*MC+LCB*MB)*COS(THB)*U2' + (LA*MB+LA*MC+LCA*MA)*
         COS(THA)*U1' + MC*(LA*SIN(THA)*U1^2+LCC*SIN(THC)*U3^2+LB*COS(THB)*U2'-
         LB*SIN(THB)*U2^2-LA*COS(THA)*U1'-LCC*COS(THC)*U3') - LCA*MA*SIN(THA)*
         U1^2 - 2*(LB*MC+LCB*MB)*SIN(THB)*U2^2 - MB*(LA*SIN(THA)*U1^2-LCB*SIN(
         THB)*U2^2) - LCC*MC*COS(THC)*U3' - LA*(MB+MC)*COS(THA)*U1' - (LCA*MA+
         LA*(MB+MC))*COS(THA)*U1'
```

C.2. MATLAB CODE FOR THREE LINK MODEL

The function `torq_3link_invdyn.m` performs the inverse dynamics calculations for the three link model. It takes the angles, angular velocities and angular accelerations as inputs, and returns the generalized torques and constraint forces for each joint. This function calls three subroutines that calculate the acceleration dependent, velocity dependent, and gravitational terms separately (`acc_torq_3link.m`, `vel_torq_3link.m`, `stat_torq_3link.m`).

torq_3link_invdyn.m

```
function [tau, Fy, Fx] = torq_3link_invdyn(theta, dtheta, ddtheta,
LINK_PARAMS);
%function [tau, Fy, Fx] = torq_3link_invdyn(theta, dtheta, ddtheta,
LINK_PARAMS);
%note returns torques in *theta* generalized forces (no conversion)

[tau_g, Fy_g, Fx_g] = stat_torq_3link(theta,LINK_PARAMS);
[tau_v, Fy_v, Fx_v] = vel_torq_3link(theta,dtheta,LINK_PARAMS);
[tau_a, Fy_a, Fx_a] = acc_torq_3link(theta,ddtheta,LINK_PARAMS);

tau = tau_g + tau_v + tau_a;
Fy = Fy_g + Fy_v + Fy_a;
Fx = Fx_g + Fx_v + Fx_a;
```

acc_torq_3link.m

```
function [tau, Fy, Fx] = acc_torq_3link(theta, ddtheta,LINK_PARAMS);
%function [tau, Fy, Fx] = acc_torq_3link(theta, ddtheta,LINK_PARAMS);
%returns acceleration-dependent torques and forces

%modified to take vector inputs

l1 = LINK_PARAMS(1,1); lc1 = LINK_PARAMS(1,2); m1 = LINK_PARAMS(1,3); i1
= LINK_PARAMS(1,4);
l2 = LINK_PARAMS(2,1); lc2 = LINK_PARAMS(2,2); m2 = LINK_PARAMS(2,3); i2
= LINK_PARAMS(2,4);
l3 = LINK_PARAMS(3,1); lc3 = LINK_PARAMS(3,2); m3 = LINK_PARAMS(3,3); i3
= LINK_PARAMS(3,4);

H11 = m1*lc1^2 + m2*l1^2 + m3*l1^2 + i1;
H12 = -(m2*l1*lc2 + m3*l1*l2)*cos(theta(:,1) + theta(:,2));
H21 = H12;
H13 = m3*l1*lc3*cos(theta(:,1) - theta(:,3));
H31 = H13;
H22 = m2*lc2^2 + m3*l2^2 + i2;
H23 = -m3*l2*lc3*cos(theta(:,2) + theta(:,3));
H32 = H23;
H33 = m3*lc3^2 + i3;
```

```
Q1 = H11*ddtheta(:,1) + H12.*ddtheta(:,2) + H13.*ddtheta(:,3);
Q2 = H21.*ddtheta(:,1) + H22*ddtheta(:,2) + H23.*ddtheta(:,3);
Q3 = H31.*ddtheta(:,1) + H32.*ddtheta(:,2) + H33*ddtheta(:,3);

tau = [Q1, Q2, Q3];

Fy_1 =     - lc3*m3*sin(theta(:,3)).*ddtheta(:,3) ...
               - (l2*m3+lc2*m2)*sin(theta(:,2)).*ddtheta(:,2) ...
               - (lc1*m1+l1*(m2+m3))*sin(theta(:,1)).*ddtheta(:,1);

Fx_1 = -( - lc3*m3*cos(theta(:,3)).*ddtheta(:,3) ...
               + (l2*m3+lc2*m2)*cos(theta(:,2)).*ddtheta(:,2) ...
               - (lc1*m1+l1*(m2+m3))*cos(theta(:,1)).*ddtheta(:,1) );

Fy_2 =         - lc3*m3*sin(theta(:,3)).*ddtheta(:,3) ...
               - (l2*m3+lc2*m2)*sin(theta(:,2)).*ddtheta(:,2) ...
               - l1*(m2+m3)*sin(theta(:,1)).*ddtheta(:,1);

Fx_2 =          -( -lc3*m3*cos(theta(:,3)).*ddtheta(:,3) ...
               + (l2*m3+lc2*m2)*cos(theta(:,2)).*ddtheta(:,2) ...
               - l1*(m2+m3)*cos(theta(:,1)).*ddtheta(:,1) );

Fy_3 = -m3*(  l1*sin(theta(:,1)).*ddtheta(:,1) ...
                + l2*sin(theta(:,2)).*ddtheta(:,2) ...
                  + lc3*sin(theta(:,3)).*ddtheta(:,3));
Fx_3 = -( m3*( -l1*cos(theta(:,1)).*ddtheta(:,1) ...
                     + l2*cos(theta(:,2)).*ddtheta(:,2) ...
                     - lc3*cos(theta(:,3)).*ddtheta(:,3)) );

Fy = [Fy_1, Fy_2, Fy_3];
Fx = [Fx_1, Fx_2, Fx_3];
```

vel_torq_3link.m

```
function [tau, Fy, Fx] = vel_torq_3link(theta, dtheta, LINK_PARAMS);
%function [tau, Fy, Fx] = vel_torq_3link(theta, dtheta, LINK_PARAMS);
%returns velocity dependent components of torques and forces

%modified to take vector inputs

%l1 = 0.4247; l2 = 0.4718; l3 = 0.8307;
%lc1 = 0.2617; lc2 = 0.2690; lc3 = 0.3064;
%m1 = 7.94; m2 = 19.00; m3 = 45.57;

l1 = LINK_PARAMS(1,1); lc1 = LINK_PARAMS(1,2); m1 = LINK_PARAMS(1,3); i1
= LINK_PARAMS(1,4);
l2 = LINK_PARAMS(2,1); lc2 = LINK_PARAMS(2,2); m2 = LINK_PARAMS(2,3); i2
= LINK_PARAMS(2,4);
l3 = LINK_PARAMS(3,1); lc3 = LINK_PARAMS(3,2); m3 = LINK_PARAMS(3,3); i3
= LINK_PARAMS(3,4);

h122 = l1*(m2*lc2 + m3*l2)*sin(theta(:,1) + theta(:,2));
h211 = h122;
h133 = m3*l1*lc3*sin(theta(:,1) - theta(:,3));
h311 = -h133;
h322 = m3*l2*lc3*sin(theta(:,2) + theta(:,3));
```

```
h233 = h322;

Q1 = h122.*(dtheta(:,2).^2) + h133.*(dtheta(:,3).^2);
Q2 = h211.*(dtheta(:,1).^2) + h233.*(dtheta(:,3).^2);
Q3 = h311.*(dtheta(:,1).^2) + h322.*(dtheta(:,2).^2);

tau = [Q1, Q2, Q3];

%Forces (distal on proximal)
Fy_1 =   - lc3*m3*cos(theta(:,3)).*(dtheta(:,3).^2) ...
            - (l2*m3+lc2*m2)*cos(theta(:,2)).*(dtheta(:,2).^2) ...
            - (lc1*m1+l1*(m2+m3))*cos(theta(:,1)).*(dtheta(:,1).^2);

Fx_1 =   -( lc3*m3*sin(theta(:,3)).*(dtheta(:,3).^2) ...
               + (lc1*m1+l1*(m2+m3))*sin(theta(:,1)).*(dtheta(:,1).^2)
...
               - (l2*m3+lc2*m2)*sin(theta(:,2)).*(dtheta(:,2).^2) );

Fy_2 =   - lc3*m3*cos(theta(:,3)).*(dtheta(:,3).^2) ...
            - l1*(m2+m3)*cos(theta(:,1)).*(dtheta(:,1).^2) ...
            - (l2*m3+lc2*m2)*cos(theta(:,2)).*(dtheta(:,2).^2);

Fx_2 = -( lc3*m3*sin(theta(:,3)).*(dtheta(:,3).^2) ...
              + l1*(m2+m3)*sin(theta(:,1)).*(dtheta(:,1).^2) ...
              - (l2*m3+lc2*m2)*sin(theta(:,2)).*(dtheta(:,2).^2) );

Fy_3 = -m3*(l1*cos(theta(:,1)).*(dtheta(:,1).^2) ...
                + l2*cos(theta(:,2)).*(dtheta(:,2).^2) ...
                  + lc3*cos(theta(:,3)).*(dtheta(:,3).^2) );

Fx_3 = -( m3*(l1*sin(theta(:,1)).*(dtheta(:,1).^2) ...
                  + lc3*sin(theta(:,3)).*(dtheta(:,3).^2) ...
                    - l2*sin(theta(:,2)).*(dtheta(:,2).^2)) );

Fy = [Fy_1, Fy_2, Fy_3];
Fx = [Fx_1, Fx_2, Fx_3];
```

stat_torq_3link.m

```
function [tau, Fy, Fx] = stat_torq_3link(theta,LINK_PARAMS);
%function [tau, Fy, Fx] = stat_torq_3link(theta,LINK_PARAMS);
%returns static gravity dependent force and torque terms

%modified to take vector inputs

g = -9.8; %m/s^2

%l1 = 0.4247; l2 = 0.4718; l3 = 0.8307;
%lc1 = 0.2617; lc2 = 0.2690; lc3 = 0.3064;
%m1 = 7.94; m2 = 19.00; m3 = 45.57;

l1 = LINK_PARAMS(1,1); lc1 = LINK_PARAMS(1,2); m1 = LINK_PARAMS(1,3); i1
= LINK_PARAMS(1,4);
l2 = LINK_PARAMS(2,1); lc2 = LINK_PARAMS(2,2); m2 = LINK_PARAMS(2,3); i2
= LINK_PARAMS(2,4);
```

```
l3 = LINK_PARAMS(3,1); lc3 = LINK_PARAMS(3,2); m3 = LINK_PARAMS(3,3); i3
= LINK_PARAMS(3,4);

G1 = m1*g*lc1*sin(theta(:,1)) + m2*g*l1*sin(theta(:,1)) +
m3*g*l1*sin(theta(:,1));
G2 = m2*g*lc2*sin(theta(:,2)) + m3*g*l2*sin(theta(:,2));
G3 = m3*g*lc3*sin(theta(:,3));

Q1 = G1;
Q2 = G2;
Q3 = G3;

tau = [Q1, Q2, Q3];

[nsamp,crap] = size(theta);
v1 = ones(nsamp,1);
Fy_1 = -g*(m1 + m2 + m3);
Fy_2 = -g*(m2 + m3);
Fy_3 = -g*(m3);
Fy = [Fy_1*v1, Fy_2*v1, Fy_3*v1];
Fx = 0*theta;
```

REFERENCES

Adamovich, S. V. (1992). "How does the nervous system control the equilibrium trajectory?" *Behavioral and Brain Sciences*, 15(4):704.

Alexander, R. M. and A. Vernon (1975). "Mechanics of hopping by kangaroos (Macropodidae)." *Journal of Zoology*, 177:265-303.

Allum, J. and C. Pfaltz (1985). "Visual and vestibular contributions to pitch sway stabilization in the ankle muscles of normals and patients with bilateral peripheral vestibular deficits." *Experimental Brain Research*, 58:82-94.

Allum, J. and F. Honegger (1992). "A postural model of balance-correcting movement strategies." *Journal of Vestibular Research*, 2:323-347.

Allum, J., F. Honegger and H. Schicks (1993). "Vestibular and proprioceptive modulation of postural synergies in normal subjects." *Journal of Vestibular Research*, 3:59-85.

Allum, J., F. Honegger and H. Schicks (1994). "The influence of a bilateral peripheral vestibular deficit on postural synergies." *Journal of Vestibular Research*, 4:49-70.

An, K. N., K. R. Kaufman and E. Y. S. Chao (1989). "Physiological considerations of muscle force through the elbow joint." *Journal of Biomechanics*, 22:1249-1256.

Antonsson, E. K. and R. W. Mann (1989). "Automatic 6-D.O.F. kinematic trajectory acquisition and analysis." *Journal of Dynamic Systems, Measurement, and Control*, 111:31-39.

Asada, H. and J.-J. Slotine (1986). Robot Analysis and Control. New York: John Wiley & Sons.

Baker, J. T., A. E. Nicogossian, G. W. Hoffler, R. L. Johnson and J. Hordinsky (1977). Changes in the achilles tendon reflexes following Skylab missions. In R. S. Johnston and L. F. Dietlein (Eds.), Biomedical Results from Skylab (pp. 104-112). NASA.

Barin, K. (1989). "Evaluation of a generalized model of human postural dynamics and control in the sagittal plane." *Biological Cybernetics*, 61:37-50.

Bizzi, E., N. Accornero, W. Chapple and N. Hogan (1984). "Posture control and trajectory formation during arm movement." *Journal of Neuroscience*, 4:2738-2744.

Bizzi, E., N. Hogan, F. A. Mussa-Ivaldi and S. Giszter (1992a). "Does the nervous system use equilibrium-point control to guide single and multiple joint movements?" *Behavioral and Brain Sciences*, 15:603-613.

Bizzi, E., N. Hogan, F. A. Mussa-Ivaldi and S. Giszter (1992b). "The equilibrium point framework: A point of departure." *Behavioral and Brain Sciences*, 15:808-844.

Bloomberg, J., M. Reschke, W. Huebner and B. Peters (1992). "The effects of target distance on eye and head movement during locomotion." *Annals of the New York Academy of Sciences*, 656(Sensing and Controlling Motion):699-707.

Bloomberg, J. J., B. T. Peters, W. T. Huebner, S. L. Smith and M. F. Reschke (1997). "Locomotor head-trunk coordination strategies following space flight." *Journal of Vestibular Research*, (in press).

Bortolami, S. B., P. O. Riley and D. E. Krebs (1997). "Numerical differentiation of tracking data of human motion: the virtual accelerometer." *Journal of Dynamic Systems, Measurement and Control* (in review).

Camana, P. C., H. Hemami and C. W. Stockwell (1977). "Determination of feedback for human posture control without physical intervention." *Journal of Cybernetics*, 7:199-225.

Cavagna, G. A. (1970). "Elastic bounce of the body." *Journal of applied physiology*, 29:279-282.

Chekirda, I. F., A. V. Bogdashevskiy, A. V. Yeremin and I. A. Kolosov (1971). "Coordination structure of walking of Soyuz-9 crew members before and after flight." *Kosmicheskaya Biologiya i Meditsina*, 5(6):48-52.

Cl_ment, G., V. S. Gurfinkel, F. Lestienne, M. I. Lipshits and K. E. Popov (1984). "Adaptation of postural control to weightlessness." *Experimental Brain Research*, 57:61-72.

Dyhre-Poulsen, P. and A. M. Laursen (1984). "Programmed Electromyographic Activity and Negative Incremental Muscle Stiffness in Monkeys Jumping Downward." *Journal of Physiology*, 350:121-136.

Dyhre-Poulsen, P., E. B. Simonsen and M. Voigt (1991). "Dynamic Control of Muscle Stiffness and H Reflex Modulation During Hopping and Jumping in Man." *Journal of Physiology*, 437:287-304.

Farley, C. T. and O. González (1996). "Leg Stiffness and Stride Frequency in Human Running." *Journal of Biomechanics*, 29(2):181-186.

Feldman, A. G. (1966). "Functional tuning of the nervous system during control of movement or maintenance of a steady posture. III. Mechanographic analysis of the execution by man of the simplest motor task." *Biophysics*, 11:766-775.

Feldman, A. G. (1986). "Once more for the equilibrium point hypothesis (λ model) for motor control." *Journal of Motor Behavior*, 18(1):17-54.

Feldman, A. G. and M. F. Levin (1995). "The origin and use of positional frames of reference in motor control." *Behavioral and Brain Sciences*, 18:723-806.

Fijan, R. S. (1985). Axes of rotation of the joints of the human lower extremity. Masters thesis, M.I.T.

Flanagan, J. R. and A. M. Wing (1993). "Modulation of grip force with load force during point-to-point arm movements." *Experimental Brain Research*, 95:131-143.

Flash, T. (1987). "The Control of Hand Equilibrium Trajectories in Multi-Joint Arm Movements." *Biological Cybernetics*, 57:257-274.

Fregly, A. R. and A. Graybiel (1966). An ataxia test battery not requiring the use of rails (No. NAMI-985. NASA R-93.) Naval Aerospace Medical Institute/NASA.

Gelb, A. (Ed.). (1974). Applied Optimal Estimation. Cambridge, MA: MIT Press.

Gibran, K. (1923). The Prophet. New York: Alfred A Knopf.

Gomi, H. and M. Kawato (1996). "Equilibrium-Point Control Hypothesis Examined by Measured Arm Stiffness During Multijoint Movement." *Science*, 272:117-120.

Gottlieb, G. L., Q. Song, D. Hong and D. M. Corcos (1996). "Coordinating two degrees of freedom during human arm movement: Load and speed invariance of relative joint torques." *Journal of Neurophysiology*, 76(5).

Grace, A. (1993). Optimization Toolbox User's Guide. Natick, MA: The MathWorks, Inc.

Greene, P. R. and T. A. McMahon (1979). "Reflex Stiffness of Man's Anti-Gravity Muscles During Kneebends While Carrying Extra Weights." *Journal of Biomechanics*, 12:881-891.

Greenwood, R. and A. Hopkins (1976). "Muscle responses during sudden falls in man." *Journal of Physiology (London)*, 254:507-518.

Gribble, P. L., D. J. Ostry, V. Sanguineti and R. Laboissiere (1997). "Are complex control signals required for human arm movement?" *(in review)*.

Grierson, Y. (1992). A Three-Dimensional Whole Body Model for Dynamic Motion Analysis. Masters Thesis, Massachusetts Institute of Technology.

Grillner, S. (1972). "The role of muscle stiffness in meeting the changing postural and locomotor requirements for force development by the ankle extensors." *Acta Physiol. Scand.*, 86:92-103.

Gurfinkel, V. (1994). "The Mechanisms of Postural Regulation in Man." *Soviet Scientific Reviews, Section F: Physiology and General Biology Reviews*, 7(5):59-89.

Gutman, S. R. and G. L. Gottlieb (1992). "Virtual trajectory as a solution of the inverse dynamic problem." *Behavioral and Brain Sciences*, 15(4):752-754.

Hasan, Z. (1992). "Is stiffness the mainspring of posture and movement?" *Behavioral and Brain Sciences*, 15(4):756-758.

He, J., R. Kram and T. A. McMahon (1991). "Mechanics of Running under Simulated Low Gravity." *Journal of Applied Physiology*, 71(3):863-870.

Hemami, H. and A. Katbab (1982). "Constrained inverted pendulum model for evaluating upright postural stability." *Journal of Dynamic Systems, Measurement, and Control*, 104:343-349.

Hill, A. V. (1922). "The maximum work and mechanical efficiency of human muscles, and their most economical speed." *Journal of Physiology*, 56:19-41.

Hogan, N. (1984a). "Adaptive control of mechanical impedance by coactivation of antagonist muscles." *IEEE Transactions on Automatic Control*, AC-29(8):681-690.

Hogan, N. (1984b). "An organizing principle for a class of voluntary movements." *The Journal of Neuroscience*, 4(11):2745-2754.

Hogan, N. (1985). "Impedance control: An approach to manipulation--Part I: Theory." *Jornal of Dynamic Systems, Measurement, and Control*, 107:1-7.

Hogan, N. (1987). Stable execution of contact tasks using impedance control. In IEEE International Conference on Robotics and Automation.

Hogan, N., E. Bizzi, F. Mussa-Ivaldi and T. Flash (1987). Chapter 6: Controlling Multijoint Motor Behavior. In K. B. Pandolf (Eds.), Exercise and Sport Sciences Reviews (pp. 153-190). MacMillan Publishing Company.

Hollerbach, J. M. and C. G. Atkeson (1987). "Deducing planning variables from experimental arm trajectories: Pitfalls and possibilities." *Biological Cybernetics*, 56:279-292.

Homick, J. L. and M. F. Reschke (1977). "Postural equilibrium following exposure to weightless space flight." *Acta Otolaryngologica*, 83:455-464.

Horstmann, G. and V. Dietz (1990). "A basic posture control mechanism: the stabilization of the centre of gravity." *Electroencephalography and clinical Neurophysiology*, 76:165-176.

Houk, J. C. (1979). "Regulation of Stiffness by Skeletomotor Reflexes." *Annual Reviews in Physiology*, 41:99-114.

Hull, D. G. (1997). "Conversion of optimal control problems into parameter optimization problems." *Journal of Guidance, Control and Dynamics*, 20(1):57-60.

Kenyon, R. V. and L. R. Young (1986). "M.I.T./Canadian vestibular experiments on the Spacelab-1 mission: 5. Postural responses following exposure to weightlessness." *Experimental Brain Research*, 64:335-346.

Kozlovskaya, I. B., Y. V. Kriendich, V. S. Oganov and O. P. Koserenko (1981). "Pathophysiology of motor functions in prolonged manned space flights." *Acta Astronautica*, 8(9-10):1059-1072.

Krauss, T. P., L. Shure and J. N. Little (1994). Signal Processing Toolbox User's Guide. Natick, MA: The MathWorks, Inc.

Kuo, A. (1992). "An Optimal Control Model for Analyzing Human Postural Balance." *IEEE Transactions on Biomedical Engineering.*

Kuo, A. D. and F. E. Zajac (1992a). "Human Standing Posture: Multijoint Movement Strategies Based on Biomechanical Constraints." *Progress in Brain Research.*

Kuo, A. D. and F. E. Zajac (1992b). "What is the nature of the feedforward component in motor control?" *Behavioral and Brain Sciences*, 15(4):767.

Kwakernaak, H. and R. Sivan (1972). Linear Optimal Control Systems. New York: John Wiley & Sons, Inc.

Lackner, J. R. and P. DiZio (1994). "Rapid adaptation to Coriolis force perturbations of arm trajectory." *Journal of Neurophysiology*, 72:299-313.

Latash, M. L. and G. L. Gottlieb (1991). "Reconstruction of elbow joint compliant characteristics during fast and slow voluntary movements." *Neuroscience*, 43(697-712).

Layne, C. S., P. V. McDonald, C. J. Pruett, G. Jones and J. J. Bloomberg (1995). "Preparatory postural control after space flight." *Society for Neuroscience Abstracts*, 21:138.

Layne, C. S., P. V. McDonald and J. J. Bloomberg (1996). "Neuromuscular activation patterns during locomotion after space flight." *Experimental Brain Research*, 113(1):104.

LeBlanc, A., R. Rowe, V. Schneider, H. Evans and T. Hedrick (1995). "Regional muscle loss after short duration spaceflight." *Aviation, Space, and Environmental Medicine*, 66(12):1151-1154.

Ljung, L. (1993). System Identification Toolbox User's Guide. Natick, MA: The MathWorks, Inc.

MacKinnon, C. and D. Winter (1993). "Control of whole body balance in the frontal plane during human walking." *Journal of Biomechanics*, 26(6):633-644.

Martin, T. P., V. R. Edgerton and R. E. Grindeland (1988). "Influence of spaceflight on rat skeletal muscle." *Journal of Applied Physiology*, 65:2318-2325.

McCollum, G. and T. Leen (1989). "Form and exploration of mechanical stability limits in erect stance." *Journal of Motor Behavior*, 21:225-244.

McConville, J., T. Churchill, I. Kaleps, C. Clauser and J. Cuzzi (1980). Anthropometric Relationships of Body and Body Segment Moments of Inertia (Technical Report No. AFAMRL-TR-80-119). Anthropology Research Project, Inc.; Aerospace Medical Division, AFSC.

McDonald, P. V., C. Basdogan, J. J. Bloomberg and C. S. Layne (1996). "Lower limb kinematics during treadmill walking after space flight: Implications for gaze stabilization." *Experimental Brain Research*, 112(2):325.

McIntyre, J. and E. Bizzi (1993). "Servo hypotheses for the biological control of movement." *Journal of Motor Behavior*, 25(3):193-202.

McKinley, P. A. and J. L. Smith (1983). "Visual and Vestibular Contributions to Prelanding EMG During Jump-downs in Cats." *Experimental Brain Research*, 52:439-448.

McKinley, P. A., J. L. Smith and R. J. Gregor (1983). "Responses of Elbow Extensors to Landing Forces During Jump Downs in Cats." *Experimental Brain Research*, 49:218-228.

McKinley, P. and A. Pedotti (1992). "Motor strategies in landing from a jump: the role of skill in task execution." *Experimental Brain Research*, 90:427-440.

McMahon, T. A. and P. R. Greene (1979). "The influence of track compliance on running." *Journal of Biomechanics*, 12:893-904.

McMahon, T. (1984). Muscles, Reflexes, and Locomotion. Princeton, NJ: Princeton University Press.

McMahon, T. A. and G. C. Cheng (1990). "The Mechanics of Running: How Does Stiffness Couple with Speed?" *Journal of Biomechanics*, 23(Suppl. 1):65-78.

McNitt-Gray, J. (1993). "Kinetics of the lower extremities during drop landings from three heights." *Journal of Biomechanics*, 26(9):1037-1046.

Melvill Jones, G. and D. G. D. Watt (1971a). "Observations on the control of stepping and hopping movements in man." *Journal of Physiology*, 219:709-727.

Melvill Jones, G. and D. G. D. Watt (1971b). "Muscular Control of Landing from Unexpected Falls in Man." *Journal of Physiology*, 219:729-737.

Molina-Negro, P., R. A. Bertrand, E. Martin and Y. Gioani (1980). "The role of the vestibular system in relation to muscle tone and postural reflexes in man." *Acta Otolaryngologica*, 89:524-533.

Mussa-Ivaldi, F., N. Hogan and E. Bizzi (1985). "Neural, mechanical, and geometric factors subserving arm posture in humans." *The Journal of Neuroscience*, 5(10):2732-2743.

Nagata, S., M. Sekiguchi and K. Asakawa (1990). "Mobile Robot Control by a Structured Hierarchical Neural Network." in *IEEE Control Systems Magazine* pp. 69-76.

Nashner, L. M. and A. Berthoz (1978). "Visual contribution to rapid motor responses during postural control." *Brain Research*, 150:403-407.

Nashner, L. and G. McCollum (1985). "The organization of human postural movements: A formal basis and experimental synthesis." *The Behavioral and Brain Sciences*, 8:135-172.

Nichols, T. R. and J. C. Houk (1976). "The improvement in linearity and the regulation of stiffness that results from the actions of the stretch reflex." *Journal of Neurophysiology*, 39:119-142.

Nicogossian, A., C. Huntoon and S. Pool (1994). Space Physiology and Medicine (3 ed.) Philadelphia: Lea & Febiger.

Paloski, W. H., M. F. Reschke, F. O. Black, D. D. Doxey and D. L. Harm (1993). "Vestibular ataxia following shuttle flights: Effects of transient microgravity on otolith-mediated sensorimotor control of posture." *American Journal of Otolaryngology*, 14(1).

Pandy, M., F. Zajac, E. Sim and W. Levine (1990). "An optimal control model for maximum-height jumping." *Journal of Biomechanics*, 23(12):1185-1198.

Pandy, M. and F. Zajac (1991). "Optimal muscular coordination strategies for jumping." *Journal of Biomechanics*, 24(1):1-10.

Parker, D. E., M. F. Reschke, A. P. Arrot and B. K. Lichtenberg (1985). "Otolith tilt-translation reinterpretation following prolonged weightlessness: Implications for preflight training." *Aviation, Space, and Environmental Medicine*, 56:601-606.

Rack, P. M. and D. R. Westbury (1974). "The short range stiffness of active mammalian muscle and its effect on mechanical properties." *Journal of Physiology (London)*, 240:331-350.

Rack, P. M. H. (1981). "Limitations of somatosensory feedback in control of posture and movements." In: Handbook of Physiology: The Nervous System, vol 2. V. B Brooks (ed.) American Physiological Society.

Raibert, M. (1990). "Trotting, Pacing and Bounding by a Quadruped Robot." *Journal of Biomechanics*, 23(Suppl. 1):79-98.

Reschke, M. F., D. J. Anderson and J. L. Homick (1986). "Vestibulo-spinal response modification as determined with the H-reflex during the Spacelab-1 flight." *Experimental Brain Research*, 64:367-379.

Riley, D. A. and S. Ellis (1983). "Research on the adaptation of skeletal muscle to hypogravity: past and future directions." *Advances in Space Research*, 3(9):191-197.

Riley, P. O. (1988). Modeling the biomechanics of posture and balance. Ph.D. Thesis, M.I.T.

Schultz, K. U. (1995). Etiology of perceived strength changes in the muscles of the legs following locomotion under simulated low gravity. Masters thesis, M.I.T.

Selbie, W. S. and G. E. Caldwell (1996). "A simulation study of vertical jumping from different starting postures." *Journal of Biomechanics*, 29(9):1137-1146.

Shadmehr, R. and F. Mussa-Ivaldi (1994). "Adaptive representation of dynamics during learning of a motor task." *Journal of Neuroscience*, 14(5):3208-3224.

Slotine, J.-J. E. (1985). "The robust control of robot manipulators." *International Journal of Robotics Research*, 4:49-64.

Thompson, H. W. and P. A. McKinley (1988). "Effect of visual perturbations in programming landing from a jump in humans." *Society for Neuroscience Abstracts*, 14:66.

Watt, D. G. D., K. E. Money, R. L. Bondar, R. B. Thirsk, M. Garneau and P. Scully-Power (1985). "Canadian medical experiments on Shuttle Flight 41-G." *Canadian Aeronautics and Space Journal*, 31(3):215-226.

Watt, D. G. D., K. E. Money and L. M. Tomi (1986). "M.I.T./Canadian vestibular experiments on the Spacelab-1 mission: 3. Effects of prolonged weightlessness on a human otolith-spinal reflex." *Experimental Brain Research*, 64:308-315.

Wicke, R. W. and C. M. Oman (1982). "Visual and graviceptive influences on lower leg EMG activity in humans during brief falls." *Experimental Brain Research*, 46:324-330.

Wilkinson, L. (1989). SYSTAT: The System for Statistics. Evanston, IL: SYSTAT, Inc.

Winters, J., L. Stark and A.-H. Seif-Naraghi (1988). "An analysis of the sources of musculoskeletal impedance." *Journal of Biomechanics*, 21(12):1011-1025.

Woltring, H. J. (1986). "A Fortran package for generalized, cross-validatory spline smoothing and differentiation." *Advances in Engineering Software*, 8(2):104-113.

Won, J. and N. Hogan (1995). "Stability properties of human reaching movements." *Experimental Brain Research*, 107:125-136.

Young, J., R. Chandler and C. Snow (1983). Anthropometric and Mass Distribution Characteristics of the Adult Female (No. FAA-AM-83-16). Civil Aeromedical Institute, Federal Aviation Administration.

Young, L., C. Oman, D. Watt, K. Money, B. Lichtenberg, R. Kenyon and A. Arrot (1986). "M.I.T./Canadian vestibular experiments on the Spacelab-1 mission: 1. Sensory adaptation to weightlessness and readaptation to one-g: an overview." *Experimental Brain Research*, 64:291-298.

Zajac, F. (1993). "Muscle Coordination of Movement: A Perspective." *Journal of Biomechanics*, 26(Suppl. 1):109-124.